

Winter 1993

The structure of water mass, salt, and temperature transports within intermediate depths of the western tropical Atlantic Ocean

Frank Lee Bub

University of New Hampshire, Durham

Follow this and additional works at: <https://scholars.unh.edu/dissertation>

Recommended Citation

Bub, Frank Lee, "The structure of water mass, salt, and temperature transports within intermediate depths of the western tropical Atlantic Ocean" (1993). *Doctoral Dissertations*. 1762.

<https://scholars.unh.edu/dissertation/1762>

This Dissertation is brought to you for free and open access by the Student Scholarship at University of New Hampshire Scholars' Repository. It has been accepted for inclusion in Doctoral Dissertations by an authorized administrator of University of New Hampshire Scholars' Repository. For more information, please contact nicole.hentz@unh.edu.

INFORMATION TO USERS

This manuscript has been reproduced from the microfilm master. UMI films the text directly from the original or copy submitted. Thus, some thesis and dissertation copies are in typewriter face, while others may be from any type of computer printer.

The quality of this reproduction is dependent upon the quality of the copy submitted. Broken or indistinct print, colored or poor quality illustrations and photographs, print bleedthrough, substandard margins, and improper alignment can adversely affect reproduction.

In the unlikely event that the author did not send UMI a complete manuscript and there are missing pages, these will be noted. Also, if unauthorized copyright material had to be removed, a note will indicate the deletion.

Oversize materials (e.g., maps, drawings, charts) are reproduced by sectioning the original, beginning at the upper left-hand corner and continuing from left to right in equal sections with small overlaps. Each original is also photographed in one exposure and is included in reduced form at the back of the book.

Photographs included in the original manuscript have been reproduced xerographically in this copy. Higher quality 6" x 9" black and white photographic prints are available for any photographs or illustrations appearing in this copy for an additional charge. Contact UMI directly to order.

U·M·I

University Microfilms International
A Bell & Howell Information Company
300 North Zeeb Road, Ann Arbor, MI 48106-1346 USA
313/761-4700 800/521-0600

Order Number 9420570

**The structure of water mass, salt, and temperature transports
within intermediate depths of the western tropical Atlantic
Ocean**

Bub, Frank Lee, Ph.D.

University of New Hampshire, 1993

U·M·I

300 N. Zeeb Rd.
Ann Arbor, MI 48106

**THE STRUCTURE OF WATER MASS, SALT, AND TEMPERATURE TRANSPORTS
WITHIN INTERMEDIATE DEPTHS OF THE WESTERN TROPICAL ATLANTIC OCEAN**

BY

FRANK LEE BUB

**B. S., Lehigh University, 1968
M. S., Naval Postgraduate School, 1974**

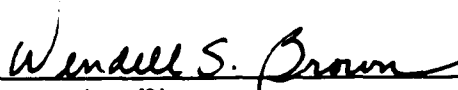
DISSERTATION

**Submitted to the University of New Hampshire
in Partial Fulfillment of
the Requirements for the Degree of**

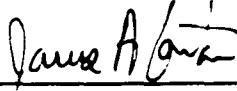
**Doctor of Philosophy
in
Earth Sciences: Oceanography**

December, 1993

This dissertation has been examined and approved.



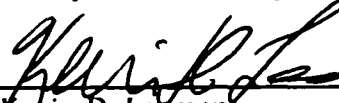
Dissertation Director,
Dr. Wendell S. Brown
Professor of Earth Sciences
and Earth, Oceans and Space
University of New Hampshire



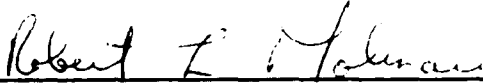
Dr. James A. Carton
Associate Professor of Meteorology
University of Maryland



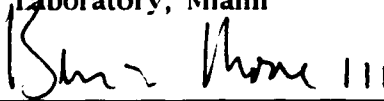
Dr. Robert C. Harriss
Professor of Earth Sciences
and Earth, Oceans and Space
University of New Hampshire



Dr. Kevin D. Leaman
Professor of Physical Oceanography
Rosenstiel School of Marine and Atmospheric Science
University of Miami



Dr. Robert L. Molinari
Director, Physical Oceanography
Atlantic Oceanographic and Meteorological
Laboratory, Miami



Dr. Berrien Moore, III
Associate Professor of Mathematics
and Professor of Earth, Oceans and Space
University of New Hampshire

1 December 1993

Date

DEDICATED TO

Susan Rines Bub

**My wife, partner, and friend, whose love and understanding
kept me going and helped me finish,**

AND

Kristen Lee Bub

Our daughter, who said we could do it,

AND

Robert A. and Ruth R. Bub

**My parents, who taught me the value of
hard work and perseverance.**

ACKNOWLEDGEMENTS

My heartfelt appreciation is extended to Dr. Wendell Brown, who was my able and enthusiastic advisor in this research.

I am indebted to the other members of my committee whose sage advice and timely assistance made this a better piece of work. In particular, I appreciate the attention and interest of Dr. Robert Molinari.

The friendship and intellectual discussions by Ilson Da Silveira helped me clarify my thoughts and explain myself better. The assistance of Karen Garrison and Russ Gelinas are appreciated. The many efforts by Mariellen Lee to find the money and keep us going, despite some hard times, are much appreciated.

The dedication and hard work of the crews of the NOAA Ships Mount Mitchell and Malcolm Baldrige are to be commended. The CTD observations by AOML, and Pegasus velocity observations by University of Miami scientists were essential. The combined efforts by these various groups produced the beautiful data sets upon which this research is based.

Many of the graphics in this dissertation were prepared in the University of New Hampshire Visualization Laboratory which was donated for the University's use by the Digital Equipment Company.

I am deeply indebted to the National Oceanographic and Atmospheric Administration (NOAA) and the National Science Foundation (NSF), whose funding supported this work.

TABLE OF CONTENTS

DEDICATION	iii
ACKNOWLEDGEMENTS	iv
TABLE OF CONTENTS	v
LIST OF TABLES	vii
LIST OF FIGURES	viii
ABSTRACT	xii
I. INTRODUCTION	
A. Goals and objectives	1
B. Context	2
C. The WESTRAX region	2
D. Historical background	6
E. Dissertation framework	11
II. MEASUREMENTS AND DATA REDUCTION	
A. WESTRAX expeditions	14
B. CTD hydrographic measurements	16
C. Pegasus velocity measurements	22
D. A comparison between Pegasus and ADCP observations	27
III. DATA ANALYSES - INTERPOLATION AND STREAM FUNCTION	
A. Interpolation of data to a grid	32
B. Divergent versus non-divergent transports	37
C. Stream function analysis	37
IV. VELOCITY STRUCTURE	
A. Overview	42
B. WESTRAX region transport structure	49
C. Transport associated with retroflection eddies	55
V. WATER MASSES	
A. Definitions and background	61

B. Tropical Atlantic water masses	62
C. WESTRAX region water masses	70
VI. WATER MASS TRANSPORT STRUCTURE	
A. Northern and southern water mass origins	89
B. Water mass transport pathways	91
D. Transport associated with retroflection eddies	91
E. Estimated mixing transports	102
VII. DISCUSSION	
A. Oceanic current summary	106
B. Eddy-scale transport summary	109
C. Mixing transport summary	109
D. Some comparisons with other studies	110
E. A speculative model of the annual evolution of structure	112
F. Unresolved issues	115
VIII. CONCLUSIONS	117
APPENDICES	
A. INTERPOLATION ALGORITHM	119
B. THE STREAM FUNCTION EQUATION	122
C. TWO-DIMENSIONAL FINITE DIFFERENCE ANALYSIS	126
D. THE COMPUTATION OF VERTICAL VELOCITY	132
E. A COMPARISON OF DATA ANALYSIS TECHNIQUES	136
F. VELOCITY STRUCTURE	146
G. HYDROGRAPHIC STRUCTURE	170
H. THE ANALYSIS OF WATER MASS FORMATION, MOVEMENT, AND MIXING USING A TEMPERATURE-SALINITY DIAGRAM	200
I. WATER MASS STRUCTURE	205
J. VOLUME, SALT, TEMPERATURE AND FRESHWATER TRANSPORT CALCULATIONS	217
LIST OF REFERENCES	220

LIST OF TABLES

1. Summary of WESTRAX observations	14
2. CTD salinity corrections and precision estimates	18
3. Typical depth-averaged Pegasus velocities and systematic velocity errors in the upper 1500 m	27
4. Comparison of Pegasus and ADCP zonal transports across simultaneously observed portions of section B (44 W)	30
5. Intermediate layer divergent and non-divergent transports through the WESTRAX region	36
6. Tropical Atlantic Ocean water types	66
7. WESTRAX region water mass classifications	80
8. Transport comparisons between the CME model and WESTRAX	111
E-1. Comparison between different velocity analysis techniques based on transports across section B during WESTRAX 1	142
F-1. Transports along WESTRAX region pathways	151
G-1. Horizontally averaged (a) depths, (b) temperatures, and (c) salinities of selected WESTRAX 1-4 density surfaces	176
G-2. Intermediate layer depth-averaged temperatures and salinities across section B.	179

LIST OF FIGURES

1. Bathymetry and geography of the western tropical Atlantic Ocean.....	3
2. Schematic of Atlantic Ocean surface current patterns.....	5
3. Volume transports across sections of the North Brazil Current	9
4. Annual averaged stream function field for wind-driven transports.....	13
5. Pegasus station locations in the WESTRAX study region.....	15
6. WESTRAX 1-5 tracks, CTD stations, and Pegasus transponder locations....	17
7. CTD minus bottle salinity measurement differences versus depth.....	20
8. Sample from the archive of CTD profiles.....	21
9. Horizontally averaged profiles of Pegasus velocity magnitudes.....	24
10. Sample from the archive of Pegasus velocity profiles.....	25
11. Horizontally averaged Pegasus systematic velocity error estimates.....	26
12. Comparison between ADCP and Pegasus velocity structures during September 1990 (WESTRAX 2).....	28
13. Same as Figure 12 during January 1991 (WESTRAX 3).....	29
14. WESTRAX region interpolation grid.....	33
15. The extrapolation of interpolated data to region corners.....	35
16. Interpolation error estimates using objective analysis.....	38
17. Pegasus (a) observed velocity, (b) interpolated velocity, (c) stream functions, (d) non-divergent velocity vectors during WESTRAX 2.....	39
18. Same as Figure 17 during WESTRAX 3.....	40
19. Conceptual model of a four-cell circulation pattern for the (a) Atlantic Ocean and (b) WESTRAX region.....	43
20. Intermediate layer circulation (a) schematic of features and (b) depth-averaged, weighted 4-survey average streamline structure.....	45
21A. Intermediate layer depth-averaged Pegasus transport streamline structure for the WESTRAX 1-4 surveys.....	46
21B. Intermediate layer depth-averaged, non-divergent Pegasus velocity vector fields for the WESTRAX 1-4 surveys.....	47
22. Depth-averaged, 4-survey averaged transport streamline structures in the (a) surface, (b) upper, (c) mid, (d) lower intermediate layers.....	48
23. Volume transports via four pathways using (a) WESTRAX average flows and (b) wind-driven return flows.....	50

24. Intermediate layer volume transports during WESTRAX 1-4	53
25. Track of surface drifter Buoy 02571	56
26. Vertical (a) Pegasus velocity and (b) water mass structure at section D during WESTRAX 2	57
27. Depth-averaged Pegasus transport streamlines for WESTRAX 2 in the (a) surface, (b) upper, (c) mid, (d) lower intermediate layers	58
28. Historical temperature-salinity (T-S) relationships for waters of the equatorial Atlantic Ocean	63
29. Climatological T-S relationships for the western tropical Atlantic	64
30. Envelope of the WESTRAX observed T-S relationship using CTD data	65
31. Schematic of the Atlantic intermediate layer current structure	68
32. Generalized T-S diagram for the tropical Atlantic Ocean	71
33A. Spreadsheet for the T-S inventory of WESTRAX CTD data	73
33B. Histogram for the T-S inventory of WESTRAX CTD data	74
34. WESTRAX T-S water types and mixing lines	75
35. Velocity structures and density surface comparisons for the (a) upper layer during WESTRAX 4 & (b) lower layer during WESTRAX 1	77
36. T-S envelope for the WESTRAX region showing water mass 'slices'	78
37A. Water masses and density structure comparison during WESTRAX 3	81
37B. Water masses and zonal velocity comparison during WESTRAX 3	82
38. Antarctic Intermediate Water and zonal velocity comparisons	83
39A. Intermediate water mass classifications for the WESTRAX temperature-salinity relationships over the range 0°C to 25°C	84
39B. Same as Figure 33A for the range 0°C to 10°C	85
40. Intermediate water masses and relative proportions by origin	86
41. Time series of intermediate water masses interplays by origin (A) within and (B) flowing into and out of the region	90
42. Time series of relative proportions of intermediate water masses (A) within, (B) flowing into, and (C) flowing out of the region	92
43A. Schematic of WESTRAX region upper, mid, and lower intermediate layer water mass pathways during late summer 1990 (WESTRAX 2)	95
43B. Water mass pathways during the winter 1991 (WESTRAX 3)	96
43C. Water mass pathways during the winter 1990 (WESTRAX 1)	97
43D. Water mass pathways during the early summer 1991 (WESTRAX 4)	98
44. WESTRAX 1-4 budgets of northern/southern water mass transports	101
45. Water mass budgets for upper and lower intermediate layers	103
46. WESTRAX intermediate layer volume, salt, & temperature transports	105

47. Intermediate layer flow structure schematic (a) without a retroflection eddy present, and (b) soon after retroflection eddy separation	107
48. Conceptual model of annual WESTRAX circulation pattern cycles	113
A-1. Interpolation algorithm gridding system	119
A-2. Illustration of Akima (1978) algorithm	120
B-1. Conventions for stream function analyses	123
C-1. The 'FPS2II' coordinate system	126
C-2. The 'natural order' gridding system	129
D-1. Horizontally divergent and convergent velocity fields	135
E-1. Comparison between zonal velocity structures across section B (44°W) using six different computation methods during WESTRAX 1	137
E-2. Same as Figure E-1 for WESTRAX 2	138
E-3. Same as Figure E-1 for WESTRAX 3	139
E-4. Same as Figure E-1 for WESTRAX 4	140
E-5. A comparison of volume transports through section B using 6 different analysis techniques	143
F-1A. Depth-averaged Pegasus streamline structure during WESTRAX 2	152
F-1B. Depth-averaged, non-divergent velocity fields during WESTRAX 2	153
F-2. Vertical alongshore non-divergent Pegasus velocity structures normal to Sections B, C, D, and E during WESTRAX 2	154
F-3. Major circulation features in the surface, upper, mid, and lower intermediate layers during WESTRAX 2	155
F-4A. Same as Figure F-1A for WESTRAX 3	156
F-4B. Same as Figure F-1B for WESTRAX 3	157
F-5. Same as Figure F-2 for WESTRAX 3	158
F-6. Same as Figure F-3 for WESTRAX 3	159
F-7A. Same as Figure F-1A for WESTRAX 1	160
F-7B. Same as Figure F-1B for WESTRAX 1	161
F-8. Same as Figure F-2 for WESTRAX 1	162
F-9. Same as Figure F-3 for WESTRAX 1	163
F-10A. Same as Figure F-1A for WESTRAX 4	164
F-10B. Same as Figure F-1B for WESTRAX 4	165
F-11. Same as Figure F-2 for WESTRAX 4	166
F-12. Same as Figure F-3 for WESTRAX 4	167
F-13A/B. Volume transports by intermediate layer during WESTRAX 2/3	168
F-13C/D. Same as Figure F-13A/B for WESTRAX 1/4	169

G-1A. Vertical structure of interpolated (a) potential density, (b) potential temperature, (c) salinity at section B during WESTRAX 2	180
G-1B. Same as Figure G-1A at section D during WESTRAX 2	181
G-2. (a) Depth, (b) potential temperature, (c) salinity of selected isopycnals across sections B and D (right) during WESTRAX 2	182
G-3A. Upper intermediate (a) depth, (b) average velocity, (c) temperature, (d) salinity at sigma theta 27.00 during WESTRAX 2	183
G-3B. Same as Figure G-3A at sigma theta 27.45 during WESTRAX 2	184
G-4A. Same as Figure G-1A for WESTRAX 3	185
G-4B. Same as Figure G-1B for WESTRAX 3	186
G-5. Same as Figure G-2 for WESTRAX 3	187
G-6A. Same as Figure G-3A for WESTRAX 3	188
G-6B. Same as Figure G-3B for WESTRAX 3	189
G-7A. Same as Figure G-1A for WESTRAX 1	190
G-7B. Same as Figure G-1B for WESTRAX 1	191
G-8. Same as Figure G-2 for WESTRAX 1	192
G-9A. Same as Figure G-3A for WESTRAX 1	193
G-9B. Same as Figure G-3B for WESTRAX 1	194
G-10A. Same as Figure G-1A for WESTRAX 4	195
G-10B. Same as Figure G-1B for WESTRAX 4	196
G-11. Same as Figure G-2 for WESTRAX 4	197
G-12A. Same as Figure G-3A for WESTRAX 4	198
G-12B. Same as Figure G-3B for WESTRAX 4	199
H-1. Cartoon illustrating the formation, movement and interactions of water types in a hypothetical ocean using the T-S diagram	202
H-2. T-S diagram mixing nomogram for WESTRAX intermediate waters	204
I-1. Water mass distribution on density surfaces during WESTRAX 2	209
I-2. Water mass structure across sections B, C, D, and E during WESTRAX 2	210
I-3. Same as Figure I-1 for WESTRAX 3	211
I-4. Same as Figure I-2 for WESTRAX 3	212
I-5. Same as Figure I-1 for WESTRAX 1	213
I-6. Same as Figure I-2 for WESTRAX 1	214
I-7. Same as Figure I-1 for WESTRAX 4	215
I-8. Same as Figure I-2 for WESTRAX 4	216
J-1. Illustration of transport through a segment	217

ABSTRACT

THE STRUCTURE OF WATER MASS, SALT, AND TEMPERATURE TRANSPORTS WITHIN INTERMEDIATE DEPTHS OF THE WESTERN TROPICAL ATLANTIC OCEAN

by

Frank Lee Bub
University of New Hampshire, December 1993

Water mass flow patterns within the 150-1300 m intermediate layer of the western tropical Atlantic were determined from observations during four 1990-1991 Pegasus velocity and CTD hydrographic surveys. Non-divergent flows were analyzed to determine transports.

A survey-average 29 Sverdrups ($1 \text{ Sv} = 10^6 \text{ m}^3/\text{s}$) of southern hemisphere water masses flowed northwestward across 44°W near the equator as part of the subsurface South Equatorial Current (SEC). 21 Sv retroflected anticyclonically around the Amazon Eddy ($2^\circ \text{N } 45^\circ \text{W}$) and flowed eastward toward the North Equatorial Undercurrent (NEUC). The other 8 Sv moved northwestward within a series of anticyclonic retroflexion eddies which periodically separate from the Amazon Eddy. 61 Sv of a northern/southern water mass mixture flowed southeastward across 9°N as part of the North Equatorial Current (NEC) and bifurcated: 32 Sv turned anticyclonically northwestward, and 29 Sv turned cyclonically around a low ($6^\circ \text{N } 44^\circ \text{W}$), merged with the southern water, and flowed toward the NEUC. The 50 Sv NEUC, a mixture of mostly southern water, flowed eastward into the interior. The remaining NEC and SEC branches blended to form a 40 Sv northwestward transport across 53°W . These observed transports were generally about three times larger than the wind-driven equatorial and

tropical gyre return transports (Mayer and Weisberg 1993): suggesting the existence of subgyre-scale recirculation eddies in the western tropics.

One of the retroflection eddies was measured during September 1990. Its structure was approximated by a 300 km diameter cylinder which extended vertically through the surface and intermediate layers to 1300 m. During two other surveys, retroflection eddies were identified at the region's northwestern corner. Instantaneous transport associated with an eddy which translated at 10 cm/s was about 30 Sv. Assuming three were generated each year, retroflection eddy translation could account for the 8 Sv alongshore flow through the region.

According to water mass budgets, 21 Sv of northern water masses were transformed by mixing within the region. Temperature-salinity relationships indicated this mixing effectively transports the cool, low salinity Antarctic Intermediate Water into the North Atlantic by as yet unknown pathways.

I.

INTRODUCTION

The goals, objectives, and a context for the research are presented. The area geography and the current structure within the ocean surface layer are described. Historical physical oceanographic studies of the western tropical Atlantic are reviewed and related to the current work.

Goals and objectives...

The goal of this dissertation is to describe the physical oceanography of the intermediate layer within the western tropical Atlantic Ocean in terms of:

- Velocity structure
- Hydrographic structure
- Water masses, and
- The transports of volume, temperature, and salt.

The objectives include:

- Determine the is three-dimensional structure of the region's intermediate layer current patterns
- Define and describe the water masses of the region, relating the water mass and velocity structures
- Describe water mass and water property transports through the region
- Determine paths by which southern water is moved into the North Atlantic
- Investigate evidence of seasonal changes and cycles, and
- Relate circulation within the study region to that of the equatorial Atlantic.

Context...

By learning how North and South Atlantic waters meet and mix within the western tropical Atlantic Ocean, we will gain a better understanding of this region's role in the global exchanges of sea water volume, salt, and thermal energy. Until recently, observations of the velocity and hydrographic structures of this western boundary current regime were sparse, and the important physical processes at work within the region were not well understood. There was a particular lack of knowledge about the intermediate level. To learn more, four oceanographic expeditions surveyed the region during 1990 and 1991 under the Western Tropical Atlantic Experiment (WESTRAX) program (Brown *et al.* 1992). These cruises have provided both the data and the impetus for this dissertation.

The WESTRAX region...

This study addresses the intermediate layer of the western tropical Atlantic Ocean which is located off the coast of South America (Figure 1). Political boundaries include the coasts of Brazil, French Guiana, and Suriname. The continental break, which is at the 200 m isobath and lies between 100 and 300 km offshore, separates the continental shelf from the deep ocean of the study region. The continental slope drops steeply to the abyssal plain of the Guyana Basin, where depths reach more than 4000 m. This abyssal plain is bounded in the northeast by the Mid-Atlantic Ridge and in the west by the Lesser Antilles island chain. The Ceara Rise crosses the eastern boundary of the study region. Sediment from the Amazon River outflow has created a large deposition fan along the continental slope. The continental slope, acting as a nearly vertical wall along the region's southeastern boundary, affects intermediate layer flow.

Oceanographers typically divide the ocean into three zones: (1) a warm, well-mixed surface layer, (2) a transitional intermediate layer, and (3) a vast deep ocean layer. These layers are bound within the tropics as follows: The 50-200 m

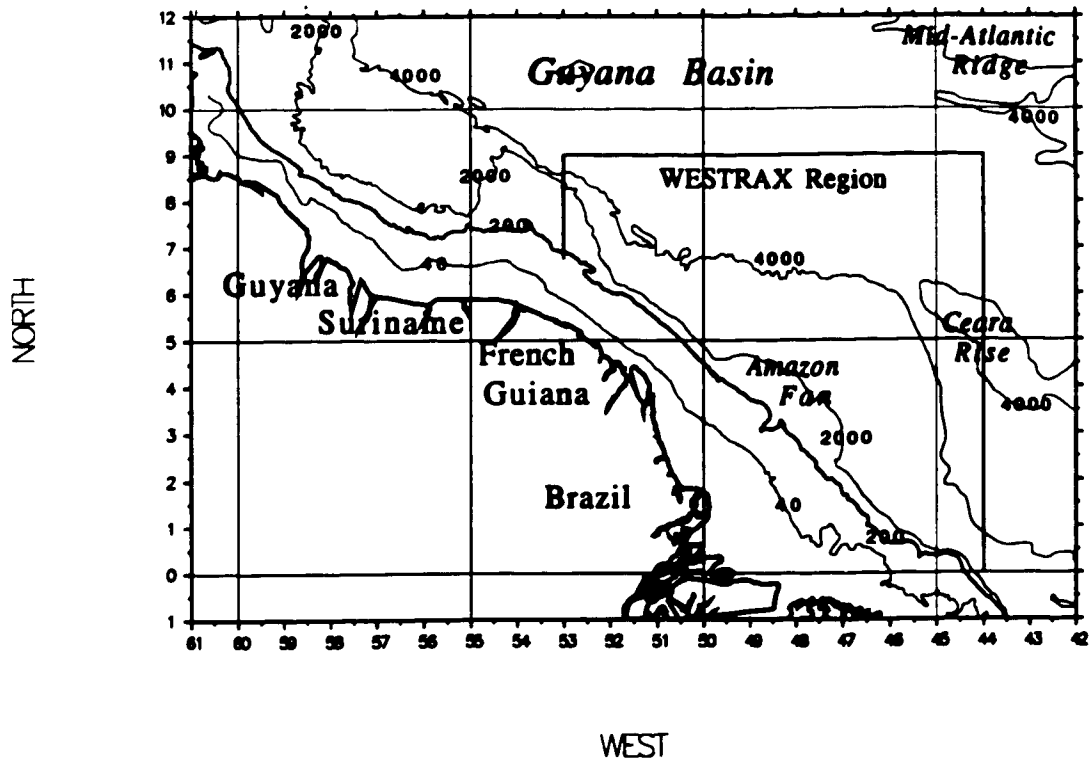


Figure 1. Bathymetry and geography of the western tropical Atlantic Ocean. Isobaths are at 40, 200, 2000, and 4000 m. The darkened line indicates the 200 m isobath which marks the continental shelf break. The box outlines the WESTRAX analysis region.

thick warm surface layer lies above a strong thermocline and contains a core of high salinity. At depths between 1200 and 1500 m, the top of the cold deep layer is associated with a second relative salinity maximum. Spanning these boundary layers is the tropical intermediate layer. This layer contains a zone of low salinity between the depths of 600 and 900 m.

A review of the well-documented current structure within the upper level (150 m or so) of the western tropical Atlantic will set the scene. By the end of this dissertation, we will have a better understanding of a somewhat different flow structure within the western tropical Atlantic intermediate layer. Other members of the WESTRAX group are examining other flow structures.

In the surface layer, southern Atlantic water is carried northwestward into the western tropical Atlantic by a northern branch of the South Equatorial Current (SEC) (Figure 2). This branch, which follows the continental break as it flows along the northeastern coast of Brazil, is defined as the North Brazil Current (NBC) (Cochrane 1963). During boreal summer, the NBC is observed to reverse its course in a clockwise direction by a full 180°. This 'retroflexion' occurs around one, or sometimes two, anticyclonic eddies. The retroflected southern water flows eastward toward the equatorial Atlantic interior within the North Equatorial Countercurrent (NECC) (Cochrane 1969). From the north, a branch of the westward flowing North Equatorial Current (NEC) turns cyclonically and merges into the NECC. During boreal winter, the NBC retroflexion weakens and a portion of its flow appears to continue northwestward toward the Caribbean Sea as the Guyana Current (GC). Also during winter, the NECC weakens considerably. The NECC occasionally reverses its direction in the interior tropical Atlantic (Garzoli and Katz 1983). As summer returns, the retroflexion of NBC water is re-established, the NECC restrengthens, and the northwestward flow of the GC reduces and disappears.

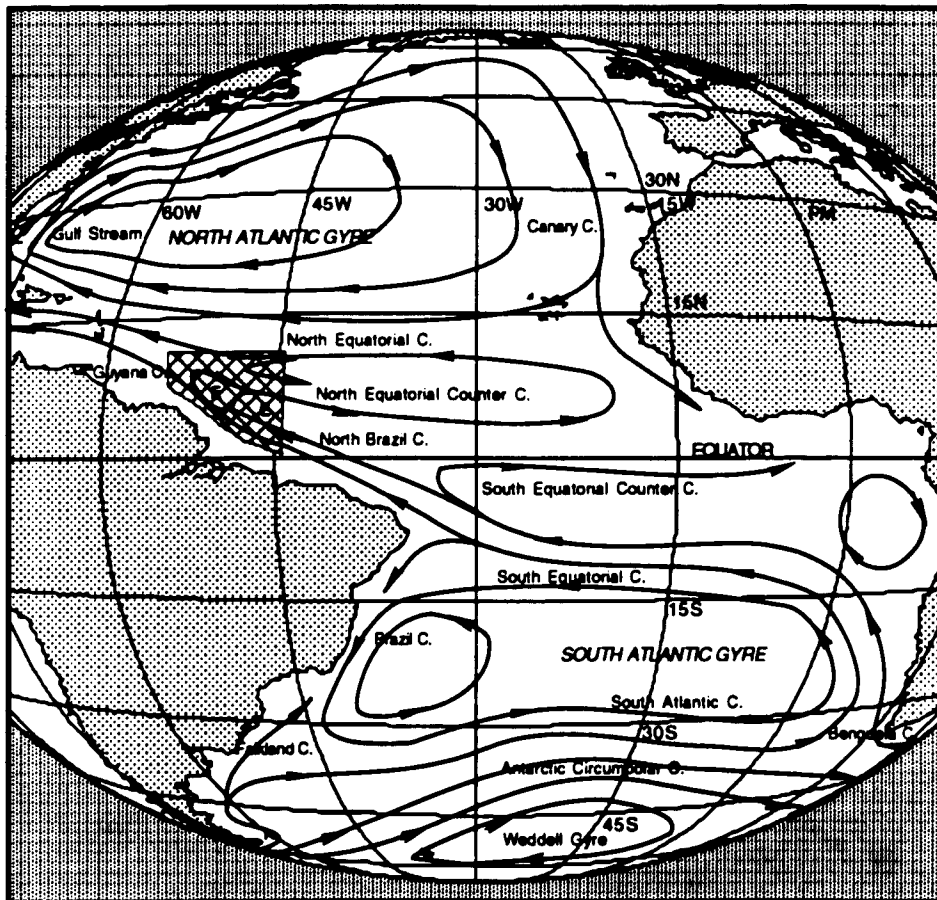


Figure 2. Schematic of surface current patterns for the Atlantic Ocean. The WESIRAX region is shaded and the Amazon and Demerara Eddies are marked by E.

The largest and most often observed retroflection anticyclone has been named the 'Amazon Eddy,' as this permanent feature is found near that river's mouth (Bruce and Kerling 1984). A second retroflection feature, called the 'Demerara Eddy,' is observed further to the northwest (Cochrane, Kelly, and Olling 1979). Recent studies indicate the Demerara Eddy may be a northwestward migrating 'retroflection eddy,' instead of a permanent fixture within the region (Johns *et al.* 1990 and Richardson *et al.* 1993). Oceanic frontal zones, within which southern and northern Atlantic waters mix, are found to the west and north of these eddies.

The complex processes which lead to the NBC retroflection have drawn, and continue to draw, the attention of oceanographers.

Historical Background...

In 1886, Buchanan noted an unexpected eastward counterflow in the subsurface waters of the equatorial Atlantic Ocean (Krümmel 1911, cited in Neumann 1960). Modern studies began with the discovery of an eastward flowing current beneath the surface of the equatorial Pacific Ocean (Cromwell, Montgomery, and Stroup 1954). Noting that surface water was 'piling up' at the western boundary of the equatorial region under the stress of westward equatorial trade winds, Neumann (1960) suggested that an undercurrent similar to the Pacific's Cromwell Current should also exist in the Atlantic Ocean. The presence of this current was confirmed by a 1958 International Geophysical Year expedition (Metcalf, Voorhis, and Stalcup 1962).

Cochrane (1963) studied the EUC on a transect along 38°W which sequentially cut through five near-surface currents. These were identified as: a northwestward NBC, a southeastward Equatorial Undercurrent (EUC), another westward branch of the NBC, an eastward NECC, and a westward NEC. The author speculated that the EUC, associated with a tongue of maximum salinity near the

top of the thermocline, began as the NBC turned as a clockwise eddy near the Amazon River mouth.

Metcalf and Stalcup (1967) investigated the origins of the EUC. They suggested that a strong northwestward NBC flowed along the Brazilian coast, reversed its course near the Amazon delta, and fed subsurface South Atlantic water into both the EUC and a zonal current beneath the NECC. Temperature-dissolved oxygen (T-O₂) relationships indicated that South and North Atlantic water masses met and mixed within the study region. Southern water with a high O₂ content was not evident west of the mixing region. This led the authors to suggest that South Atlantic water was not passing directly into the Caribbean Sea.

Metcalf (1968) observed that very little of the NBC flowed directly into the Caribbean. Westward flowing North Atlantic water was instead filling the area to the northwest of a 'great meander' through which the NBC retroflected and returned its flow eastward. T-O₂ relationships illustrated a major west-to-east discontinuity between North and South Atlantic water masses.

Cochrane, Kelly, and Olling (1979) compared consolidated sets of winter and summer observations. Although there were some seasonal differences, they noted general features on density surfaces which included a zonal ridge (crest) along 3°N and zonal troughs (valleys) along 7.5°S and 9°N. A portion of the southern water NBC which flowed northwestward past the eastern tip of Brazil retroflected near the equator at 39°W and fed into the eastward flowing EUC. Additional NBC waters continued northwestward and retroflected around the zonal ridge at 3°N, within either the Amazon anticyclone (near 3.5°N 47°W) or a second center further along the coast (e.g., the Demerara Eddy). Retroflected southern water, which was evident as deep as 800 m, fed along 5°N into an eastward current beneath the surface layer NECC. The authors considered this flow to be distinctly different from the NECC (this eastward intermediate layer flow was later labeled the NEUC by Molinari *et al.* 1981). Retroflexion within the upper levels was

weakest during the winter. The authors observed that the subsurface eastward flow (e.g., the NEUC) was strong, permanent, and quite deep.

The results of two expendable bathythermograph (XBT) surveys were presented by Bruce and Kerling (1984). The topography of the 20°C isothermal surface suggested two semi-permanent anticyclonic eddies were being supplied from the southeast by the NBC. The northern cell (Demerara Eddy) was centered near 7°N 52°W during both surveys. The southern cell (Amazon Eddy) was at approximately 5°N 49°W on the summer survey and 4°N 46°W on the winter survey. Both eddies were wider and deeper during the late summer. A number of smaller cyclonic circulations were also evident in the analyses.

Flagg, Gordon, and McDowell (1986) examined the winter structure of currents and water masses within the upper levels of the Amazon Eddy region (Figure 3). With T-S and T-O₂ diagrams, South and North Atlantic Central Water masses (SACW and NACW respectively) were identified between the top of the thermocline (150-200 m) and a depth of 800 m. A core of northwestward flowing Antarctic Intermediate Water (AAIW) lay against the continental slope near a depth of 700 m. Strong currents were noted, and a substantial northwestward transport of $52 \times 10^6 \text{ m}^3/\text{s}$ flowed across the southeastern boundary (Section A, Figure 3). Three distinct layers were described: (1) Above the thermocline, influences at the surface such as freshwater Amazon inflow and rainfall (or evaporation) made water mass identification difficult. South Atlantic surface water entered the region from the southeast, flowed along the Brazil coast as the NBC, and split. Portions either continued northwestward or turned north then presumably eastward to exit the region as the NECC. (2) Within the upper thermocline, a second northwestward flow split near 3°N 48°W and either continued northwestward, or turned anticyclonically and returned back toward the equator and into the EUC. (3) In the lowest layer, all incoming flow retroflected and fed into the eastward flowing NEUC before it reached 4°N.

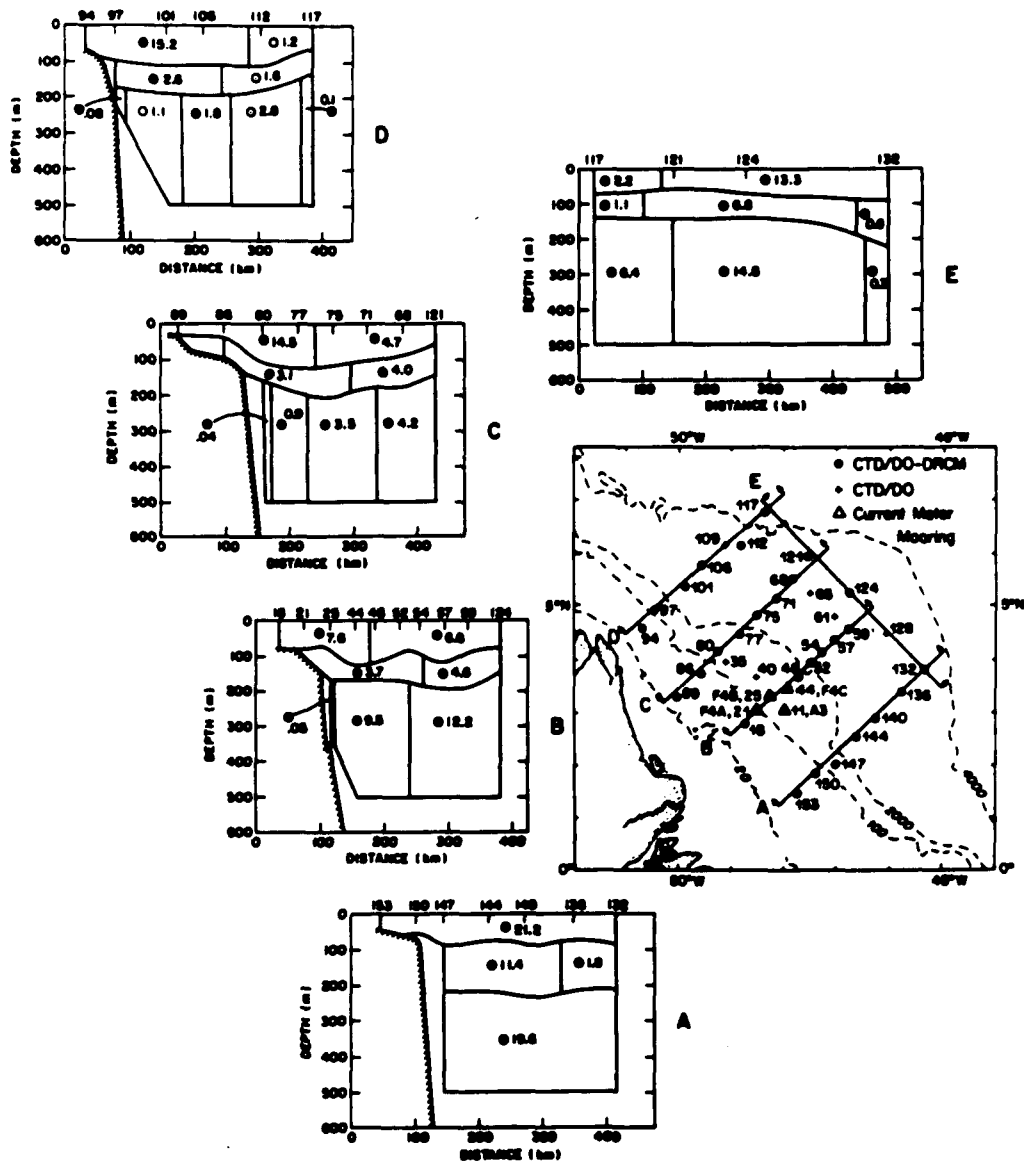


Figure 3. Volume transports across vertical sections in the North Brazil Current region (in Sverdrups, $1 \text{ Sv} = 10^6 \text{ m}^3/\text{s}$). (Flagg, Gordon, and McDowell 1986)

Based on current meter time series measurements taken on a survey line off the French Guiana coast, Johns *et al.* (1990) proposed that the northwestern anticyclone (e.g., the Demerara Eddy) was not a permanently fixed feature. Instead, they suggested it was actually a transient 'retroflexion eddy' which formed within the southeastern anticyclone (e.g., the Amazon Eddy), separated, and translated northwestward as a rotating body. From late summer to January, the northwestward flow was strongest and the Amazon Eddy retroflexion was most apparent. The authors suggested that the retroflexion eddies were an important mechanism for the northwestward transport of southern water.

Schott and Böning (1991) presented the current structure of the upper 500 m of the western tropical Atlantic according to the National Center for Atmospheric Research (NCAR) Community Modeling Effort (CME) general circulation model. In the sub-surface layer, the CME model retroflected intermediate water from the South Atlantic, allowing very little of this southern water to pass through the region toward the Caribbean. During summer, retroflexion was nearly complete at all levels. On the winter analyses, retroflexion in the surface layer disappeared, while sub-surface retroflexion into the EUC and NEUC continued. A southeastward flowing intermediate layer undercurrent was observed to develop along the continental slope near the French Guiana coast. I will present further evidence of this coastal undercurrent in the WESTRAX water mass and velocity structure analyses.

Richardson *et al.* (1993) discussed the formation and northwestward translation of retroflexion eddies according to surface drifter tracks. They suggested three such eddies formed each year and annually carried approximately 3 Sv toward the Caribbean. The WESTRAX surveys transect a number of these retroflexion eddies and this study will help to define their form and size.

A framework for this dissertation...

In a recent paper, Mayer and Weisberg (1993) described seasonal cycles in the current structure of the tropical and extratropical Atlantic Ocean. This work was based on a Sverdrup analysis of the wind-driven circulation using COADS data between 1947 and 1988. The climatological monthly wind stress on the ocean surface between 30°S and 60°N was determined. The curl of the wind stress, divided by beta and integrated through the water column, provided a meridional Sverdrup mass transport flux. The Sverdrup stream function field was determined by integrating the mass transport flux zonally from east to west (Figure 4).

The authors presented four Atlantic Ocean circulation cells: (1) a large subtropical gyre in the North Atlantic, (2) an elongated tropical gyre which lies north of the equator, (3) an equatorial gyre that straddles the equator, and (4) a subtropical gyre in the South Atlantic. These gyres are bound from north to south by the westward, eastward, and westward zonal flows of the NEC, NECC/NEUC, and SEC respectively. I have taken the liberty to indicate these flows by direction arrows on the authors' streamline analyses.

The NEC and SEC feed anticyclonically into the Northern and Southern Atlantic subtropical gyre return flows which are the Gulf Stream and Brazil Current western boundary current systems respectively. The equatorial gyre's return flow occurs as a portion of the SEC turns anticyclonically northwestward, flows along the Brazil coast as the NBC, and retroflects within the Amazon Eddy. Mayer and Weisberg (1993) suggest the major undocumented return flow in this system lies along the northern coast of South America between 5°N and 10°N. There, a cyclonic flowing, southeastward boundary current (marked by the question marks) would be required to complete the return flow of the tropical gyre.

The work of Mayer and Weisberg (1993) brings the investigation into the western tropical Atlantic velocity structure into sharper focus, and provides a

framework by which my results can be described. In particular, I will demonstrate that the intermediate layer velocity and water mass structures of the WESTRAX region document closure for the cyclonic tropical gyre.

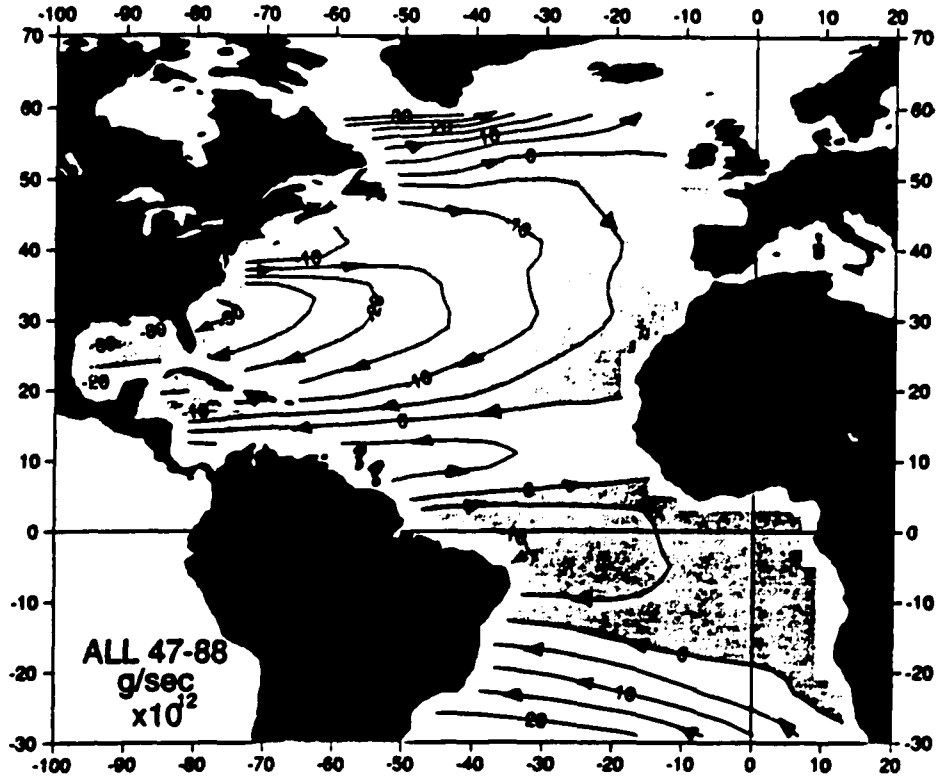


Figure 4. Annually averaged stream function field for wind-driven transports in the Atlantic Ocean, based on surface wind stress analyses of forty-two years of COADS data. (Mayer and Weisberg 1993).

II. MEASUREMENTS AND DATA REDUCTION

The WESTRAX data sets of CTD hydrographic profiles (temperature and salinity) and Pegasus velocity profiles are described. Data preparation, corrections, and precision estimates are discussed. Pegasus and ADCP velocity structures are compared.

WESTRAX Expeditions...

This research is based on hydrographic and current profile information gathered during four oceanographic surveys to a region of the deep Atlantic Ocean north of the South American coast (Figure 5). The profile measurements made during each expedition were concentrated along four primary transects of the region (Figure 5). The typical suite of measurements included Conductivity-Temperature-Depth (CTD), expendable bathythermographs (XBT), Pegasus current profiler, and Acoustic Doppler Current Profiler (ADCP) observations. The easternmost transect (Section B) runs northward along 44°W from the equator to approximately 8.25°N . The other three transects (Sections C, D, and E) extend from southwest to northeast (approximately 26° true) between the continental break (the 200 m isobath) and 9°N to 10°N . Figure 6 presents the locations of Pegasus and CTD observations during each cruise. Table 1 details the number of CTD, XBT, and Pegasus stations occupied during each WESTRAX expedition. During September 1991 (WESTRAX 5) only Section B and a part of Section C were revisited. Thus the data from this last cruise were not used as part of the general analyses presented herein.

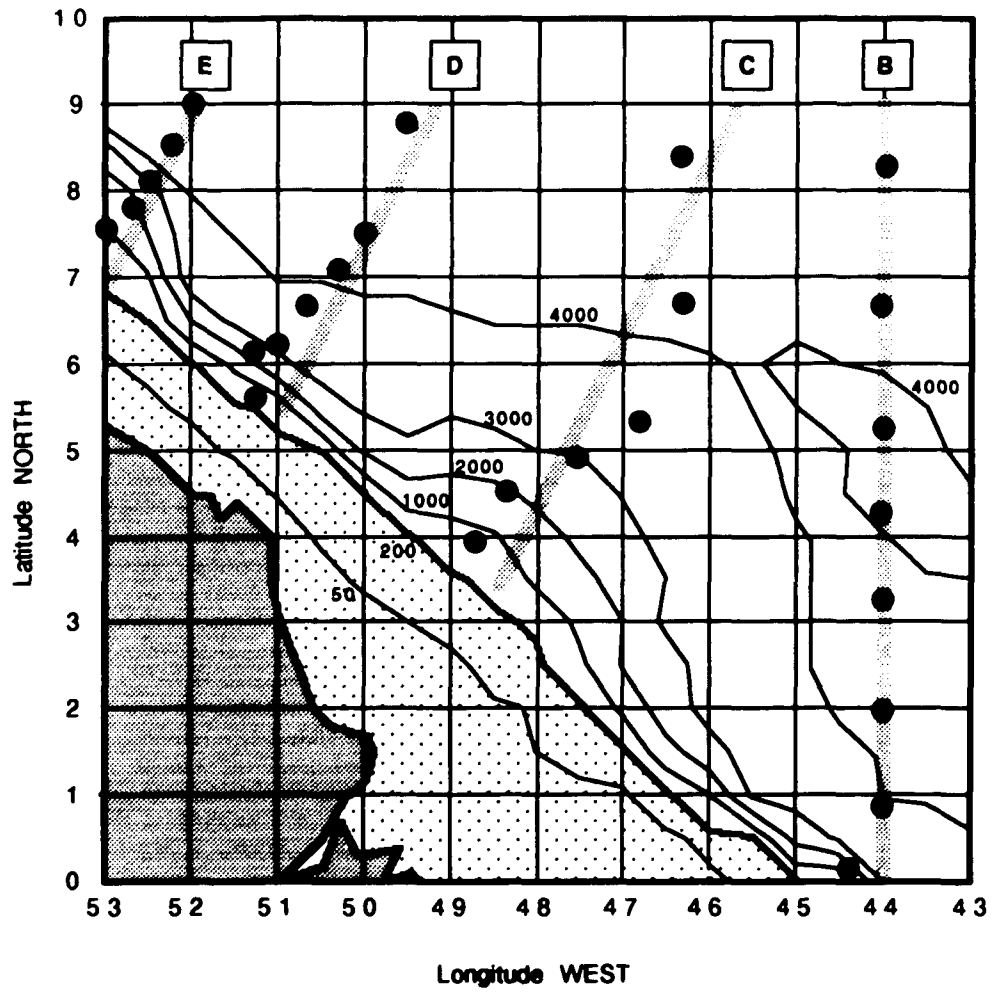


Figure 5. Pegasus station locations (dots) during WESTRAX. Gray lines are transects B, C, D, and E. Bathymetric contours are in meters. The South American continent is darkened, and the continental shelf within the 200 m shelf break is stippled.

The first expedition aboard the NOAA Ship Mount Mitchell and the next four aboard the NOAA Ship Malcolm Baldrige were designed to observe the hydrographic and current structure of this region during different oceanographic seasons (Table 1).

Table 1. Summary of WESTRAX observations.

WESTRAX Cruise	Inclusive Dates	Boreal Season	Number of Stations:			ADCP*
			CTD	XBT	Pegasus	
1	1/1/90-19/2/90	winter	33	78	24	no
2	17/9/90-4/10/90	late summer	38	148	27	yes
3	16/1/91-30/1/91	winter	25	86	24	yes
4	20/6/91-3/7/91	transition	42	98	26	yes
5	7/9/91-17/9/91	late summer	14	51	7	yes
Station totals			152	461	108	
* Acoustic Doppler Current Profiler data provided by D. Wilson, AOML.						

CTD Hydrographic Measurements...

Water property profiles were measured using Neil-Brown Instrument Mark III CTDs by scientists and technicians from the Atlantic Oceanographic and Meteorological Laboratory (AOML). The CTD measures *in situ* values of pressure, conductivity, and temperature at a scan rate of 30 observations per second. A separate sensor measures the parameters required for a post-survey computation of dissolved oxygen (which will not be discussed here). Mark III CTD temperature and depth precisions are $\pm 0.005^\circ\text{C}$ and ± 6.5 decibar respectively (Johns and Wilburn 1993). One decibar (10^4 Pascal, abbreviated dbar) is approximately equivalent to the increase in pressure during each one meter of descent through

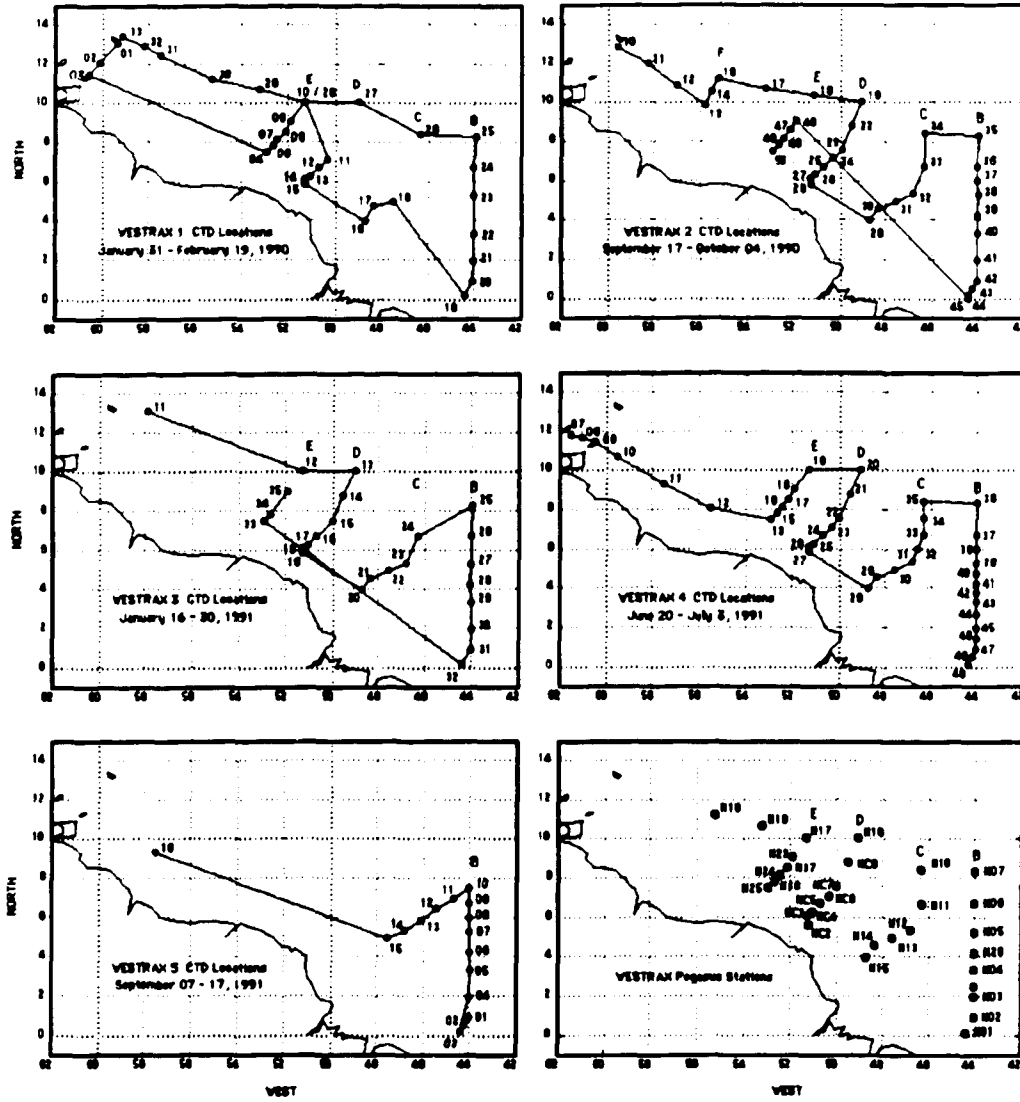


Figure 6. Expedition tracks, CTD stations, and Pegasus transponder locations for VESTRAX expeditions 1 through 5.

the ocean.

Between the surface and 200 m, the nominal CTD descent rate was 30 m/minute (0.5 dbar/s). Descent and ascent rates were increased to 60 m/minute (1.0 dbar/s) between 200 m and the bottom. In most cases, CTD profiles were within 50 m of the bottom of the ocean. An AOML program on the ships' VAX systems computed CTD salinity and averaged all observation data over 1.0 dbar increments (Johns and Wilburn 1993). While data were recorded during both descent and ascent, inconsistencies due to pressure hysteresis problems precluded the direct use of CTD ascent data.

The CTD measurements were prepared for interpolation at UNH. Near-surface temperature and salinity data were sometimes highly variable, probably due to an unknown combination of measurement problems and natural upper ocean variability. Because anomalies due to solar heating, Amazon runoff, rainfall, etc., were normally confined to the upper 10 m, I assumed that their effects upon intermediate layer analyses were minimal. These anomalies were thus eliminated by a linear extrapolation of temperature and salinity data upward from the first depth at which a 'reasonable' observation in each profile occurred.

Table 2. CTD salinity corrections and precision estimates [psu]

<u>Data Set</u>	<u>Correction</u>	<u>Precision*</u>
WESTRAX 1	+0.0098	±0.011
WESTRAX 2.a	+0.0269	±0.005
WESTRAX 2.b	+0.1229	±0.013
WESTRAX 3	+0.0081	±0.025
<u>WESTRAX 4</u>	<u>-0.0531</u>	<u>±0.013</u>
Mean precision estimate		±0.014
* See text.		

It was necessary to correct the salinities measured by the CTDs. Bottle samples were collected during each cast and their salinities were determined by AOML personnel using a Guideline Autosol unit at a precision of ± 0.002 psu (Johns and Wilburn 1993). Plots of CTD minus bottle salinity differences (at equivalent pressures) for the WESTRAX 1 to 4 CTD observations are presented in Figure 7. Two corrections were required during WESTRAX 2 because the CTD instrument was changed midway through the cruise. The appropriate depth-averaged salinity difference (Table 2) were used to correct respective CTD salinity profiles. The salinity random uncertainty (e.g., precision error) estimated on Table 2 represents a range of ± 2 standard deviations about the mean difference. This means that if a Gaussian distribution is assumed, then there is a 95% probability that the true salinity lies within these limits.

The corrected CTD measurements were reduced using algorithms described by Fofonoff and Millard (1983) as follows;

- In situ temperatures were converted to potential temperature, referenced to the surface (θ or θ_0),
- Pressure, potential temperature and salinity were used to compute potential density, referenced to the surface (σ_θ or σ_θ), and
- CTD pressures were converted to depths at 1.0 m increments.

By using depth rather than pressure, I could make direct comparisons between CTD and Pegasus observations and determine related volume transports. Standardized sets of depth, potential temperature, salinity, and potential density profiles ($z/\theta/S/\sigma_\theta$) at 1.0 m increments for each WESTRAX cruise were created for most of the analyses discussed here. Pressure, potential temperature, and salinity ($p/\theta/S$) profiles at 1.0 dbar increments were used to analyze geostrophic velocities. A typical WESTRAX CTD profile from the UNH archive is presented (Figure 8).

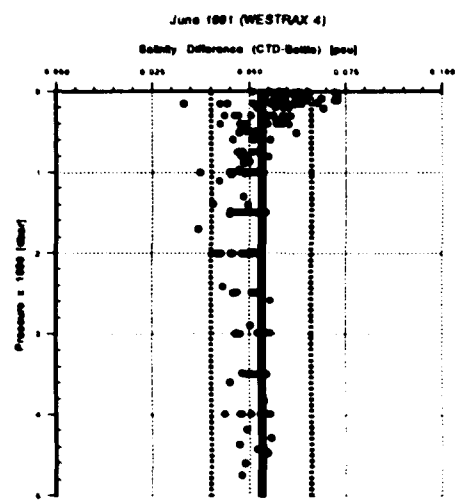
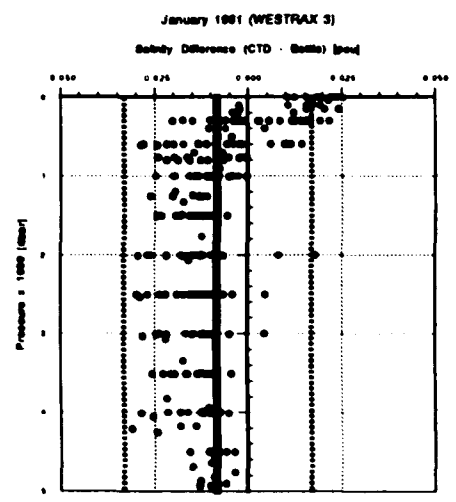
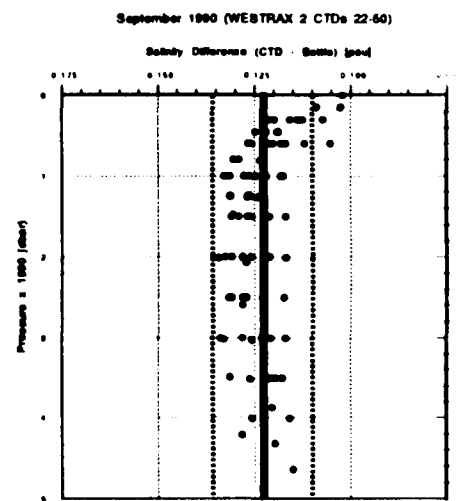
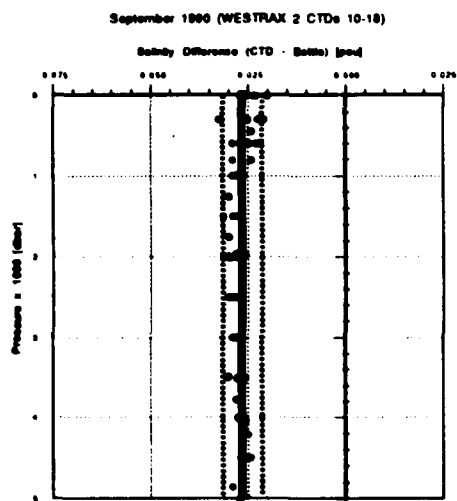
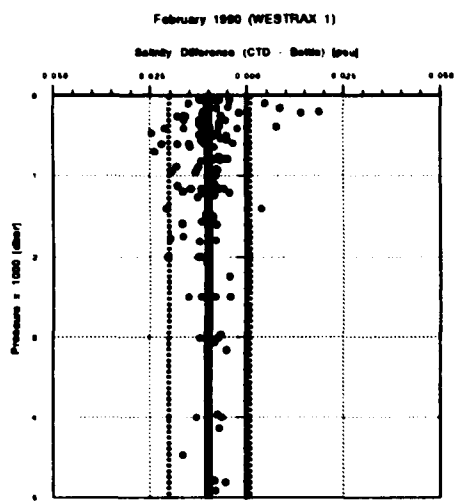


Figure 7. WESTRAX salinity differences (CTD minus bottle) versus depth. Depth-averaged differences are indicated by the heavy vertical dashed line, and two standard deviation by the lighter vertical dashed lines.

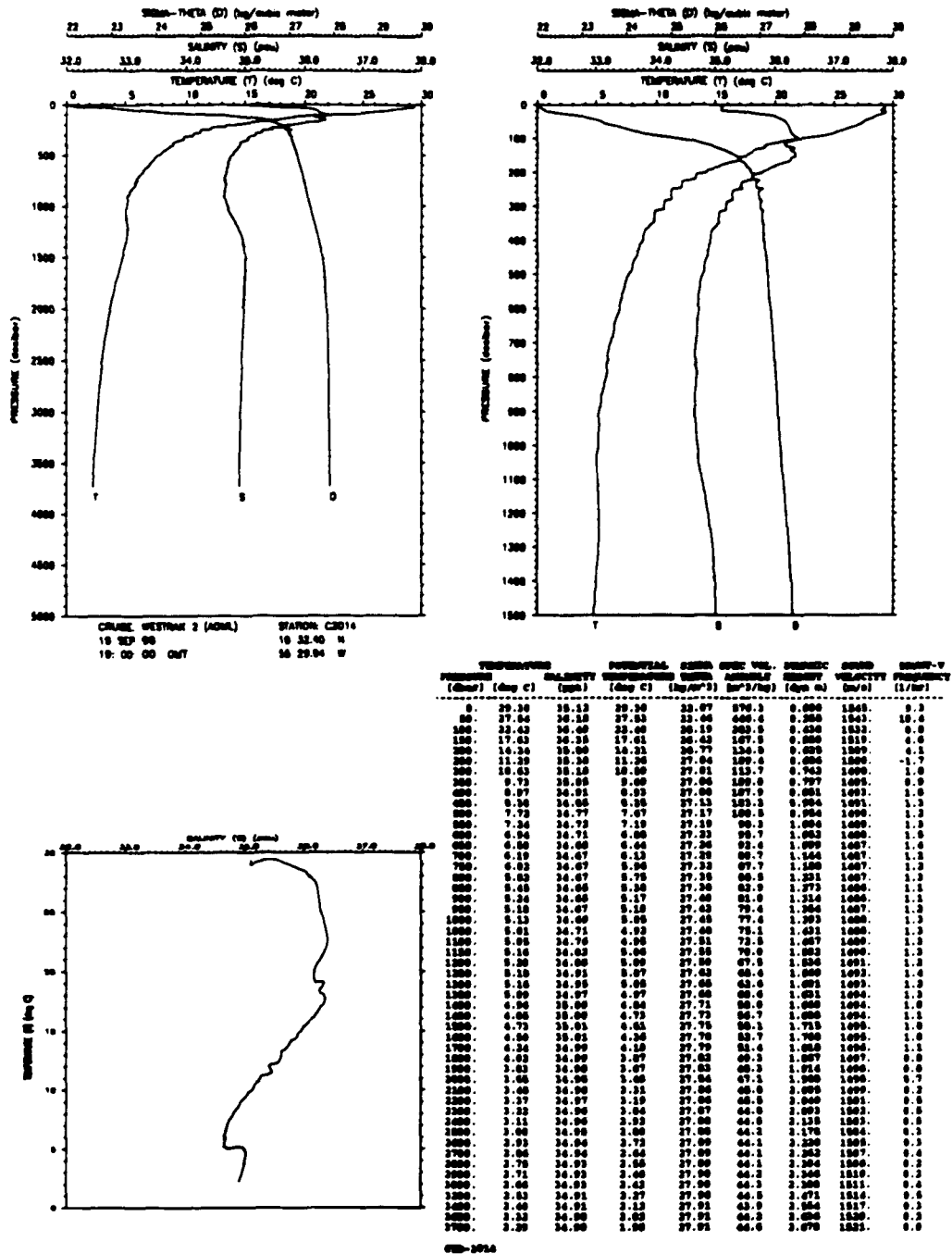


Figure 8. Sample from the archive of WESTRAX CTD profiles. (a) Potential temperature (T), salinity (S), and potential density (D) between 0- 5000 dbar. (b) The same for 0-1500 dbar. (c) Potential temperature-salinity (θ -S) relationship. (d) Observed and computed in situ temperature, salinity, potential temperature, potential density, specific volume anomaly, dynamic height (referenced to the surface), sound velocity, and stability (Brünt-Väisäla frequency) at selected pressures.

A rough estimate of the potential density uncertainty is ± 0.021 sigma theta units. I determined this by comparing pairs of density profiles computed using: (a) the temperature and salinity profiles of the January 1991 CTDs (see Table 2), and (b) the same profiles after I created worst-case profiles by adding a maximum positive temperature error (+0.005°C) and a minimum negative salinity error (-0.025 psu). The depth averaged difference between these profiles was assumed to represent an uncertainty in sigma theta. Expendable bathythermograph (XBT) observations were not used in this dissertation work.

Pegasus velocity measurements...

The Pegasus instrument was used to determine vertical profiles of horizontal currents in the WESTRAX region (Spain *et al.* 1981, Leaman and Vertes 1983). The Pegasus velocity measurement program was conducted by K. Leaman and P. Vertes of the University of Miami. As the autonomous Pegasus sinks through the ocean, its instantaneous location is determined by measuring the ranges to two transponders which were previously surveyed into place on the ocean floor. Every 16 seconds, Pegasus transmits an inquiry acoustic signal, activating a response signal from each of the sea floor transponders. Water pressure, temperature, the time of the inquiry signal, and the times of receipt for each response are recorded. When Pegasus reaches the bottom, weights are released and the unit returns to the surface, continuing to record these data during ascent.

While speeds varied depending on setup, a nominal fall rate of 40 m/minute produced a resolution in depth during descent of approximately 10.7 m. A nominal upward rate of 25 m/minute produced an approximate depth resolution of 6.7 m during ascent. In this study, Pegasus ascent profiles were used exclusively because of their greater vertical resolution. Additionally, ascending profiles often terminated closer to the ocean surface than their descending

counterparts, providing better upper ocean information. In retrospect, I may have avoided some of the aliasing due to internal waves which Send (1993) discussed by averaging the ascent and descent profiles.

Upon instrument recovery, the acoustic travel times, temperature, and pressure data are downloaded into a laboratory desktop computer. The slant distances between the Pegasus and each transponder are computed using a sound velocity profile derived from the temperature data and instrument-transponder travel times. The geometry of the pressure data, the slant distances, and the line between transponder locations is applied to determine the three-dimensional position of Pegasus at the time of each record entry. The depth-averaged horizontal velocity components for particular depth intervals are found by dividing successive changes in zonal and meridional position by the appropriate time increment.

At UNH, the Pegasus profiles were linearly interpolated to 10 m depth increments. The four-cruise mean magnitude of typical Pegasus velocities ranged from 56 cm/s at the ocean's surface, to 31 cm/s at the top of the thermocline (150 m), to 15 cm/s at 500 m, to a relatively constant 11 cm/s at 800 m and below (Figure 9). An example from the UNH Pegasus velocity profile archive is shown in Figure 10.

Systematic error profiles ($u_{err}(z)$, $v_{err}(z)$) were produced for each Pegasus velocity profile according to methods described by Leaman and Vertes (1983). These are estimates of the upper limit of measurement errors, based on uncertainties in transponder depths, the baseline length, Pegasus to baseline orientation, and vertical pressure (depth) measurements. Average u_{err} and v_{err} profiles between the surface and 1500 m were calculated for each of the WESTRAX data sets (Figure 11). The four-cruise mean of these systematic error magnitudes ranged from 4.0 cm/s (surface), to 3.4 cm/s (150 m), to 2.8 cm/s (500 m), to 2.3 cm/s (1000 m), and to 2.0 cm/s (1500 m). These values are similar to the

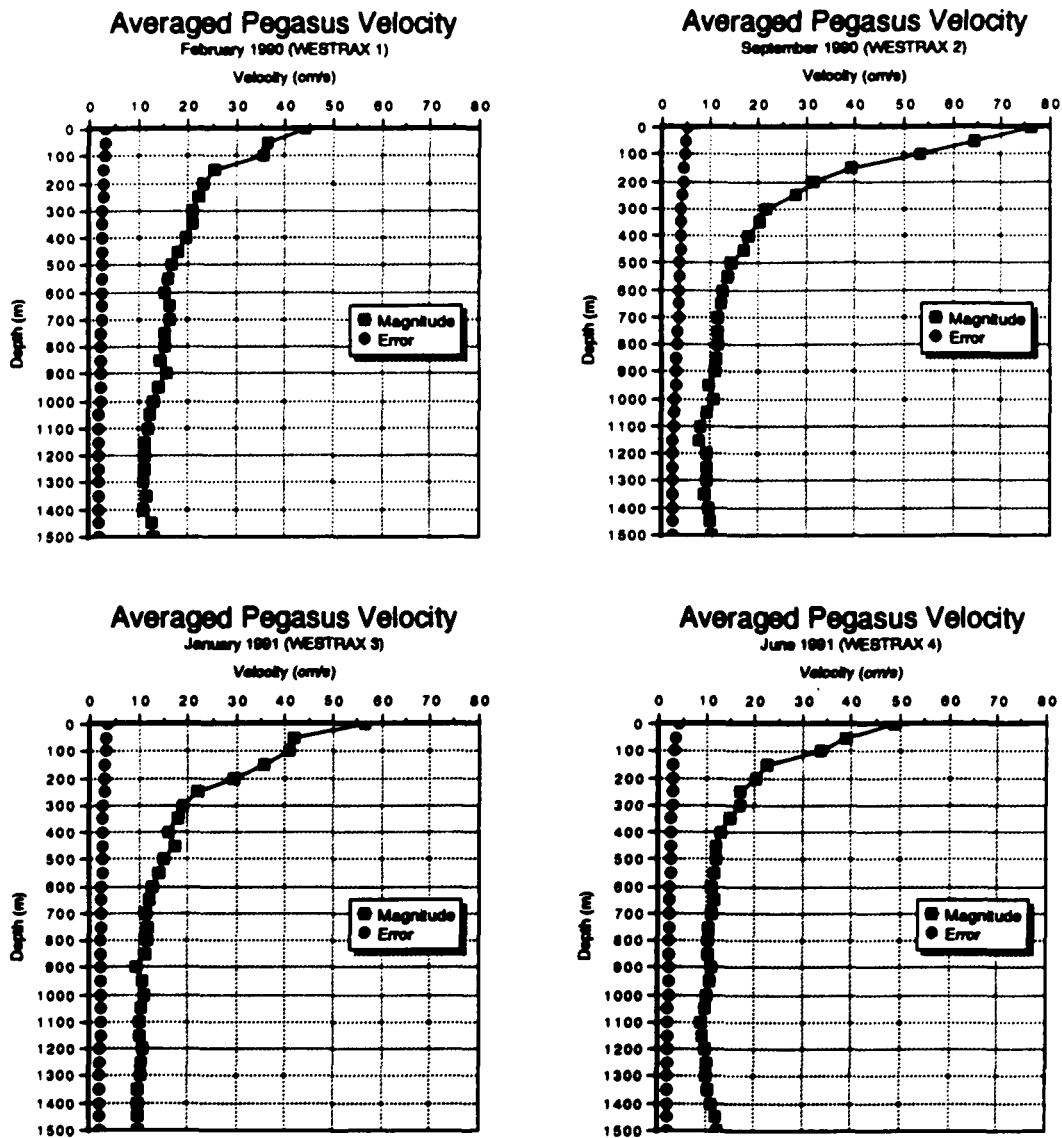


Figure 9. Horizontally averaged profiles of Pegasus velocity magnitudes (squares) and systematic velocity errors (dots). Velocities in cm/s at 50 m depth intervals.

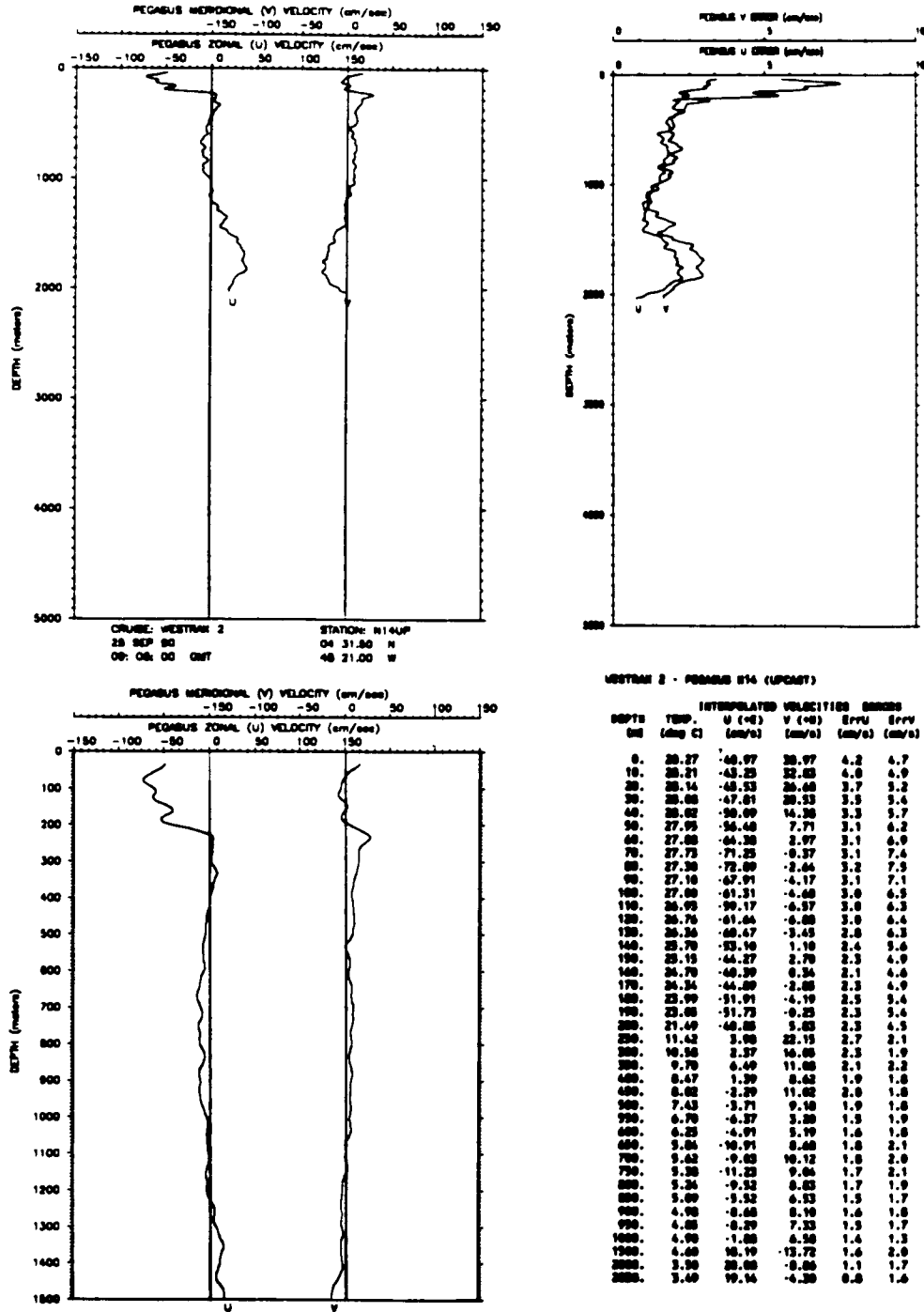
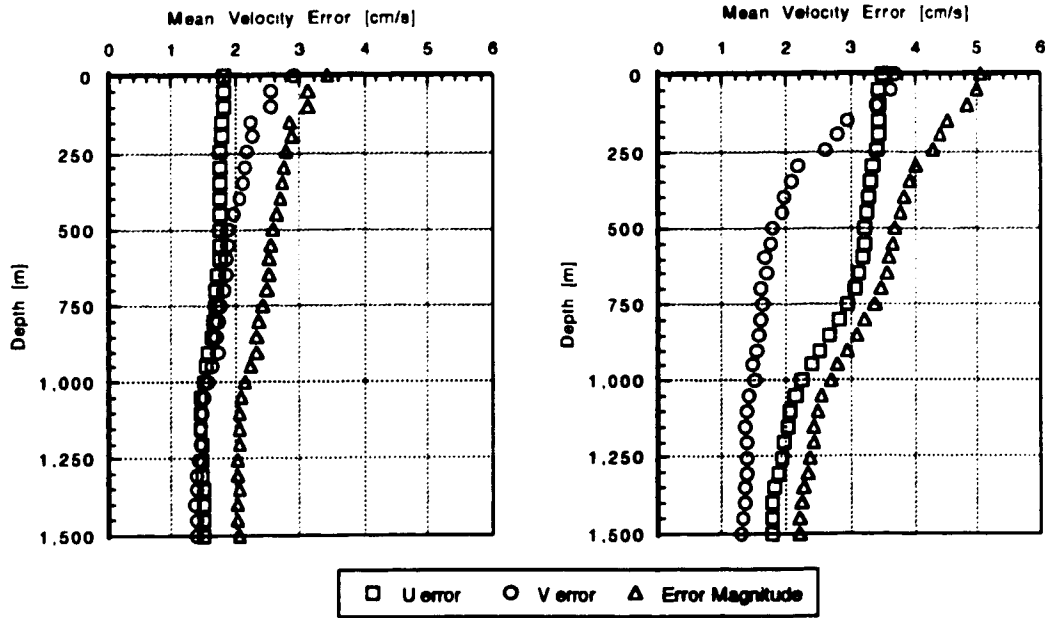


Figure 10. Sample from the archive of WESTRAX Pegasus velocity profiles. (a) Zonal (u) and meridional (v) velocity between 0-5000 m, offset 150 cm/s left and right respectively, according to scales at the top of the plot. (b) Corresponding u_{err} and v_{err} calculated by University of Miami analysts. (c) Same as 'a' for 0-1500 m. (d) Observed Pegasus temperature, u, v, u_{err} and v_{err} at selected depths.

February 1990 (WESTRAX 1)

September 1990 (WESTRAX 2)



January 1991 (WESTRAX 3)

June 1991 (WESTRAX 4)

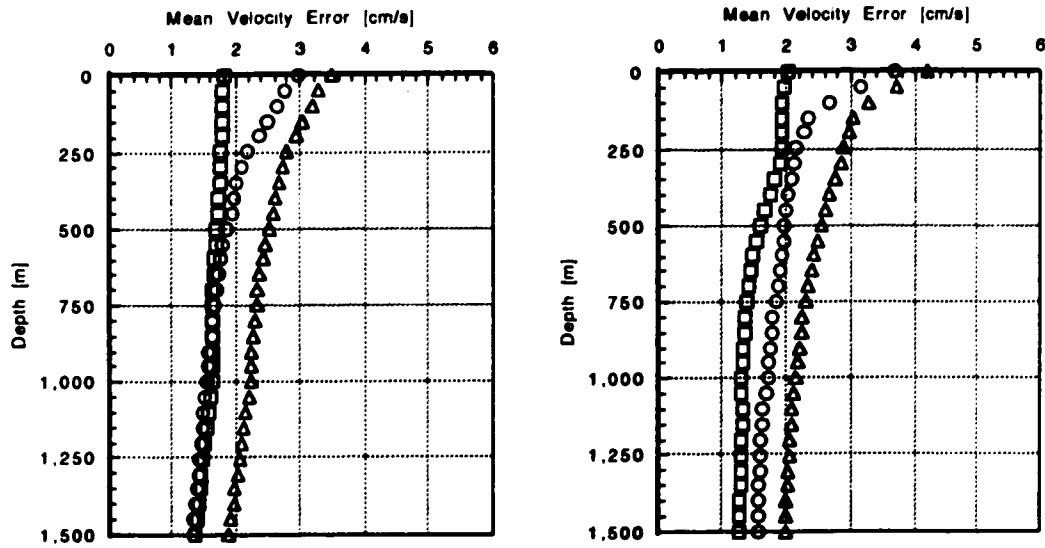


Figure 11. Horizontally averaged Pegasus systematic velocity error estimates: zonal (u, square), meridional (v, circle), and magnitude (triangle) in cm/s.

typical root mean square velocity errors due to internal wave motion estimated by Send (1993) (5.0 cm/s within the thermocline and 2.5 cm/s at depth). The corresponding mean percentage errors were 7% (surface), 11% (150 m), 20% (500 m), 21% (1000 m), and 18% (1500 m). An overall estimate of the four-cruise, depth-averaged Pegasus maximum systematic error within the upper 1500 m is 18%. The depth-average velocity errors over the upper 1500 m are presented in Table 3. K. Leaman (personal communication, 1993) suggests the actual errors are probably less than 10%, or half of the estimated systematic errors, since random station deployment errors would tend to cause velocity errors all of the same sign.

Table 3. Typical depth-averaged Pegasus velocities and systematic velocity errors [cm/s] in the upper 1500 m.

WESTRAX	Depth-Averaged Pegasus Velocities (u / v)	Depth-Averaged Max. Velocity Errors Absolute (u _{err} / v _{err})	Depth-Averaged Percentage of u / v *
1	13.0 / 12.1	1.6 / 1.8	14 / 16%
2	12.3 / 14.5	2.7 / 1.9	29 / 16%
3	12.1 / 12.0	1.6 / 1.8	17 / 17%
4	10.3 / 10.7	1.5 / 2.0	17 / 20%

A comparison between Pegasus and ADCP velocity observations...

The zonal and meridional velocity structures derived from Acoustic Doppler Current Profiler (ADCP) observations (Wilson and Rount 1992) and Pegasus interpolated fields on Section B (44°W) are compared (Figures 12 and 13). The zonal transports in Sverdrups (1 Sv = 10⁶ m³/s) through equivalent portions of Section B according to each method are listed on Table 4. While there is less detail in the Pegasus section (based on casts at only eight positions) than that of

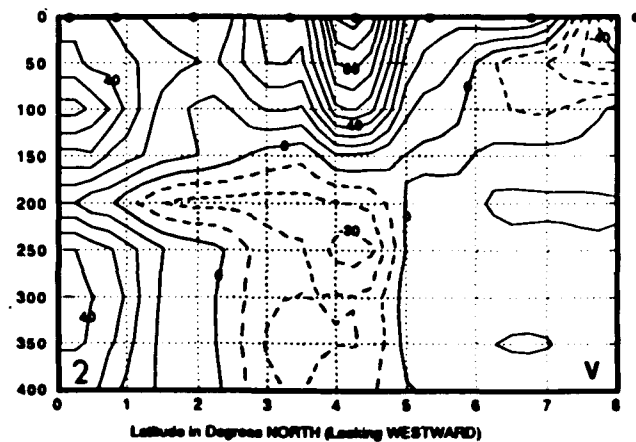
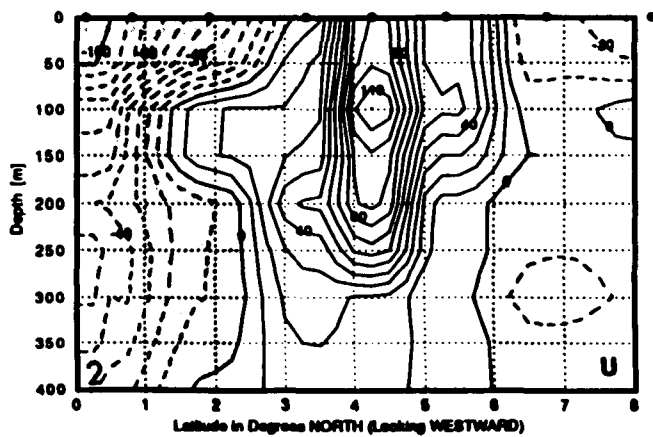
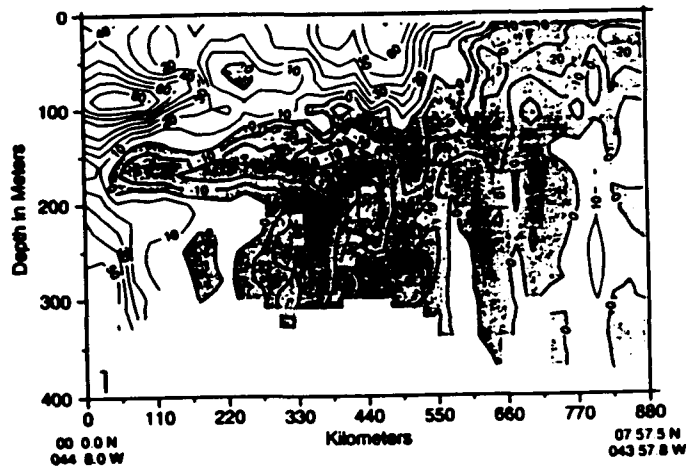
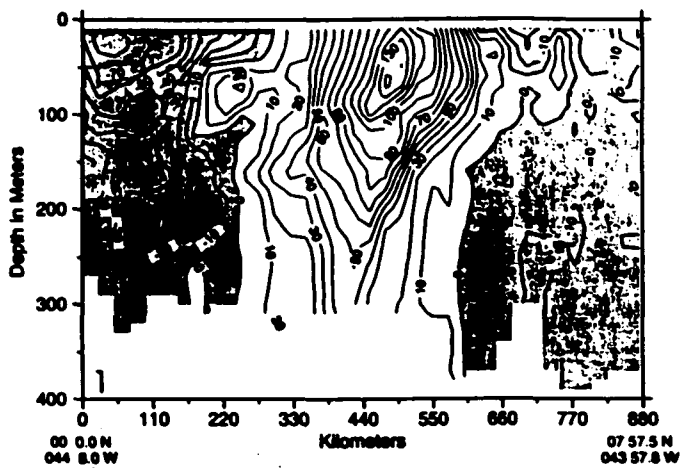


Figure 12. (1) ADCP and (2) interpolated Pegasus velocity structures during September 1990 (WESTRAX 2). Zonal (left) and meridional (right) velocities are compared. Negative (westward/southward) velocities are shaded. Pegasus stations are marked by dots. Contour intervals are 10 cm/s. ADCP plots are from Wilson and Routt (1992).

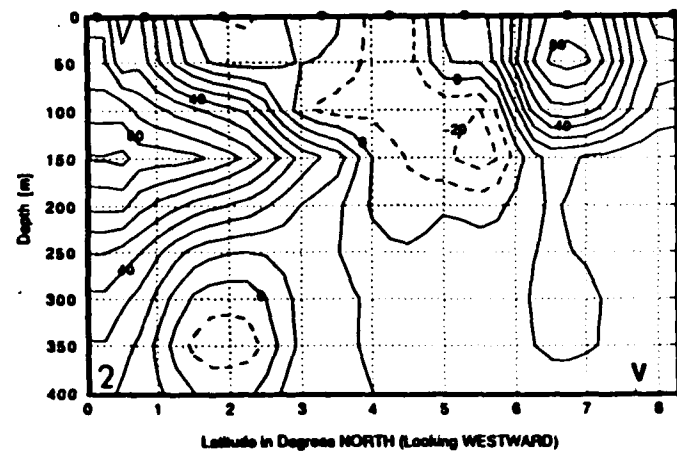
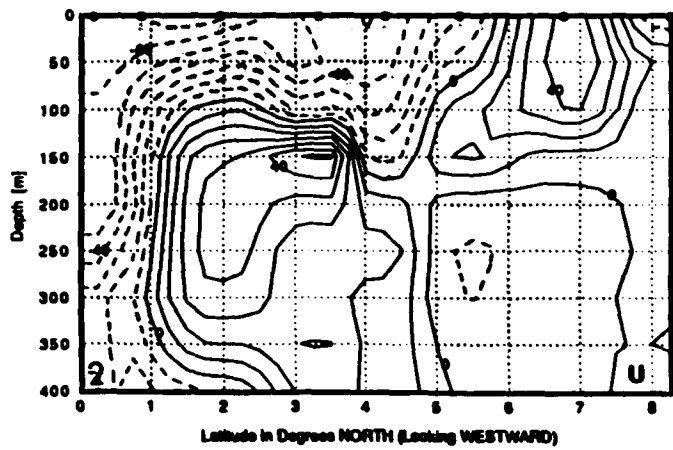
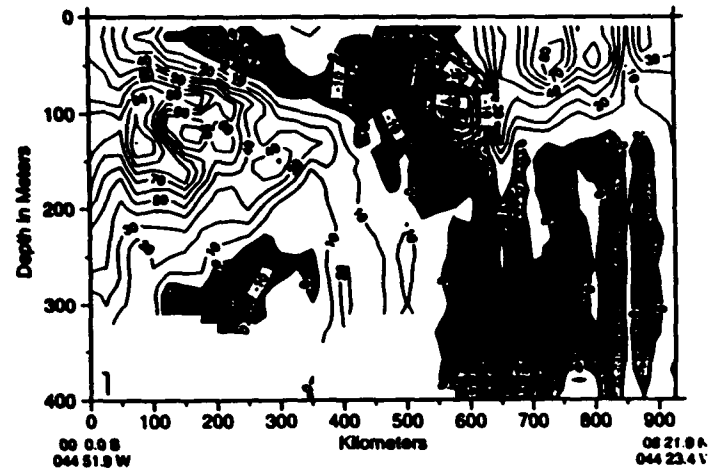
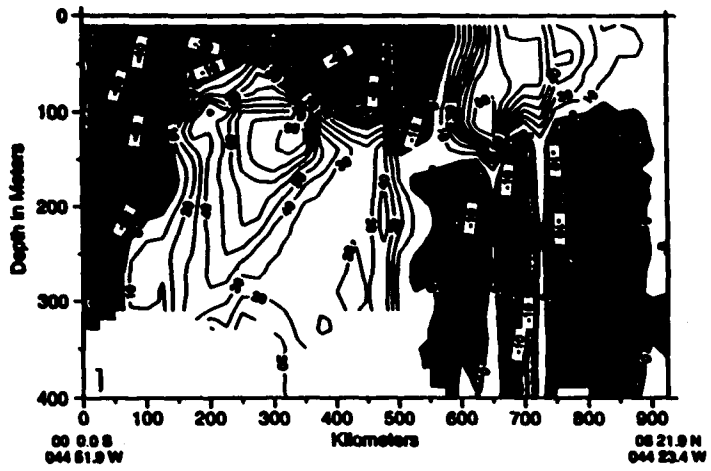


Figure 13. Same as Figure 12 for January 1991 (WESTRAX 3).

the ADCP section (derived from quarter degree averages of a continuous observation record), the structure and transport during September 1990 are similar (Figure 12). The largest differences include: the Pegasus analysis indicates the maximum westward flow of the NBC is 100 cm/s, compared to the ADCP maximum of 80 cm/s. The Pegasus 110 cm/s core of NECC return flow is 50 m deeper but at about the same latitude as the 140 cm/s NECC core according to ADCP.

Table 4. Comparison of Pegasus and ADCP* zonal transports across simultaneously observed portions of Section B (44°W) between 0-400 m (see Figures 12 and 13).

<u>WESTRAX 2 (September 1990)</u>					
Flow:	Westward	Eastward	Westward		Total
Latitudes:	(0-2°N)	(2-6°N)	(6-8°N)		(0-8°N)
ADCP	-20	+49	-5		+24
Pegasus	-22	+51	-6		+23
<u>WESTRAX 3 (January 1991)</u>					
Flow:	Westward	Eastward	Westward	Eastward	Total
Latitudes:	(0-5°N)	(1-5°N)	(5-8°N)	(5-8°N)	(0-8°N)
ADCP	-25	+34	-5	+14	+18
Pegasus	-30	+28	-3	+11	+6

* Provided by D. Wilson, AOML.
 Transports in Sverdrups (1 Sv = 10⁶ m³/s)

The January 1991 Pegasus and ADCP structures are less comparable (Figure 13). The 5 Sv difference in westward transport between 0-5°N is attributed to a near-surface region of NBC flow which is larger on the Pegasus compared with the ADCP section. The 6 Sv discrepancy in eastward transport occurs because the Pegasus survey missed the 90 cm/s core of flow in the NECC which was observed

by the ADCP. Otherwise, the many similarities between Pegasus and ADCP observations support the validity of the Pegasus velocity observations.

III.

DATA ANALYSES - INTERPOLATION AND STREAM FUNCTION

The interpolation of temperature, salinity, and velocity profiles onto regularly gridded horizontal surfaces is described. Assumptions, error estimates and limitations are presented. The use of non-divergent velocities, and the stream function analyses which produce non-divergent velocity fields, are discussed.

Interpolation of data to a grid...

The initial step in the WESTRAX data analysis is to interpolate the unevenly-spaced profile measurements onto an evenly-spaced horizontal grid (Figure 1-4). It is desirable to work with gridded data so that:

- Direct comparisons between different physical variables can be made
- Derived variables can be computed at all locations, regardless of the original distribution of observations, and
- Volume, temperature, and salinity transports can be computed for comparable sections throughout the region.

The interpolation of potential temperature, salinity, potential density, zonal velocity, and meridional velocity measurements were interpolated onto evenly spaced horizontal grids was accomplished using the National Center for Atmospheric Research (NCAR) algorithm 'CONRAN' (Clare, Kennison, and Lackman 1987) as described by Akima (1978) (see Appendix A). The main advantage of this algorithm is that it fits a surface exactly to the observed values. The disadvantage of the Akima (1978) algorithm is that it does not provide an

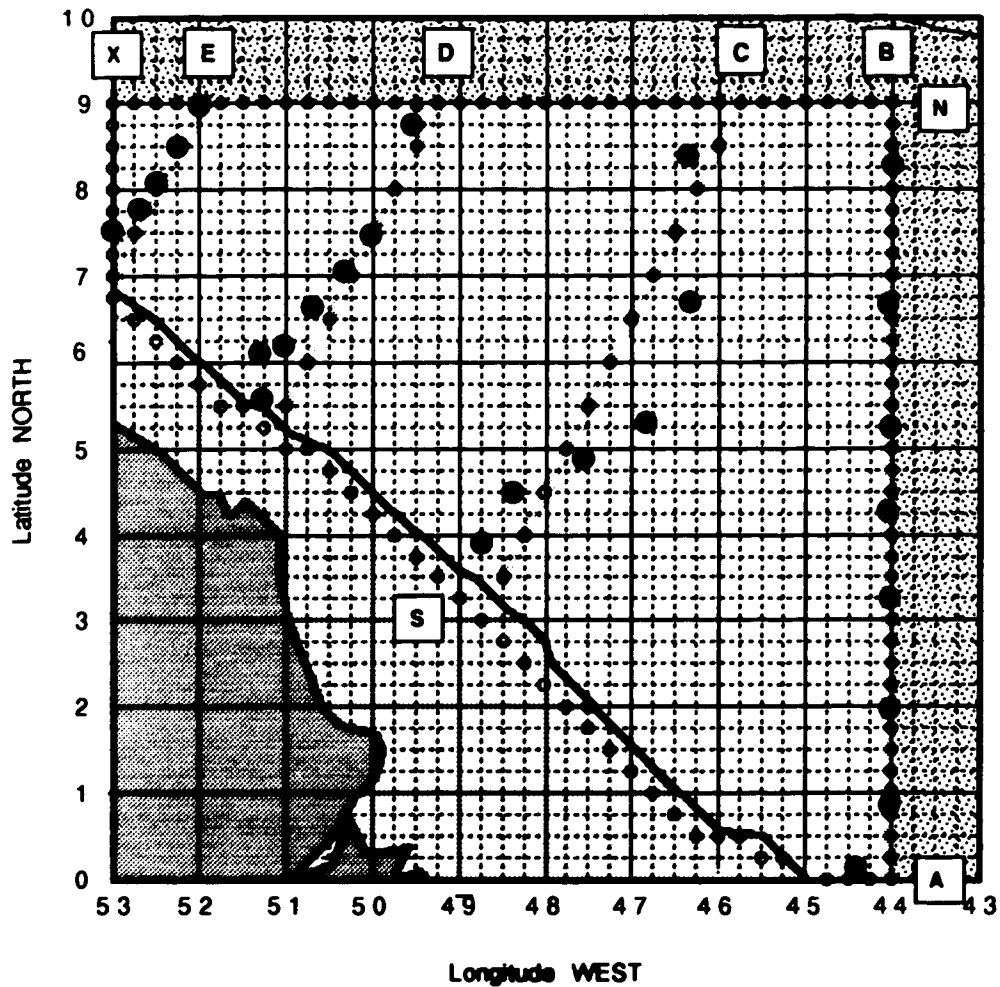


Figure 14. WESTRAX region analysis grid at one-quarter degree. Pegasus sites are marked by black dots. Gray lines indicate the transects at sections B, C, D, and E. Open dots are at points used for the interpolations of data on these sections. South America is darkened and the continental shelf is shaded. The stippled areas are beyond the boundaries of the interpolation analysis.

objective means to determine uncertainties at other locations (e.g., at grid points).

A grid spacing of one-quarter degree (27.8 km) was selected for the interpolation of WESTRAX fields (Figure 14). This is of the same order as the 30 km mean along-track distance between CTD and XBT stations. Tests using smaller grid spacings produced significant increases in run time and larger space requirements for the storage of fields. Larger grid spacings did not display the principal circulation features of interest as well as the chosen grid. Appendix A notes that the Akima (1978) algorithm creates a three-dimensional 'surface' which passes exactly through each point of the observation data set. The interpolation scheme extracts gridded data from this surface as a set of 'heights' at the selected points. While the accuracy of these gridded data cannot be determined, the resultant shape of the surface is fixed and thus independent of the extraction grid spacing. That is, whether the grid spacing is 1/4 or one degree, the information interpolated at a set of 1 x 1 degree grid points, and the associated error field, does not change.

Akima (1978) was careful to note that large errors are likely if the algorithm is used to extrapolate beyond the edges of the observed data field. After some experimentation, the WESTRAX analyses were limited to the region bounded by 44°W to 53°W and from the equator to 9°N (Figure 14). This region enclosed WESTRAX transects: B, C, D, and E. Spurious information in the corners of the region were corrected via linear extrapolation of nearby interior data (Figure 15). By assuming the grid sizes were constant and square between the equator and 9°N, a maximum spatial error due to spherical effects of -1.3% in longitude measurements (Δx) occurred at 9°N. The selected quarter degree grid spacing yielded sets of 1369 data points on each of thirty-one depth surfaces at intervals of 50 m, between the ocean surface and 1500 m.

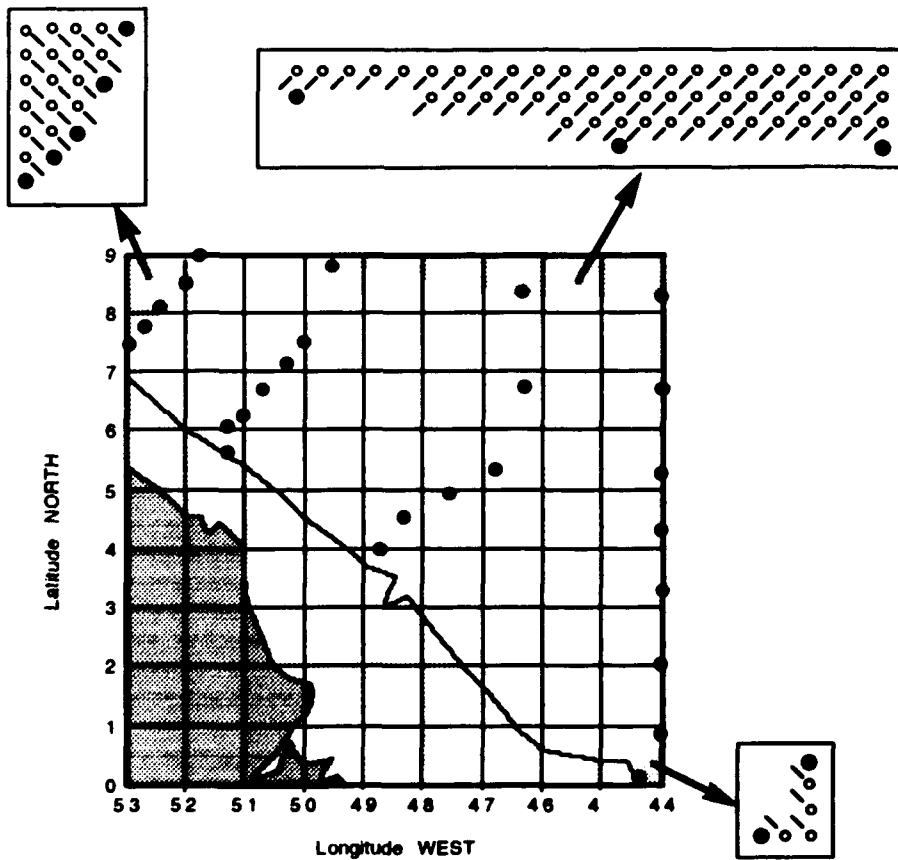


Figure 15. Illustrates the method used to extrapolate interpolated data to the corners of the WESTRAX region. Pegasus sites are at the solid dots. The interpolation is initially performed on an 1/4 by 1/4 degree grid. Interpolated data from 'good' grid points (e.g., inside the black dots or enclosed by the observations) are then linearly extrapolated to the corners (the shaded areas) diagonally through the open circles.

A set of error maps associated with an objective analysis of WESTRAX data is included to indicate the interpolation errors which could be attributed to distance from observation points (Figure 16). These errors range from less than 10% along cruise transects to greater than 40% in the large open areas between Sections B and C (DaSilveira, personal communication 1993).

Table 5. Intermediate layer transports through the boundaries of the WESTRAX region. Positive transports (Sverdrups, $10^6 \text{ m}^3/\text{s}$) flow into the region.

WESTRAX	(1)	(2)	(3)	(4)	+Survey	Weighted*
	FEB 90	SEP 90	IAN 91	JUN 91	Average	Std Dev
<i>Divergent (interpolated) transports...</i>						
A. Inflow from the southeast:						
	+54	+33	+26	+43	+37	10.6
B. Outflow toward the east (NEUC):						
	-45	-43	-61	-41	-46	7.9
C. Inflow from the north:						
	+102	+78	+51	+65	+73	18.8
D. Outflow toward the west or northwest:						
	-58	-36	-32	-22	-34	13.2
Net interpolated (divergent) transport imbalances:						
	+53	+32	-16	+45	+30	26.8
<i>Non-divergent (stream function) transports...</i>						
A. Inflow from the southeast:						
	+40	+26	+23	+29	+29	6.4
B. Outflow toward the east (NEUC):						
	-54	-48	-57	-46	-50	4.4
C. Inflow from the north:						
	+70	+62	+60	+53	+61	6.0
D. Outflow toward the west or northwest:						
	-56	-40	-26	-36	-40	10.8
There are no horizontal transport imbalances in non-divergent flow.						
* To ensure seasonal balances, the two winter cruises were assigned 1/2 weight compared to one for the early and late summer transports.						

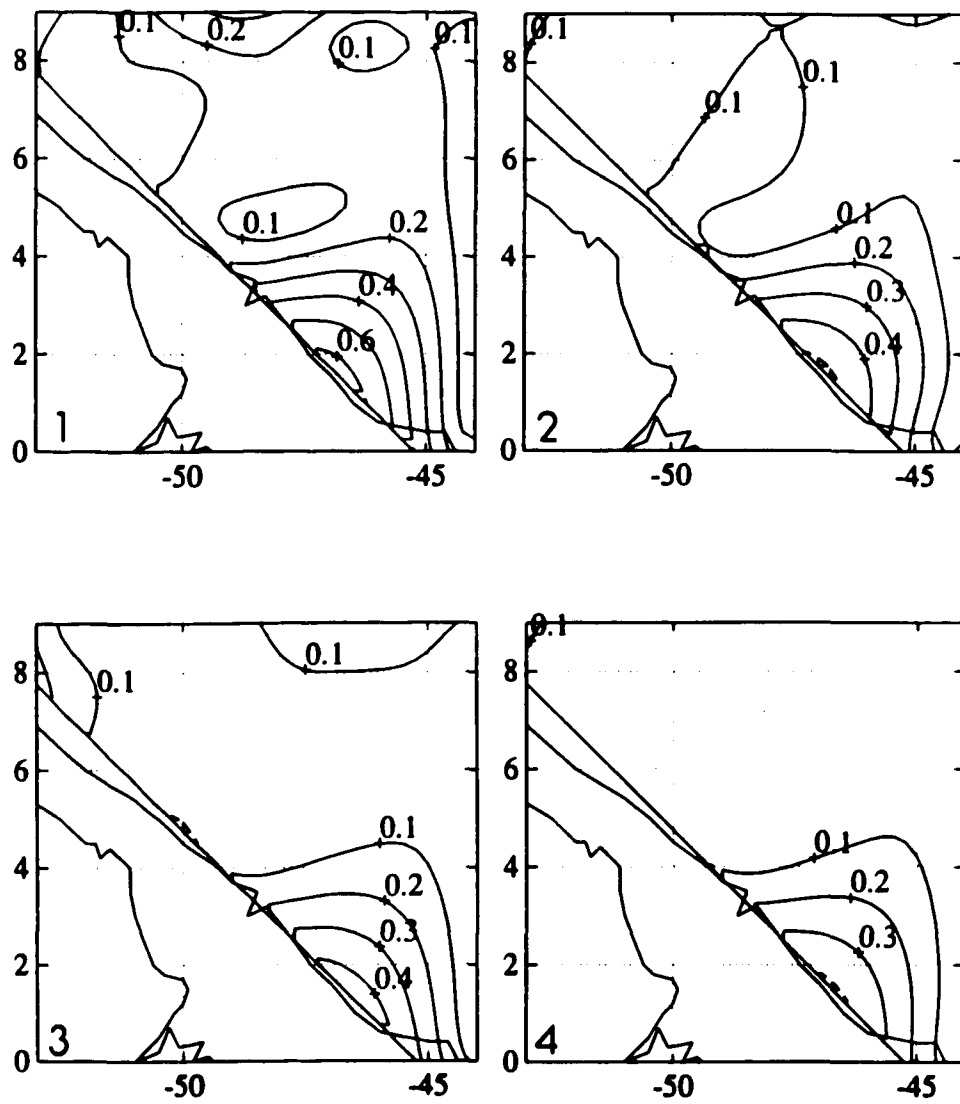


Figure 16. Interpolation error estimates using objective analysis techniques for the WESTRAX observation suite. The contours indicate normalized expected errors (1.0 = 100%) due to distance from the observations (DaSilveira, personal communication 1993).

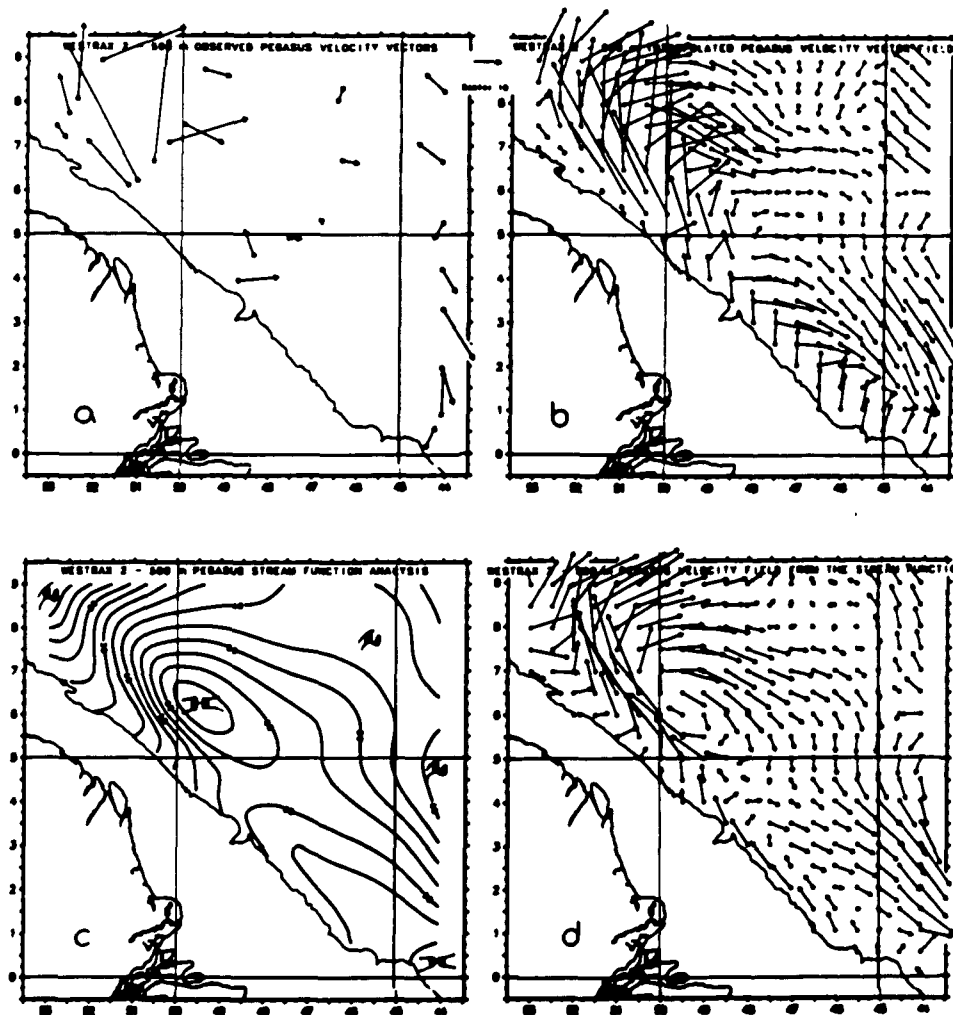


Figure 17. Horizontal fields of observed and analyzed Pegasus velocity vectors at the 500 m depth during September 1990 (WESTRAX 2).

(a) The original observations. Velocity vectors originate at the solid dot, extend to the arrowhead, and point toward the direction of flow. Vector lengths indicate velocity magnitude relative to the 10 cm/s reference vector in the upper center. Velocities on all panels are at the same scale.

(b) Results of the Akima (1972) interpolation. Vectors are displayed at a half degree spacing for clarity

(c) Results of the stream function analysis, contoured at 5 s^{-1} intervals.

(d) Non-divergent velocity vector fields derived from the stream function.

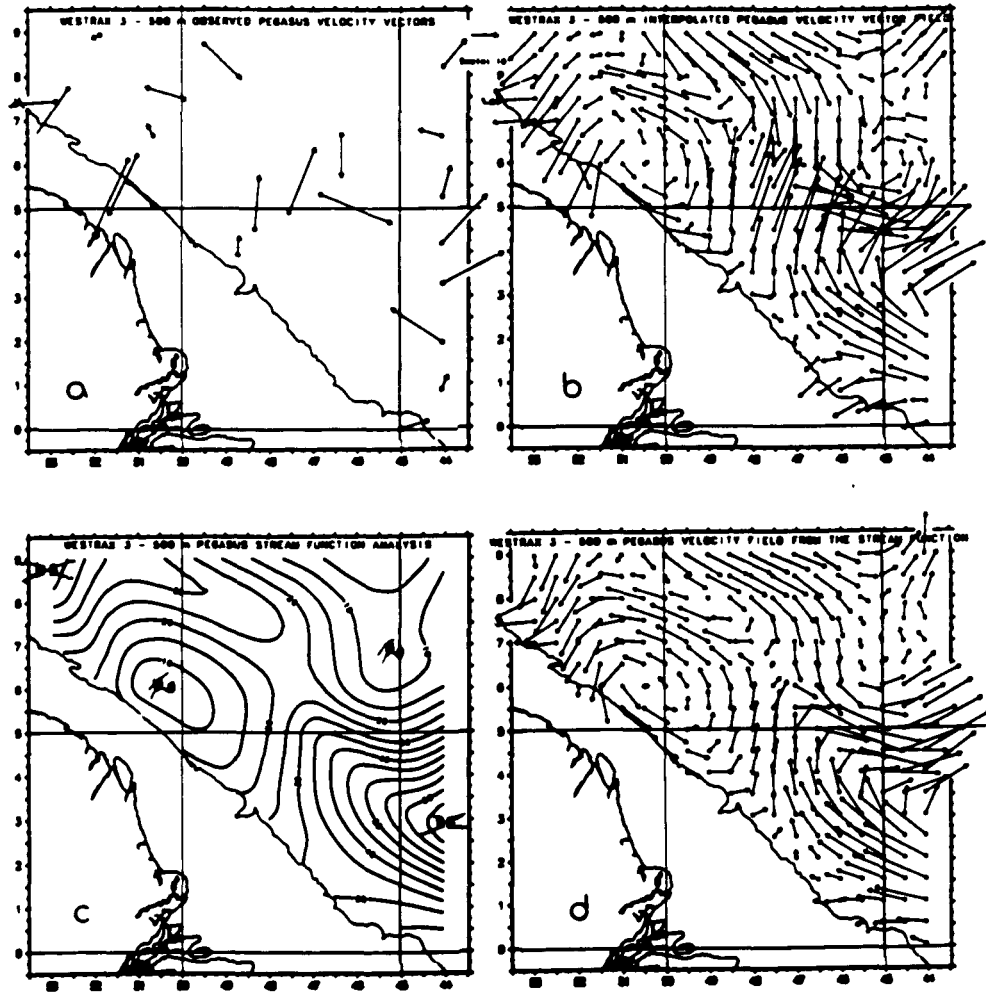


Figure 18. Same as Figure 17 for January 1991 (WESTRAX 3).

Divergent versus non-divergent transports...

Initially, I anticipated that the interpolated (e.g., divergent) Pegasus velocity fields would, within the observational uncertainty, best represent the velocity structure of the WESTRAX region. However, I was unable to explain large imbalances within intermediate layer horizontal transports (see Table 5). I had expected to account for transport differences by determining vertical velocity through the region according to the continuity equation (see Appendix D). My vertical velocity transports were an order of magnitude larger than the IFM-IR model (Schott and Böning 1991) mean vertical transports of -2.7, +2.5, and +2.3 Sv across the 72, 206, and 519 m surfaces respectively, within a similar region between 2.5-10°N and 44-53°W.

Since vertical velocity analyses could not corroborate horizontal transport imbalances, it became necessary to use non-divergent velocity structure to compute transports. This simplification is unfortunate, as I suspect that convergence and divergence, and therefore vertical motion, play a significant transport role in some areas of the WESTRAX region.

Stream Function analysis...

The zonal (u) and meridional (v) components of velocity were interpolated separately and then combined to produce vector fields of horizontal flow. The original observation vectors were determined (Figures 17a and 18a) and, using the Akima (1978) algorithm, were interpolated to an evenly spaced grid depicting divergent flow (Figures 17b and 18b). As Pegasus velocity measurements did not generally extend to the surface, the shallowest velocity map at 25 m was assumed to represent the surface flow field. There was some extrapolation as far as the 100 m isobath over the shelf.

Stream functions of the interpolated velocity fields (Figures 17c and 18c) are computed using an algorithm provided by Doug Wilson of AOML (see

Appendices B and C). This approach required me to assume that the flow was horizontally non-divergent and that vertical velocities were zero (see Appendix B). As a result, the net transports through the region are zero. With vertical motion eliminated, the analyzed horizontal velocity fields represent a lower limit to the actual flow structure. Additionally, vertical linkages in the flow structures between layers are reduced. The non-divergent velocity fields (Figures 17d and 18d) are then derived from the stream function.

Different transports across section B (44°W) which have been derived from six different absolute (Pegasus) and geostrophic analysis techniques are compared in Appendix E.

The interpolated, non-divergent velocity structure of the WESTRAX region is described in the next section and detailed in Appendix F.

The WESTRAX region's hydrographic structures according to interpolated temperature and salinity data are described in Appendix G.

IV. VELOCITY STRUCTURE

The current structure of the region is described. Volume transports through the boundaries of the WESTRAX region are presented. A four-pathway flow pattern is suggested. Late summer, winter, and early summer features, flow structure, and seasonal changes are presented. Transport associated with the retroflection eddies is introduced.

Overview...

Ocean circulation can be defined, as meteorologists do, in terms of a system of intersecting 'ridges' (crests) and 'troughs' (valleys). In the northern hemisphere, water in a high pressure center (H) or 'anticyclone' within a ridge tends to flow in a clockwise direction. Water in a low pressure center (L) or 'cyclone' within a trough tends to flow counterclockwise.

A circulation structure for the WESTRAX region is suggested by the climatological wind-driven circulation patterns of the Atlantic Ocean presented in Mayer and Weisberg (1993) (Figure 4, section I). If the gyres within the western tropical Atlantic are closed by the return flows necessary for continuity, a regional flow structure would include:

- The westward flowing NEC of the North Atlantic subtropical gyre
- The cyclonic return flow of the NEC through the tropical gyre and into the NEUC
- The westward flowing SEC of the South Atlantic subtropical gyre
- Its anticyclonic return flow eastward into the NEUC as part of the equatorial gyre (Figure 19a).

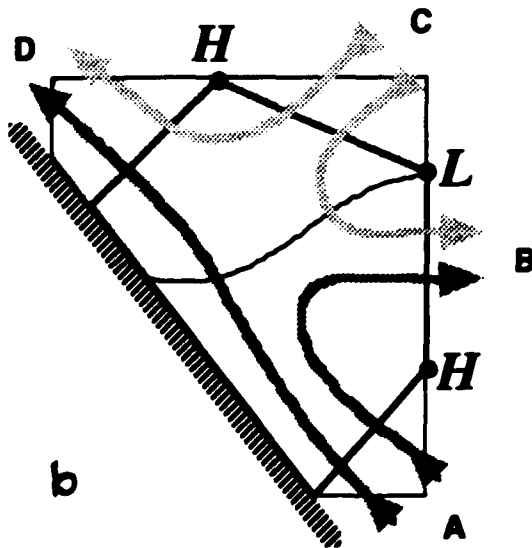
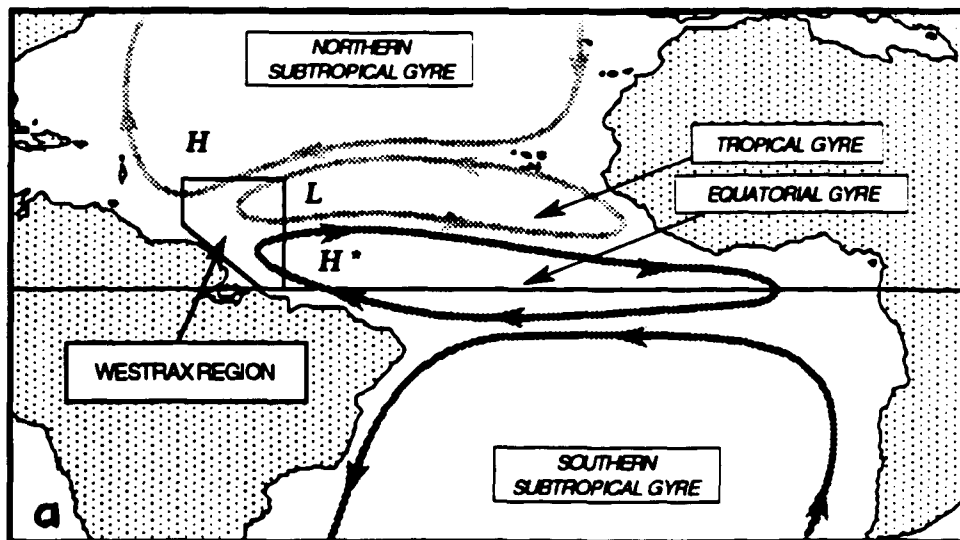


Figure 19. (a) A four cell circulation pattern for the Atlantic Ocean based on Mayer and Weisberg (1993). The WESTRAX region is indicated.

(b) A conceptual model of intermediate layer flow in the WESTRAX region. Pathways around three centers represent the western extremes of the northern subtropical gyre (H), the tropical gyre (L), and the equatorial gyre (H). A fourth pathway flows northwestward along the continental slope. The sides of the heavier polygon are normal to the flows which enter through:

- A. Northwestward inflow through the southeast corner
- B. Eastward outflow toward the North Equatorial Undercurrent (NEUC)
- C. Southeastward inflow from the northeast or east
- D. Northwestward outflow toward the Caribbean.

No intermediate water crosses the hatched continental shelf. Flow from the shaded to unshaded regions represents southward flow around the tropical gyre and into the NEUC, or visa-versa.

I will initially describe the region's intermediate layer velocity structure in terms of a schematic streamline analysis (Figure 20a). This is based on the depth-averaged (150-1300 m), four-survey weighted average of the non-divergent Pegasus velocity structure (Figure 20b). The schematic also incorporates major features which are evident on the depth-averaged analyses of the individual WESTRAX surveys (Figure 21). To reduce seasonal bias, 'average' transports are based on four-survey weighted-averages which are computed by assigning half weight to data from the two winter cruises (WESTRAX 1 and 3) and full weight each to data from the late summer (WESTRAX 2) and early summer (WESTRAX 4) cruises.

An 'alongshore ridge' is the dominant circulation feature of the western tropical Atlantic intermediate layer during the summer (Figure 21b/d). This ridge extends from the region's eastern to western boundaries, 100 to 300 km northeast of the continental shelf break (marked by the 200 m isobath). The anticyclones which form the alongshore ridge are the 'retroflexion' or Amazon Eddy (*Hae*, near 2°N 45°W) and the Demerara Eddy (*Hde*, in the center or northwest). Throughout this dissertation, I will refer to the Demerara Eddy (*Hde*) as the semi-permanent anticyclone which is evident near the center of WESTRAX region. The relation between *Hde* and the northwestward translating 'retroflexion eddy' will be discussed later.

A 'central trough' is most evident during the winter surveys. This trough extends southwestward from the low on the region's eastern boundary (*Le*, near 6°N 44°W), crosses the alongshore ridge, and follows the continental slope northwestward. A low located off the coast of French Guiana (*Lfg*, near 6°N 50°W) is evident within this trough (Figure 21a and 21c). I note that during each of the WESTRAX surveys, *Le* is a well-defined feature of the intermediate layer.

There are distinct differences between the average flow structures of the surface, upper, and lower intermediate layers (Figure 22). Transports are

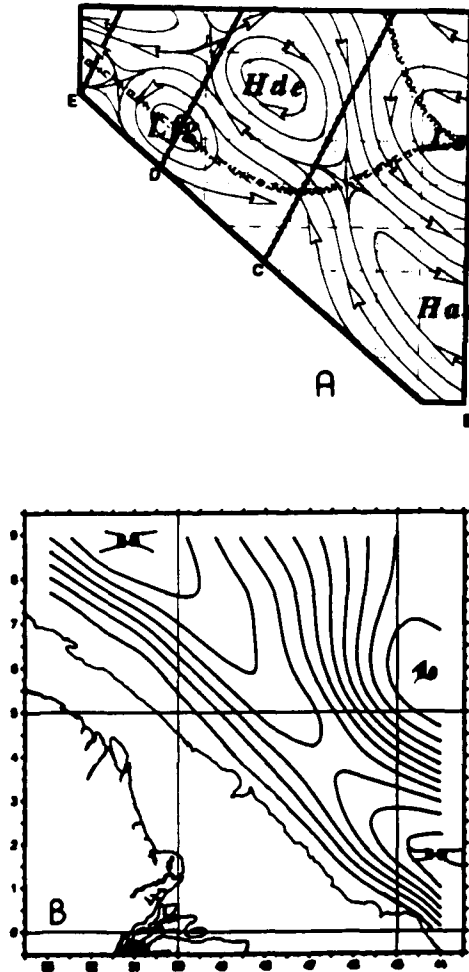


Figure 20. Intermediate layer circulation features of the WESTRAX region.

(a) Schematic to illustrate the **Highs** within the **alongshore ridge** (hatched): *Hae* - Amazon Eddy or main retroflexion and *Hde* - Demerara Eddy or central high; the **Lows** within the **central trough** (gray): *Le* - eastern low and *Lfg* - low along the French Guiana Coast. Flows along streamlines are indicated by arrows. WESTRAX survey transects B, C, D, and E are marked.

(b) The depth-averaged, 4-survey weighted-average Pegasus transport streamline structure for the WESTRAX region intermediate layer (150-1300 m). Each streamline represents approximately $5 \times 10^6 \text{ m}^3/\text{s}$ (5 Sverdrups)

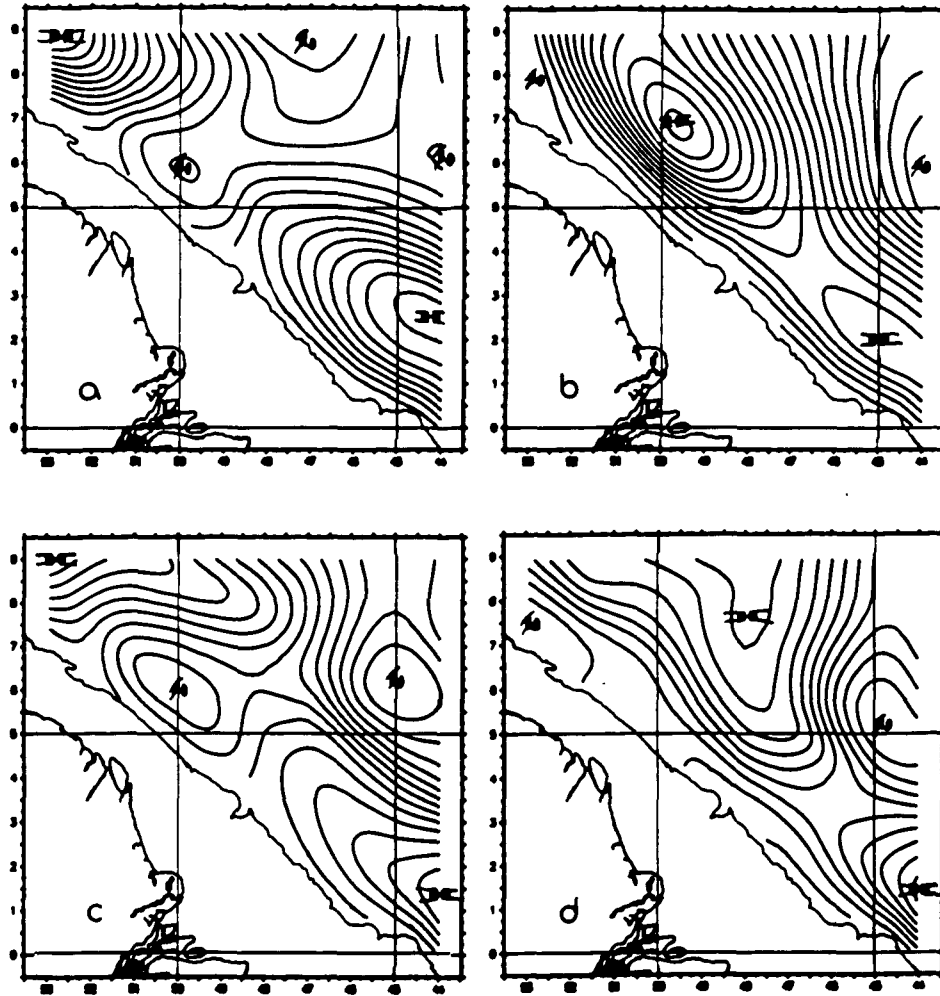


Figure 21A. Depth-averaged Pegasus transport streamline structure for the WESTRAX region intermediate layer (150-1300 m) during:

- (a) winter (February 1990)
- (b) late summer (September 1990)
- (c) winter (January 1991)
- (d) early summer (June 1991).

Each streamline represents approximately $5 \times 10^6 \text{ m}^3/\text{s}$ (5 Sverdrups).

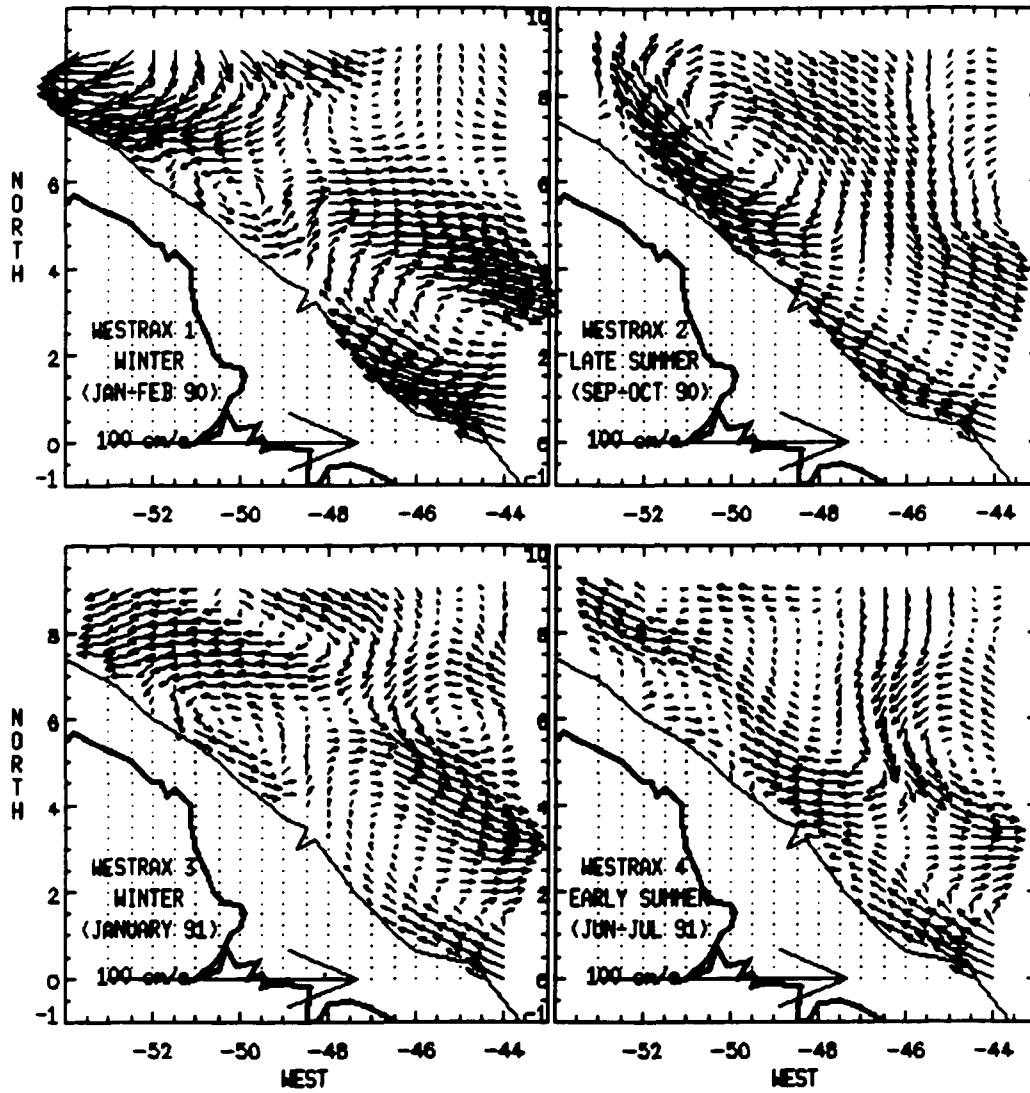


Figure 21B. Depth-averaged, non-divergent Pegasus velocity vector fields according to Figure 21A. An 100 cm/s reference vector is at the lower left.

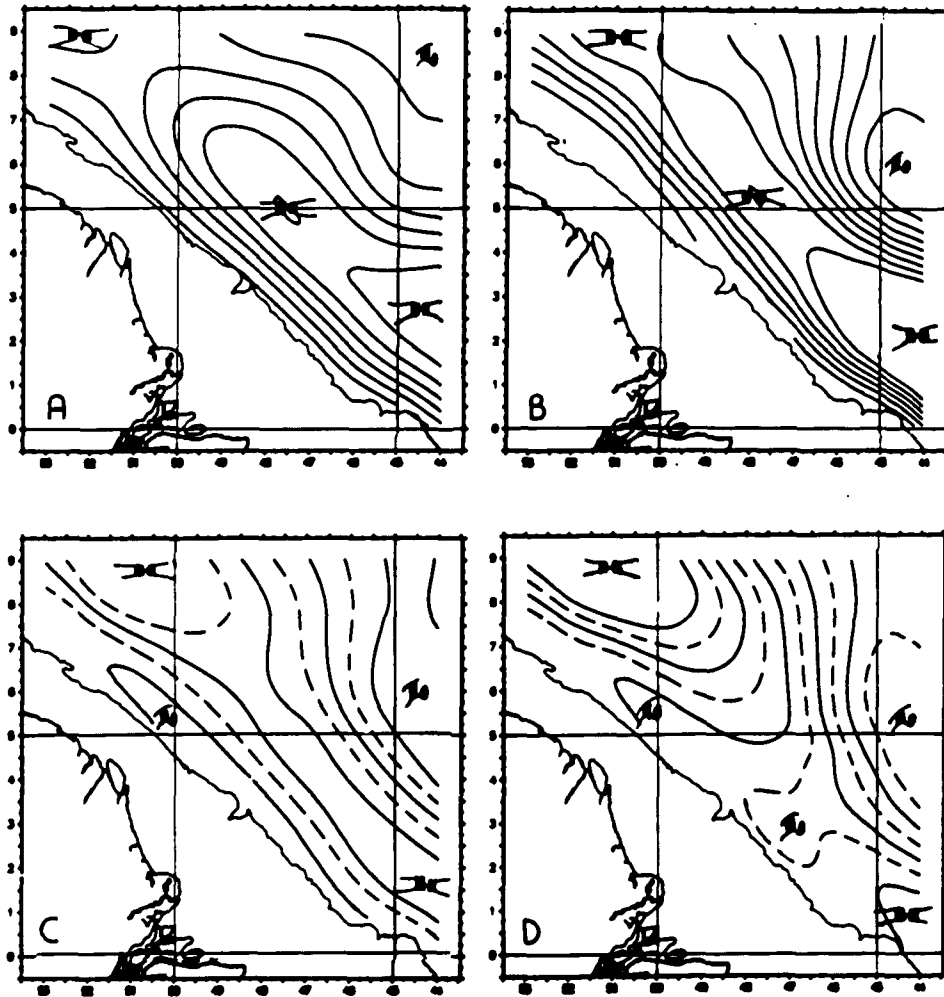


Figure 22. The depth-averaged, +survey weighted-average Pegasus transport streamline structure for the WESTRAX region within the:

- (a) Surface layer (0-150 m)
- (b) Upper intermediate layer (150-750 m)
- (c) Middle intermediate layer (Antarctic Intermediate Water, 650-850 m)
- (d) Lower intermediate layer (750-1300 m).

Each solid streamline represents approximately $5 \times 10^6 \text{ m}^3/\text{s}$ (5 Sverdrups)

approximately four times greater in the upper layer. A strong *Hae* within the upper layer diminishes with depth to a small anticyclonic cell in the region's southeastern corner. The lower layer is bisected by a trough which extends westward from *Le* toward *Lfg*. During the winter surveys, the greatest differences between the velocity structures of the surface and intermediate layers are apparent, while there is more vertical consistency during summer (see Appendix F). Flow within the middle layer (*i.e.*, AAIW) is more like flow within the upper vice the lower intermediate layers (Figures 22b and 22c).

WESTRAX region transport structure...

Guided by the Mayer and Weisberg (1993) flow pattern as a framework, I have constructed a conceptual model for the transport structure of the WESTRAX region (Figure 19b). The computations of volume transports in Sverdrups (1 Sv = 10^6 m³/s) are described in Appendix H.

A survey-average 29 Sv (Figure 23a) enter the intermediate layer of the region from the southeast via the SEC (*e.g.*, through point A, Figure 19b). Another 61 Sv enter from the northeast via the NEC (point C). To balance these, 50 Sv depart the region flowing eastward into the NEUC (point B) and 40 Sv depart flowing northwestward toward the Caribbean (point D).

There are four principal pathways within the WESTRAX region (Figure 19b). Volume transports along these pathways are derived from streamline structures across sections C, D, and E (Figure 21). An average 21 Sv (Figure 23a) of the water entering from the southeast turn anticyclonically around the Amazon Eddy and flow into the NEUC (path A->B). The remaining 8 Sv continue northwestward along the continental slope (A->D). Similarly, 29 Sv of the water entering from the north turn cyclonically around the region's eastern low (and some flows around the French Guiana low if it is present) and into the NEUC (C->B). 32 Sv of the northern inflow turn anticyclonically and join the

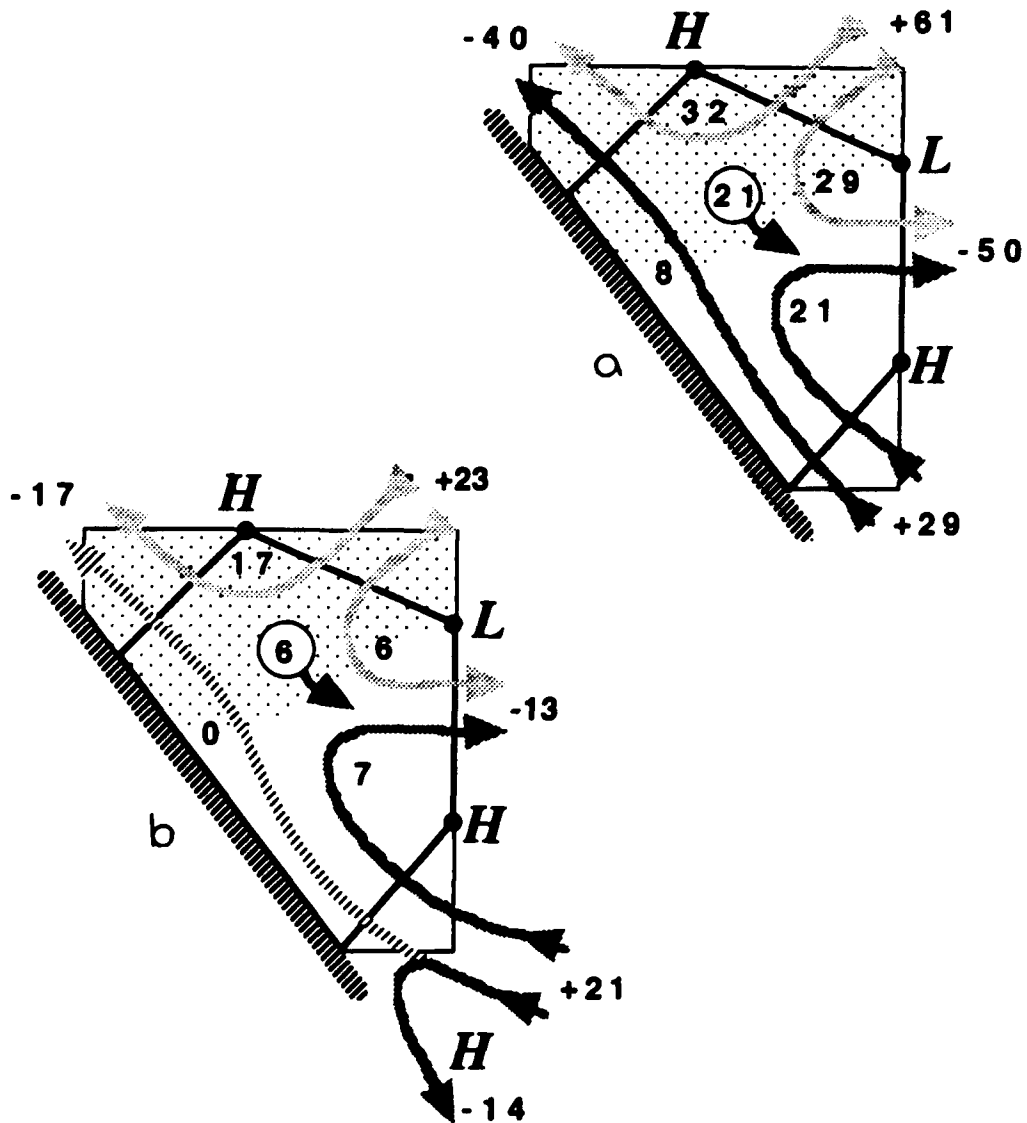


Figure 23. Volume transports via the pathways of Figure 19b according to:
 (a) WESTRAX intermediate layer weighted-average, non-divergent Pegasus velocity structure.
 (b) Return flows required by continuity to balance the wind-driven Atlantic circulation (Mayer and Weisberg 1993).
 Transports in Sv ($10^6 \text{ m}^3/\text{s}$) into the region are positive. The net southward transports around the tropical gyre and into the NEUC are circled.

northwestward flow (C->D). Path C->D may be the continued westward flow of the NEC, or it could include anticyclonic circulation around the Demerara Eddy.

There is a net 21 Sv which move cyclonically southward through the axis of the tropical gyre. This represents a meridional transport between northern (shaded) and southern ocean regimes of the WESTRAX region.

The WESTRAX transports are two to four times larger than the wind-driven return flows (Mayer and Weisberg 1993). I have interpreted Mayer and Weisberg's (1993) annual averages in terms of the WESTRAX conceptual model (Figure 23b). The 21 Sv in the westward flowing wind-driven SEC bifurcate. 7 Sv enter the region and retroreflect anticyclonically into the NECC/NEUC (path A->B) as the western extension of the equatorial gyre. The other 14 Sv within the SEC have turned southward far to the south of the WESTRAX region as part of the South Atlantic subtropical gyre. Similarly, the 23 Sv which flow westward within the NEC also split. 6 Sv turn cyclonically around the tropical gyre and join the eastward flowing NECC/NEUC system (path C->B). The remaining 17 Sv of the NEC continue northwestward into the Caribbean (path C->D). There is no flow along the continental slope (path A->D) in the Mayer and Weisberg (1993) wind-driven current structure. Below I will attribute the apparent discrepancy between this and the 8 Sv flow in the WESTRAX analysis to transport associated with retroreflection eddies.

A summary of the transport structure during each WESTRAX survey follows. A more complete description of the velocity structure is presented in Appendix F. I begin by introducing the important features of the boreal late summer, represented by the September 1990 survey (WESTRAX 2). This is then followed by the winter structures during January 1991 and February 1990 (WESTRAX 3 and 1 respectively). I conclude with the features of the June 1991 transition period (WESTRAX 4).

The late summer...

During September 1990, 19 Sv of the 26 Sv which enter from the southeast flow northwestward between the alongshore ridge and the continental slope (WESTRAX 2, Figures 20A&Bb, 24, and in Appendix F, see F-1 through F-3). The other 7 Sv turn offshore within the retroflexion around *Hae*. I suspect that most of the northwestward flow retroreflects around *Hde* beyond the border and returns to the WESTRAX region. Retroflected water flows southeastward into the 48 Sv NEUC. In the north, 62 Sv enter the region by either flowing generally southeastward through the northern border or westward across 44 W. 41 Sv of this northern inflow turn cyclonically around *Le*, contributing 85% to the flow of the NEUC. The remaining 21 Sv blend into the anticyclonic flow around *Hde*. Net southward flow around the tropical gyre is 22 Sv.

During September 1990, most of the major circulation features extend vertically throughout the upper kilometer of the WESTRAX region. This is demonstrated by the similarity between the flow patterns of the surface, upper, and lower intermediate layers (Figure F-1).

The winter...

By the following winter, the structures of the principal anticyclones are not as vertically organized as they were during the previous summer (January 1991, WESTRAX 3, Figures 20A&Bc, 24, F-4 through F-6). For example, the large, well-developed *Hae* of the WESTRAX 3 surface layer does not extend below 150 m (see sections B, C, and D on Figure F-5). Flow patterns in the upper and lower intermediate layers are also quite different (Figure F-4). In the surface layer, a strong NBC flows northwestward along the continental break and into the GC.

In the intermediate layer, 23 Sv within the SEC cross the southeast corner. This flow completely retroreflects around *Hae* before reaching the *Lfg* - *Le* central trough. There is no northwestward flow along path A->D (although some

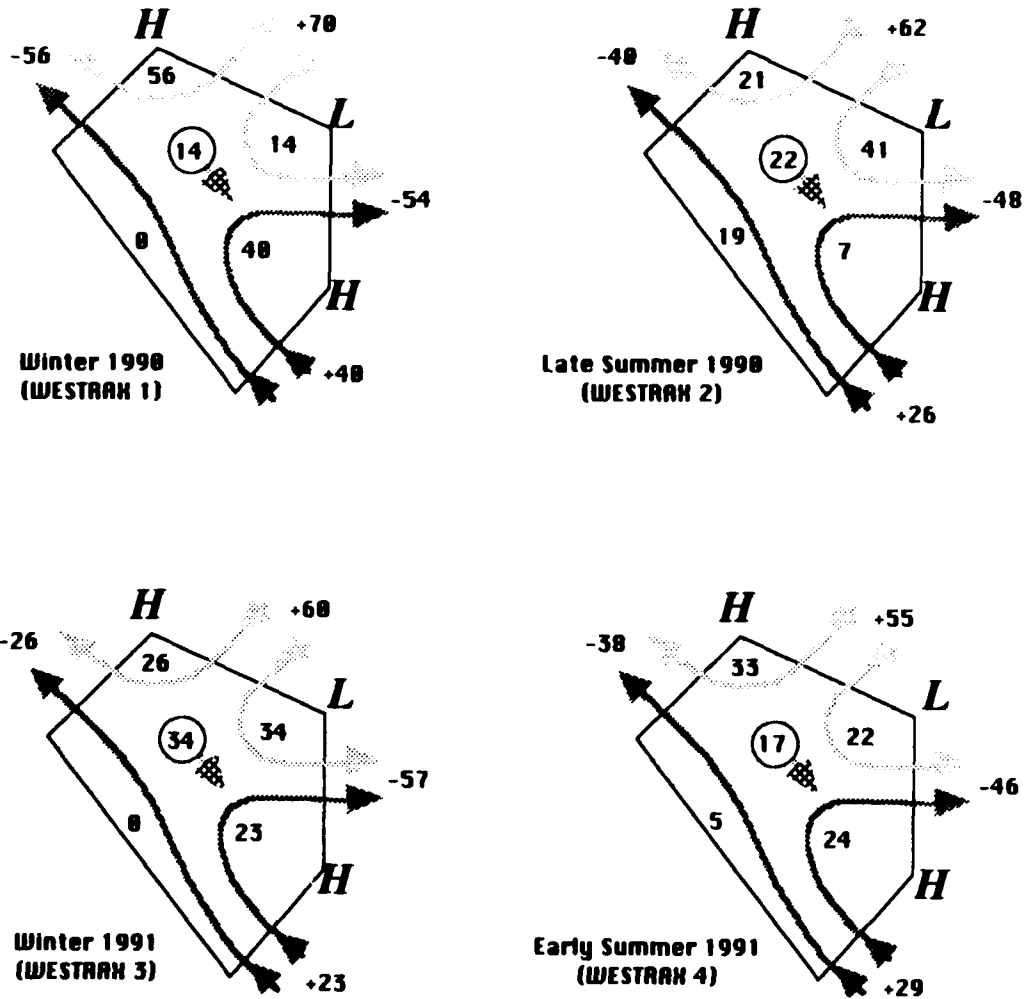


Figure 24. Intermediate layer volume transports during WESTRAX 1-4 (see Figure 23b). Positive transports in Sverdrups ($10^6 \text{ m}^3/\text{s}$) flow into the region. Internal transports are derived from flow across sections C, D, and E. Net southward flow around the tropical gyre and into the NEUC are circled.

northwestward streamlines are seen on analyses at individual depths). To the northwest of the central trough, 60 Sv enter the region across 9°N. 26 Sv of this northern flow turn anticyclonically around a northwestern ridge and exit through the western boundary. The other 34 Sv continue southeastward and flow around *Le* or *Lfg*, contributing to 60% of the 57 Sv NEUC. The cyclonic circulation around *Lfg*, which carries 1-2 Sv toward the NEUC, is an example of the southeastward coastal undercurrent which is discussed in Schott and Böning (1991). Net southward flow around the tropical gyre is 34 Sv.

The prominent ridge across the northwestern corner of the region may be a remnant of a translating retroflection eddy which was identified as *Hde* during the previous fall (see below).

While the flow patterns during the first winter (WESTRAX 1, Figures 20A&Ba, 24, F-7 through F-9) are similar to those of the WESTRAX 3 structure, the transports are quite different. A much larger 40 Sv enter through the southeast corner and retroflect completely around *Hae*. As during WESTRAX 3, no water flows northwestward along the coast. The *Lfg* - *Le* central trough once more divides the northern and southern flow regimes. In the north, 70 Sv enter across 9°N. 56 Sv of this flow turn anticyclonically and exit within a strong northwestward current through the western boundary. 14 Sv from the north continue southeastward and flow around *Le* or *Lfg*, contributing to 26% of the 54 Sv NEUC. Net southward flow around the tropical gyre is 14 Sv. A ridge in the northwest again hints at the presence of a translating retroflection eddy.

The early summer...

The velocity structure during the early summer (June 1991, WESTRAX 4, Figures 20A&Bd, 24, and F-10 through F-12) is a mixture of winter and summer features, indicating that this survey was made during a seasonal transition period. As observed during the winter surveys, surface and intermediate patterns

are distinctly different. Water mass analyses (described later) will help determine whether the north-central anticyclone is a separated retroflection eddy, or a cell of northern water which has been carried into the region by the NEC.

During June 1991, 29 Sv enter through the southeast corner. Of this, 24 Sv retroflect around *Hae* and 5 Sv continue toward the northwest. Of the 55 Sv which enter across 9 N, 33 Sv turn anticyclonically and exit across the western boundary as part of the 38 Sv outflow. The remaining 22 Sv turn southeastward and flow cyclonically around *Ie*, contributing to 48% of the 46 Sv NEUC. Net southward flow around the tropical gyre is 17 Sv.

Transports associated with the movement of retroflection eddies...

Johns *et al.* (1990) suggest 'retroflection eddies' are periodically released from the area of the Amazon Eddy retroflection and move northwestward through the WESTRAX region. During October 1990 (between WESTRAX 2 and 3), P. Richardson of WHOI launched a surface drifter in the northwest corner of the region (Richardson *et al.* 1993). The drifter was caught within a retroflection eddy as it passed over sections D and E and it looped anticyclonically northwestward toward the Caribbean (Figure 25). The center of the buoy's track followed a 305 degree trajectory as it translated at an average rate of 8.2 km/day (9.6 cm/s) as the buoy made a loop every 13.3 days. If the eddy was rotating as a solid body, the mean radial velocity at the estimated outer edge of the buoy's track (110 km) was 61 cm/s. This compared well with the buoy's mean radial speed between daily positions of 53 cm/s.

Evidence for the form and presence of these retroflection eddies within the region during the WESTRAX surveys includes:

- The Demerara Eddy which is centered in the region during September 1990 (WESTRAX 2). A well-developed retroflection eddy in the final stages of separation from the Amazon Eddy is indicated by: (a) the vertical

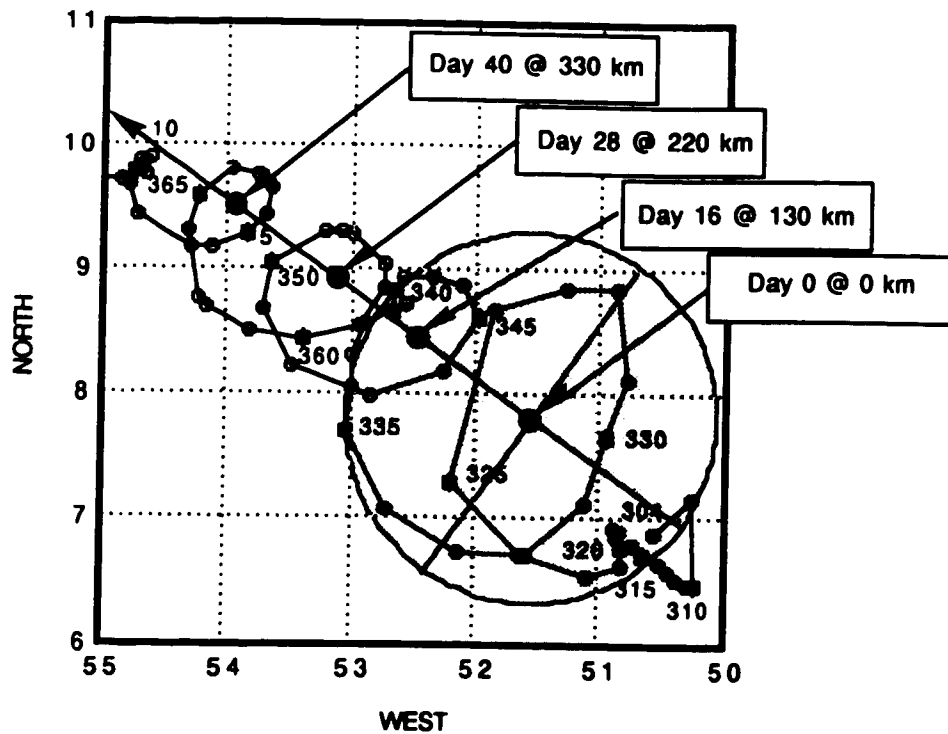


Figure 25. Track of surface drifting Buoy 02571. Daily positions (open dots) are plotted between launch on 31 October 1990 (Julian date 304) and 15 January 1991 (015). Every fifth date is marked (some are missing). The spiral track of the buoy indicates it is caught in an eddy. Four positions for the eddy's center are estimated (solid dots) and connected by a trajectory toward 305 degrees (arrow). Positions indicated by boxed day and distance after launch correspond to the day the buoy passes southward across the trajectory path. The eddy's estimated 300 km diameter is shaded.

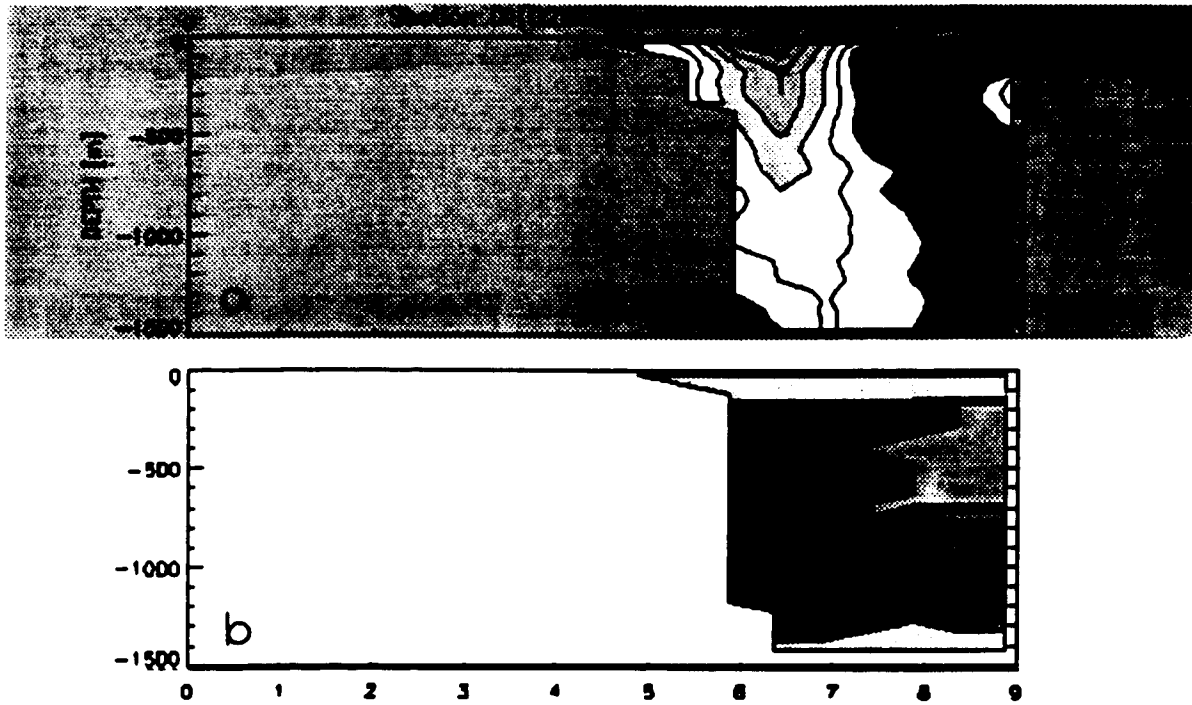


Figure 26. Vertical (a) Pegasus velocity and (b) water mass structures normal to section D during late summer (September 1990, WESTRAX 2) (see Figures I-2 and I-2 for legends).

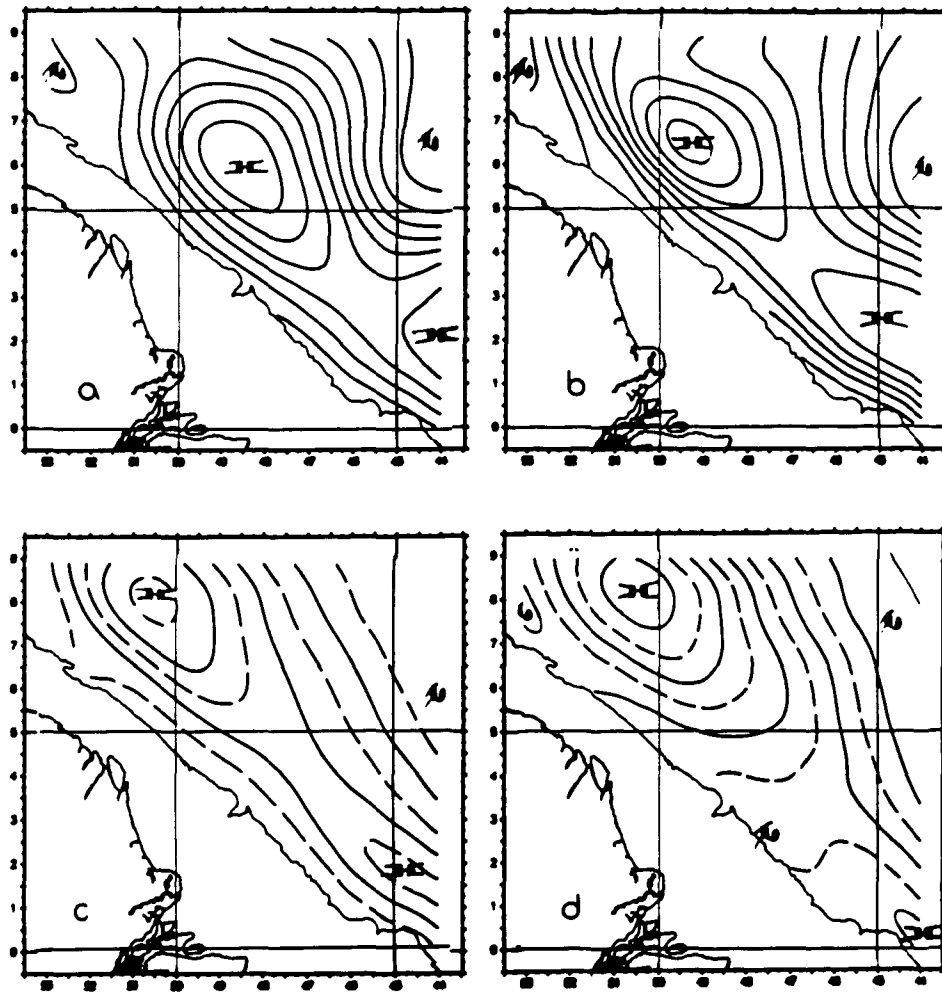


Figure 27. Depth-averaged Pegasus transport streamline structure during late summer (September 1990, WESTRAX 2):

- (a) Surface layer (0-150 m)
- (b) Upper intermediate layer (150-750 m)
- (c) Middle intermediate layer (Antarctic Intermediate Water, 650-850 m)
- (d) Lower intermediate layer (750-1300 m).

Each solid streamline represents a volume transport of approximately 5×10^6 m^3/s (5 Sverdrups).

extent of anticyclonic flow through the surface and intermediate layers across section D (Figures 26a and 27), and (b) the division between northern (NACW, on the right) and southern (MXU2) water masses which overlays this axis (compare Figures 26a and b). (see section VI).

- The anticyclonic circulations in the northwest corner of the region during both February 1990 (WESTRAX 1) and January 1991 (WESTRAX 3) (Figures F-4 through F-9) appear to be the rear quadrants of fully-developed retroflection eddies which are departing the region.
- The position of the WESTRAX 3 retroflection eddy is approximately consistent with a 10 cm/s (e.g., 820 km in 100 days) northwestward translation from the position of the WESTRAX 2 Demerara Eddy.
- Isolated parcels of southern water masses are trapped within the circulations noted above (Figures 43B and 43C). This is particularly well illustrated during WESTRAX 1, in which pockets of southern water masses (SACW, AAIW, AACP, and MXU1) are well separated from the Amazon Eddy retroflection area (see Section VI).

The WESTRAX 2 velocity and water mass structure analyses suggest that each retroflection eddy can be approximated as a 300 km diameter cylinder which extends from the surface to a depth of 1300 m. The streamline structure (Figure 21Ab), along with the velocity structure across section D, indicates that a transport of approximately 33 Sv recirculates within the eddy. An instantaneous northwestward eddy transport of 30 Sv (3 Sv and 27 Sv within the surface and intermediate layers respectively) is determined by assuming that a cylinder of volume $9.2 \times 10^{13} \text{ m}^3$ travels at 10 cm/s through the 300 km diameter of the eddy in 35 days ($3 \times 10^6 \text{ s}$). The total annual transport for the translation of three such retroflection eddies per year (Richardson *et al.* 1993) through the intermediate layer of the region is approximately 8 Sv.

This represents a maximum possible eddy transport. Richardson *et al.* (1993) suggest a 250 km diameter by 1000 km deep truncated conical eddy with a volume, and therefore transport, which is about one-third this size.

Translation of the suggested retroflection eddy can easily account for the transport of 19 Sv along path A->D observed during WESTRAX 2. With an area across the eddy's southwestern quadrant of $1.7 \times 10^8 \text{ m}^2$ (150 km wide by 1150 m deep) and total flow through the section of 52 Sv (19 Sv flow-through plus 33 Sv recirculation), an average current of 31 cm/s is necessary. This could be the combination of retroflection eddy translation (10 cm/s) and a modest average rotation speed within the eddy (21 cm/s). If this eddy is rotating as a solid body, the maximum speed along the continental shelf would be approximately 52 cm/s (10 cm/s translation plus 42 cm/s rotation).

I do not believe that the WESTRAX 2 retroflection eddy survey was biased because observations were not perfectly synoptic. It took 45 hours to survey section D as we crossed the eddy. If the eddy translated northwestward at a full speed of 10 cm/s, it would have moved 16 km during its survey. The resulting changes in flow structure by such a translation along a distance which is 5% of its diameter are insignificant compared to other uncertainties.

I have estimated that an annual transport of 8 Sv flow northwestward along the coast through the WESTRAX region (Figure 23a). I can easily account for this transport if three retroflection eddies which form and translate toward the Caribbean each year carry an annual transport of 8 Sv. Thus, there is no need for a continuous coastal current (comparable to the surface layer Guyana Current), and the wind-driven structure (Mayer and Weisberg 1993) adequately describes the flow patterns of the WESTRAX region. I believe that the various renditions of the Demerara Eddy in the region during both the WESTRAX and previous surveys are 'snapshots' of retroflection eddies as they separate and move northwestward (as previously suggested by Richardson *et al.* 1993).

V.

WATER MASSES

Historical water types and water masses of the tropical Atlantic are described. These are related to the temperature-salinity envelope of the WESTRAX data set. Density surfaces which bound the region's intermediate layer are defined. Using historical precedence and guided by velocity structure, the T-S envelope is divided into eight water masses which specifically define the structure of the region.

Definitions and background...

Water masses are described in terms of their measured temperatures and salinities. A 'Temperature-Salinity (T-S) diagram' presents relationships between salinity on a horizontal axis and corresponding temperature on a vertical axis. By using the T-S diagram of WESTRAX data, I will describe the water masses of this region.

A 'water mass' is defined by Mamayev (1975, referring to Sverdrup *et al.* 1942), as a portion of the ocean which contains water whose temperatures and salinities are bounded by a rectilinear or curvilinear relationship in T-S space. On a T-S diagram, a water mass may be represented by a point, a line, or an area. Tomczak and Large (1989) similarly define a water mass as a body of water in which each element has a common formation history. As a water mass moves away from the source region, its elements undergo similar mixing histories. Each of the physical and chemical properties of a water mass remains within definable ranges. A 'water type' is defined by a single T-S pair. A water type thus occupies a specific point on a T-S diagram (Mamayev 1975 and Sverdrup *et al.* 1942), and can

be viewed as a water mass which has a single temperature and salinity. Water masses and water types are defined and identified by source regions; maxima or minima in salinity, dissolved oxygen, nutrient content or other chemical tracers; and/or isopleths of depth, pressure, density, temperature, salinity, etc.

The pertinent T-S relationships between water types and water masses for the Atlantic Ocean, according to Sverdrup *et al.* (1942), Mamayev (1975), Emery and Dewar (1982), and Emery and Meincke (1986), are presented in Figure 28. Emery and Dewar (1982) have determined the climatological T-S relationships for subregions near the WESTRAX area (Figure 29). The WESTRAX region T-S relationships are bracketed, both geographically and in T-S space, by subregions associated with the South and North Equatorial Currents (e.g., '1' and '6' on Figure 29). The WESTRAX region T-S envelope, based on an inventory of the total WESTRAX CTD observation set, is compared with the South and North Equatorial Currents relationships of Emery and Dewar (1982) (Figure 30. Appendix H provides further discussion on the analyses of ocean water mass structure using T-S relationships.

Tropical Atlantic water masses...

The water mass structure of the Atlantic Ocean has been described by a number of investigators including Worthington (1976); Reid, Nowlin, and Patzert (1977); Wunsch and Grant (1982); Reid (1989); Peterson and Stramma (1991); and Schmitz and McCartney (1993). The tropical Atlantic Ocean can be divided into three layers: surface, intermediate, and deep. The tropical surface layer is separated from the intermediate layer by the top of the main pycnocline at depths between 100 and 200 m (Mamayev 1975). The intermediate layer is separated from the deep, or stratospheric, water of the tropical Atlantic by a relative salinity maximum near 1200-1500 m.

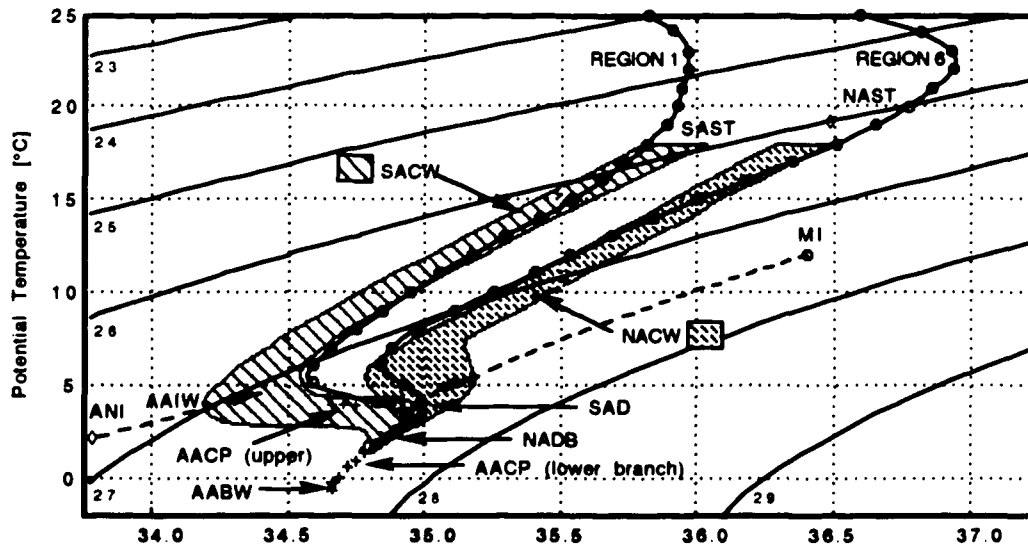


Figure 28. Historical temperature-salinity (T-S) relationships for waters of the equatorial Atlantic Ocean. Water masses and water types are:

South Atlantic Central Water in the left shaded envelope (SACW - SJF (references are cited below))

North Atlantic Central Water in the right shaded envelope (NACW - SJF)

xxx - North Atlantic Deep and Bottom Water (NADB - SJF)

+++ - Antarctic Circumpolar Water (AACP lower/upper branches - SJF/R)

o - Mediterranean Intermediate Water (MI - SJF)

* - Antarctic Bottom Water (AABW - SJF)

◊ - Antarctic Intermediate Water Type (ANI - SJF/M), South Atlantic Deep (SAD - M), South Atlantic Subtropical Tropospheric Water Type (SAST - M), and North Atlantic Subtropical Tropospheric Water Type (NAST - M).

Dashed lines from ANI to SACW envelope follows the core of the Antarctic Intermediate Water mass (AAIW - SJF). Solid lines with dots are mean T-S curves for E&D subregions 1 (southern equatorial) and 6 (northern equatorial) (see figure 29). Curved lines from lower left to upper right are sigma theta isopleths.

References: SJF - Sverdrup, Johnson & Fleming (1942); M - Mamayev (1975); E&D - Emery & Dewar (1982); and R - Reid (1989).

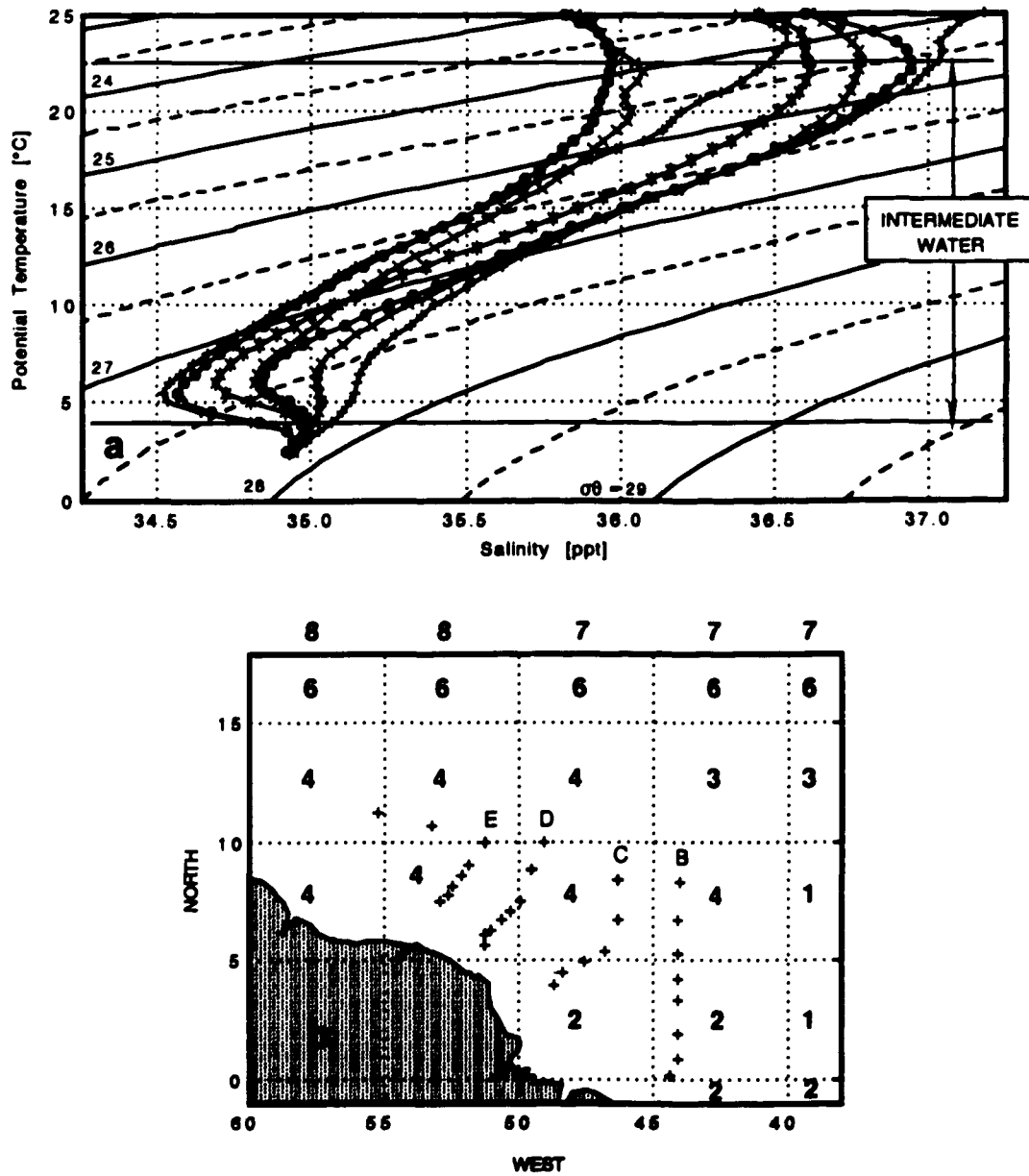


Figure 29. Climatological T-S relationships for the western tropical Atlantic Ocean (Emery & Dewar 1982). (a) T-S diagram for the tropical subregions which are located by bold numbers on (b). From left to right, the tropical subregions are labeled by: o = 1; + = 2; x = 3; * = 4; o = 6; + = 7, and x = 8. Intermediate water boundaries are marked at 22.5°C and 4°C. Curved lines are sigma theta isopleths. WESTRAX Pegasus velocity observation sites are marked on (b) with crosses and transects are lettered.

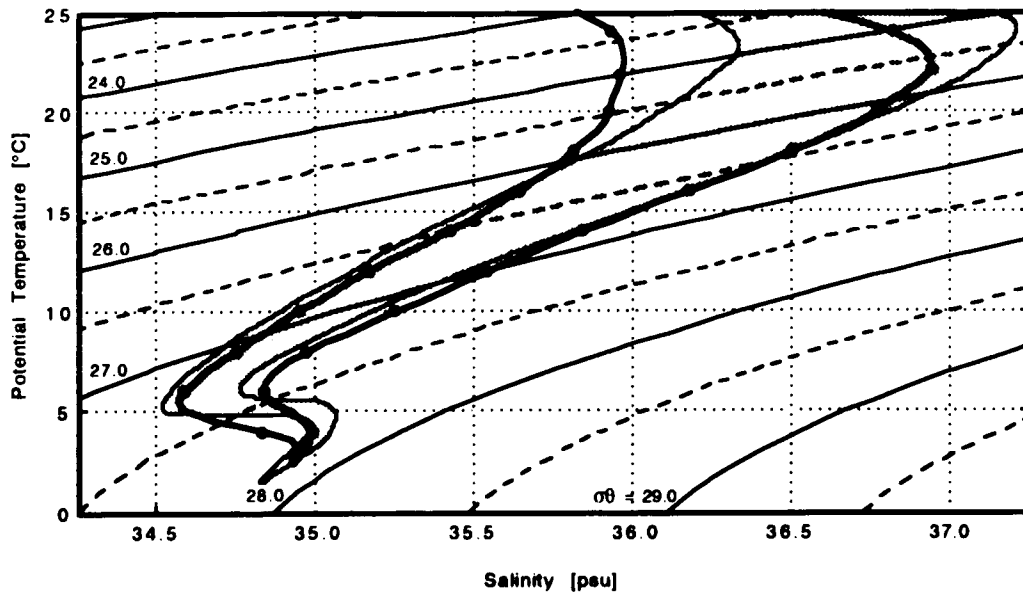


Figure 30. Envelope enclosing the observed temperature-salinity relationship for WESTRAX CTD profile data (shaded area). Lines marked by dots are Emery & Dewar (1982) climatological T-S curves for equatorial subregions 1 (south) and 6 (north) from Figure 29. Diagonal lines are sigma-theta isopleths.

The tropical surface layer is associated with a zone where salinity is maximum. In general, the surface water from the North Atlantic Ocean is saltier and warmer than the surface water of the same density from the South Atlantic (Figure 28). Mamayev (1975) associates North and South Atlantic Subtropical Tropospheric water types (NAST and SAST) with surface waters in the North and South Atlantic (Figure 28, Table 6).

Table 6. Tropical Atlantic Ocean water types.*

Symbol	Label	Characteristic		
		Temperature [θ , °C]	Salinity [S, psu]	Density [σ_t , kg/m ³]
<i>Surface Water Types...</i>				
SAST	South Atlantic Subtropical Tropospheric	18.0	35.90	25.96
NAST	North Atlantic Subtropical Tropospheric	20.0	36.50	25.91
<i>Intermediate Water Types...</i>				
ANI	Antarctic Intermediate	2.2	33.80	27.00
MI	Mediterranean Intermediate	11.9	36.50	27.77
<i>Deep Water Types...</i>				
NADW	North Atlantic Deep (**)	2.5	34.90	27.85
SAD	South Atlantic Deep	4.0	35.00	27.79
<i>WESTRAX-specific Water Types (defined in text)...</i>				
SASI	South Atlantic Surface Index	22.5	36.32	25.08
NASI	North Atlantic Surface Index	22.5	37.30	25.83
SAI	SASI / ANI Intercept	4.4	34.07	27.01
NAI	NASI / ANI Intercept	10.4	35.21	27.05
* Water types are defined by specific temperature-salinity pairs (Figure 28). ** Mamayev uses North Atlantic Deep & Bottom Water (NADB).				
Reference: Mamayev (1975)				

The water mass properties of the intermediate layer in the tropical Atlantic Ocean are strongly influenced by the presence of Antarctic Intermediate Water (AAIW) in the region (Reid 1989, crediting Wüst 1935) (Figure 28). AAIW, which has a nominal density of sigma theta 27.30 in the equatorial Atlantic (Reid 1989), is characterized by low salinity and high dissolved oxygen. AAIW originates as the Antarctic Intermediate water type (ANI, Mamayev 1975, Table 6) which forms within the Antarctic convergence zone of the Circumpolar Current.

A schematic of the intermediate level current pattern, based on the 800 dbar isosteric analysis of Reid (1989), shows how AAIW flows toward the WESTRAX region (Figure 31). He suggests that the AAIW flows along the east coast of South America to approximately 40°S where it turns eastward and enters a large anticyclonic gyre. The AAIW path turns northward near the southern tip of Africa and flows northwestward within a broad band which crosses the central South Atlantic. At the coast of Brazil, AAIW continues northward and then northwestward. AAIW flows across the equator and into the western tropical Atlantic Ocean as a western boundary current.

AAIW divides the intermediate waters of the western tropical Atlantic into upper and lower layers (Figure 28). The upper intermediate layer of the tropical Atlantic is a mixture of South Atlantic Central Water (SACW), North Atlantic Central Water (NACW), and AAIW (Sverdrup *et al.* 1942) (Figure 28). Reid's (1989) isosteric analysis at 500 dbar indicates the upper intermediate water in the South Atlantic (*e.g.*, SACW) flows toward the equator and into the WESTRAX region within the South Equatorial Current (SEC) along the same general route as the AAIW (Figure 31). The flow of North Atlantic intermediate water (*e.g.*, NACW) within the North Equatorial Current (NEC), depicted in Figure 31, is based on a subsurface westward drift along 15°N (Worthington 1976, Schmitz and McCartney 1993). The NEC appears to feed NACW from the northern tropical Atlantic into the WESTRAX region.

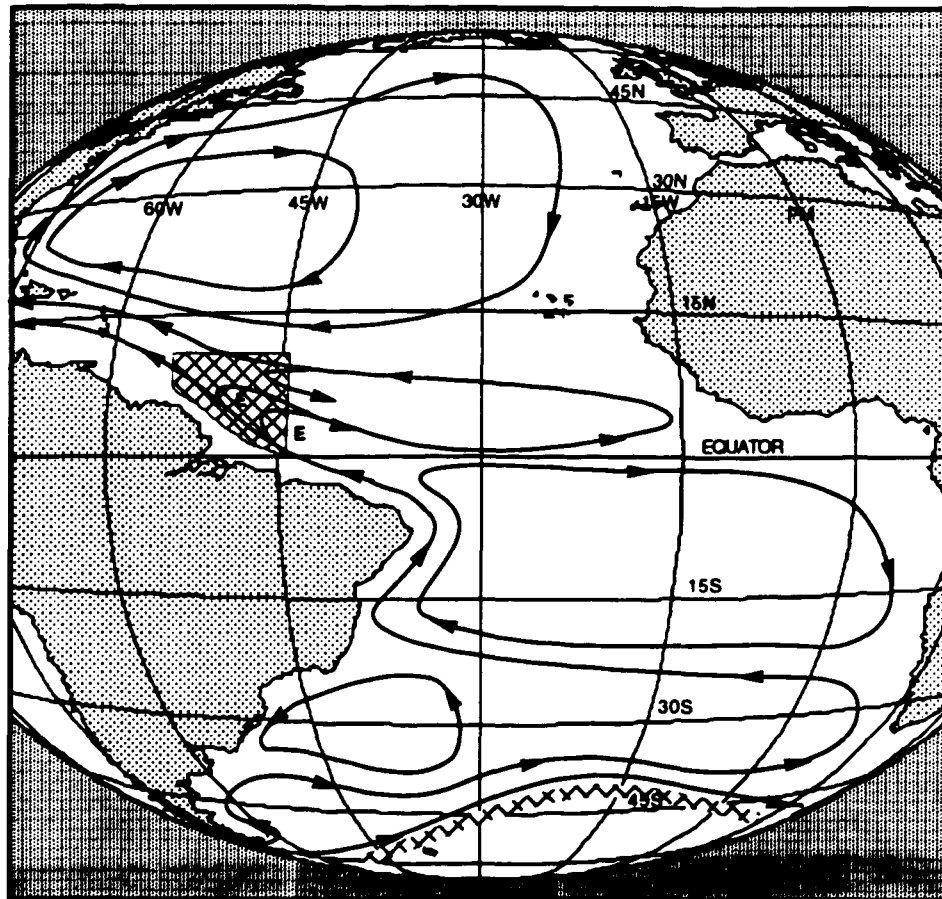


Figure 31. Schematic of the intermediate level current system structure in the Atlantic Ocean. The WESTRAX region is marked by the shaded box. The Antarctic convergence zone is cross-hatched. The circulation pattern for the South Atlantic is based on steric height analyses by Reid (1989) and the North Atlantic is based on Worthington (1976) and Schmitz & McCartney (1993).

Within the equatorial regions of the Atlantic, the current structure of upper intermediate water is quite complex. A simplified view on Figure 31 depicts two zones of westward flowing water (*e.g.*, the SEC and NEC) bracketing a broad eastward flowing North Equatorial Undercurrent (NEUC) (Molinari *et al.* 1981). This view of equatorial circulation is reinforced by the analysis of wind-driven transports in the Atlantic Ocean by Mayer and Weisberg (1993) (Figure 4).

The water masses which mix to form the lower intermediate layer of the WESTRAX region are AAIW, North Atlantic Deep Water (NADW) and an upper branch of Antarctic Circumpolar water (AACP) (Figure 28). Reid (1989) describes the upper AACP as an Antarctic transition water mass (*e.g.*, mixture) between AAIW and NADW, characterized by low dissolved oxygen and low nutrient levels. He uses the $\sigma_1 = 32.20$ isopycnal surface (equivalent to a sigma theta of approximately 26.60) to define the lower limit of this water mass. Reid's (1989) isosteric analyses at 1000 and 1500 dbar indicate that upper AACP enters the South Atlantic through the Drake Passage and flows northward, following the same general path but below the AAIW (Figure 31).

The deep waters of the WESTRAX region consist of mostly NADW (Figure 28). This water mass forms in the subpolar North Atlantic and spreads throughout the Atlantic basin. The salty Mediterranean Intermediate (MI) water contributes to the relative salinity maximum which marks the upper boundary of the NADW water mass. NADW enters the WESTRAX region as part of a southeastward flowing Deep Western Boundary Current (DWBC) and follows the continental slope along the Antilles Island chain and South American coastline (McCartney 1993). According to Mamayev (1975), the South Atlantic Deep (SAD) water type lies at the transition zone between intermediate and deep (NADW) water in the southern hemisphere. The water types which are pertinent to the definition of WESTRAX region water masses are summarized in Table 6.

In T-S space, a 'mixing line' between two water type 'sources' represents a continuous blend between the temperatures and salinities at its endpoints. Mixing lines connecting three water types enclose a 'mixing triangle.' With the water types at the vertices of a mixing triangle known, the mixing ratios between these water types at any point within the triangle can be determined. While there are normally more than three sources for the water masses of a region, it is possible to use regional observations to construct a group of appropriate mixing triangles which can be used to characterize a region's T-S relationships according to the ratios of contributions by each source (see Appendix II).

Such a generalized T-S diagram for the tropical Atlantic Ocean (Figure 32, from Mamayev 1975) shows that SACW is a water mass defined by a mixing triangle with vertices at the water types SAST, SAD, and ANI. SAD lies on a mixing line between SAST and NADB (NADW). The AAIW water mass (signified by the dotted line) is derived from ANI as it mixes with SAST and NADW (above and below respectively) while it moves toward the tropics. The NACW water mass is defined by a mixing line between NAST and AAIW. Thus, we see that NACW contains water of southern origin (e.g., ANI). Mediterranean Intermediate (MI) water does not affect the composition of NACW until density is greater than $\sigma_{\theta} 27.50$. A lower mixing triangle, which is bounded by ANI, SAD, and Antarctic Bottom Water (ANB), defines the lower intermediate water masses of the South Atlantic Ocean.

WESTRAX region water masses...

The T-S relationships described above (Figure 32) provide a basis for the analysis of intermediate water masses within the WESTRAX region. The water mass definitions presented herein are constrained by;

- Water masses which lie within, or affect intermediate depths
- Water masses of the western tropical Atlantic Ocean region, and
- Evidence based solely on WESTRAX T-S relationships.

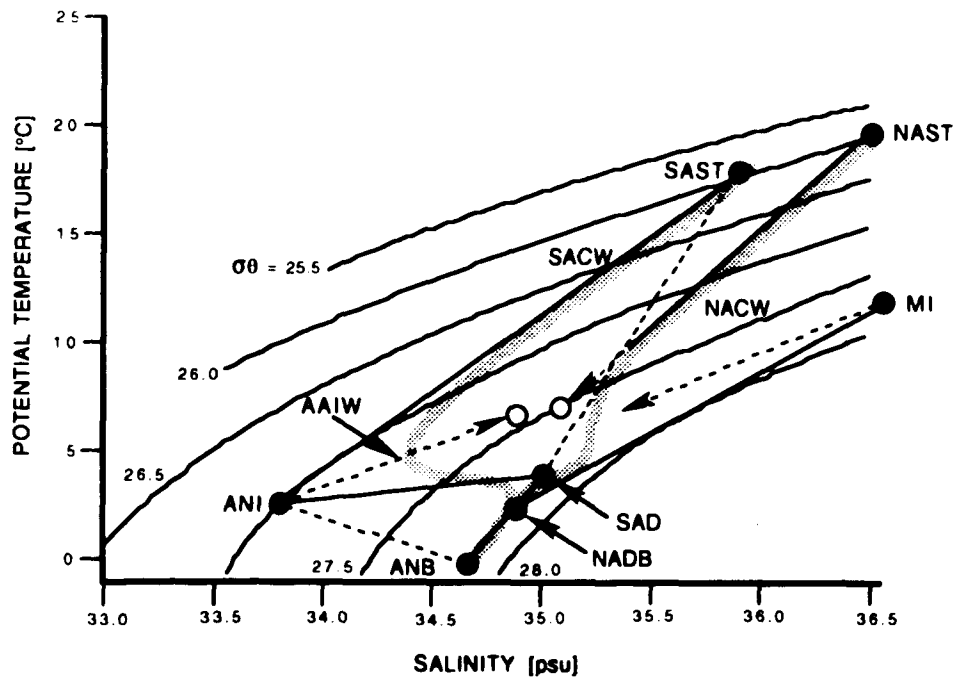


Figure 32. Generalized T-S diagram for the water masses of the tropical Atlantic Ocean according to Mamayev (1975). Shaded curves represent the water masses: South Atlantic Central Water (SACW) and North Atlantic Central Water (NACW). Solid dots are thermohaline indices for the primary water types: Antarctic Intermediate (ANI), Antarctic Bottom Water (ANB), North Atlantic Deep and Bottom Water (NADB), South Atlantic Deep (SAD), Mediterranean Intermediate (MI), South Atlantic Subtropical Tropospheric (SAST), and North Atlantic Subtropical Tropospheric (NAST). Open dots are at unspecified intermediate water types. Straight solid and dashed lines are lines of mixing which produces water types such as Antarctic Intermediate Water (AAIW). Curved lines are isopleths of sigma-theta.

The T-S envelope for the WESTRAX region (Figure 30) was produced from a composite of the CTD observations made at the 138 stations during the first four WESTRAX expeditions. Over 450,000 T-S observations at 1.0 m increments were located in T-S space bins with resolutions of $\Delta S = 0.025$ psu and $\Delta T = 0.25$ C (Figure 33). A smoothed envelope was drawn to enclose the WESTRAX T-S data (Figures 30 and 34).

The left-most boundary of the WESTRAX envelope is assumed to represent water which originates in the South Atlantic, and the right-most boundary represents water which originates in the North Atlantic. Density surfaces which intersect the envelope's salinity maxima near $22.5^{\circ}\text{C}/37.20$ psu and $4.0^{\circ}\text{C}/35.00$ psu (sigma theta 25.30 and 27.80 respectively) represent natural upper and lower boundaries for the WESTRAX intermediate layer.

The upper intermediate water masses in the region are described in terms of a mixing triangle defined by ANI and two water types which are specific to the WESTRAX T-S envelope: the South and North Atlantic Surface Indices (SASI and NASI respectively) (Figure 34, Table 6). These were defined by following the precedent set by SAST and NAST in Mamayev (1975). SASI is defined as the point where a mixing line from ANI which is tangent to the left (e.g., southern) side of the WESTRAX T-S envelope intersects the 22.5°C isotherm. NASI is similarly defined as the point where the mixing line from ANI which is tangent to the right (e.g., northern) side of the WESTRAX envelope intersects the 22.5°C isotherm.

The lower intermediate water masses are similarly described in terms of a mixing triangle defined by SAD and two secondary water types which I have defined as: the SASI-ANI Intercept (SAI) and the NASI-ANI Intercept (NAI) (Figure 34). SAI is at the intersection between the ANI-SASI mixing line and the mixing line from SAD which is tangent to the lower (e.g., southern) edge of the WESTRAX envelope. Similarly, NAI is at the intersection between the ANI-NASI

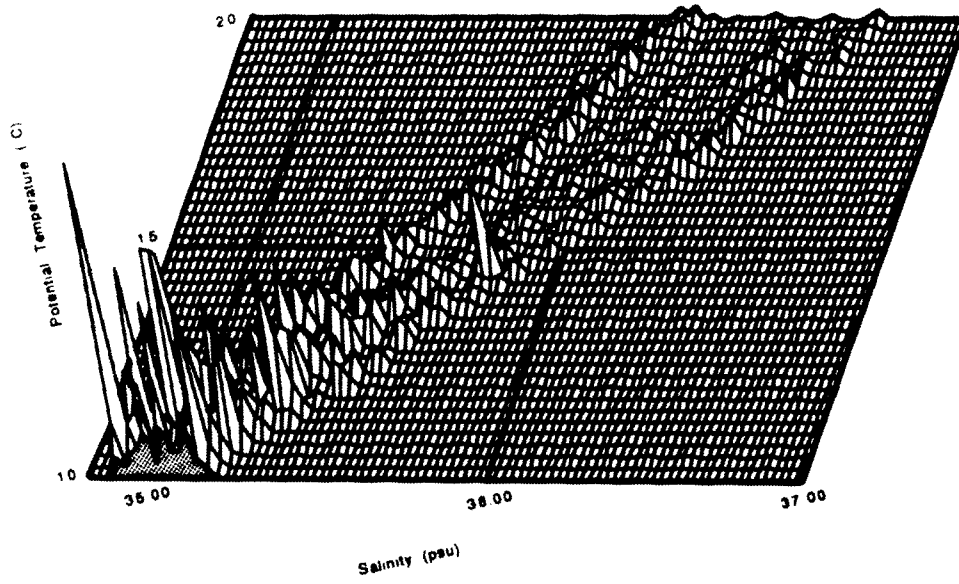


Figure 33B. A histogram of the WESTRAX temperature-salinity census of CTD data between 10 and 20°C. Plot heights represent the relative number of T-S pairs counted in each 0.25°C by 0.025 psu bin of potential temperature and salinity.

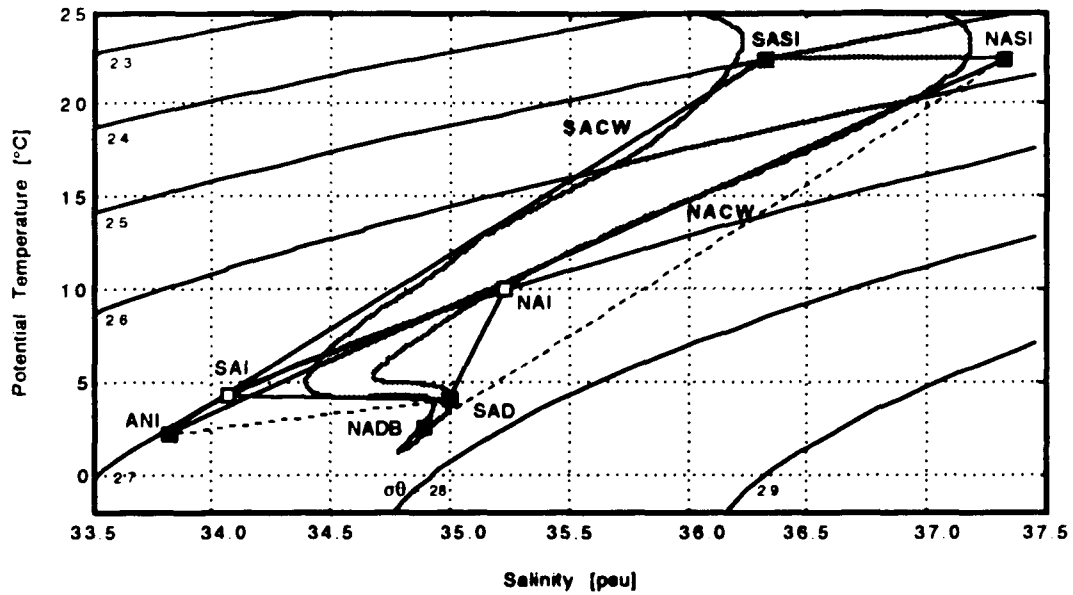


Figure 34. WESTRAX region T-S diagram showing water types and mixing lines. Shaded region is the envelope of WESTRAX T-S observations. The curve on the left (right) side of this envelope is defined as water of South (North) Atlantic origin. Dark squares mark the primary water types: Antarctic Intermediate Water (ANI), South Atlantic Deep Water (SAD), North Atlantic Deep and Bottom Water (NADB), South Atlantic Surface Index (SASI), and North Atlantic Surface Index (NASI), as discussed in the text. Open squares locate secondary water types: SAI and NAI. Solid and dashed straight lines represent linear mixing lines between water types. Thin curved lines are sigma theta isopleths.

mixing line and a mixing line from SAD which is tangent to the upper (e.g., northern) edge of the WESTRAX envelope.

In order to relate water masses and horizontal transport, WESTRAX water mass classifications are defined in terms of a few key isopycnal surfaces. The somewhat arbitrary selection of the density surfaces which bound intermediate layers is based in part on comparisons between corresponding vertical sections of water masses and Pegasus velocity. In particular, I have made an effort to match the transition zones between water masses with corresponding zones of vertical (or horizontal) velocity shear.

The sigma theta 26.00 surface near the base of the main pycnocline was selected to define the upper boundary of intermediate water within the WESTRAX region (Figure 34). Using trial and error, I found that this surface best coincided with changes between surface and intermediate layer Pegasus velocity structure (see Figure 35a for an example). Sigma theta 26.00 lies between depths of 100 and 200 m in the WESTRAX region. Flagg *et al.* (1986) used this same isopycnal to describe flow within the upper thermocline. I also note that the densities of Mamayev's (1975) SAST and NAST water types are very close to this value (Figure 34, Table 6).

The sigma theta 27.65 surface between depths of 1200 and 1400 m was selected to define the transition zone between the intermediate and deep layers of the WESTRAX region. This density surface marked significant changes in water masses and velocity over short vertical distances (for an example, see Figure 35b). In comparison with other works: Mamayev's (1975) SAD is at a slightly denser sigma theta 27.79, and Reid (1989) locates the top of the equatorial region NADW at the density surface $\sigma_1 = 32.20$ and $\theta = 4.50^\circ\text{C}$ (equivalent to sigma theta 27.60).

The water mass structure within the WESTRAX region was initially explored by dividing the envelope of intermediate water into nine water mass 'slices,' equally spaced between water mass slice [1] at the left or southern water

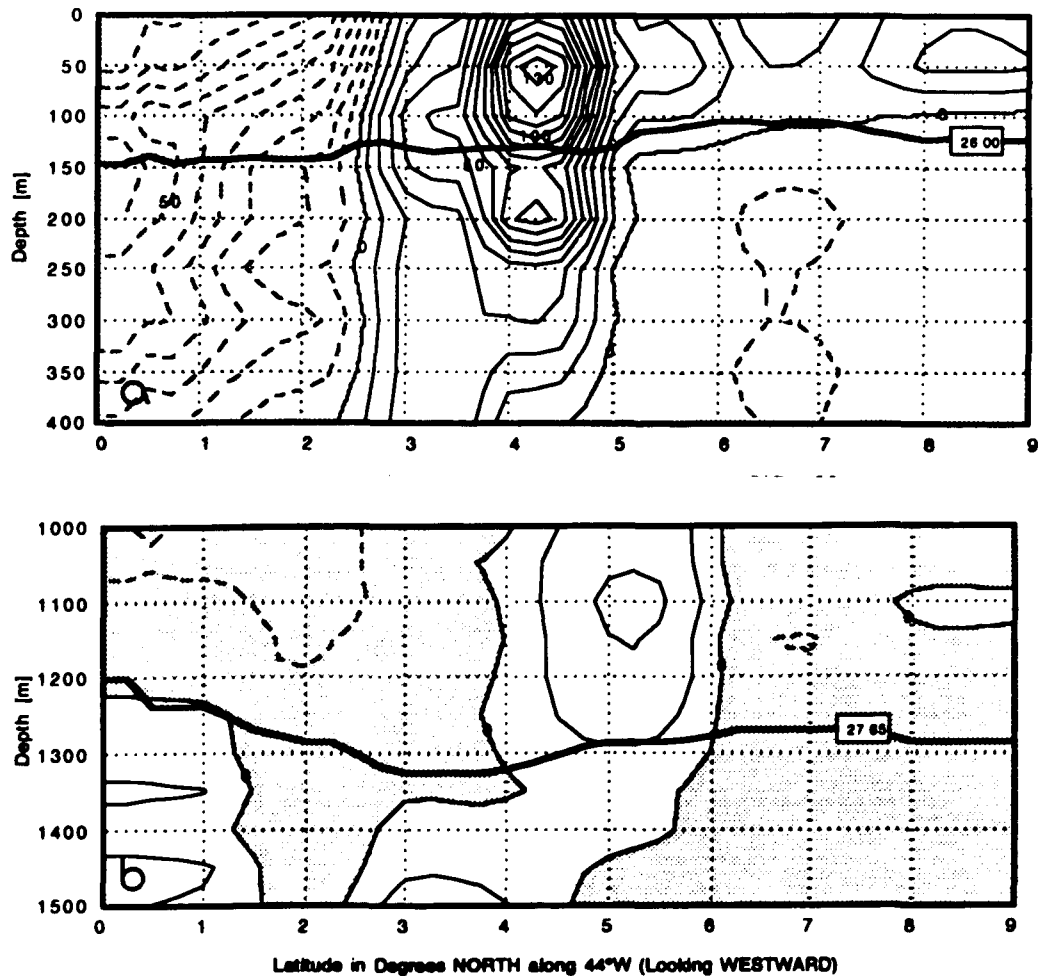


Figure 35. (a) Zonal velocity structure across the upper portion of section B during June 1991 (WESTRAX 4). Changes in velocity structure near the sigma theta 26.00 isopycnal (darkened line) suggest a choice for the intermediate layer upper limit. Isotachs at 10 cm/s are solid for eastward flow. (b) Zonal velocity structure across the lower portion of section B during February 1990 (WESTRAX 1). As above, changes in velocity structure near the sigma theta 27.65 isopycnal (darkened line) suggest a choice for the intermediate layer lower limit.

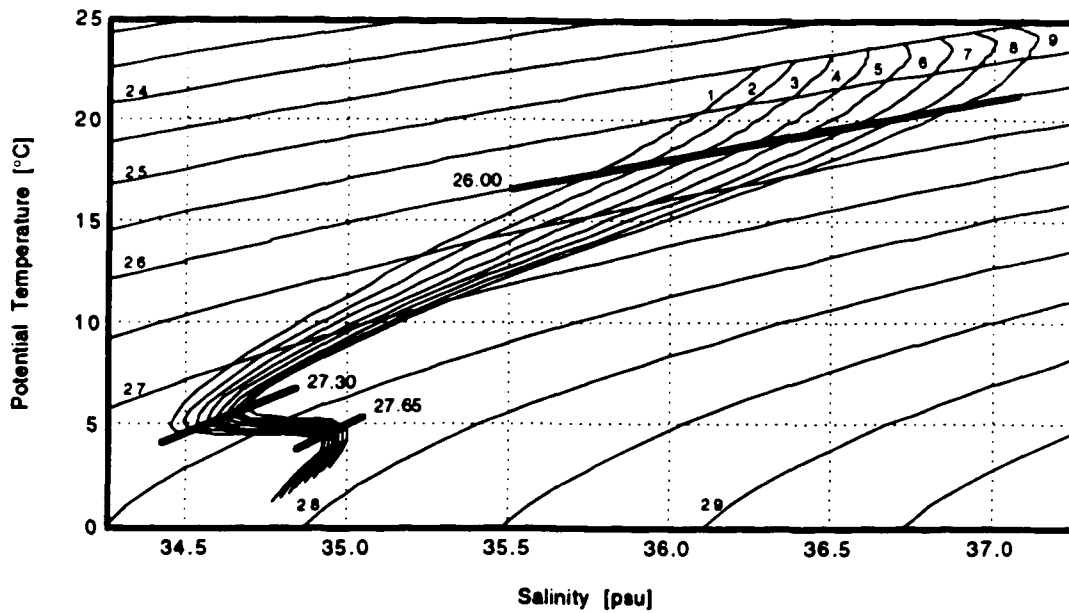


Figure 36. T-S envelope for the WESTRAX region. 'Slices' [1] to [9], represent water masses ranging between southern to northern origin respectively. Curved diagonals are isopleths of sigma theta. Isopycnal surfaces at sigma theta 26.00, 27.30 and 27.65 indicate upper and lower intermediate water limits.

boundary and slice [9] at the right or northern water boundary (Figure 36). In this way, water mass slices in the envelope's interior could be simply defined in terms of ratios between the southern/northern 'origins' at the extremes.

The distribution of these water mass slices across section B is illustrated by Figure 37. In Figure 37A, the upper and lower isopycnal boundaries for intermediate waters (sigma theta 26.00 and 27.65 respectively) are reasonably consistent with transition zones in the water mass distributions. When the water mass distribution is compared with the zonal velocity structure (Figure 37B), there is a general pattern of southern (e.g., [1] and [2]) and northern (e.g., [5] to [7]) water mass slices flowing westward into the southern and northern parts of the region respectively (shaded areas). These flank mixture water mass slices (e.g. [3] and [4]) which are flowing eastward out of the region (unshaded areas). Some of these mixture water masses are also evident in the westward flows.

My classification of the water masses of the WESTRAX region is intended to identify waters of southern and northern origin and to show how they are mixing. Further analysis suggested the nine water mass slices could be reduced to AAIW, four upper intermediate water masses, and three lower intermediate water masses without a significant loss of resolution.

The upper and lower intermediate waters of the WESTRAX region bracket the critical AAIW water mass. A salinity minimum marks a core of AAIW which flows westward along the continental slope at depths between approximately 700 and 800 m (Figure 38). Because of its distinctive character, AAIW is easy to define as a low salinity wedge crossing slices [1] through [4] between densities sigma theta 27.15 and 27.35 (Figures 39 and 40, Table 7).

The upper intermediate waters are described in terms of four water masses which are: the southern SACW, northern NACW, and two mixtures with progressively lower proportions of SACW. These mixtures are defined as Mix-Upper-One (MXU1) and Mix-Upper-Two (MXU2) respectively (Figures 39 and 40,

Table 7. WESTRAX region water mass classifications with approximate density, temperature and salinity limits and the ratios of source water types.

Water Mass Designations: Abbreviation: Slices	Upper/ Lower Limits of:			Proportions of Water Types**:			
	σ_θ	θ (°C)	S (psu)	SASI	NASI	ANI	SAD
<i>Upper Intermediate Waters</i>							
SACW [1-2]							
Upper σ_θ Surface	>26.00	17.65	35.84	63	13	24	0
Lower σ_θ Surface	<27.20	5.55	34.49	6	8	66	20
MXU1 [3]							
Upper σ_θ Surface	>26.00	18.13	36.01	55	33	21	0
Lower σ_θ Surface	<27.25	5.31	34.52	6	7	60	27
MXU2 [4]							
Upper σ_θ Surface	>26.00	18.61	36.17	47	34	19	0
Lower σ_θ Surface	<27.30	5.12	34.55	6	6	55	33
NACW [5-9]							
Upper σ_θ Surface	>26.00	21.00	36.98	7	86	7	0
Lower σ_θ Surface	<27.30	5.32	34.58	5	7	54	33
<i>Antarctic Intermediate Water</i>							
AAIW [1-4]							
Upper σ_θ Surface	>27.15	5.83	34.46	7	10	71	12
Lower σ_θ Surface	<27.35	4.50	34.52	6	2	50	42
<i>Lower Intermediate Waters</i>							
AACP [1-2]							
Upper σ_θ Surface	>27.35	4.50	34.52	6	2	50	42
Lower σ_θ Surface	<27.65	4.33	34.87	1	2	16	81
MIXL [3]							
Upper σ_θ Surface	>27.35	5.82	34.57	5	4	50	41
Lower σ_θ Surface	<27.65	4.51	34.90	1	3	16	80
NACL [4-9]							
Upper σ_θ Surface	>27.30	5.32	34.58	6	7	54	33
Lower σ_θ Surface <27.65	4.60	34.91	1	3	16	80	1
<i>North Atlantic Deep Waters</i>							
NADW [1-9]							
Denser than:	>27.65	<4.33	<34.87	1	2	16	81

* Density, temperature and salinity values at the corners of the WESTRAX T-S diagram envelope for each water mass. Corners where density is minimum (e.g., upper right for SACW) and a maximum (lower left) (Figure 39).

** Determined using WESTRAX T-S envelope mixing triangles (Figure 34).

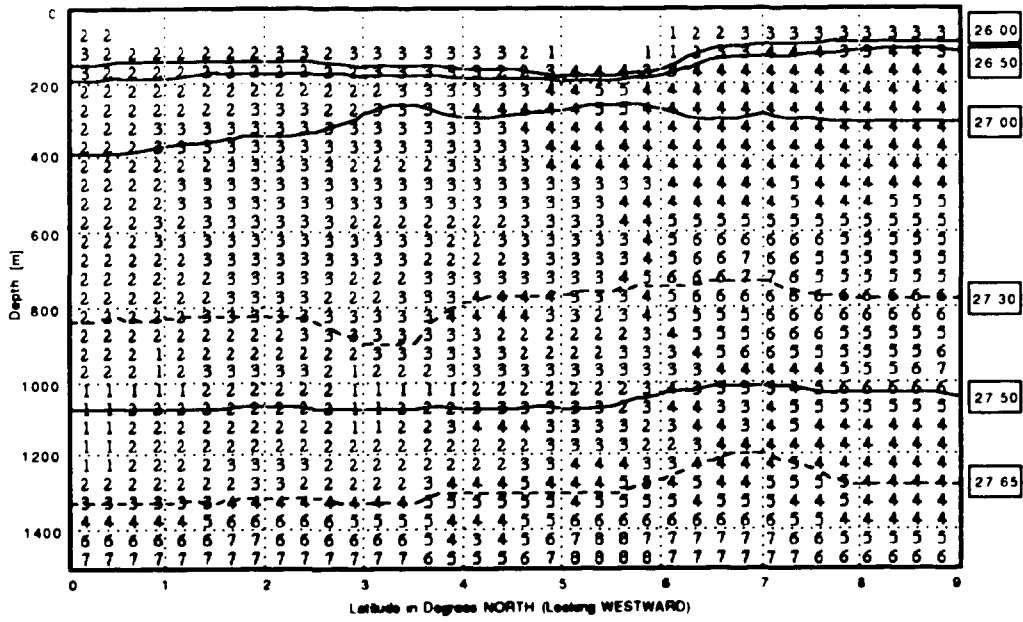


Figure 37A. Comparison between water masses and density structure across section B during January 1991 (WESTRAX 3). Water mass 'slice' designations from Figure 36 are repeated. Selected isopleths of sigma theta are marked to the right of the plot. Sigma theta 26.00 defines the upper limit; sigma theta 27.30 divides upper and lower; and sigma theta 27.65 defines the lower limit of intermediate waters.

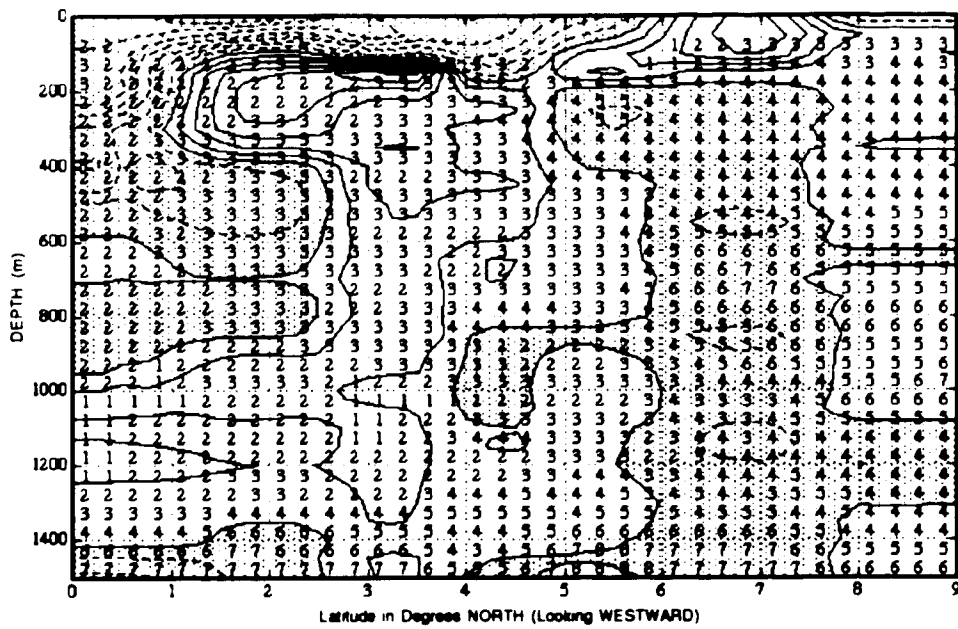


Figure 37B. Comparison between water masses and zonal velocity structure on section B during January 1991 (WESTRAX 3). Water mass 'slice' designations from Figure 36 are repeated. Isotachs at 10 cm/sec are solid for eastward and dashed (shaded regions) for westward velocities.

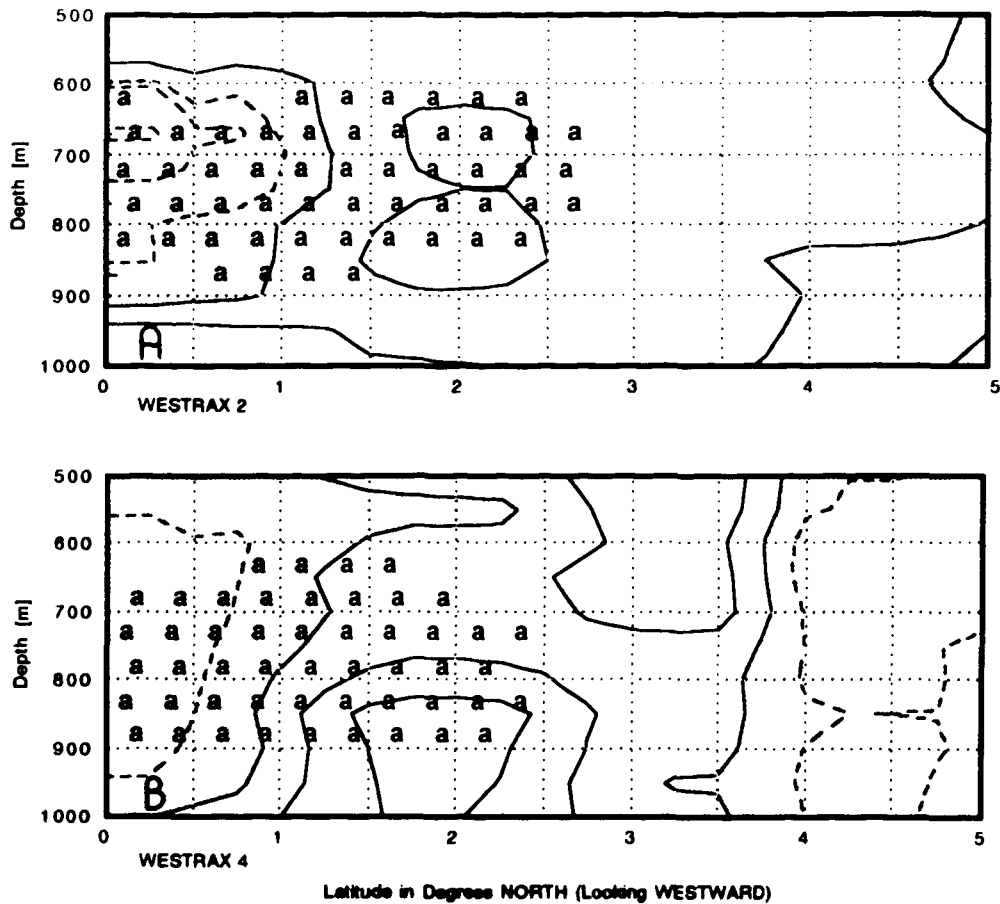


Figure 38. Comparisons between Antarctic Intermediate Water mass and zonal velocity structure across a portion of section B. September 1990 (WESTRAX 2) and June 1991 (WESTRAX 4) are shown in the upper and lower panels respectively. Isotachs at 10 cm/s are solid for eastward and dashed for westward (shaded areas) velocities. The 50 m by 1/4 degree sectors which have been defined as AAIW are marked by 'a.'

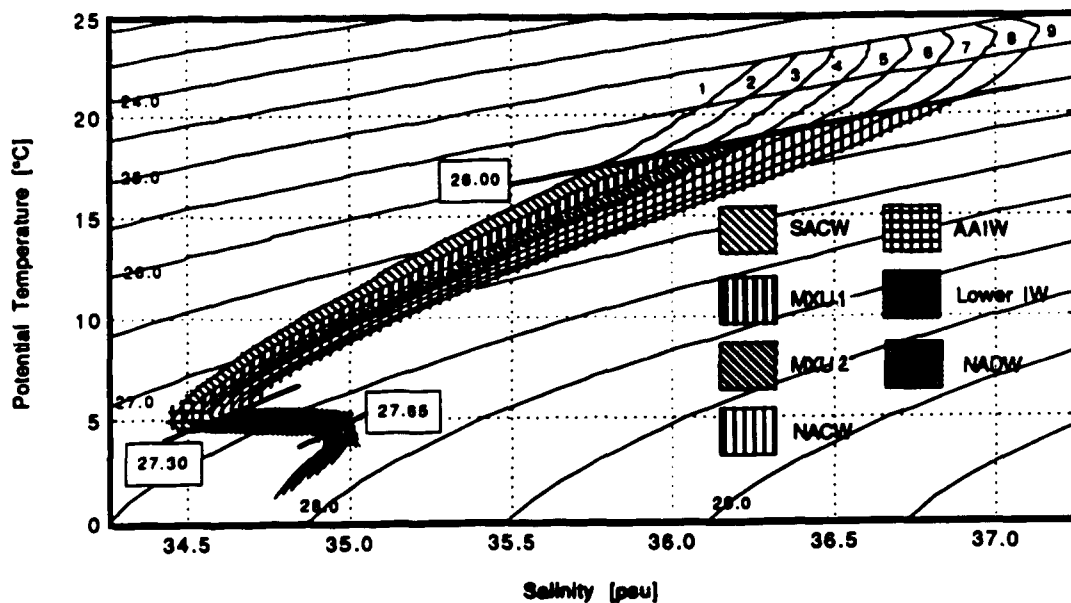


Figure 39A. Intermediate water mass classifications for the WESTRAX temperature-salinity relationships over the range 0°C to 25°C. Water masses are:
 SACW - South Atlantic Central Water
 NACW - North Atlantic Central Water
 MXU1 - Upper Intermediate Mixture with greater portion of SACW
 MXU2 - Upper Intermediate Mixture with lesser portion of SACW
 AAIW - Antarctic Intermediate Water
 Lower IW - Lower Intermediate Water
 AACP - Upper branch of Antarctic Circumpolar Water
 NACL - Lower North Atlantic Central
 MIXL - Mixed Lower Intermediate Water
 NADW - North Atlantic Deep Water.

Boundaries between the water mass slices [1] (most southern water) to [9] (most northern water) are indicated. Curved diagonals are isopleths of sigma theta, with 26.00, 27.30 and 27.65 marking the upper, middle and lower limits of intermediate waters.

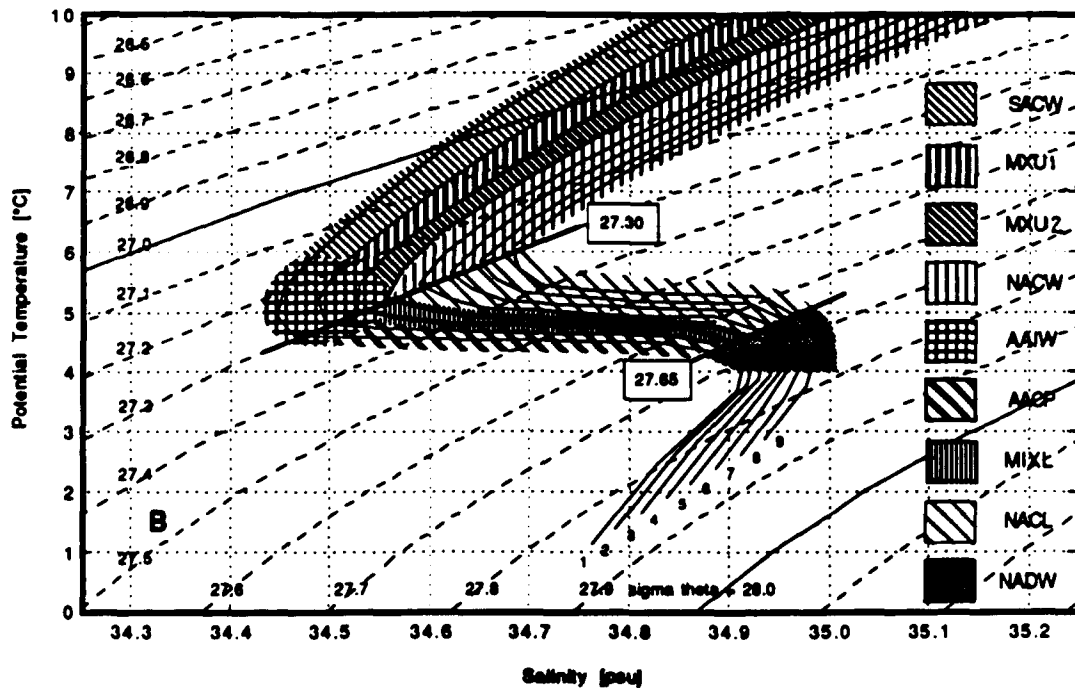


Figure 39B. Same as Figure 33A for the range 0°C to 10°C.

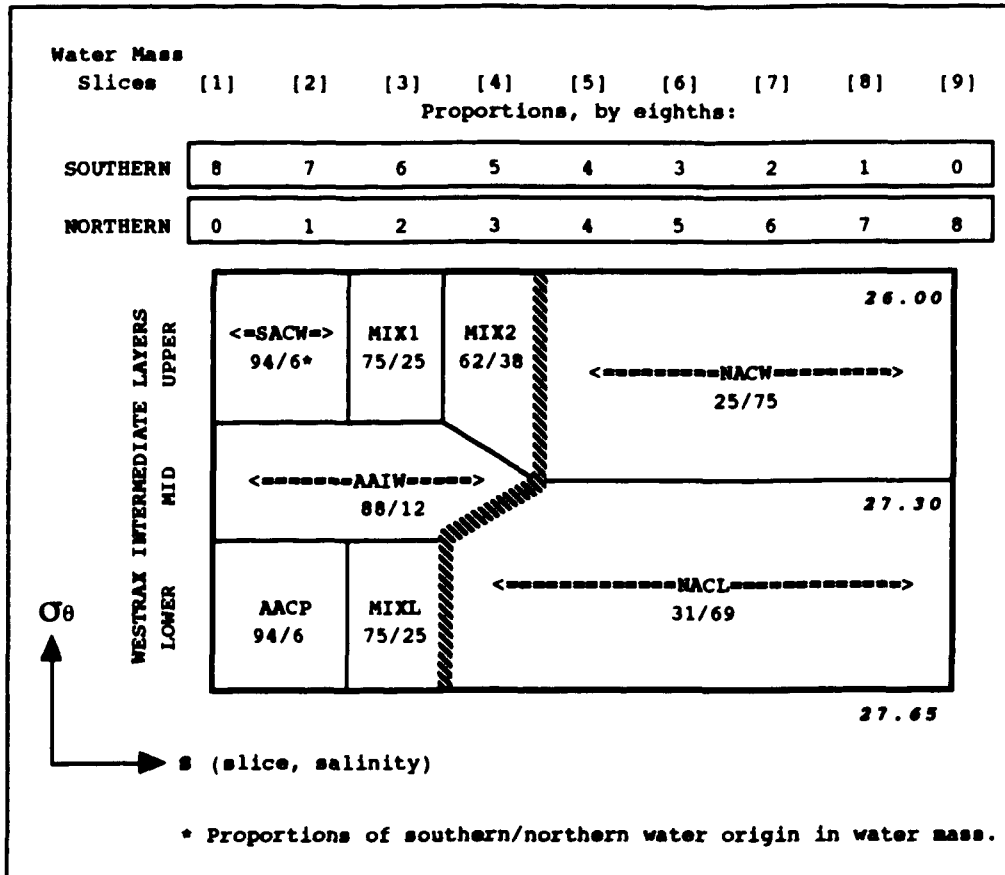


Figure 40. WESTRAX region intermediate water mass classifications and relative proportions by southern origin (left) to northern origin (right). Density is vertical axis and water mass slice (salinity) is horizontal axis. See Figure 39 for water mass abbreviations. Estimated percentage of southern/northern water mass origin are given. Heavy line is an arbitrary southern to northern water mass boundary.

Table 7). Much of the water which flows eastward across section B toward the NEUC after: (a) retroreflecting around the Amazon Eddy, or (b) flowing cyclonically around the eastern low, appears to be the water mass slices [3] and [4] (Figure 37B). By assuming that this return flow is a product of mixing, the definitions of water mass slice [3] as MXU1 and slice [4] as MXU2 are most appropriate. The upper intermediate water mass classification is thus slightly asymmetric, with a larger proportion of the T-S area classified as northern (five slices between [5] and [9]) compared to the four southern water mass slices between [1] and [4].

When the relative percentages of water with 'purely' southern [1] or northern [9] origin are assigned to each of the defined water masses, the southern water contents of SACW and NACW are found to be approximately 96% and 25% respectively (Figure 40). This demonstrates the strong influence that the southern hemisphere ANI has on all of the WESTRAX region water masses.

The lower intermediate waters are described in terms of three water masses which are: the upper branch of Antarctic Circumpolar water (AACP), Lower North Atlantic Central water (NACL), and a Lower Intermediate Mixture (MIXL) (Figures 39 and 40, Table 7). In the lower intermediate layer, the relationships between water mass slices and velocity structures are not as easy to discern as they are within the upper intermediate layer. There is no satisfactory way to separate and define mixtures as predominantly southern or northern for a variety of reasons including: (a) smaller horizontal temperature and salinity differences, (b) extensive thin-layer interleaving, and (c) the possible occurrence of more diffusive mixing in slower moving waters. AACP is defined to be a southern water which enters the region in the southeast, retroreflects, and mingles with NACL to create an eastward flowing mixture flowing toward the lower NEUC. As above, MIXL is assumed to be a southern water mass. Water mass slices [1] and [2] best represent the inflowing AACP in the sub-AAIW zone (Figure 39B). Similarly, NACL enters across 9°N and the northern portion of section B and

flows generally westward. While there is no classification for NACL, which is entirely satisfactory, water mass slices [4] through [9] appears to best describe these northern waters (Figure 37B). Even though MIXL is only designated by water mass slice [3], it still occupies a large portion of the lower intermediate waters. The asymmetry between northern and southern waters in T-S space is thus even more pronounced within the lower intermediate layer (Figure 40).

The structures of WESTRAX region water masses on horizontal density surfaces and vertical transects are presented in Appendix I.

VI.

WATER MASS TRANSPORT STRUCTURE

A cycle of summer and winter flow is suggested and a transport uncertainty is determined. Water mass analyses are combined with velocity structure to show water mass transport pathways through the region. Southern and northern water mass budgets lead to estimates of mixing transports.

The origins of WESTRAX water masses and an uncertainty estimate...

Over 60% of the water within the region can be traced to a southern hemisphere origin. According to Figure 40, the ratio between the hemispheric origin of each water mass within the WESTRAX region depends on its relative position between the most southern and most northern water mass slices (e.g., [1] and [9] respectively on Figure 39). The total relative volumes of water with northern and southern origins which are within, flowing into, and flowing out of the WESTRAX region are determined by applying these ratios to the volumes and transports of each water mass. These ratios are normalized and plotted as time series (Figure 41). Over the period shown, the average inflows and outflows of 57% and 67% respectively are traced to a southern origin. The average volume within the region with a southern origin is 62%. Since there can be no water of southern origin produced within the region, the difference between these ratios suggests a transport uncertainty of $\pm 10\%$ (as plotted to the right of each graph in Figure 41). Any cycles which are evident in the ratios between southern and northern water origin on Figure 41A or 41B lie within this range. This suggests that a 62:38% ratio between the southern:northern origins of water within the WESTRAX region is steady with time within an uncertainty of $\pm 10\%$.

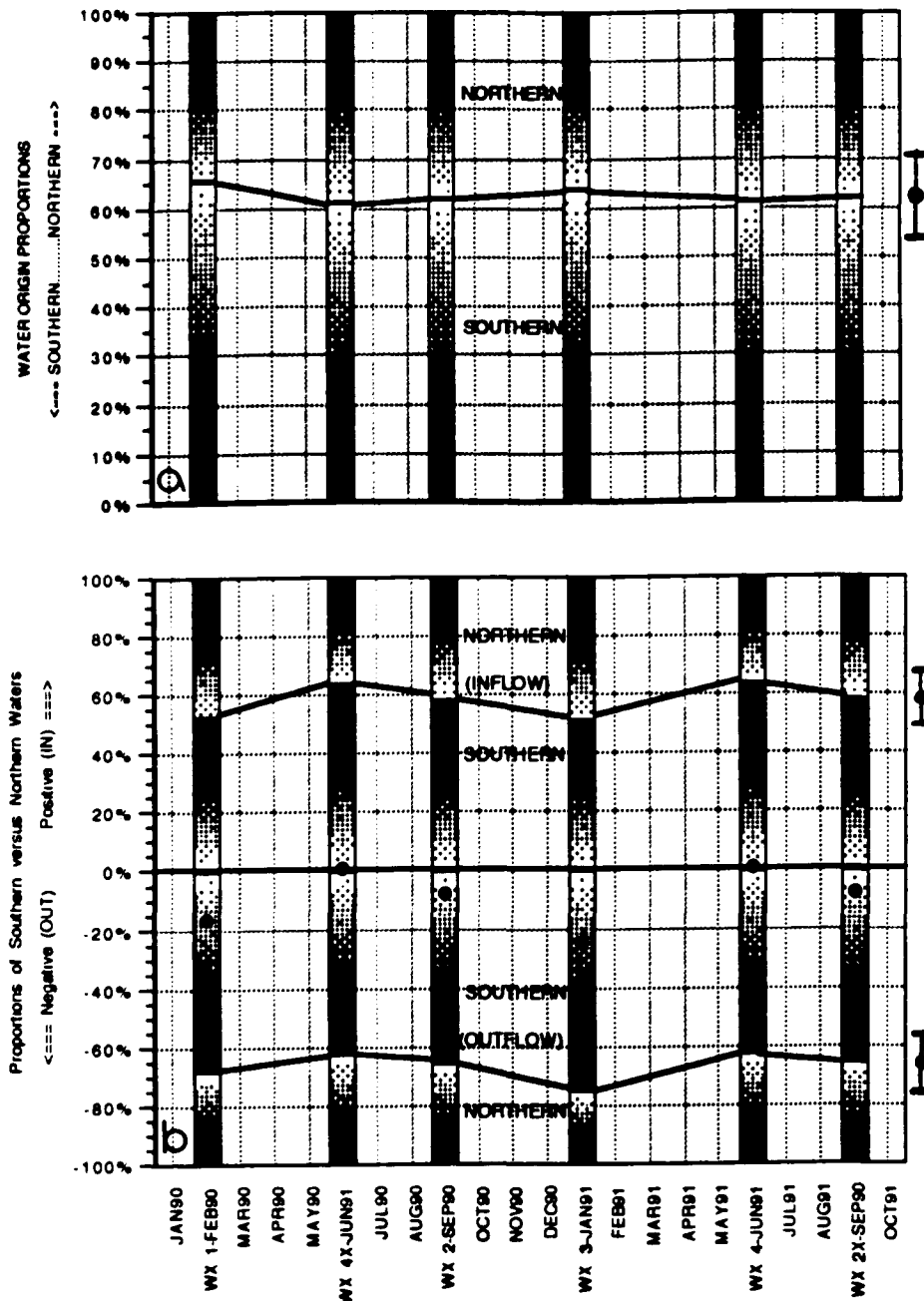


Figure 41. Eighteen month time series of the interplay between WESTRAX intermediate layer water of 'purely' northern or southern origin.

(A) Within the region

(B) Flowing into (positive) and out of (negative) the region

After the volumes of each WESTRAX water mass were determined (Figure 42), the ratio between southern and northern water for each water mass was determined according to Table 7. By assuming no interannual variability, the February 1990 and June 1991 results were used during both years to construct an 'annual' cycle.

Water mass transport cycles and a transport error estimate...

Over 70% of the water masses found within the WESTRAX region are defined as southern, according to the water mass classifications described in the previous section. The normalized transports of WESTRAX water masses are plotted to compare: (a) proportional volumes within, (b) flow into, and (c) flow out of the WESTRAX region (Figures 42A, B, and C respectively). Averages of 72%, 60%, and 79% of the water within, flowing into, and flowing out of the region respectively are included in the bottom six southern water masses and mixtures. While some of the difference between inflow and outflow can be attributed to the uncertainty estimate discussed above, some of it can also be attributed to the production of southern water mass mixtures by mixing, which will be described below.

While more realizations are required to be certain, Figures 42B and 42C lead me to speculate about an annual cycle of southern water mass transport through the region's boundaries. During winter, approximately 45% of the water masses flowing into, and 85% flowing out of the region are defined as southern. This indicates (a) the production of southern water mass mixtures within the region, and (b) the winter release of southern water from the tropical Atlantic via the WESTRAX region, as suggested by Mayer and Weisberg (1993).

During summer, southern water masses compose approximately 65% of the inflow and 75% of the outflow. From this change in ratios, I surmise there may be a continued production of southern water, but at a lower rate. These ratios indicate that there is not much southern water mass storage within the WESTRAX region during the summer. Mayer and Weisberg (1993) suggest such storage may occur further to the east within the interior Atlantic.

Water mass transport pathways...

The non-divergent Pegasus velocity structures (section IV and Appendix F) are combined with the water mass structures derived from CTD data (section V and

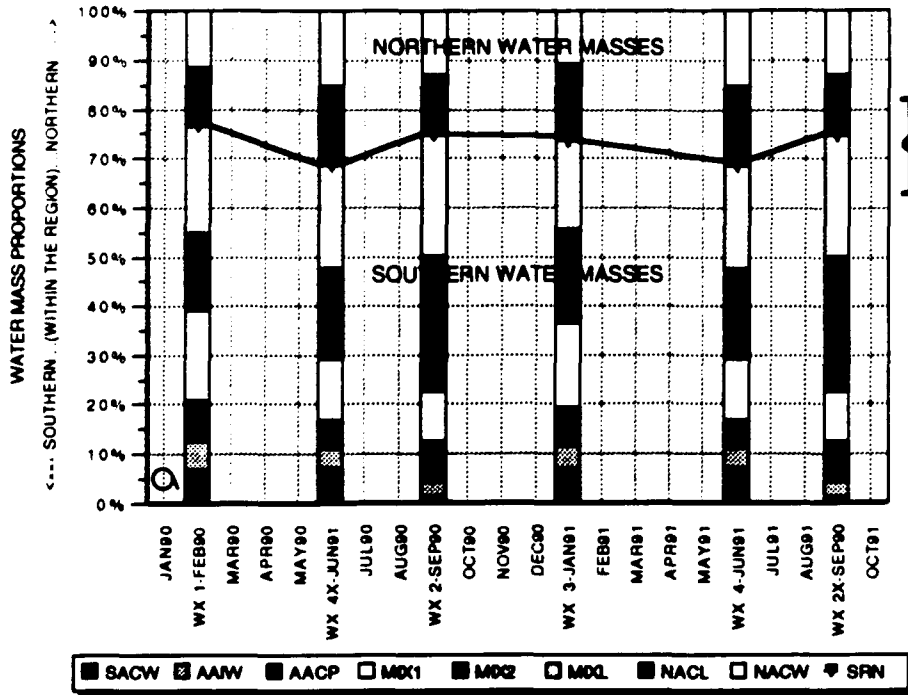


Figure 42. Eighteen month time series of the relative proportions between each WESTRAX intermediate layer water mass.

- (A) Within the region
- (B) Flowing into the region
- (C) Flowing out of the region.

The six southern water masses are stacked on the bottom and the two northern water masses are at the top. By assuming no interannual variability, the February 1990 and June 1991 results were used during both years to construct an 'annual' cycle.

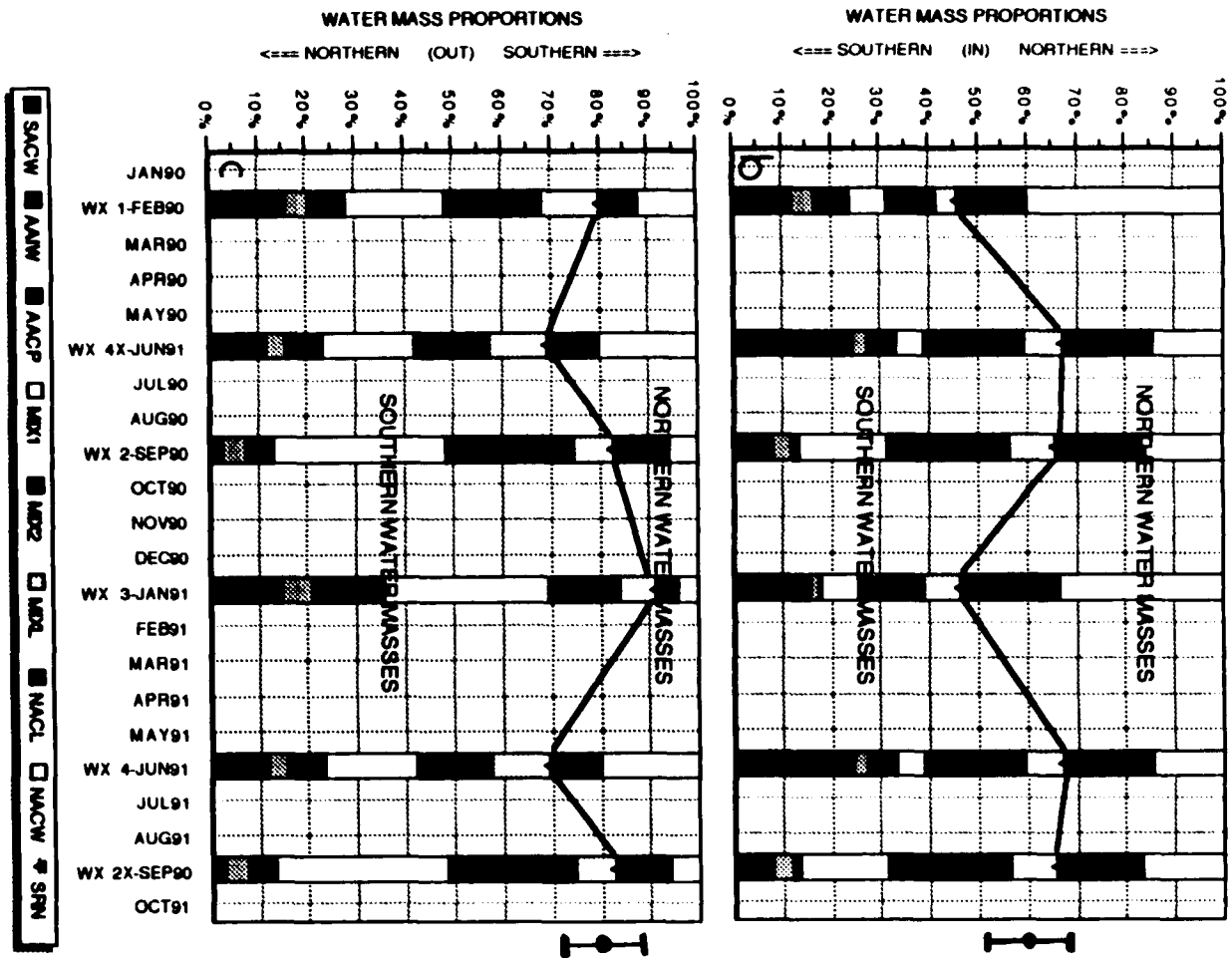


Figure 42B/C.

Appendix I) to produce a series of water mass pathway schematics (Figures 43A through 43D). These pathways highlight the major circulation features and most probable routes of the WESTRAX water masses through the upper, middle, and lower intermediate layers of the region. These pathways are constructed to be consistent with the measurements of flow across the boundaries and through internal sections C, D, and E. The intent of these schematics is to illustrate the geographic extent of each water mass, and the pathway widths are not necessarily relative to volume transports at all points. In some cases, pathways have been displaced for clarity so that all water masses which follow similar routes can be shown.

I am least confident about the accuracy of water mass pathways: (a) across the northern boundary, where there are only three or four observation points, and (b) within the large expanses between WESTRAX transects, where there are no observations. That is, I can say that SACW does not reach northwestward to section C during late summer 1990 (Figure 43A), but I can't be too specific about how close it gets to section C before retroreflecting.

In section IV, I suggested that the Demerara Eddies were instantaneous renditions of northwestward translating retroreflection eddies. In the following paragraphs, I will refer to the anticyclones which are located within the WESTRAX region to the northwest of the Amazon Eddies as Demerara Eddies, rather than try to determine whether these cells are separated from the retroreflection and translating northwestward.

During the late summer (September 1990, WESTRAX 2), the prominent feature of the region is the semi-permanent Demerara Eddy (Figure 43A). SACW retroreflects around the Amazon Eddy and flows eastward into the NEUC. While some MXU1 retroreflects, a large portion continues northwestward and either departs the WESTRAX region or retroreflects around the Demerara Eddy. NACW enters the

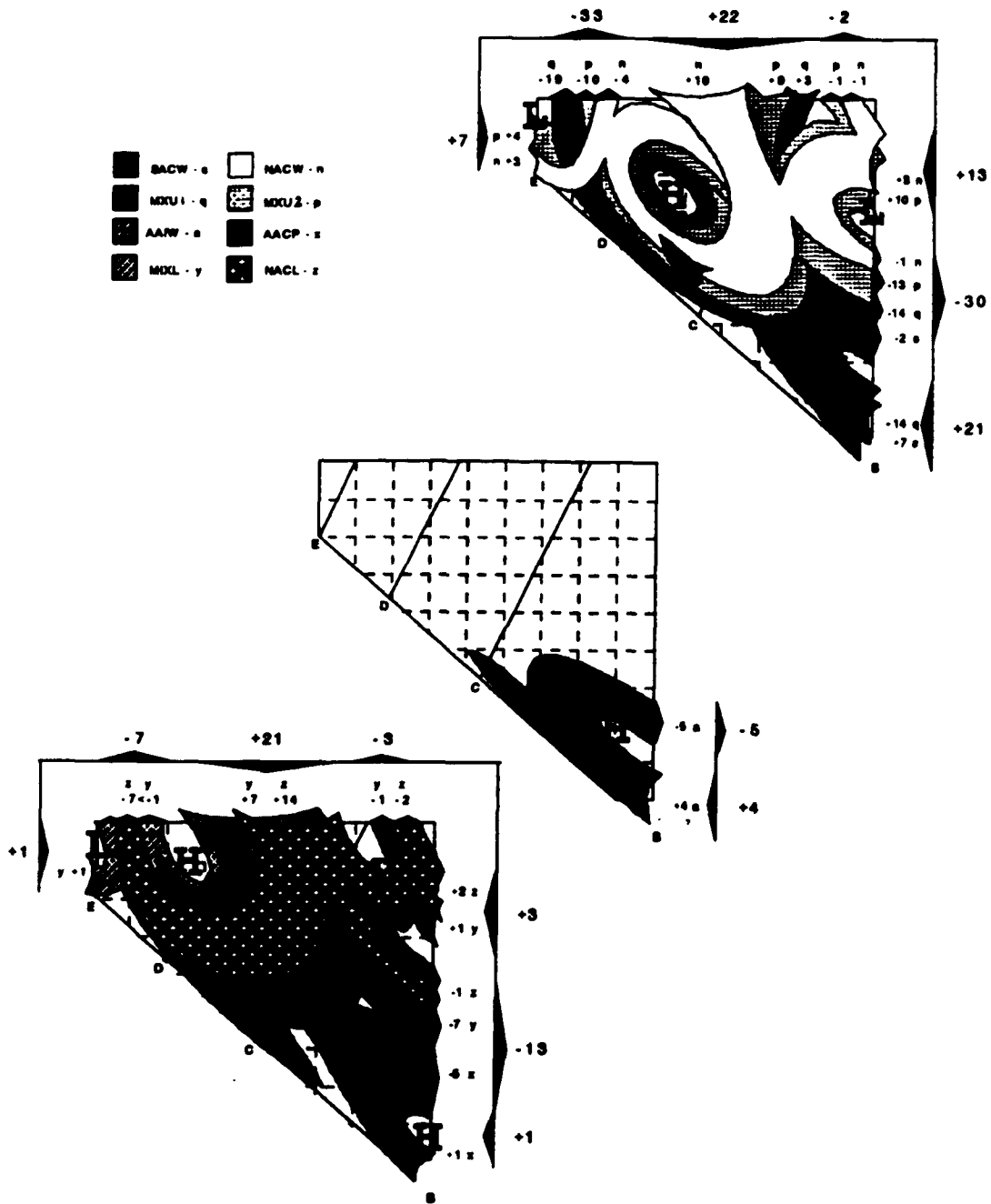


Figure 43A. Schematics of intermediate layer water mass pathways through the WESTRAX region during the late summer 1990 (WESTRAX 2).

Pathways indicate lateral extent of water masses. Transports through the boundaries are in Sverdrups ($1 \text{ Sv} = 10^6 \text{ m}^3/\text{s}$). 'H' and 'L' indicate (continued)

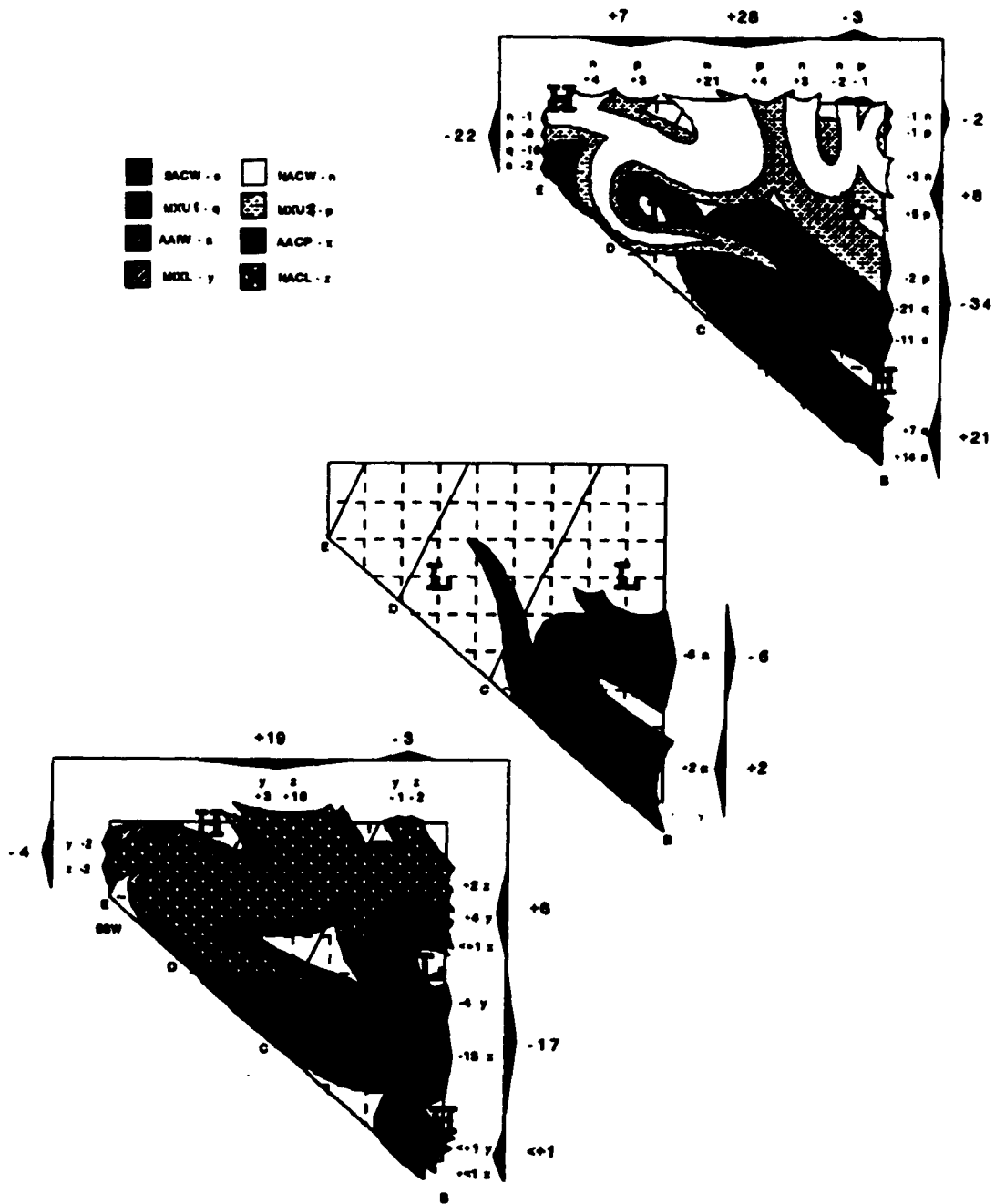


Figure 43B. Water mass pathways during the winter 1991 (WESTRAX 3).

(continued from Figure 43A) anticyclonic and cyclonic centers respectively.

Top panel: Upper intermediate water mass pathways: South Atlantic Central Water (SACW - s); North Atlantic Central Water (NACW - n); Upper Mix with a greater proportion of Southern Water (MXU1 - q), (continued)

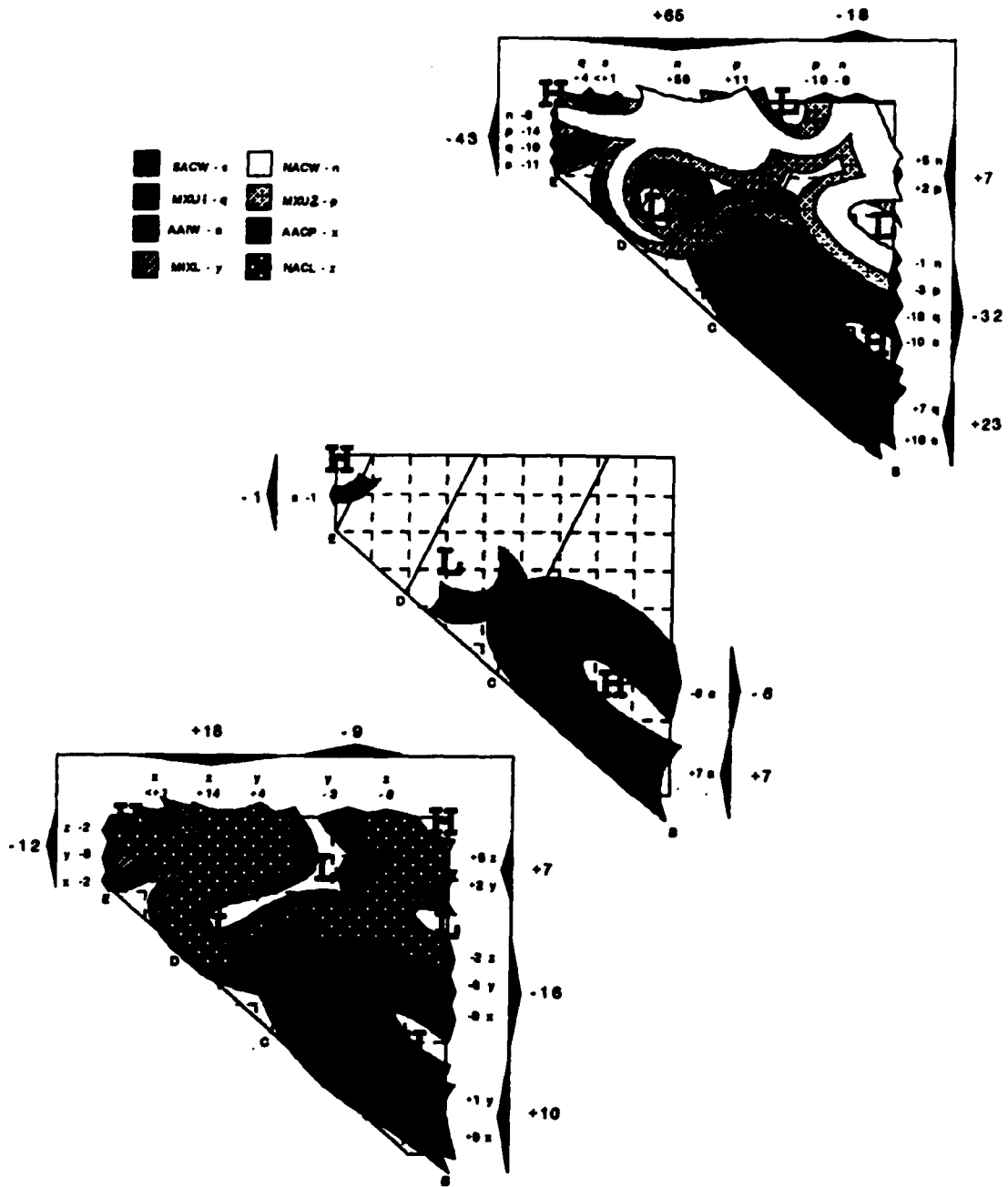


Figure 43C. Water mass pathways during the winter 1990 (WESTRAX 1).

(continued from Figure 43B) and Upper Mix with a lesser proportion of Southern Water (MXU2 - p).

Center panel: Antarctic Intermediate Water pathways (AAIW - a).

Bottom panel: Lower intermediate water mass pathways: (continued)

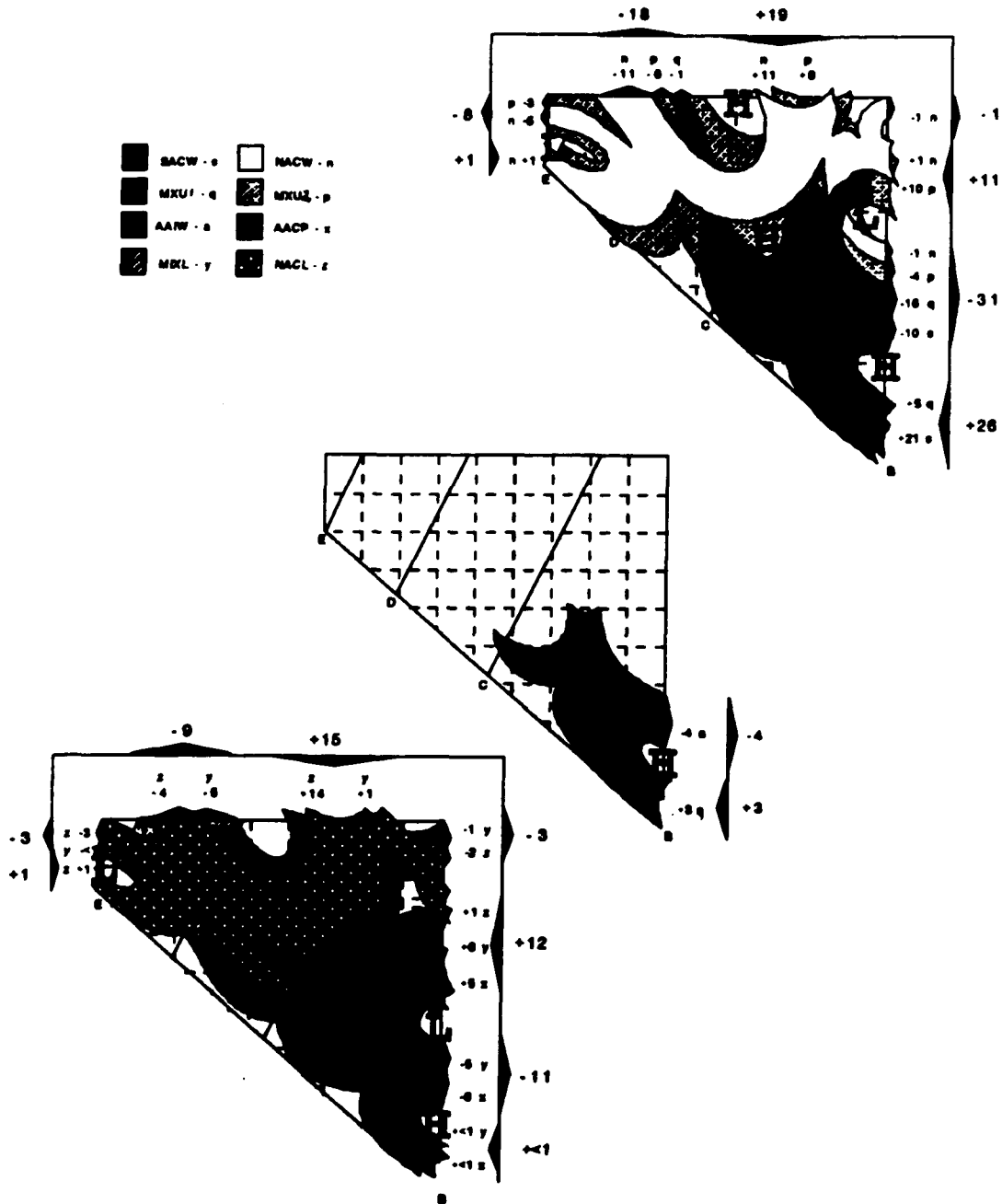


Figure 43D. Water mass pathways during the early summer 1991 (WESTRAX 4).

(continued from Figure 43C) Antarctic Circumpolar Water, Upper Branch (AACP - s); Lower Intermediate Mixture (MIXL - y), and North Atlantic Central Water, Lower Branch (NACL - z).

region as a major part of the Demerara Eddy circulation, turns anticyclonically, and departs toward the northwest. NACW also enters from the east and flows cyclonically around the eastern low to contribute to the NEUC. MXU2 follows pathways similar to NACW. AAIW retroflects around the Amazon Eddy. A small amount of AACP enters through the southeastern corner and retroflects around the Amazon Eddy. AACP is also found within the Demerara Eddy. NACL is a large part of the lower layer Demerara Eddy. MIXL is pervasive throughout the lower intermediate layer.

During the following winter (January 1991, WESTRAX 3), the Amazon Eddy extends further along the coast (Figure 43B). SACW reaches northwestward as far as 49°W before it retroflects toward the NEUC. Most of the MXU1 also retroflects, although a branch of MXU1 continues northwestward where it either turns cyclonically around the French Guiana low or flows westward through 53°W . An isolated pocket of SACW is found along the coast in the northwest. Most of the NACW which crosses 9°N flows anticyclonically around a ridge in the northwest and westward across 53°W . A branch of NACW turns cyclonically around the French Guiana low and flows eastward toward the NEUC. MXU2 follows a pathway similar to NACW except for a branch which flows around the eastern low and into the NEUC. AAIW is evident within a large retroflexion around the Amazon Eddy. A branch of AAIW extends northwestward with the MXU1 flow. Most of the AACP in the region is flowing eastward. NACL follows a serpentine path which flows southward across 9°N , turns anticyclonically around a northwestern ridge, flows cyclonically through a central trough, and finally turns eastward. MIXL again covers the whole region.

During the first winter (February 1990, WESTRAX 1), SACW flows northwestward to section C before retroflecting around the Amazon Eddy into the NEUC (Figure 43C). MXU1 also retroflects around the Amazon Eddy. A MXU1 branch flows northwestward and turns cyclonically around the French Guiana low.

Isolated parcels of SACW and MXU1 are evident in the anticyclonic flow across the northwestern corner. NACW flows across the northern border and turns anticyclonically westward toward 53°W. A branch of this NACW separates and turns cyclonically around the French Guiana low. NACW also enters through 44°W, turns cyclonically around the eastern low, and contributes to the eastward flow toward the NEUC. The retroflexion of AAIW follows the same path as the SACW. Patches of AAIW appear within the French Guiana low and the ridge in the northwest. AACP also follows the Amazon Eddy retroflexion. Regions of AACP within the circulation of the French Guiana low and the northwestern anticyclone are evident. These isolated pockets of southern water masses in the northwestern ridge suggest this is an anticyclone which has separated from the Amazon Eddy retroflexion. The circuitous pathway of the NACL during 1990 is similar to that of the following winter.

Water mass pathways during the early summer (June 1991, WESTRAX 4) are quite different from those of the other three surveys (Figure 43D). The retroflexion of SACW around the Amazon Eddy is confined to a small southeastern corner of the region. Additional SACW is evident in an anticyclonic circulation around a central Demerara Eddy. This structure suggests that this central anticyclone is separating from the Amazon Eddy. MXU1 follows the pathways of SACW except that a branch extends northwestward and exits across 9°N. NACW flows southward across 9°N, circulates around a third high center close to the northern border, and exits flowing northwestward. This third anticyclone of largely northern water masses is a separate cell from the Demerara Eddy. It probably moved into the region across the northern border. No NACW is found in the Demerara Eddy, suggesting that the entrainment process has just begun (as compared to September 1990 when NACW was a much larger part of the Demerara Eddy circulation). Some NACW flows westward across 44°W and turns cyclonically around the eastern low toward the NEUC. MXU2 is found within the anticyclonic

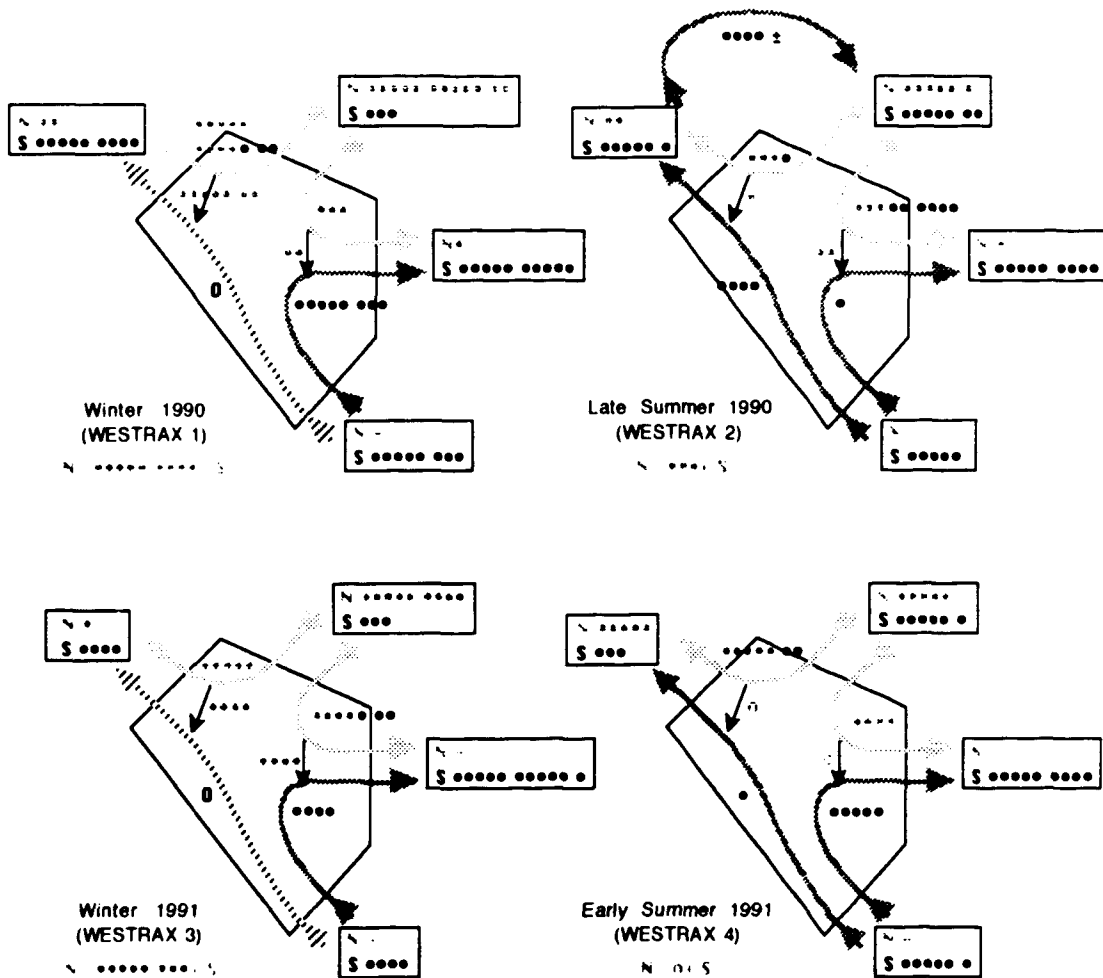


Figure 44. Flow budgets of southern and northern water mass volume transports through the WESTRAX 1-4 intermediate layers. Each dot represents a transport of approximately 5 Sv ($5 \times 10^6 \text{ m}^3/\text{s}$) by southern (black) or northern (gray) water masses. The arrows between pathways, and associated gray dots represent mixing transports between northern and southern water masses.

circulation around the Demerara Eddy. AAIW pathways are similar to SACW. A small AACP retroflection is noted around the Amazon Eddy. A large amount of the AACP appears to circulate cyclonically around the eastern low toward the NEUC. As in the upper layers, a region of southern AACP is found in the southeastern corner of the Demerara Eddy. NACL flows anticyclonically around the Demerara Eddy and exits toward the northwest.

Estimated mixing transports by water mass budgets...

When the appropriate water mass transports are interpreted in terms of the conceptual model presented in section IV (Figure 24), 'mixing transports' between southern and northern water masses can be determined. The sums of southern water mass (SACW, MXU1, MXU2, AAIW, AACP, and MIXL) transports versus northern water mass (NACW and NACL) transports are compared (Figure 44). Inflow through the southeastern corner of the region is entirely southern water. During both winters, all of this southern water retroflects into the NEUC and none continues northwestward along the coast. During September 1990, 19 Sv flow northwestward along the coast, as discussed earlier. It appears that much of this September 1990 flow retroflects around the Demerara Eddy and joins the eastward flow toward the NEUC (I've added such a pathway on Figure 44).

An average transport budget for the WESTRAX water masses indicates the 'production' of 21 Sv of southern water masses, presumably by mixing within the region (Figure 45). That is, 13 and 8 Sv of the northern water masses NACW and NACL respectively, are diluted by mixing to form MXU2 and MIXL. Conversely, we could say that southern waters are transferring their cooler, fresher properties to the northern water masses along the T-S mixing lines introduced in section V. This mixing is also indicated between the pathways on Figure 44. Mixing transport is greatest during the winter when 47 and 41 Sv of northern water mass are converted to southern during WESTRAX 1 and 3 respectively. During the early

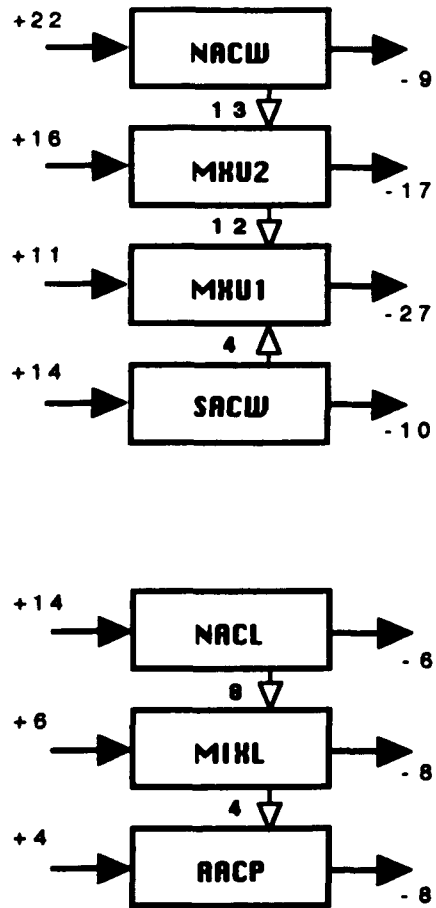


Figure 45. Weighted average water mass budgets for net upper and lower intermediate water mass transports (S_v) into (left) and out of (right) the WESTRAX region. Mixing transports are indicated by the open arrows between water masses.

and late summer, the mixing transports are much less at 2 and 16 Sv respectively. Much of this mixing appears to be associated with the separated retroflection eddies which are translating across the region's northwestern corner.

Eastward flow toward the NEUC is composed of almost all southern water from (a) the SEC retroflection within the equatorial gyre or (b) production by mixing within the WESTRAX region. While westward flow into the northern part of the region (within the NEC) contains large proportions of northern water, there are also some southern water masses. These can be attributed to (a) trapped parcels of southern water circulating within a retroflection eddy or (b) the return flow of southern water which comes from within the tropical gyre.

The net Pegasus-derived intermediate layer average transports of volume, salt, and temperature of 21 Sv, 732×10^3 metric tonnes/s, and 127°C-Sv respectively are southward around the tropical gyre and into the NEUC (Figure 46). Temperature transports are biased toward the flow in the upper, or warmer levels of the intermediate layer. The almost constant eastward transport of temperature into the NEUC is noted.

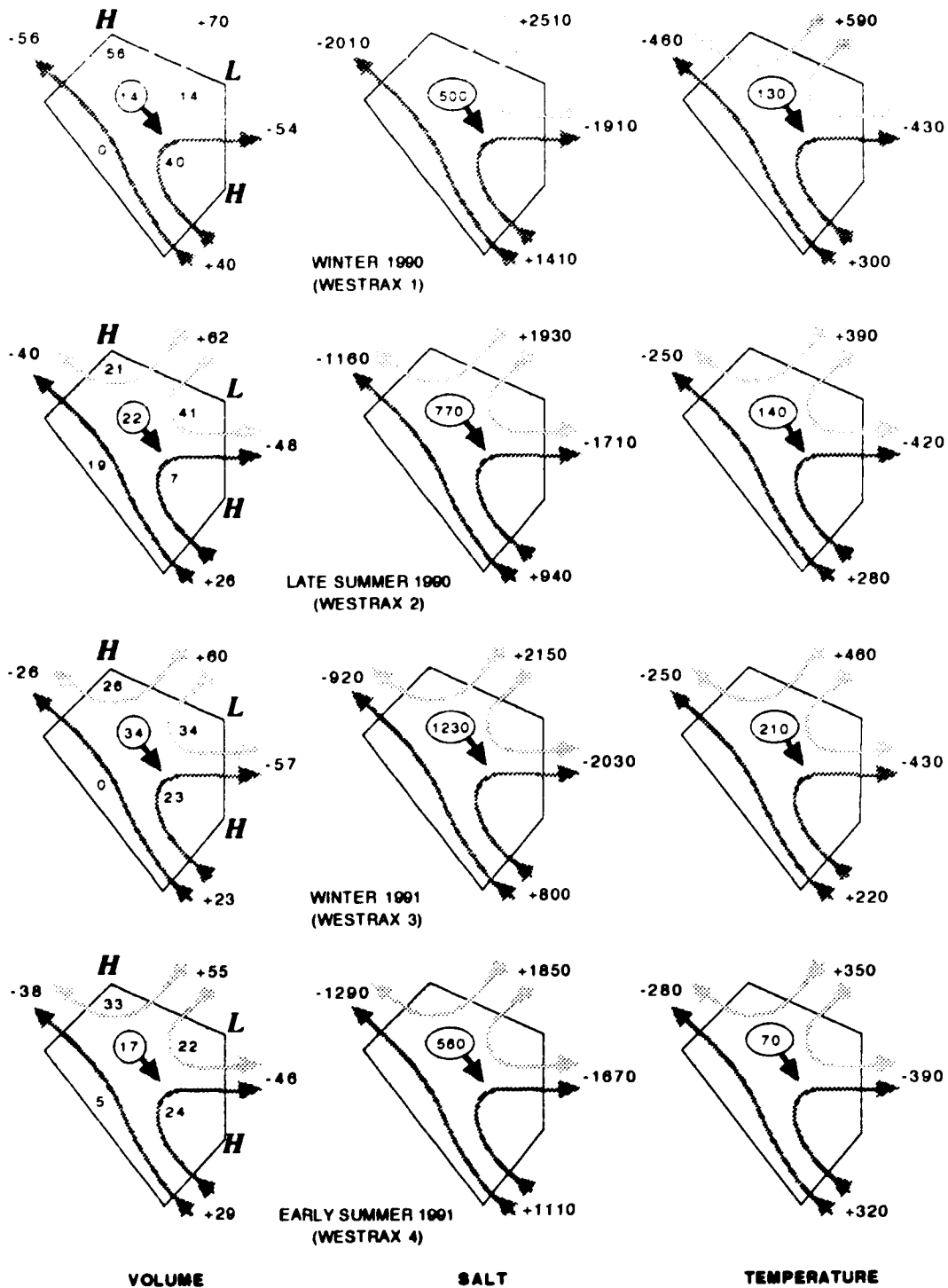


Figure 46. Volume, salt, and temperature transports within the intermediate layer of the WESTRAX region (see Figure 38). From left to right, the transports of volume (Sverdrups, $10^6 \text{ m}^3/\text{s}$), salt (10^3 metric tonnes/s), and temperature ($^{\circ}\text{C}\cdot\text{Sv}$, relative to 0°C) through the boundaries are presented. Net cyclonic transports around the tropical gyre are circled. Internal volume transports are based on the analyses of depth-averaged non-divergent flows across sections C, D, and E.

VII.
DISCUSSION

I have described an intermediate layer water mass flow structure in which water moves through the WESTRAX region by:

- *Gyre-scale ocean currents (10^3 km, seasonal to decadal, and $1-10^2$ cm/s)*
- *Mesoscale eddy transports (10^2 km, months, and 10 cm/s)*
- *Meso- to microscale mixing (unspecified).*

(The relevant length, time, and speed scales are in parentheses). The results are summarized with a conceptual model to illustrate the velocity structure of the region with and without a retroflection eddy (Figure 47).

Oceanic current summary...

The WESTRAX region intermediate layer flow structure includes:

- A 29 Sv* northwestward inflow of southern water masses (SACW, AAIW, AACCP) and mixtures of primarily southern water (MXU1, MXU2 and MIXL) which enter through the region's southeastern corner as part of the subsurface SEC;
- The retroflection of 21 Sv of these southern water masses around a semi-permanent Amazon Eddy (near 2°N 45°W) and toward the NEUC;

This anticyclonic flow is a western part of the Atlantic wind-driven equatorial gyre described by Mayer and Weisberg (1993).

* Four-survey weighted average transport with a $\pm 10\%$ uncertainty.

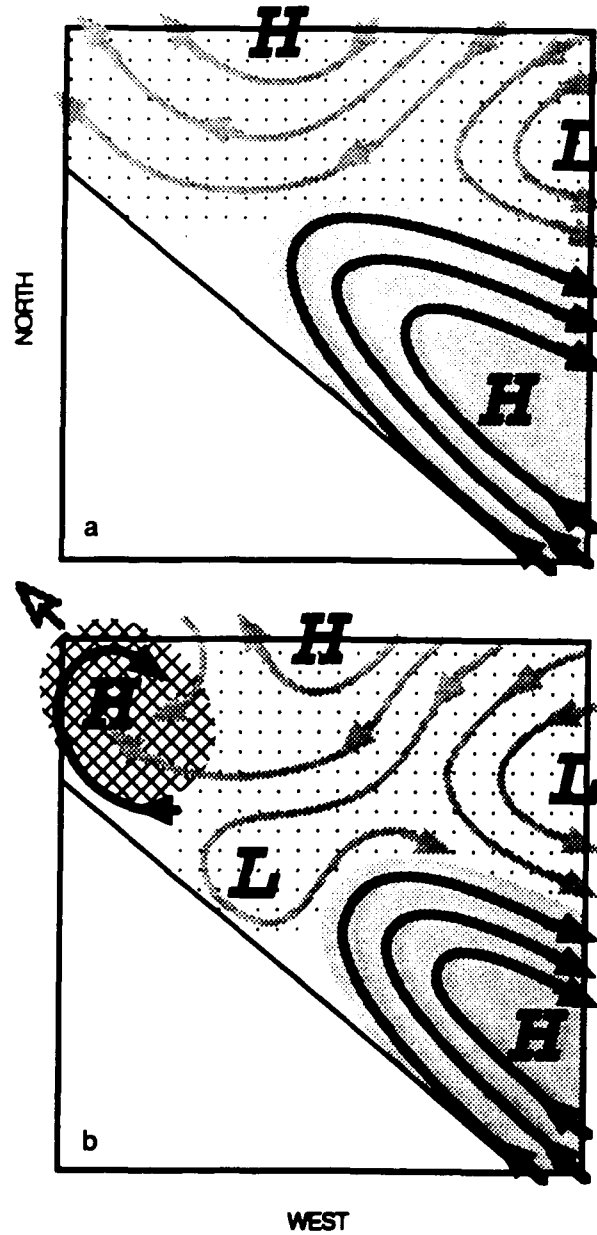


Figure 47. Schematic of WESTRAX region intermediate layer flow structure:
 (a) Without a retroreflection eddy
 (b) After the separation of a retroreflection eddy.
 Southern water mass streamlines (darker) trace the retroreflection in the Amazon Eddy (H). Northern water mass streamlines (lighter) trace westward flow and the eastern and French Guiana lows (L). Northern and southern water masses swirl into the retroreflection eddy (hatched H) as it translates northwestward.

- A 61 Sv southwestward flow of northern water masses (NACW and NACL) and southern water mass mixtures (MXU1, MXU2, and MIXL) across the northern boundary as part of the NEC;

On average:

- 32 Sv turn anticyclonically and continue northwestward toward the Caribbean as part of the North Atlantic subtropical gyre
- 29 Sv turn cyclonically around an eastern low (near 6°N 44°W) and feed into the NEUC as part of the Atlantic tropical gyre
- Approximately 2 Sv of this 29 Sv flow southwestward and turn cyclonically around a low located off the coast of French Guiana (near 6°N 50°W). During the winter surveys, the tropical gyre extends to the coast to the southeast of a translating retro-reflection eddy (Figure 46b). An associated alongshore undercurrent which feeds southeastward toward the NEUC appeared in the CME model results discussed by Schott and Böning (1991).

Because I have based water mass definitions solely on T-S relationships, there is the distinct possibility that some of the low-salinity water within the NEC which has been classified as southern actually has a northern hemisphere origin. The analysis of additional tracers would be necessary to clarify this point.

- A 50 Sv eastward flow toward the NEUC which carries a mixture of water masses from the north and south into the interior of the tropical Atlantic;

Most of the water within the NEUC has southern hemisphere origins. In contrast with the surface NECC in which flow is greatest in summer (33 Sv) and least in winter (11 Sv), flow within the

intermediate layer NEUC is relatively steady during the four surveys (the range of four transports is 46 to 57 Sv).

- A 40 Sv northwestward flow toward the Caribbean which contains a mixture of northern and southern water masses;

This transport is the combined result of:

- A 32 Sv continuation of the NEC,
- 8 Sv within an alongshore transport of southern water masses, associated with the northwestward translation of a series of retroflection eddies.

Eddy-scale transport summary...

By entraining swirls of southern and northern water masses, retroflection eddies provide a mechanism for the northwestward transport of large amounts of southern water masses (Figure 47b). Each eddy's instantaneous transport is estimated to be 30 Sv (27 Sv within the intermediate layer). If three such eddies form and move through the region during a year, the annual transport is 8 Sv.

Retroflection eddies are identified as cells of well-developed anticyclonic circulation which contain isolated pockets of southern water masses. The September 1990 retroflection eddy is a 300 km diameter cylinder which extends through the surface and intermediate layers (e.g., 0-1300 m). Over 30 Sv appear to recirculate within the intermediate layer of this cell. The separated retroflection eddies translate northwestward at 10 cm/s.

Mixing transport summary...

An average of 21 Sv of northern water masses are being diluted by mixing within the WESTRAX region to produce southern mixture water masses. In

accordance with temperature-salinity relationships, mixing processes are transferring the cool, less salty properties associated with AAIW to intermediate waters of the North Atlantic. A large part of this mixing appears to occur within retroflection eddies.

Some comparisons with other tropical Atlantic structure studies...

The western extensions of the tropical and equatorial gyres of the Atlantic wind-driven circulation described by Mayer and Weisberg (1993) are permanent features of the WESTRAX region. Closure of the tropical gyre is suggested by cyclonic flow through the eastern portion of the WESTRAX region. A net 21 Sv southward transport through the tropical gyre is three times greater than the Mayer and Weisberg (1993) transport needed for closure. This indicates a robust meridional circulation in the western tropical Atlantic.

There are few opportunities for direct comparisons between earlier work and the observed WESTRAX intermediate layer transports. The average WESTRAX transports which flow eastward within the NECC and NEUC are 26 and 50 Sv respectively. Cochrane *et al.* (1979) estimate eastward flows across 33.5°W of 14 Sv in the NECC and 21 Sv through the upper 800 dbar (geostrophic, relative to 800 dbar). Katz (1981) estimated a NECC transport of 20-25 Sv across 33.5°W (geostrophic, relative to 500 dbar). Carton and Katz (1990) use inverted echosounder (IES) data at 38°W to estimate an average NECC transport of 20 Sv, with a maximum of 40 Sv.

The northwestward WESTRAX transports within the surface NBC (seaward of the 100 m isobath) and intermediate layer SEC are 19 and 21 Sv respectively. Flagg *et al.* (1986) use lowered current meter data to estimate transports of 21 and 31 Sv between depths of approximately 0-100 m and 100-500 m respectively (see Figure 3, section I).

The Philander and Pacanowski (1986) general circulation model estimates annual mean mass transports across 30°W for upper (0-50 m), mid (50-317 m) and lower (below 317 m) layers as follows:

- Between 2.5°S and 2.5°N (roughly equivalent to the SEC and EUC):
-4, +15, and 0 Sv respectively (positive transports are eastward)
- Between 2.5°N and 8.0°N (NECC and upper NEUC):
+4, +5, and -2 Sv respectively.

Table 8. Zonal transport comparisons between the CME model results (Schott and Böning 1991) and WESTRAX data across equivalent sections of 44°W.

Layer	Annual Mean (CME)	4-Survey Average (WESTRAX)
<i>Inflow of the NBC and SEC¹:</i>		
Upper ²	-12	-12
Mid	+1	-7
Lower	<u>-1</u>	<u>-12</u>
	-12	-31
<i>Outflow of the NECC and NEUC²:</i>		
Upper	+6	+16
Mid	+8	+12
Lower	<u>+2</u>	<u>+12</u>
	+16	+40
<p>Positive transports in Sverdrups are eastward. ¹ Between 2.5°S and 2.5°N (CME) or 0°N and 2.5°N (WESTRAX) ² Layers are 0-72 m, 72-206 m, 206-519 m (CME) or 0-100 m, 100-200 m, 200-500 m (WESTRAX). ³ Between 2.5-10°N (CME) or 2.5- 9°N (WESTRAX)</p>		

The CME model (Schott and Böning 1991) annual mean transports across 44°W provide the best transport comparisons between model results and WESTRAX

data (Table 8).

The net WESTRAX transports are 2 to 4 times larger than wind-driven estimates (Mayer and Weisberg 1993), and 2.5 times larger than the Schott and Böning (1991) model transports. The reasons for these differences include:

- When compared to the vertically integrated wind-driven currents, the WESTRAX transports do not include surface and deep flows which may be counter to the intermediate flow
- The WESTRAX results are the average of 4 realizations and present a flow structure which is not averaged over long time periods or wide grid spacing
- I suspect the Amazon Eddy and the eastern low are both closed cells with large amounts of internal western boundary recirculation.
- The model velocities may be incorrect.

A speculative model of the annual evolution of WESTRAX region structure...

A possible cycle for changes in the velocity structure of the intermediate layer of the WESTRAX region is suggested (Figure 48). I have assumed that there is no interannual variability in structure, and therefore each of the four available depth-averaged stream function patterns is representative of the month during which it was observed. With eight unobserved months, the conceptual model is very subjective.

There are three permanent features in the WESTRAX region: (a) the retroflexion of the SEC around the Amazon Eddy, (b) the cyclonic flow of a branch of the NEC around the low near 6°N 44°W, and (c) the consistent eastward flow of toward the NEUC. The remaining features may follow a seasonal cycle as described below.

In this model, three retroflexion eddies are formed each year. Richardson *et al.* (1993) observed that the surface layer Guyana Current is dominated by retroflexion eddies during July to December. From this I have inferred a spring

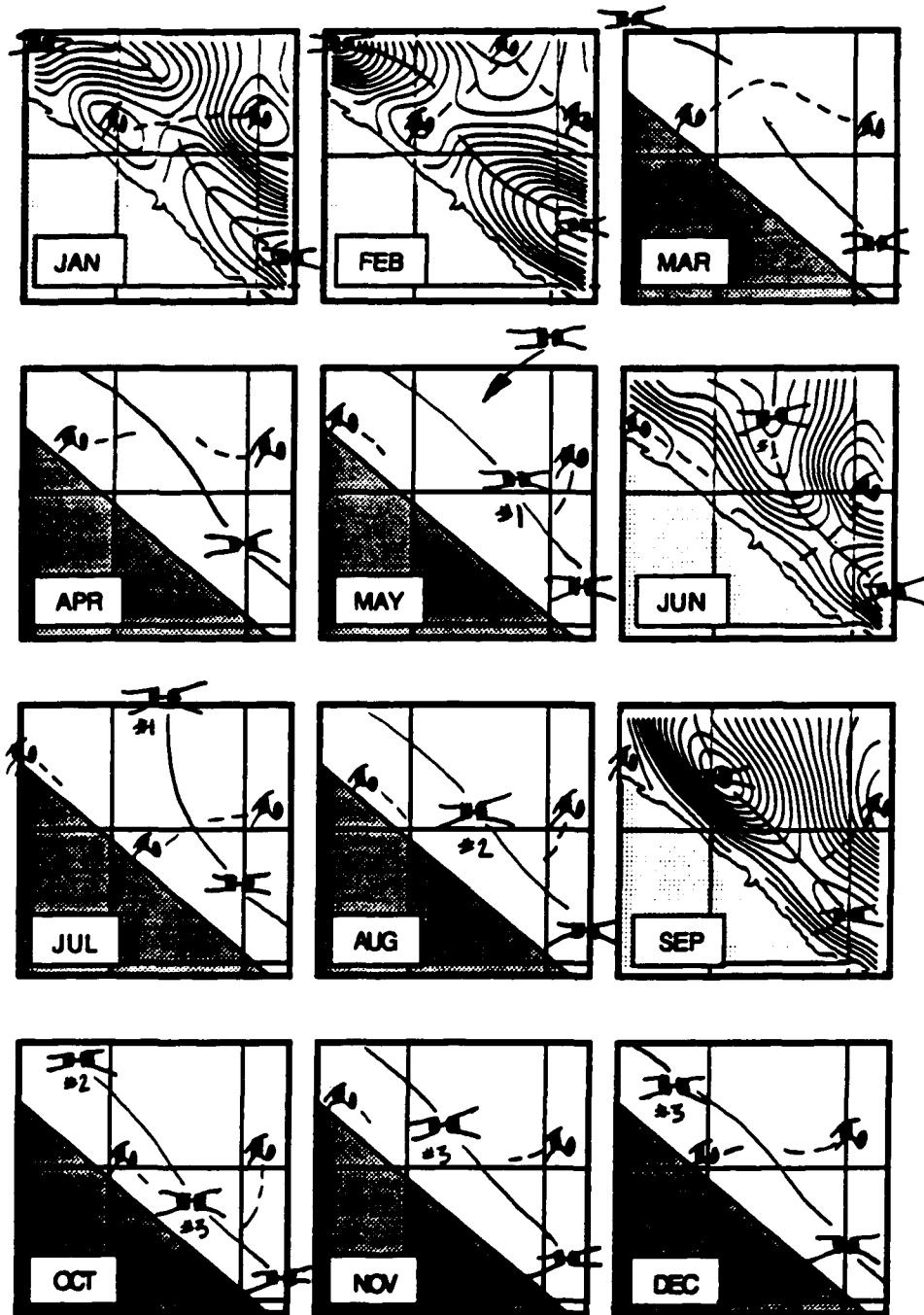


Figure 48. Conceptual model to show a cycle of WESTRAX region circulation patterns. The vertically integrated velocity streamlines for January 1991 (WESTRAX 3), February 1990 (WESTRAX 1), June 1991 (WESTRAX 4), and September 1990 (WESTRAX 2) are considered representative of those months. Each streamline is 5 Sv ($5 \times 10^6 \text{ m}^3/\text{s}$). Anticyclones (H), cyclones (L), ridges (solid) and troughs (dashed) are moved to illustrate the evolution of structure through the seasons (see the text). The three annual retroreflection eddies are numbered. The H in the northeast on the May plot is a northern water mass eddy which enters the region embedded within the NEC.

to early winter season during which retroflection eddies form and move through the WESTRAX region. These model eddies translate northwestward at approximately 250 km/month.

During the late winter, the structure of the WESTRAX region changes little. The NEUC is fed by mainly southern water from the retroflection of the SEC around the Amazon Eddy. Branches of the NEC flow around the eastern and/or French Guiana lows and feed some northern water into the NEUC. The rear quarter of the previous year's third retroflection eddy departs slowly across the northwest corner. A well established zonal trough lies along 6°N between the French Guiana and eastern lows.

As spring progresses, the Amazon Eddy extends northwestward. By late spring, an eddy begins to pinch off from the extended retroflection. As the zonal trough weakens, the first retroflection eddy separates. It moves northwestward during early summer. I believe the anticyclone on the June 1991 analysis is the result of a merger between the season's first retroflection eddy which has recently separated and a cell of northern water which entered the region from the northeast. These anticyclones eventually combine and depart the region on a trajectory which is more northward than usual.

During summer, more northern water branches from the NEC and flows around the eastern low toward the NEUC. By mid-summer, the season's second retroflection eddy forms and separates. It moves northwestward along a track approximately 200 km seaward of the continental break. Behind this retroflection eddy, a low forms against the coast near French Guiana. This low eventually follows the retroflection eddy northwestward.

The season's third retroflection eddy forms and is separated by late fall. The fall NEUC contains the greatest proportion of input from the north. As winter returns, the 6°N zonal trough re-forms behind this last retroflection eddy. The cyclonic flow of northern water from the NEC diminishes, and the NEUC is once

more composed of mostly southern water.

Unresolved issues...

I have not presented a complete analysis of uncertainties in the flow fields. An objective analysis of the hydrographic and velocity data would provide this information. I was unable to include vertical transports in the analyses. Objective analysis techniques could provide sufficient information about the data fields resolution to allow an estimate of divergent vertical velocities.

I could not fully partition the relative importances of the ocean current, retroflection eddy, and mixing transport mechanisms. An 'inverse analysis' of the region, with the addition of available dissolved oxygen measurements, could provide the mixing coefficients by which these estimates could be made.

The differences between Pegasus and geostrophic derived flows across Section B suggest that an in-depth study of ageostrophy within the WESTRAX region would be instructive. This also could be done using an objective analysis approach. As I worked with these data, I became convinced that ocean velocity structure cannot be defined by geostrophy. The information gained over the next few years from Pegasus, ADCP, and other absolute measurement techniques will revolutionize our understanding of the ocean's currents as the geostrophic structure which produced our present understanding is superseded.

Unfortunately, only one retroflection eddy was completely surveyed within the WESTRAX analysis area. Without additional subsurface observation sets like the WESTRAX Pegasus and CTD surveys, we will not be able to answer important questions about the internal water mass and velocity structure of retroflection eddies. In particular:

- What is the size, depth and form of a fully separated, translating eddy?
- How do the rotational and vertical currents flow through an eddy?
- How much water, and especially southern water, does an eddy carry?

- How does mixing occur within and around an eddy?
- How is northern water entrained as an eddy moves, and how much?
- What happens to the eddies at the Antilles Chain?

Additional questions about eddy formation and dynamics can be explored by assimilating the WESTRAX data sets into physical models.

Long term observations are necessary to further understand temporal cycles in the western tropical Atlantic's structure. An important tool will be the routine analyses of surface topography using the satellite altimetry recently available from TOPEX-Poseidon. The velocity structure of the upper layer (but not the intermediate depths), and the movement of major features like the fully developed retroflection eddies, can be inferred from ocean surface shape. The tropical ocean surface layer is too uniformly warm to use surface thermal information to define structure. Ocean biological color information has been demonstrated to be useful in this area, and we can look forward to the wealth of data which SEAWIFS promises. Still, I believe subsurface surveys will be necessary to resolve the retroflection eddy process.

While highly unlikely (because they are so expensive), an exploration across the entire tropical Atlantic from the surface to the bottom similar to the WESTRAX surveys would, in my opinion, be the most definitive way to determine the equatorial region's role in the global transport budget.

VIII.

SUMMARY OF CONCLUSIONS

- As part of the intermediate layer SEC, a survey-average of 29 Sv flow northwestward into the WESTRAX region. This flow includes 20 Sv of the southern water masses defined as SACW, AAIW, and AACW, and 9 Sv of the predominantly southern water mass mixtures MXU1, MXU2, and MIX1.

- 21 Sv of this flow retrofect anticyclonically around the Amazon Eddy and return eastward toward the NEUC.

- Annually, an estimated 8 Sv of this southern water move northwestward along the coast within a series of retroflection eddies.

- Retroflection eddies composed of southern water masses form within the WESTRAX region and translate toward the Caribbean, entraining northern water as they go. These anticyclonically rotating cells move northwestward at 10 cm/s with an estimated instantaneous transport of 30 Sv. These eddies are modeled by a 300 km cylinder which extends from the surface to 1300 m and has a 30 Sv internal recirculation. Assuming three eddies per year, an annual retroflection eddy transport of 8 Sv toward the Caribbean and North Atlantic is estimated.

- As part of the NEC, 61 Sv flow into the WESTRAX region from the northeast. This inflow consists of 36 Sv of the northern water masses NACW and NACL and 25 Sv of the southern water mass mixtures.

- 32 Sv of this flow combine with the 8 Sv of southern water and form a 40 Sv northwestward transport toward the Caribbean. This is a mixture of 26 and 14 Sv of southern and northern water masses respectively.

— 29 Sv turn cyclonically around a low in the east of the region, merge with the retroflecting SEC branch, and form a 50 Sv eastward flow toward the NEUC. The NEUC is a mixture of 48 and 2 Sv of southern and northern water masses respectively.

— Within the interior Atlantic, it appears that the NEUC contributes to both the equatorial and tropical gyres. The westward flows of the SEC and NEC contain 9 and 25 Sv respectively of the southern water mass mixtures MIX1, MIX2, and MIXL.

- There is a relatively constant ratio of 62:38% between waters of a southern and northern origin within the region.

- The region's velocity structure is dominated by an alongshore ridge during the summer and a zonal trough during the winter. The anticyclonic retroflection of the SEC in the southeast and cyclonic circulation of the NEC in the northeast of the region appear to be permanent features.

- Water mass budgets indicate 21 Sv of the southern mixtures MXU2 and MIXL are produced from NACW and NACL by mixing. Similarly, 4 Sv of the mixture MXU1 are produced by mixing from SACW. An estimated 10 and 15 Sv of these mixtures flow eastward into the NEUC or northwestward in eddies respectively.

- Part of the southeastern retroflection of the SEC closes the wind-driven equatorial gyre with a 21 Sv northward flow toward the NEUC. Part of the cyclonic flow of the NEC through the northeastern corner of the WESTRAX region closes the tropical gyre with a 29 Sv southward flow toward the NEUC.

— The transports measured during WESTRAX are more than three times larger than the return flows required to close the wind-driven gyres, indicating that there is substantial recirculation within the Amazon Eddy and eastern low.

APPENDIX A.
THE INTERPOLATION ALGORITHM

An algorithm described by Akima (1978) is used to interpolate the unevenly spaced WESTRAX observations onto an evenly spaced grid (Figure A-1). $P(x_i, y_i, z_{0i})$ is defined as an i -element set of randomly located data on the surface z_0 . $P(x_j, y_j, z_{0j})$ is the desired j -element set of evenly gridded data on the same surface. With the depth assumed to be a constant, the scalar magnitudes of the observation data are said to represent a third dimension in x - y - p space. Thus fields of temperature, salinity or velocity data which are observed at randomly spaced points on the x - y plane provide the heights of a 'tent-like' surface relative to that plane.

The solid dots A through F on Figure A-2 represent a set of randomly spaced observations, $P(x_i, y_i)$. Their locations project onto open dots a through f on the x - y plane. The Akima (1978) algorithm fits a curved surface to these observations and then extracts the evenly spaced, interpolated field from that surface.

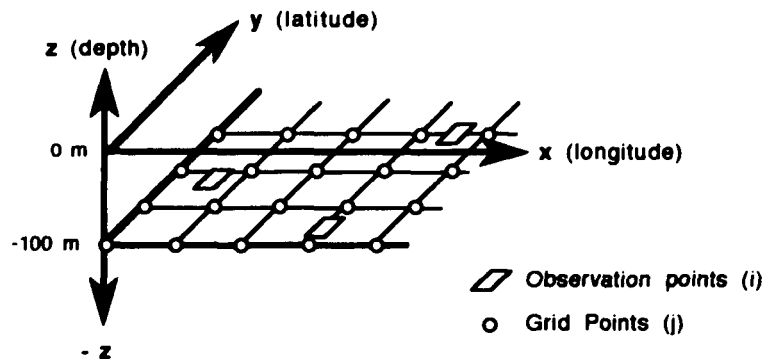


Figure A-1. Interpolation algorithm gridding system.

Initially, the method divides the space occupied by the observation data set $P(x_i, y_i)$ into triangles (e.g., A-B-C in Figure A-2). A user-specified number of nearby points (N) is used to analyze the various slopes associated with each triangle. The algorithm selects the N 'closest points' for each triangle. The shaded dots D-E-F in Figure A-2 represent a set of $N = 3$ 'closest points' for triangle A-B-C. For each triangle, the algorithm then uses all of the $(3 + N)$ data points (in this example, A-B-C-D-E-F) to determine the first and second order partial derivatives of p with respect to x and y , and the slopes normal to each of its sides (p_t of AB, BC, and CA). These slopes are used to mathematically describe a curved surface which passes through vertices A-B-C.

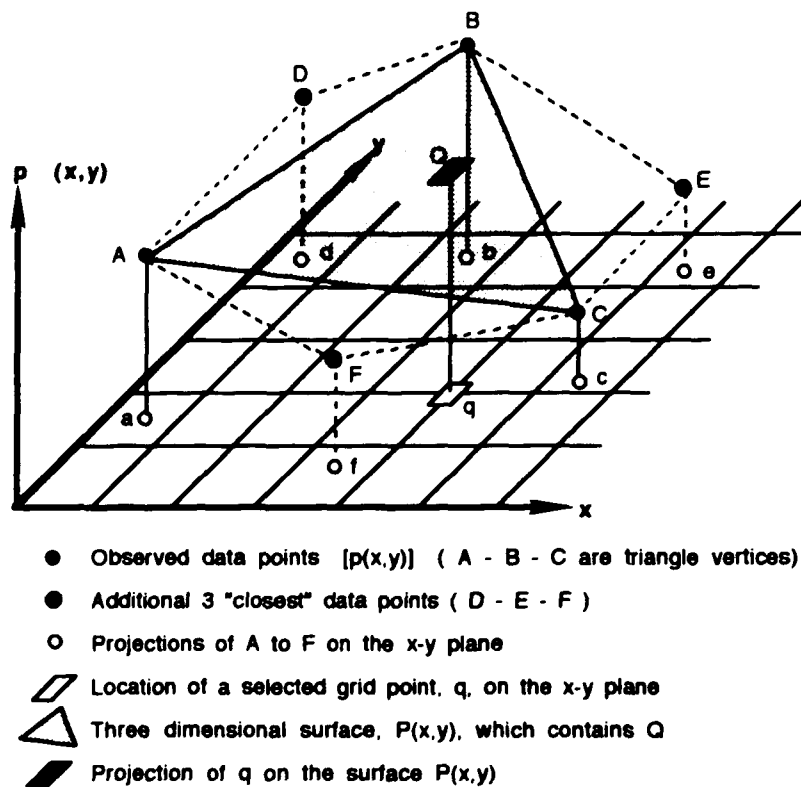


Figure A-2. Illustration of Akima (1978) algorithm.

Thus, for each triangle, a set of twenty-one known values is created

$$\begin{aligned}
 &P_A, P_{XA}, P_{YA}, P_{XXA}, P_{XYA}, P_{YYA}, P_B, P_{XB}, P_{YB}, P_{XXB}, P_{XYB}, P_{YYB}, \\
 &P_C, P_{XC}, P_{YC}, P_{XXC}, P_{XYC}, P_{YYC}, P_{TAB}, P_{TBC}, P_{TCA}
 \end{aligned}
 \tag{A-1}$$

where subscripts x, y, and t indicate derivatives.

The surface that contains A-B-C (Figure A-2) is described in terms of the twenty-one term polynomial

$$p(x_i, y_j) = \sum_{m=0}^5 \sum_{n=0}^{m-5} \Lambda_{mn} x^m y^n .
 \tag{A-2}$$

For each triangle, the coefficient set (Λ_{mn}) is then determined by inserting the gradient values (Equation A-1) into Equation (A-2) and solving for a new, evenly gridded j-element set of data points, P_j .

This is a computationally intensive program, and there are significant tradeoffs between the size of N and the time required to complete the interpolation. Each observation data set requires experimentation, as there appears to be a N , beyond which CPU run times rise dramatically while interpolated surfaces become no smoother. For the WESTRAX data set, $N = 25$ 'closest points' were used to ensure a smooth surface.

Akima (1978) points out that the analyzed surface passes through all observation points, implying that there are no errors at these locations. The author is careful to note, however, that large errors are likely when extrapolating beyond the domain of the data.

APPENDIX B.
THE STREAM FUNCTION EQUATION

The velocity vector is

$$\mathbf{V} = u \mathbf{i} + v \mathbf{j} + w \mathbf{k} . \quad (\text{B-1})$$

The vertical component of vorticity is defined by

$$\omega_z \mathbf{k} = (\mathbf{V} \times \mathbf{V})_z = \left(\frac{\partial v}{\partial x} - \frac{\partial u}{\partial y} \right) \mathbf{k} . \quad (\text{B-2})$$

When the vertical velocity (w) is assumed to be negligible compared to the horizontal velocities, the zonal and meridional velocity components u and v can be defined in terms of a stream function Ψ

$$u = -\frac{\partial \Psi}{\partial y} \quad \text{and} \quad v = \frac{\partial \Psi}{\partial x} . \quad (\text{B-3})$$

Thus, in terms of the stream function, Equation (B-2) can be written as

$$\omega_z(x,y) = \frac{\partial^2 \Psi}{\partial x^2} + \frac{\partial^2 \Psi}{\partial y^2} = \nabla_H^2 \Psi . \quad (\text{B-4})$$

where ∇_H^2 represents the Laplacian on the horizontal plane and vorticity is assumed to be a function of position. Equation (B-4) is known as the Poisson equation.

Equation (B-4) can be solved for the stream function (Ψ) in a general

singly-connected region by applying any one of three different boundary conditions. For the purpose of this discussion, we consider a rectangular domain A with a boundary C (Figure B-1).

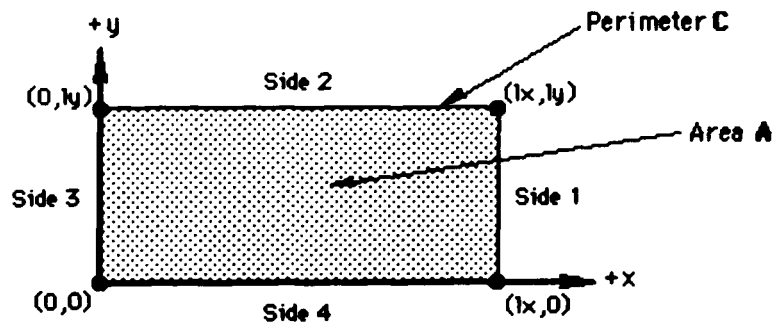


Figure B-1. Conventions for stream function analyses.

- The Dirichlet boundary value problem is solved when ψ on the boundaries is specified in terms of the integral of the velocities which are normal to the boundary C . Mass and vorticity are conserved in this problem.
- The Neumann boundary value problem is solved when the gradients of ψ normal to the boundaries are specified in terms of the velocities which are tangent to the boundary C . Mass is conserved in this problem.
- The third, or periodic boundary value problem is not discussed here.

Solving the Poisson equation, subject to the Dirichlet boundary condition, results in flow that is both non-divergent and irrotational. For flow in the region to be irrotational, the circulation must be zero according to

$$\Gamma = \oint_C (\mathbf{V} \cdot d\mathbf{S})_z = \oint_C (u \, dy - v \, dx) = 0$$

$$\text{where, } dS = dy \mathbf{i} - dx \mathbf{j} . \quad (\text{B-5a})$$

For our rectangular region, Equation (B-5a) becomes

$$\int_0^{l_y} u(l_x, y) dy + \int_{l_x}^0 v(x, l_y) dx + \int_{l_y}^0 -u(0, y) dy + \int_0^{l_x} -v(x, 0) dx = 0 . \quad (\text{B-5b})$$

For non-divergent flow, i.e, in terms of Ψ , Equation (B-5b) is

$$\begin{aligned} -\int_0^{l_y} \frac{\partial \Psi}{\partial x}(l_x, y) dy + \int_{l_x}^0 \frac{\partial \Psi}{\partial y}(x, l_y) dx + \int_{l_y}^0 \frac{\partial \Psi}{\partial x}(0, y) dy - \int_0^{l_x} \frac{\partial \Psi}{\partial y}(x, 0) dx = \\ -\int_C d\Psi(x, y) = 0 . \end{aligned} \quad (\text{B-5c})$$

Thus, the boundary condition is reduced to the sum of Ψ differences which must be zero. The Dirichlet boundary condition is therefore stated as

$$g(x, y) = \sum \begin{aligned} & \int +u dy && \text{for } (x = l_x) \text{ \& } (0 \leq y \leq l_y) \text{ (Side1)} \\ & \int +v dx && \text{for } (0 \leq x \leq l_x) \text{ \& } (y = l_y) \text{ (Side2)} \\ & \int -u dy && \text{for } (x = 0) \text{ \& } (0 \leq y \leq l_y) \text{ (Side3)} \\ & \int -v dx && \text{for } (0 \leq x \leq l_x) \text{ \& } (y = 0) \text{ (Side4)} . \end{aligned} \quad (\text{B-6})$$

Solving the Poisson equation, subject to the Neumann boundary defined in terms of Ψ , results in flow that is non-divergent. For this problem, the gradient of Ψ normal to the boundary C is defined by the expression

$$g(x, y) = \frac{\partial \Psi}{\partial \eta} , \quad (\text{B-7})$$

where η is the generalized coordinate normal to the boundary (Figure B-1). In

terms of our rectangular region, Equation (B-7) becomes

$$g(x,y) = \frac{\partial \Psi}{\partial x} |_{\text{side 1}} + \frac{\partial \Psi}{\partial y} |_{\text{side 2}} - \frac{\partial \Psi}{\partial x} |_{\text{side 3}} - \frac{\partial \Psi}{\partial y} |_{\text{side 4}} . \quad (\text{B-8})$$

In terms of the velocity on the boundary, the Neumann boundary condition (Equation B-8) is

$$g(x,y) = \begin{cases} +v(x,y) & \text{for } (x = l_x) \ \& \ (0 \leq y \leq l_y) \ \text{(Side1)} \\ -u(x,y) & \text{for } (l_x \leq x \leq 0) \ \& \ (y = l_y) \ \text{(Side2)} \\ -v(x,y) & \text{for } (x = 0) \ \& \ (l_y \leq y \leq 0) \ \text{(Side3)} \\ +u(x,y) & \text{for } (0 \leq x \leq l_x) \ \& \ (y = 0) \ \text{(Side4)} . \end{cases} \quad (\text{B-9})$$

The finite difference scheme which was used to solve Equation (B-4) numerically, with either the Dirichlet (B-6) or Neumann (B-9) boundary conditions, is presented in Appendix C.

APPENDIX C.
TWO-DIMENSIONAL FINITE DIFFERENCE ANALYSIS
(THE IMSL FPS2H ALGORITHM)

The Poisson equation which was developed in Appendix B is solved numerically using the IMSL algorithm FPS2H (IMSL 1987). This routine uses the HODIE FFT method to solve the more general Helmholtz equation for the scalar variable $U(x,y)$ where

$$U_{xx}(x,y) + U_{yy}(x,y) + f U(x,y) = g(x,y) . \tag{C-1}$$

Equation C-1 is the Poisson equation (B-4) when $U(x,y)$ represents the stream function $\Psi(x,y)$, $g(x,y)$ represents the vorticity expression $\omega_z(x,y)$, and the coefficient f is set to zero. Herein is described a second order accurate ($O(h^2 + k^2)$) five-point compact finite difference algorithm (Figure C-1) which provides a linear solution to Equation C-1 using a Fast Fourier Transform (FFT) solution. The fourth order, 9-point solution to accuracy $O(h^4 + k^4)$ could be similarly developed.

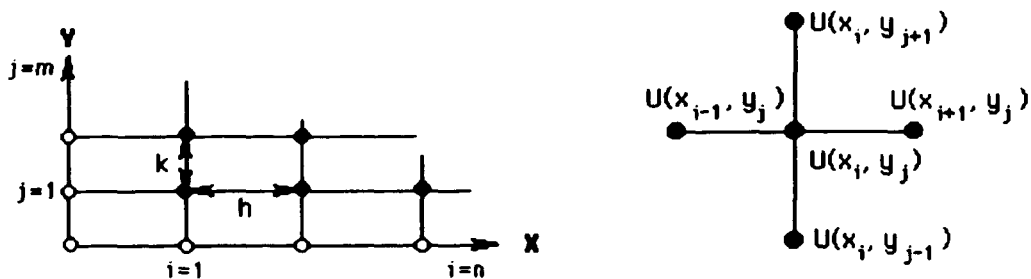


Figure C-1. The FPS2H coordinate system.

Equation C-1 is solved on the rectangular domain, R, with any combination of the boundary conditions:

∂R_1 : U is prescribed (the Dirichlet boundary condition, designated BC1)

∂R_2 : U_{η} , the gradient of U normal to the border is prescribed
(the Neumann boundary condition, BC2)

∂R_3 : where there is periodicity in x, y or both (BC3).

That is

$$\partial R = \partial R_1 \cup \partial R_2 \cup \partial R_3 . \tag{C-2}$$

The region R is overlaid by an uniform (n × m) grid with mesh spacing ‘h’ in the x direction and ‘k’ in the y direction (Figure C-1) and (0 ≤ i ≤ n), (0 ≤ j ≤ m).

The centered difference formula is found by a Taylor expansion of U(x,y) around x_i . We set $h = x - x_i$ and evaluate the expressions at x_{i+1} and x_{i-1} , add the results, and apply the intermediate value theorem. Solving for the second derivative term, we arrive at

$$U_{xx}(x_i, y_j) = \frac{1}{h^2} [U(x_{i+1}, y_j) - 2U(x_i, y_j) + U(x_{i-1}, y_j)] - \frac{h^2}{12} U_{xxxx}(\zeta_i, y_j)$$

where $x_{i-1} < \zeta_i < x_{i+1}$. (C-3a)

A similar expression for $U_{yy}(x,y)$ is produced with $k = y - y_j$

$$U_{yy}(x_i, y_j) = \frac{1}{k^2} [U(x_i, y_{j+1}) - 2U(x_i, y_j) + U(x_i, y_{j-1})] - \frac{k^2}{12} U_{yyyy}(x_i, \eta_j)$$

where $y_{j-1} < \eta_j < y_{j+1}$. (C-3b)

If an estimated solution to Equation C-1 within order $O(h^2 + k^2)$ is defined by

$$w_{i,j} = U(x_i, y_j) - \frac{h^2}{12} U_{xxxx}(\zeta_i) - \frac{k^2}{12} U_{yyyy}(\eta_j) \quad (C-4)$$

for some point (ζ_i, η_j) such that $x_{i-1} < \zeta_i < x_{i+1}$ and $y_{j-1} < \eta_j < y_{j+1}$. The sum of Equations C-3a and C-3b becomes

$$\frac{(w_{i+1,j} - 2w_{i,j} + w_{i-1,j})}{h^2} + \frac{(w_{i,j+1} - 2w_{i,j} + w_{i,j-1})}{k^2}, \quad (C-5a)$$

and Equation C-1 is written

$$\begin{aligned} & \frac{(w_{i+1,j} - 2w_{i,j} + w_{i-1,j})}{h^2} + \frac{(w_{i,j+1} - 2w_{i,j} + w_{i,j-1})}{k^2} + f w_{i,j} \\ & = h^2 g(x_i, y_j). \end{aligned} \quad (C-5b)$$

Equation C-5b is rearranged to yield

$$\begin{aligned} w_{i,j} \left[2 \frac{h^2}{k^2} + 2 - h^2 f \right] - w_{i+1,j} + w_{i-1,j} - \frac{h^2}{k^2} w_{i,j+1} - \frac{h^2}{k^2} w_{i,j-1} \\ = h^2 g(x_i, y_j), \end{aligned}$$

for $i = 1, 2, \dots, n-1$ and $j = 1, 2, \dots, m-1$. (C-6a)

The boundary conditions, BC1, BC2, BC3, or a combination, are now;

$$\begin{aligned} w_{0,j} &= BC(x_0, y_j) \text{ and;} \\ w_{n,j} &= BC(x_n, y_j) \text{ for } j = 0, 1, \dots, m; \\ \\ w_{i,0} &= BC(x_i, y_0) \text{ and;} \\ w_{i,m} &= BC(x_i, y_m) \text{ for } i = 1, 2, \dots, n-1. \end{aligned} \quad (C-7)$$

The result is a star-shaped relationship between five adjacent points on the

analysis field. If the appropriate boundary conditions are inserted when one or two points of the star touch the borders, this is an $(n-1) \times (m-1)$ set of equations with $(n-1) \cdot (m-1) = (nm - n - m + 1)$ unknowns. Equations and subscripts are renumbered in the "natural order," row-wise from the lower left corner to the top (Figure C-2)

$$P_q = (x_j, y_j) \text{ and } w_q = w_{i,j} ,$$

$$q = i + (j-1) \cdot (n-1); \quad i = 1, 2, \dots, n-1; \quad j = 1, 2, \dots, m-1 . \quad (C-8)$$

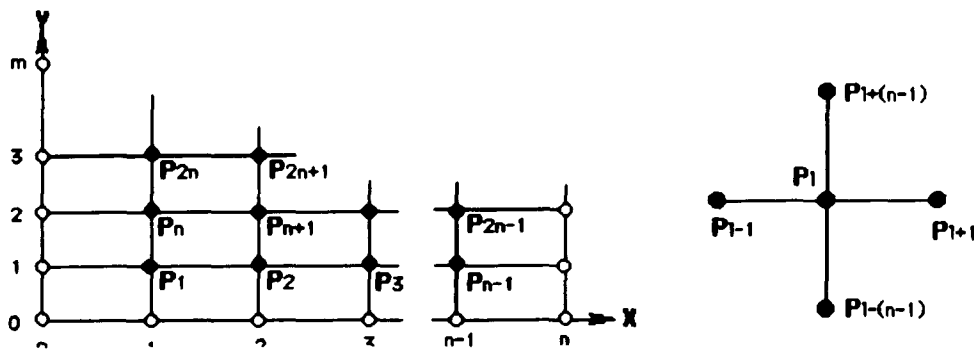


Figure C-2. The 'natural order' gridding system.

Equation C-6 becomes

$$a \cdot w_q + b \cdot w_{q+1} + b \cdot w_{q-1} + c \cdot w_{q+n-1} + c \cdot w_{q-n+1} = d \cdot g_q ,$$

where $a = -2 \frac{h^2}{k^2} - 2 + h^2 f ;$

$$b = 1; \quad c = \frac{h^2}{k^2}; \quad d = h^2 . \quad (C-9a)$$

If $h = k$, these expressions simplify to

$$a = -4 + h^2f; \quad b = c = 1; \quad d = h^2. \quad (C-9b)$$

This is a $(q \times q)$ system of equations in matrix form

$$M \cdot w = g. \quad (C-10)$$

After application of the boundary conditions and some matrix manipulation, Rice and Boisvert (1985) present a tri-diagonal system for this expression which can be solved by FFT methods

$$\begin{bmatrix} \Lambda/\mu & B & & \theta \cdot B \\ B & \Lambda & B & \\ & \dots & \dots & \\ & & B & \Lambda \\ \theta \cdot B & & B & \Lambda/\mu \end{bmatrix} \cdot \begin{bmatrix} w_1 \\ w_2 \\ \dots \\ w_{q-1} \\ w_q \end{bmatrix} = d \begin{bmatrix} g_1/\mu \\ g_2 \\ \dots \\ g_{q-1} \\ g_q/\nu \end{bmatrix}; \quad (C-11)$$

with

$$\Lambda = \begin{bmatrix} a/\eta & b & & \tau \cdot b \\ a & b & a & \\ & \dots & \dots & \\ & & b & a \\ \tau \cdot b & & b & a/\sigma \end{bmatrix}, \quad B = \begin{bmatrix} b/\eta & c & & \tau \cdot c \\ b & c & b & \\ & \dots & \dots & \\ & & c & b \\ \tau \cdot c & & c & b/\sigma \end{bmatrix}. \quad (C-12)$$

A and B are $(n \times n)$ matrices. The scalars μ , ν , η , and σ depend on boundary

conditions on the top (μ), bottom (ν), left (η), and right (σ) of ∂R . These are either '1' for the Dirichlet (BC1) or '2' for the Neumann (BC2) boundary conditions. Scalars θ and τ are '1' when the boundary condition is periodic (BC3) and '0' otherwise.

APPENDIX D.

THE COMPUTATION OF VERTICAL VELOCITY USING THE CONTINUITY EQUATION

The equation of continuity in an incompressible fluid

$$\frac{1}{\rho} \frac{\partial \rho}{\partial t} + \left[\frac{\partial u}{\partial x} + \frac{\partial v}{\partial y} + \frac{\partial w}{\partial z} \right] = 0, \quad (D-1)$$

with density (ρ) constant reduces to

$$\frac{\partial u_t}{\partial x} + \frac{\partial v_t}{\partial y} + \frac{\partial w_t}{\partial z} = 0. \quad (D-2)$$

The velocity variables u , v , and w are functions of position (x,y,z) and the subscript (t) indicates total velocity. Total velocity can be separated into divergent (d) and non-divergent (n) terms, or

$$\begin{aligned} u_t &= u_d + u_n , \\ v_t &= v_d + v_n , \\ w_t &= w_d + w_n . \end{aligned} \quad (D-3)$$

In computing the stream function fields (Appendix B), horizontal flows (u_n, v_n) were assumed to be non-divergent and vertical motion was assumed to be zero (*i.e.*, $w_n = 0$), leading to

$$\frac{\partial u_n}{\partial x} + \frac{\partial v_n}{\partial y} = 0. \quad (D-4)$$

The interpolated velocity fields (i) are assumed to represent the total (t) horizontal velocity (e.g., $(u_i, v_i) = (u_t, v_t)$). When Equation D-4 is subtracted from Equation D-2, the vertical gradient of the total vertical velocity (w_t) can be determined

$$\left[\frac{\partial u_i}{\partial x} - \frac{\partial u_n}{\partial x} \right] + \left[\frac{\partial v_i}{\partial y} - \frac{\partial v_n}{\partial y} \right] + \left[\frac{\partial w_t}{\partial z} - 0 \right] = 0. \quad (D-5)$$

Setting the divergent velocities equal to the difference between interpolated (i) and non-divergent (n) velocities yields

$$\begin{aligned} u_d &= u_i - u_n, \\ v_d &= v_i - v_n, \end{aligned} \quad (D-6)$$

and Equation D-5 reduces to

$$\frac{\partial w_t}{\partial z} = - \left[\frac{\partial u_d}{\partial x} + \frac{\partial v_d}{\partial y} \right]. \quad (D-7)$$

In a layer between an upper and lower level (z_1 and z_2), mean horizontal divergence through the layer can be determined by the finite difference expression

$$\begin{aligned} D(x,y,z_{1-2}) &= \\ \frac{1}{2} \left[\left(\frac{\partial u_d}{\partial x}(x,y,z_1) + \frac{\partial v_d}{\partial y}(x,y,z_1) \right) + \left(\frac{\partial u_d}{\partial x}(x,y,z_2) + \frac{\partial v_d}{\partial y}(x,y,z_2) \right) \right] \end{aligned} \quad (D-8)$$

or

$$\frac{\partial w_t}{\partial z}(x,y,z_{1-2}) = -D(x,y,z_{1-2}). \quad (D-9)$$

Integrating between layers z_1 and z_2

$$\int_{z_1}^{z_2} dw_t = \int_{z_1}^{z_2} -D(x,y,z_{1-2}) dz, \quad (D-10)$$

yields

$$w_t(x,y,z_2) = -D(x,y,z_{1-2}) \times [z_2 - z_1] + w(x,y,z_1). \quad (D-11)$$

This algorithm is illustrated by Figure D-1. At the surface of the ocean, $w_t(x,y,z_0)$ can be set to zero (a rigid lid). The vertical velocity analysis then steps layer-by-layer downward to find each vertical velocity field, relative to the surface, at increasingly deeper layers.

A unit analysis follows.

$$\text{If } u \text{ \& } v \text{ are } \left[\frac{\text{cm}}{\text{s}} \right], z \text{ is } [\text{m}], \text{ and } x \text{ \& } y \text{ are } [\text{km}] \quad (D-12)$$

$$\frac{dw}{dz} = \frac{du}{dx} + \frac{dv}{dy} \Rightarrow \left[\frac{\frac{\text{cm}}{\text{s}}}{\frac{\text{km}}{1}} \times \frac{\frac{1 \text{ m}}{1000 \text{ m}}}{\frac{1 \text{ km}}{1}} \right] \Rightarrow 10^{-5} \left[\frac{1}{\text{s}} \right] \quad (D-13)$$

$$\text{Thus, } w \Rightarrow \left[\frac{10^{-5}}{\text{s}} \right] \times dz [\text{m}] \times \left[\frac{100 \text{ cm}}{\text{m}} \right] \Rightarrow 10^{-3} \left[\frac{\text{cm}}{\text{s}} \right],$$

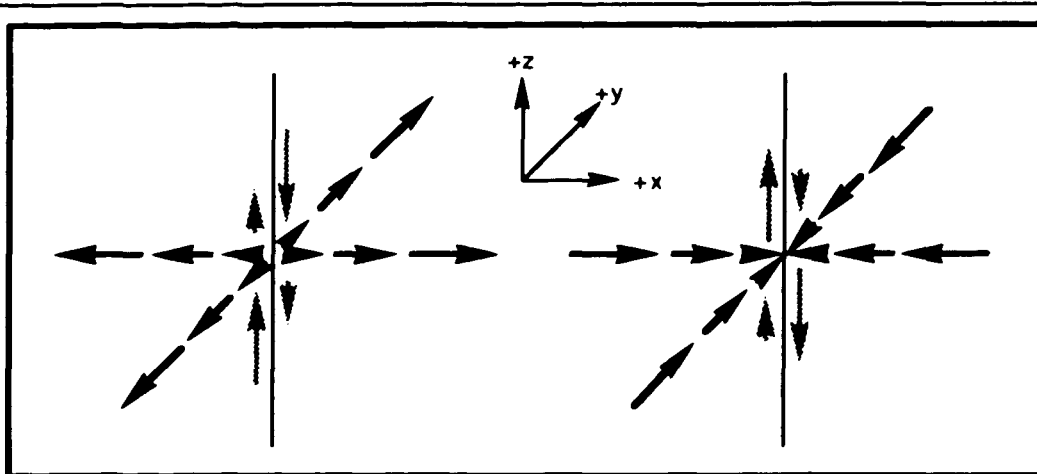
$$\text{which is of the order: } 10^{-3} \left[\frac{\text{cm}}{\text{s}} \right] \times \left[\frac{3600 \text{ s}}{\text{hr}} \right] \times \left[\frac{24 \text{ hr}}{\text{day}} \right] \Rightarrow$$

$$86.4 \left[\frac{\text{cm}}{\text{day}} \right] \quad (D-14)$$

Check by applying: du & $dv = 10 \frac{\text{cm}}{\text{s}}$, dx & $dy = 100 \text{ km}$, $dz = 50 \text{ m}$

$$\frac{dw}{dz} = 10^{-5} \times \frac{\frac{10 \text{ cm}}{\text{s}}}{\frac{100 \text{ km}}{1}} = 10^{-6} \frac{1}{\text{s}} \quad (\text{D-15})$$

$$dw = 50 \text{ m} \times 10^{-6} \frac{1}{\text{s}} \times \frac{100 \text{ cm}}{\text{m}} = 0.005 \frac{\text{cm}}{\text{s}} = 4.32 \frac{\text{m}}{\text{day}} \checkmark \quad (\text{D-16})$$



HORIZONTAL DIVERGENCE
(positive divergence)

$$\left[\frac{\partial u_d}{\partial x} + \frac{\partial v_d}{\partial y} \right] > 0$$

$$\frac{\partial w_t}{\partial z} < 0$$

HORIZONTAL CONVERGENCE
(negative divergence)

$$\left[\frac{\partial u_d}{\partial x} + \frac{\partial v_d}{\partial y} \right] < 0$$

$$\frac{\partial w_t}{\partial z} > 0$$

EFFECTS ON VERTICAL VELOCITIES

In ASCENT, $\partial z > 0$, $\partial w_t < 0$
 + w_t decreases in magnitude
 - w_t magnitude increases

In DESCENT, $\partial z < 0$, $\partial w_t > 0$
 + w_t increases in magnitude
 - w_t magnitude decreases

In ASCENT, $\partial z > 0$, $\partial w_t > 0$
 + w_t magnitude increases
 - w_t decreases in magnitude

In DESCENT, $\partial z < 0$, $\partial w_t < 0$
 + w_t magnitude decreases
 - w_t increases in magnitude

Figure D-1. An illustration of horizontally divergent and convergent velocity fields (dark arrows) and the resultant changes in vertical velocity (grey arrows).

APPENDIX E.
A COMPARISON OF DATA ANALYSIS TECHNIQUES

The zonal velocity structures across section B (44°W) determined using six different analysis techniques are qualitatively compared (Figures E-1 to E-4 for WESTRAX 1 to 4 respectfully). The methods used are:

- a. Vertical interpolation of velocity (u) structure using the original Pegasus profiles;*
- b. Divergent Pegasus velocities extracted from horizontal velocity fields interpolated at 50 m depth intervals;*
- c. Non-divergent Pegasus velocities derived from stream function analyses of the fields presented on panel b;*
- d. Geostrophic analysis of CTD profile data with a reference level of 1300 m;*
- e. Same as panel d with the Pegasus reference velocity at 1300 m added; and*
- f. Geostrophic analysis from horizontally interpolated fields of CTD temperature and salinity data, referenced to 1300 m and including the 1300 m interpolated Pegasus reference velocity.*

These results are quantitatively compared using the February 1990 data.

The structural similarities between panels a and b indicate no information is lost when horizontally interpolated Pegasus fields are used, although there is some smoothing. There are some changes between the divergent (panel b) and non-divergent (panel c) structures. While most differences are subtle at section B (as shown), there are larger structural disparities across the more data-sparse sections such the northern boundary (9°N, not shown). Differences between interpolated and stream function analyses also occur across the internal sections

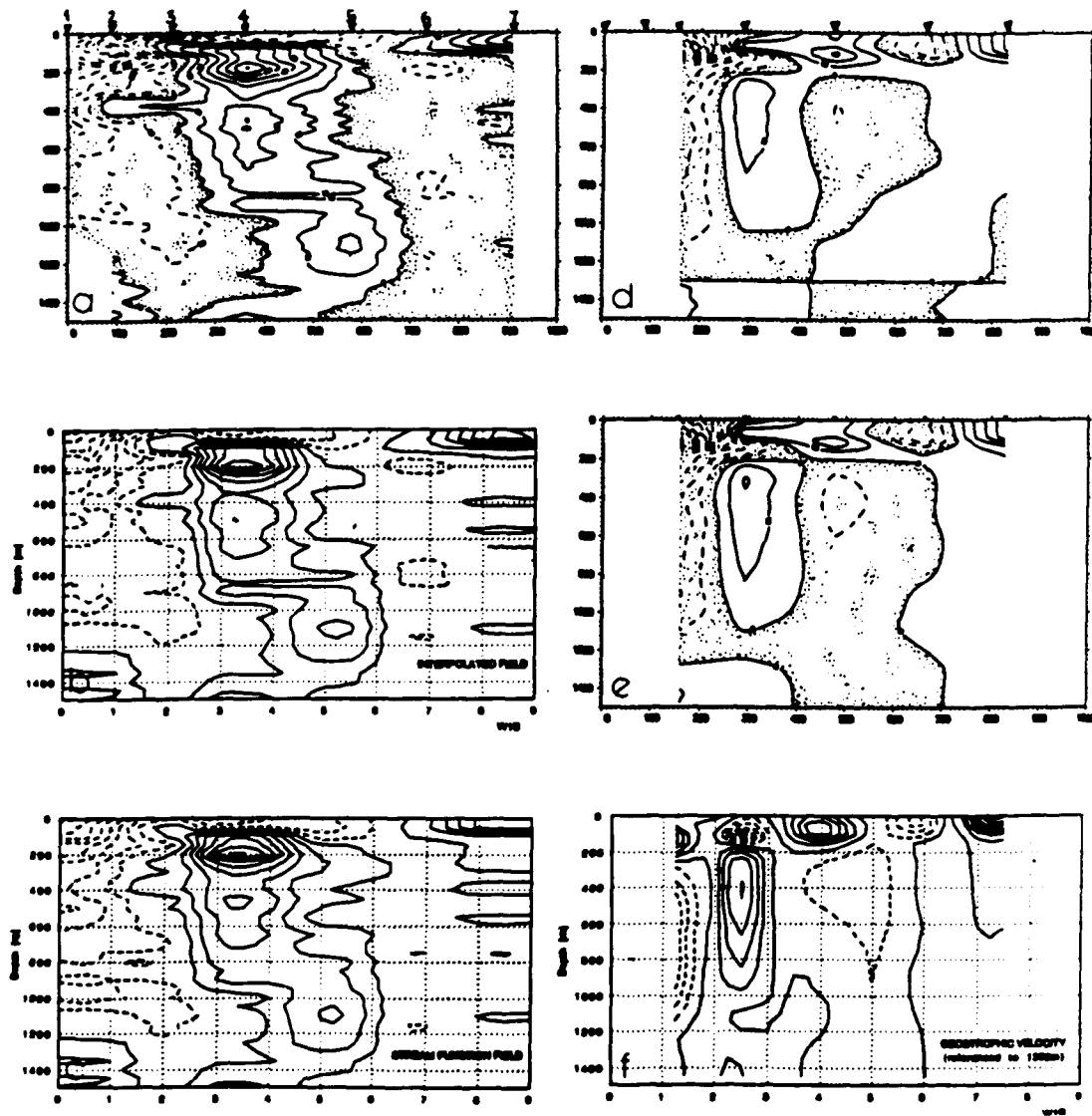


Figure E-1. Comparison between zonal (u) velocity structures during February 1990 (WESTRAX 1) across section B (44°W) using six different computation methods. Velocity contours at 10 cm/s intervals. Dashed contours and gray/stippled regions indicate negative westward flow.

a. Vertical interpolation of Pegasus profiles which were observed along section B at the marks on top of the plot

b. From horizontally interpolated (e.g., divergent) fields of Pegasus data at 50 m depth intervals

(continued on Figure E-2)

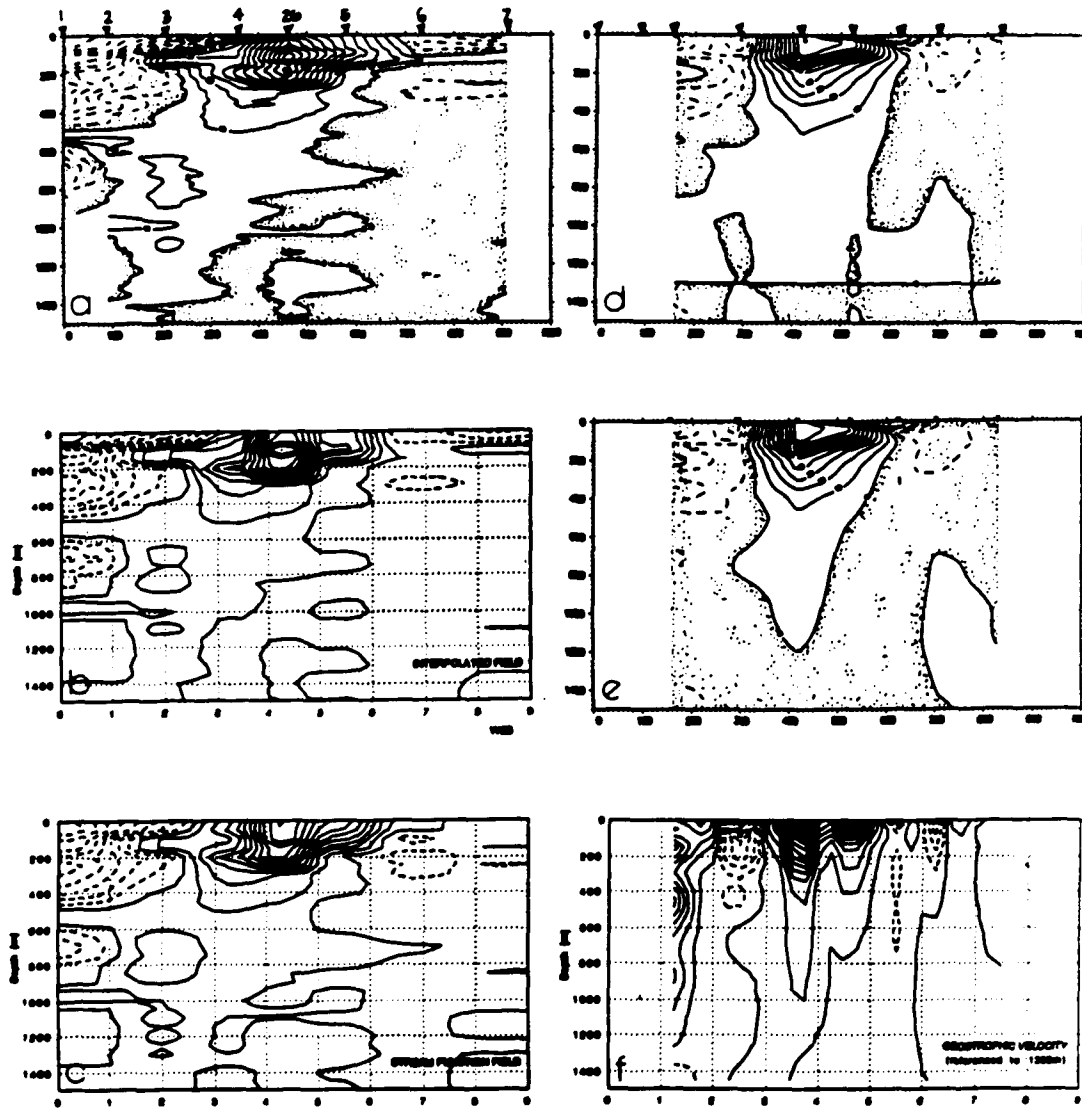


Figure E-2. Same as Figure E-1 for September 1990 (WESTRAX 2).
(continued from Figure E-1)

c. From stream function (e.g., non-divergent) analyses of Pegasus fields presented on panel b.

d. Geostrophic analysis of CTD profile data which were observed along section B at marks. Reference level set at 1300 m

e. Same as panel d with 1300 m Pegasus reference velocity added

f. Geostrophic analysis from horizontally interpolated fields of CTD temperature and salinity data, referenced to 1300 m and including the 1300 m interpolated Pegasus reference velocity.

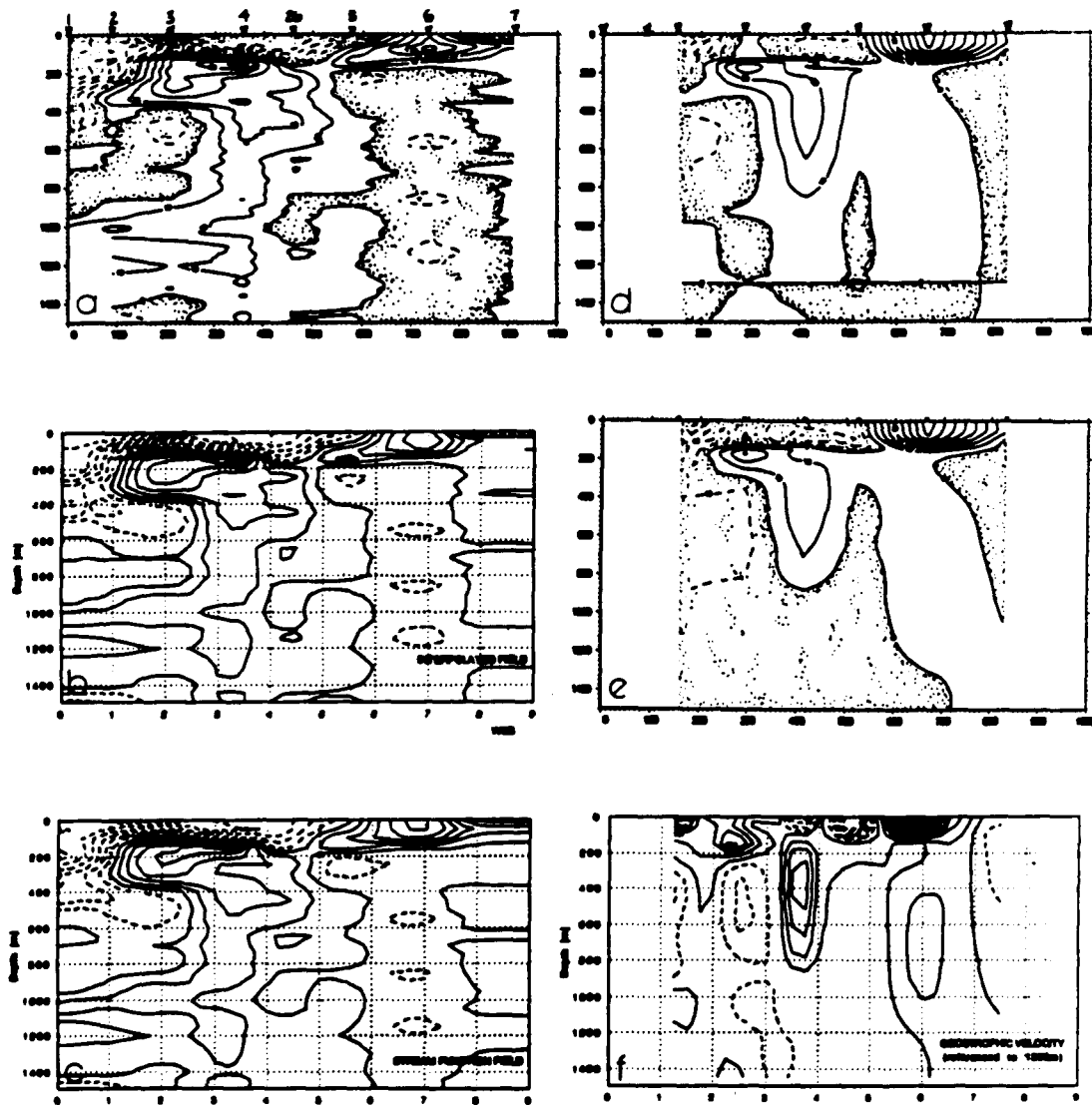


Figure E-3. Same as Figure E-1 for January 1991 (WESTRAX 3).

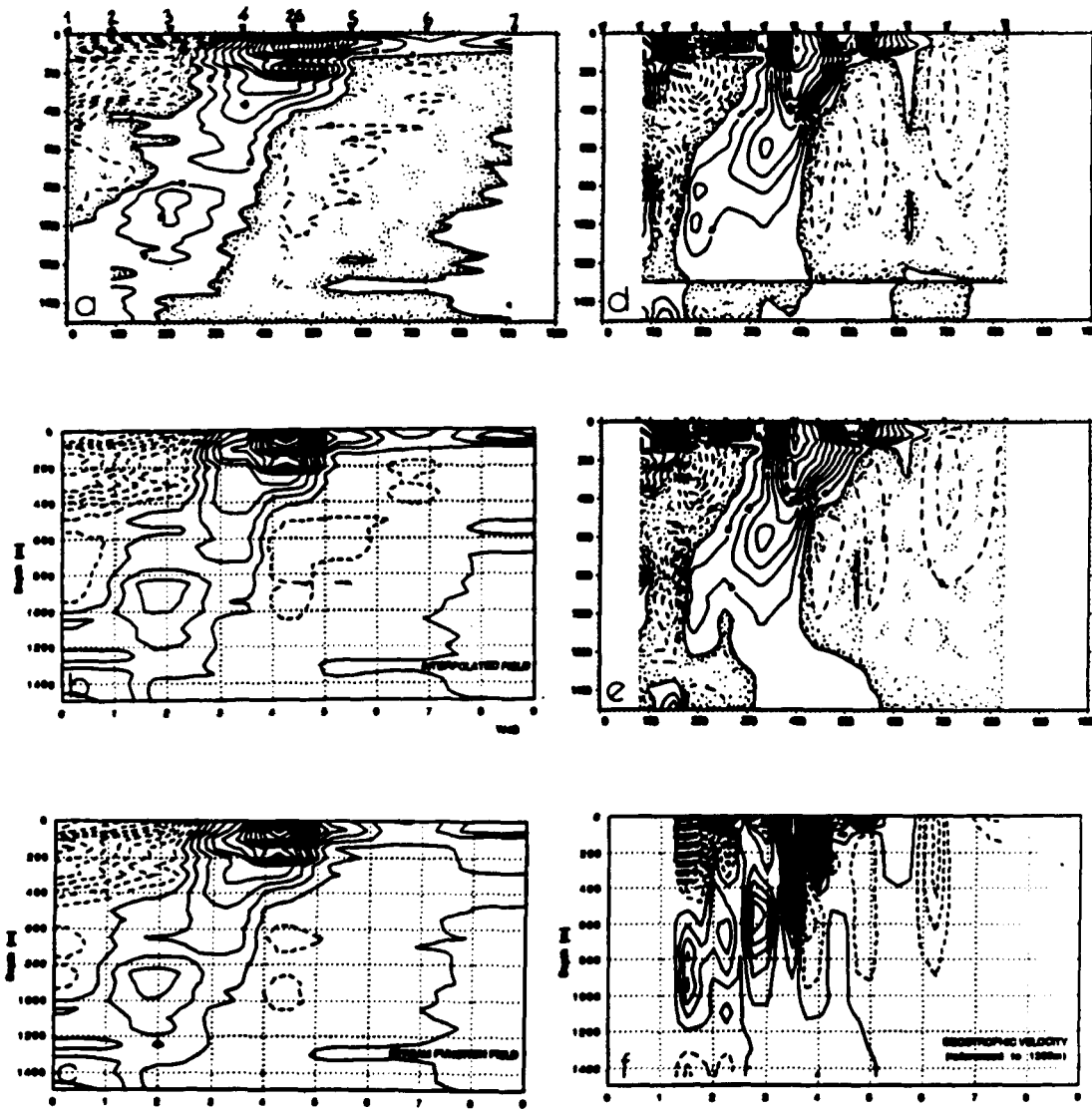


Figure E-4. Same as Figure E-1 for June 1991 (WESTRAX 4).

C, D, and E (not shown), where flow through the region is smoothed by the non-divergent analyses.

Many of the major features on the Pegasus analyses (panels b and c) are evident on the geostrophic velocity structures (panels d and e). The 1300 m reference level was selected to be at the lower boundary of the intermediate layer. Geostrophic flows were not plotted for areas south of 1.25°N (140 km) because of the very large velocity magnitudes and associated errors near the equator. Similarities between Pegasus and geostrophic analyses include the cores of the NECC and upper NEUC (as an example, the near-surface structures are noted on Figures E-1 or E-3). Beneath approximately 800 m, the resulting structural differences between these analysis methods become more apparent. This is mostly because velocities are weak (*i.e.*, 10 cm/s or less) and the estimate of observed velocity errors are relatively large (*i.e.*, greater than the systematic error of approximately 18%).

Panel f illustrates geostrophic velocities derived from temperature and salinity fields which were initially interpolated on the horizontally gridded surfaces. I had planned to use these fields to derive the zonal and meridional geostrophic velocity for transects throughout the region. While some of the major features are similar on panels e and f, the overall results are not as I had hoped. Within the surface layers on panel f, velocity structures seem to be more 'wavy' (see Figures E-1 through E-4). The sides of features seem to be very vertical (Figure E-4), even though the horizontal fields from which they were derived were interpolated independently. It appears that further smoothing would be necessary before these geostrophic fields can be useful. As this dissertation did not depend on geostrophic velocity structure, I pursued this investigation no further.

A qualitative comparison between the six techniques discussed is provided in an analyses of the transports through section B during the February 1990

Table E-1. Comparison between different velocity analysis techniques based on transports (Sverdrups, $10^6 \text{ m}^3/\text{s}$) across section B during February 1990.

Profile Station	1	2	3	4	5	6	7						
Profile Pair	--	1:2	--	2:3	--	3:4	--	4:5	--	5:7	--	6:7	(1:7)
CID #	19	20	21	22	23	24	25						
Peg #	N01	N02	N03	N04	N05	N06	N07						
Latitude (N)	0.13	0.87	1.95	3.28	5.25	6.68	8.28						
Nominal (N)	0.25	1.00	2.00	3.25	5.25	6.75	8.25						
								<u>Sum</u>					
<i>Surface layer (0-150 m)...</i>													
a. *	-8	-5	+2	+1	-1	+4	-7	-7					
b.	-6	-2	+1	0	-1	+4	-6	-4					
c.	-7	-3	+1	-1	-2	+3	-9	-9					
d.	+9	-21	+7	+3	+5	+10	+53	+53					
e.	+9	-20	+6	+1	+6	+11	+53	+53					
f.	+1	+3	-2	+5	-2	+8	+13	+13					
<i>Upper intermediate layer (150-750 m)...</i>													
a.	-13	-8	+11	+20	-4	-7	-1	-1					
b.	-12	-7	+9	+20	-4	-6	0	0					
c.	-10	-5	+12	+25	-1	-3	+18	+18					
d.	-4	-12	+4	+2	+4	+4	-2	-2					
e.	-6	-9	+1	-13	+7	+8	-12	-12					
f.	-18	-7	+14	-12	0	+9	-14	-14					
<i>Lower intermediate layer (750-1300 m)...</i>													
a.	-3	-7	-4	+11	+3	-6	-6	-6					
b.	-3	-6	-2	+10	+2	-6	-5	-5					
c.	-3	-5	-3	+11	+3	-5	-2	-2					
d.	-29	-8	+1	+1	+1	0	-34	-34					
e.	-30	-5	-2	-5	+4	+3	-35	-35					
f.	-18	-6	+4	-5	+1	+5	-19	-19					
* See Figure E-1 for definitions of entries 'a' through 'f.'													

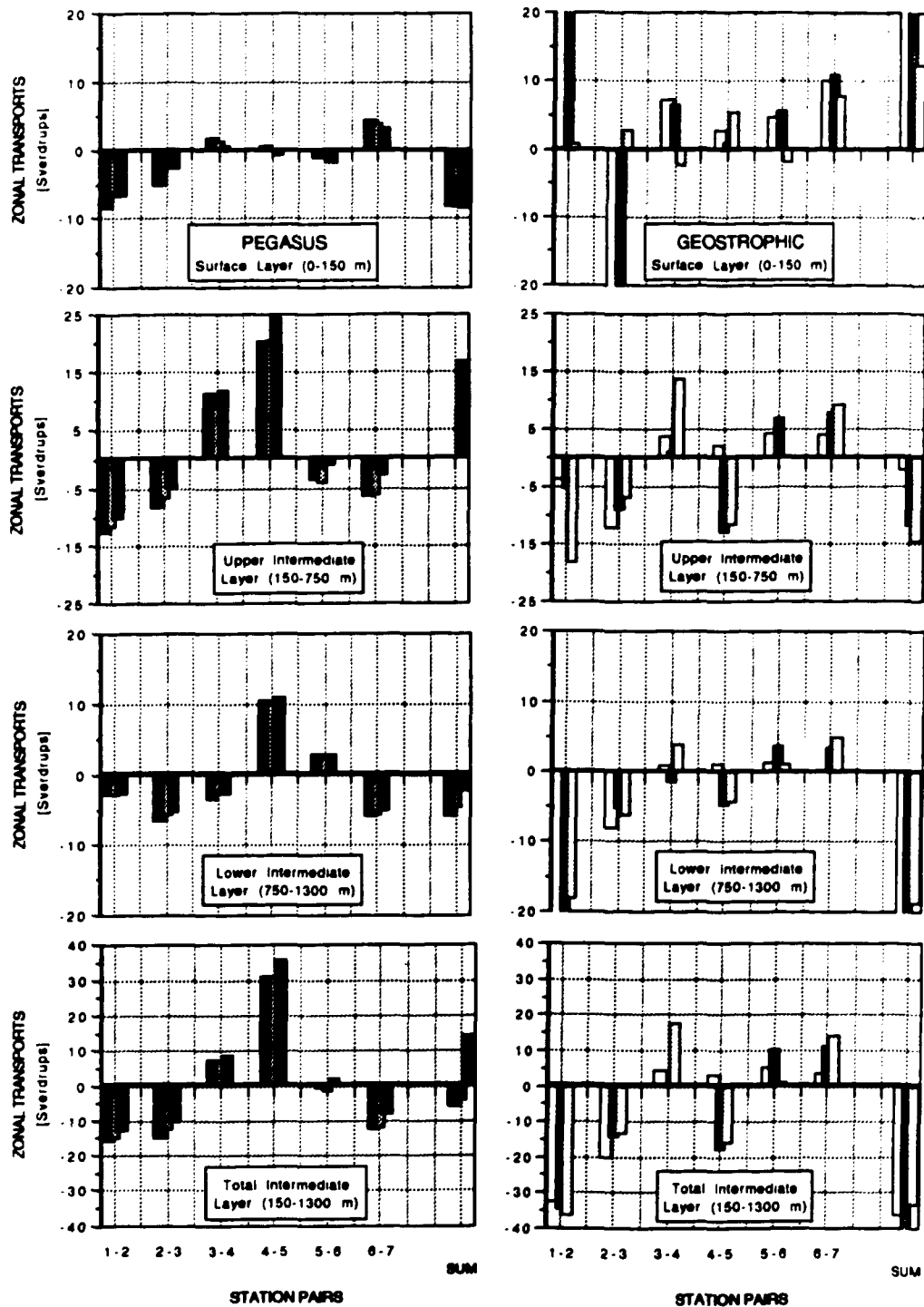


Figure E-5. A comparison of volume transports through section B during February 1990 (WESTRAX 1), as presented on Table E-1. Pegasus-derived transports ($10^6 \text{ m}^3/\text{s}$), which correspond to Figure E-1 panels a, b, and c, are plotted on the left panels. Geostrophic-derived transports, corresponding to panels d, e, and f, are plotted to the right.

survey (WESTRAX 1, Table E-1). Entries 'a' through 'f' on Table E-1 correspond to panels a through f on Figure E-1. On a series of bar graphs (Figure E-5), the disparities between Pegasus and geostrophic analyses within the surface layer are particularly evident. Within the intermediate layers, the flow directions determined by geostrophic analyses are often consistent with the Pegasus results (except for pair 4:5 at the core of the NEUC, Figure E-1), but the transports computed for individual station pairs (and the layer totals) are seldom comparable (*cf.* entries 'c' and 'e' on Table E-1).

Within the surface layer, Pegasus-derived transports using techniques 'a', 'b', or 'c' are similar. Entry 'c' indicates an overall adjustment of -5 Sv was applied to the divergent transports of 'b' to produce the non-divergent fields. Geostrophic analyses tell another story. In a region where we would expect to find the westward flowing NBC, the surface layer geostrophic transports for the first station pair (entries 'd' and 'e') are positive, or eastward, and velocity magnitudes are much higher than the corresponding Pegasus results. These inappropriate flows were evident near the equator during each of the WESTRAX geostrophic analysis (Figures E-1 to E-4), leading me to surmise that geostrophic velocities and transports within approximately two degrees of the equator should not be used. This would mean, for example, that if geostrophic velocity structure were my only source of information for the WESTRAX 1 survey, all information about the flow of the NBC into the region would have been lost.

In the upper intermediate layer, the stream function (non-divergent) analysis added 18 Sv to the interpolated (divergent) transports (compare entries 'b' and 'c' on Table E-1). This is evident as the unshaded NEUC appears to cover a larger area on panel c than on b on Figure E-1. In the lower intermediate layer, an additional 3 Sv was required to produce non-divergent flow. Within the lower layer, both the Pegasus ('c') and referenced geostrophic ('e') transports between the equator and 2°N were -15 Sv. This apparent agreement is deceptive, as the

total lower intermediate layer Pegasus transport (-8 Sv for entry 'c') is much different from the total geostrophic transport (-35 Sv for entry 'e').

The differences between Pegasus and geostrophic transports presented in Table E-1 are large. A comprehensive comparison between WESTRAX region velocity structures derived from Pegasus (and/or ADCP) and hydrographic data would provide an interesting assessment of analyses uncertainties and the ageostrophy of the region. This is beyond the scope of this work (although both W. Brown and I. DaSilveira are addressing this in additional work). The objective analysis technique (as opposed to the Akima (1978) interpolation algorithm) provides both the proper uncertainty information and a method to smooth the hydrographic features, making such comparisons meaningful.

APPENDIX F.
VELOCITY STRUCTURE

The current structures of the WESTRAX region during late summer, winter, and early summer are detailed (see section IV). Transports through the region's boundaries are summarized and averaged on Table F-1.

The late summer 1990 velocity structure...

During September 1990 (WESTRAX 2), flow at all levels within the region is dominated by an alongshore ridge which is formed by the well-defined *Hae* and *Hde* anticyclonic centers (Figures F-1 through F-3). Most of the inflowing southern water (SEC) continues northwestward between the alongshore ridge and the continental slope, turning offshore within the retroflexion around *Hde*. Retroflexion around *Hae* is weak. Very little southern water exits the region across 53°W, as it mostly retroflects around *Hde* and flows southeastward, feeding into the eastward flowing NEUC. The NEUC is augmented during the summer by northern water which has entered the region by: (a) flowing southeastward through the northern border, or (b) first entering the region flowing westward across 44°W and turning cyclonically around *Le*. Thus, the NEUC is carrying a mixture of water from both hemispheres eastward toward the interior equatorial Atlantic Ocean by late summer. Some of the northern water which enters through the northern border turns anticyclonically around *Hde* and flows northwestward, blending with the alongshore flow of southern water as part of the circulation around *Hde*.

During September 1990, a number of major features extend vertically throughout the upper kilometer of the WESTRAX region (Figures F-2 and F-3). A

vertical consistency is evident in the similarity between flow patterns of the surface, upper, and lower intermediate layers (Figure F-1). The surface core of a strong northwestward NBC flows above the continental break through sections B, C, and D. The NBC retroflects around *Hde* before it reaches section E. The upper and mid layer flows of intermediate southern water follow a similar path into the retroflection around *Hde*. A core of concentrated westward flow through section B near the equator and a depth of 700 m is associated with the influx of Antarctic Intermediate Water (AAIW). The eastward return current, which feeds into the NECC/NEUC in the surface/intermediate layers, is seen flowing through sections B, C, and D. *Hde* extends throughout the upper 1500 m, with strong opposing currents on either side of a nearly vertical axis across sections C and D (Figures F-2 and F-3). There is evidence of cyclonic flow through the western boundary and across section E.

The winter 1991 velocity structure...

By the following winter (January 1991, WESTRAX 3), the structures of the principal anticyclones are less vertically organized than they were during the previous summer (Figures F-4 through F-6). This is particularly evident in the distinct differences between surface and intermediate layer structures (Figure F-4). In the surface layer, a very large, well-developed *Hae* lies in the alongshore ridge which crosses the center of the region. Below 150 m, the locations and intensity of features are completely different (*cf.* surface and intermediate vertical structures on sections B, C, and D on Figure F-5). In the surface layer, a strong NBC flows along the continental break and continues westward into the GC. Within the upper intermediate layer, a similar alongshore flow of southern water crosses the southeast corner (at a core depth of approximately 600 m) and retroflects before it reaches the *Lfg -Le* central trough which divides intermediate layer flow into southeastern and northwestern regimes (Figure F-

4). To the north of the central trough, northern water crosses 9 N, turns anticyclonically around a ridge, and flows as a strong westward current across 53 W. A portion of the inflowing northern water continues southeastward and flows toward the NEUC. Cyclonic circulation around *Lfg* also directs some northern water toward the eastward flowing NEUC within a southeastward coastal undercurrent (as discussed by Schott and Böning 1991). The prominent ridge across the northwestern corner may be a remnant of the translating retroflection eddy which was identified as *Hde* during the previous fall. If so, this eddy would have separated from the retroflection around *Hae* and then translated northwestward, as discussed by Johns *et al.* (1990) and Richardson *et al.* (1993).

When compared with the previous summer, there is less vertical consistency in the structure of some features during January 1991. For example, the retroflection around *Hae* now occurs in two layers, separated by a vertical shear zone at approximately 400 m (section B, Figure F-5). A small isolated area of anticyclonic circulation evident on section B between 800-1000 and 4-6 N is unique. The circulation of the upper and lower intermediate layers are very different. In the latter, *Lfg* is absent and retroflection around *Hae* is essentially non-existent (Figure F-4). On the other hand, there are some vertical consistencies during January 1991. For example, the cyclone *Le* penetrates vertically throughout the mid and lower intermediate layers (section B, Figure F-5). At section D, the axes of the anticyclonic circulation around the northwestern ridge, and the cyclonic circulation around *Lfg*, are also both nearly vertical through the upper and lower intermediate layer.

The winter 1990 velocity structure...

The flow patterns of the two winter surveys are quite similar. For example, the NBC during February 1990 (WESTRAX 1) flows northwestward through the

region and into the GC, as it does during 1991 (Figures F-7 through F-9). Surface and intermediate layer circulations are distinctly different during both winter surveys (Figure F-7). The central *Lfg-Le* trough again splits the region within the intermediate layer. The strong retroflexion of southern water around *Hae* and into the NEUC is evident during 1990. Most of the February 1990 NEUC appears to come from the south. Some northern water flows cyclonically around *Lfg* and continues eastward as a coastal undercurrent. *Hae* is separated into upper and lower cells, with a vertical shear zone near 1000 m (sections B and C, Figure F-8).

The 1991 transition period velocity structure...

The velocity structure of the WESTRAX region during the early summer (June 1991, WESTRAX 4) displays a mixture of winter and summer features, indicating that this survey was made during a seasonal transition period (Figures F-10 through F-12). The surface and intermediate patterns are distinctly different, a signature of the winter surveys. The anticyclone in the north-central part of the intermediate layer may be a separated retroflexion eddy, or it may have entered the region from the north as a cell within the NEC. Water mass analyses will help clarify this dilemma.

In the surface and upper intermediate layers, the northwestward flow of southern water associated with the NBC/SEC is evident through the region. Northern water flows anticyclonically through the central high or cyclonically around *Le*, and into the NEUC. As during each of the previous surveys, *Le* is well developed within the intermediate layer (Figure F-10 and section B, Figure F-11). A trough extends southwestward from *Le* to the continental slope, confining retroflexion to a small portion of the southeastern corner (Figure F-10).

Upper, mid (AAIW), and lower intermediate layer transports based on non-divergent Pegasus velocity fields through the region's boundaries during each of the WESTRAX surveys are summarized (Figures F-13 and F-14).

Table F-1. Transports in Sv (1 x 10⁶ m³/s) along pathways described in section IV.

WATER MASSES =>	1	2	3	4	5	6	7	8	SOUTHERN SUM	NORTHERN SUM	TOTAL FLOW	Via Internal Pathways	
	SACW	AAIW	AACP	MIX1	MIX2	MIXL	NACW	NAEL					
	<-----SOUTHERN----->						<-----NORTHERN----->						
WESTRAX 1 - FEBRUARY 1990													
in A.	18	7	9	7		1			40	0	40	40	A->B
out B.	-10	-6	-8	-18	-3	-6	-1	-2	-51	-3	-54	0	A->D
in C.				4	3	3	47	13	10	60	70	14	C->B
out D.	-11	-1	-2	-10	-14	-8	-8	-2	-46	-10	-56	56	C->D
sum	-5	0	-1	-17	-14	-10	38	9					
							Net change (mixing) =>		47	-47	0		
WESTRAX 2 - SEPTEMBER 1990													
in A.	7	4	1	14					26	0	26	7	A->B
out B.	-2	-5	-5	-14	-13	-7	-1	-1	-46	-2	-48	19	A->D
in C.				3	22	8	15	14	33	29	62	41	C->B
out D.				-19	-10		-4	-7	-29	-11	-40	21	C->D
sum	5	-1	-4	-16	-1	1	10	8					
							Net change (mixing) =>		16	-16	0		
WESTRAX 3 - JANUARY 1991													
in A.	14	2		7					23	0	23	23	A->B
out B.	-11	-6	-13	-21	-2	-4			-57	0	-57	0	A->D
in C.					10	6	28	16	16	44	60	34	C->B
out D.	-2			-10	-9	-2	-1	-2	-23	-3	-26	26	C->D
sum	1	-4	-13	-24	-1	0	27	14					
							Net change (mixing) =>		41	-41	0		
WESTRAX 4 - JUNE 1991													
in A.	21	3		5					29	0	29	24	A->B
out B.	-10	-4	-6	-16	-4	-5	-1		-45	-1	-46	5	A->D
in C.			5		18	6	12	14	29	26	55	22	C->B
out D.				-1	-9	-5	-16	-7	-15	-23	-38	33	C->D
sum	11	-1	-1	-12	5	-4	-5	7					
							Net change (mixing) =>		2	-2	0		
WEIGHTED 4-SURVEY AVERAGES:													
in A.	14	4	2	9	0	0	0	0	29	0	29	21	A->B
out B.	-8	-5	-7	-17	-7	-6	-1	-1	-48	-2	-50	8	A->D
in C.	0	0	2	2	16	6	22	14	25	36	61	29	C->B
out D.	-2	-0	-0	-10	-10	-3	-8	-5	-26	-14	-40	32	C->D
sum	5	-1	-4	-16	-1	-3	13	8					
							Net change (mixing) =>		21	-21	-0		

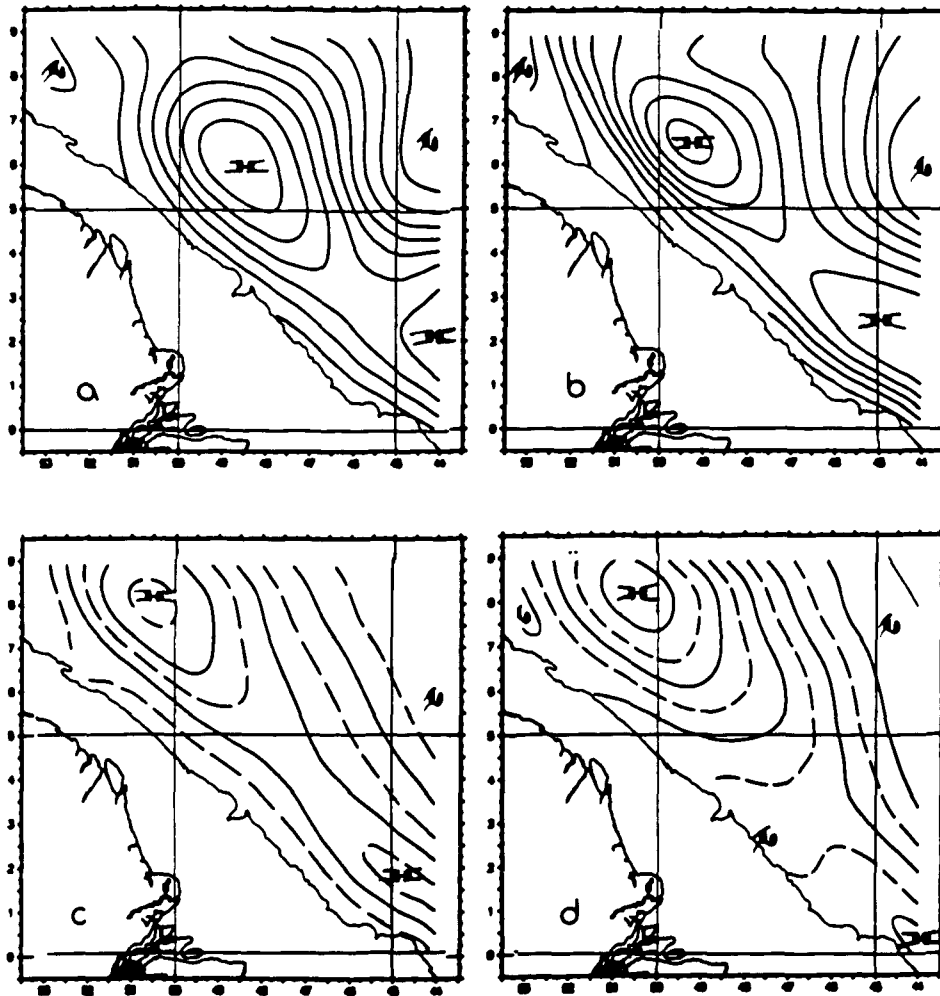


Figure F-1A. Depth-averaged Pegasus transport streamline structure during late summer (September 1990, WESTRAX 2). Panels: (a) Surface layer (0-150 m), (b) Upper intermediate layer (150-750 m), (c) Middle intermediate layer (Antarctic Intermediate Water, 650-850 m), and (d) Lower intermediate layer (750-1300 m). Each solid streamline represents a volume transport of approximately 5×10^6 m³/s (5 Sverdrups)

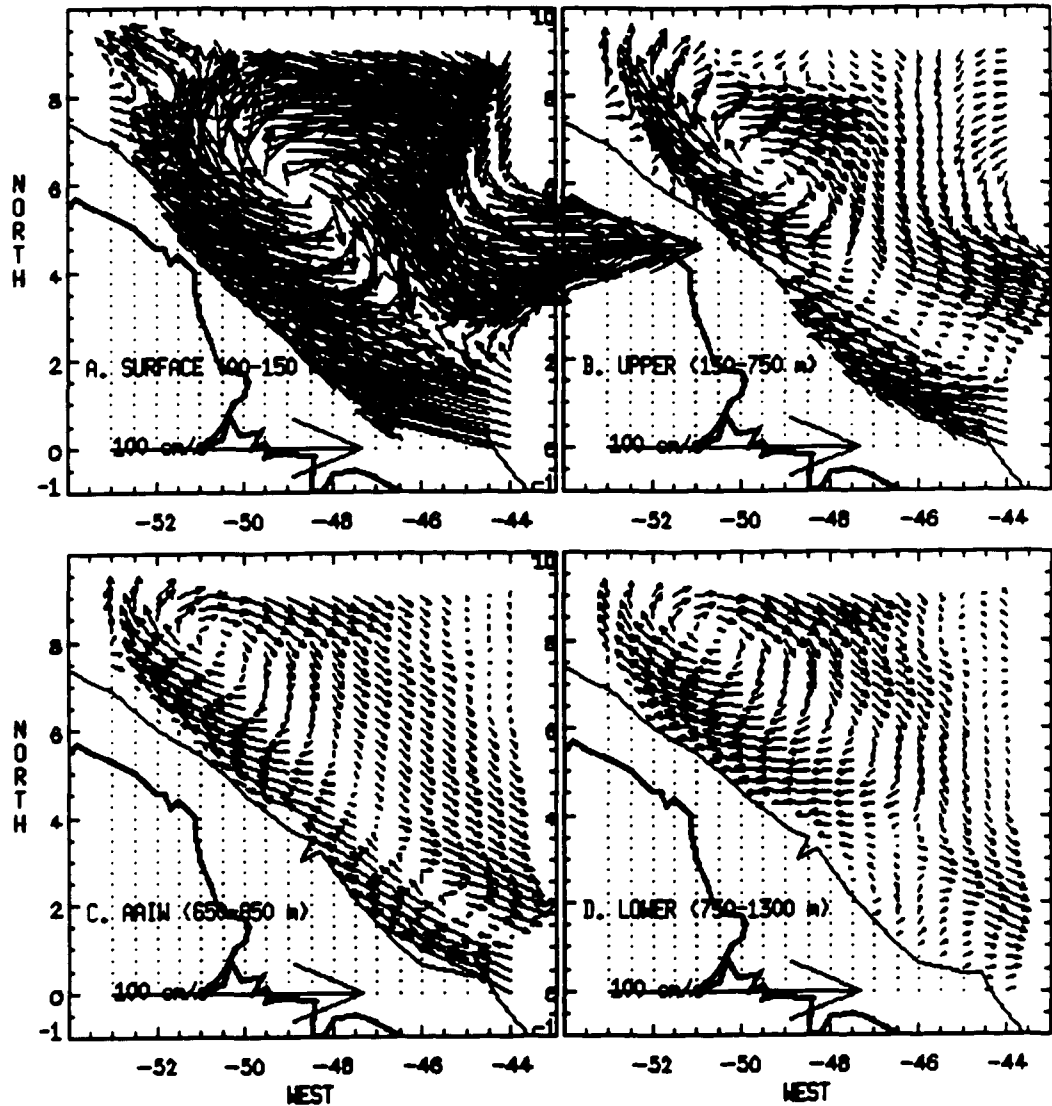


Figure F-1B. Depth-averaged, non-divergent Pegasus velocity vector fields during late summer (September 1990, WESTRAX 2). Panels: (a) Surface layer (0-150 m), (b) Upper intermediate layer (150-750 m), (c) Middle intermediate layer (Antarctic Intermediate Water, 650-850 m), and (d) Lower intermediate layer (750-1300 m). An 100 cm/s reference vector is in the lower left.

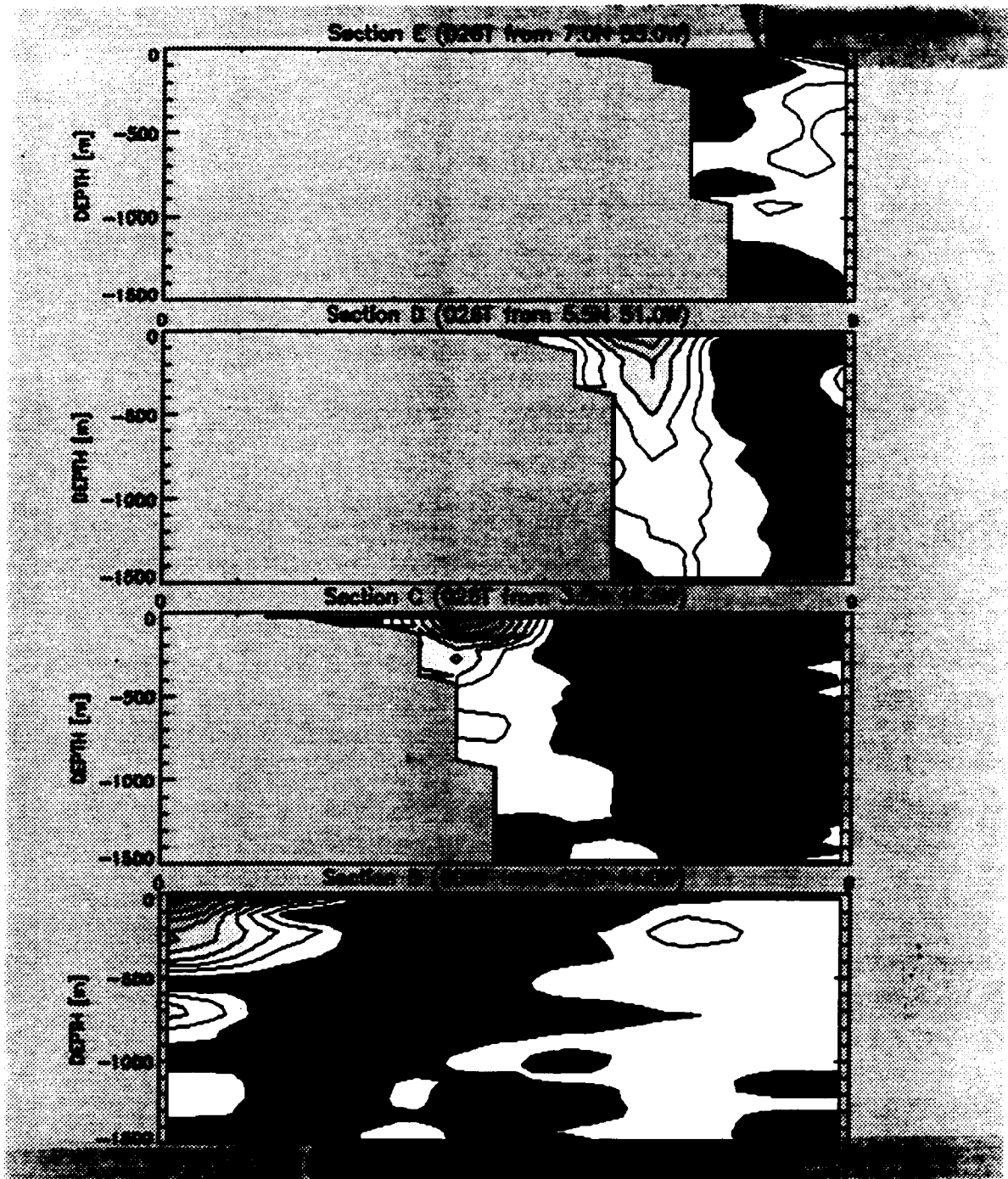


Figure F-2. Vertical alongshore non-divergent Pegasus velocity structures normal to Sections B, C, D, and E during late summer (September 1990, WESTRAX 2). Transects extend from the equator to 9°N. Contoured shades of dark gray to light indicate progressively higher positive east or southeastward flow at 10 cm/s intervals. Shades of white to light gray indicating progressively higher negative west or northwestward flow.

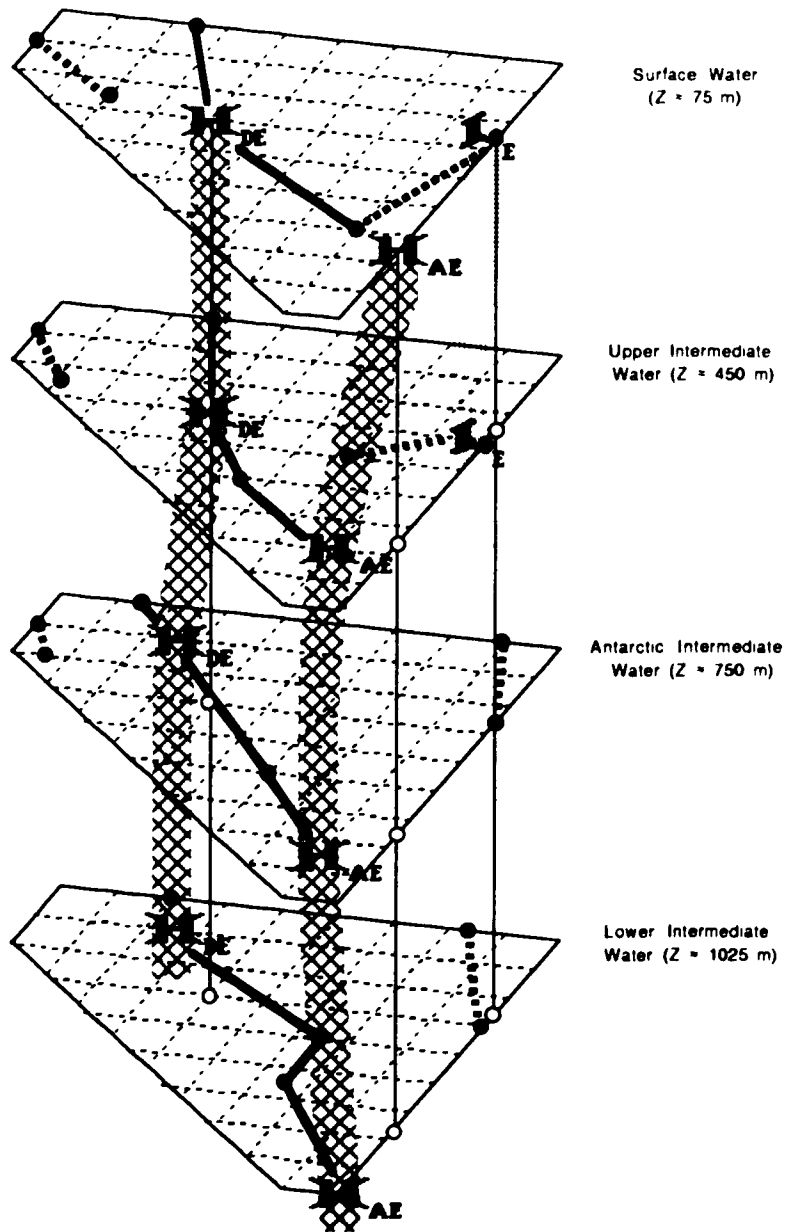


Figure F-3. Major circulation features that penetrate the surface, upper, mid, and lower intermediate layers of the WESTRAX region during the late summer (September 1990, WESTRAX 2) are schematically shown in terms of depth averaged stream function analyses of Pegasus data. The structure of the high and low centers are indicated by hatched and gray columns respectively. The thin vertical lines are provided for reference.

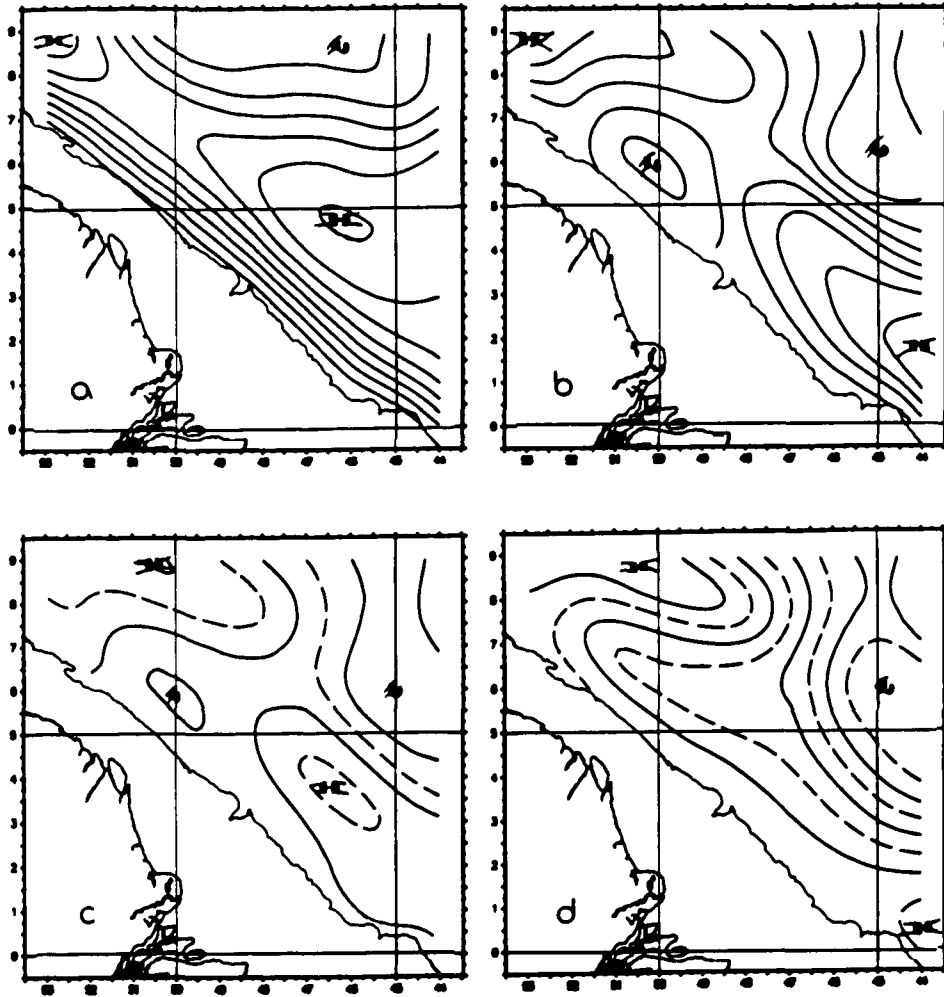


Figure F-4A. Same as Figure F-1A for winter (January 1991, WESTRAX 3).

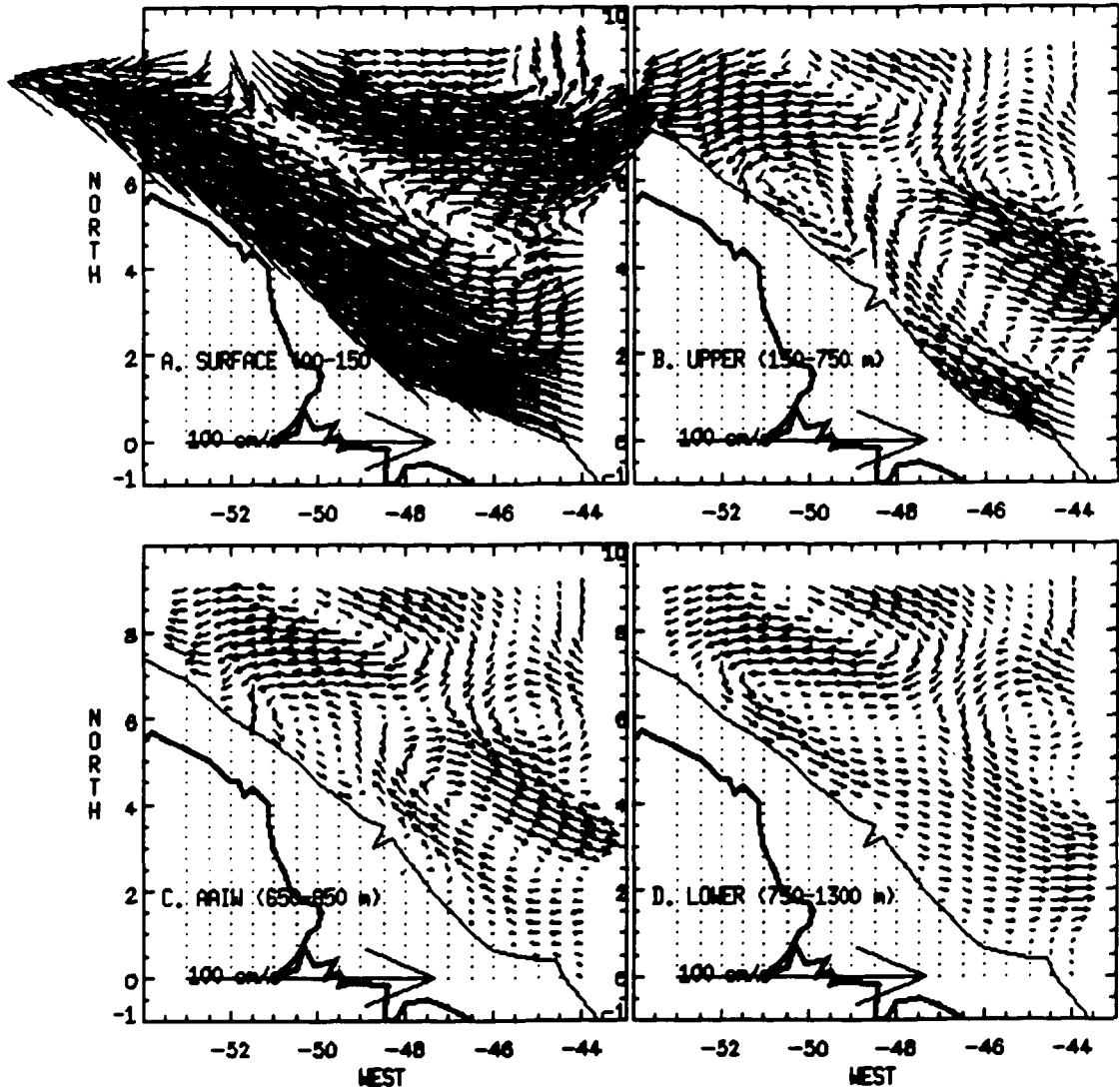


Figure F-4B. Same as Figure F-1B for winter (January 1991, WESTRAX 3).

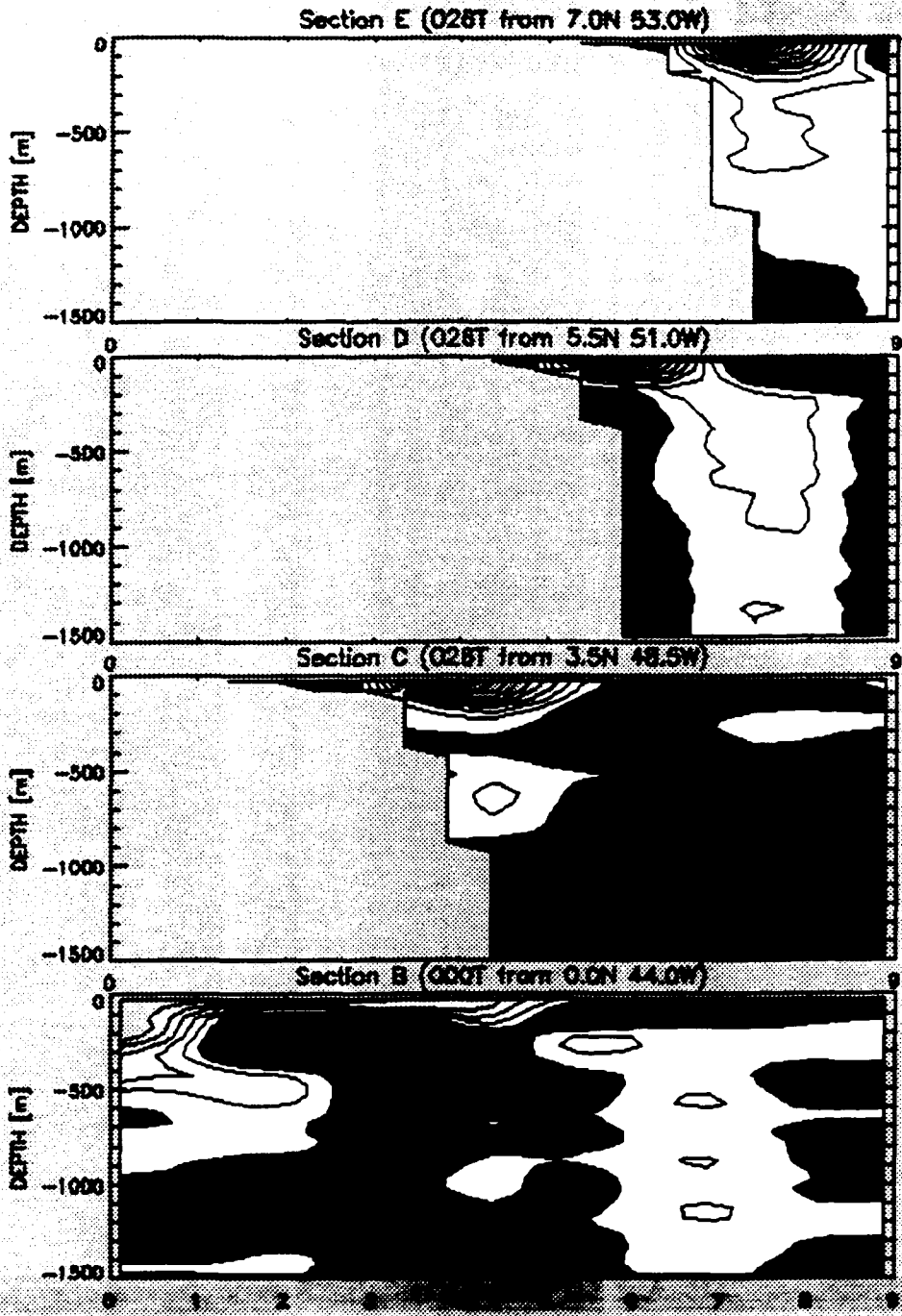


Figure F-5. Same as Figure F-2 for winter (January 1991, WESTRAX 3).

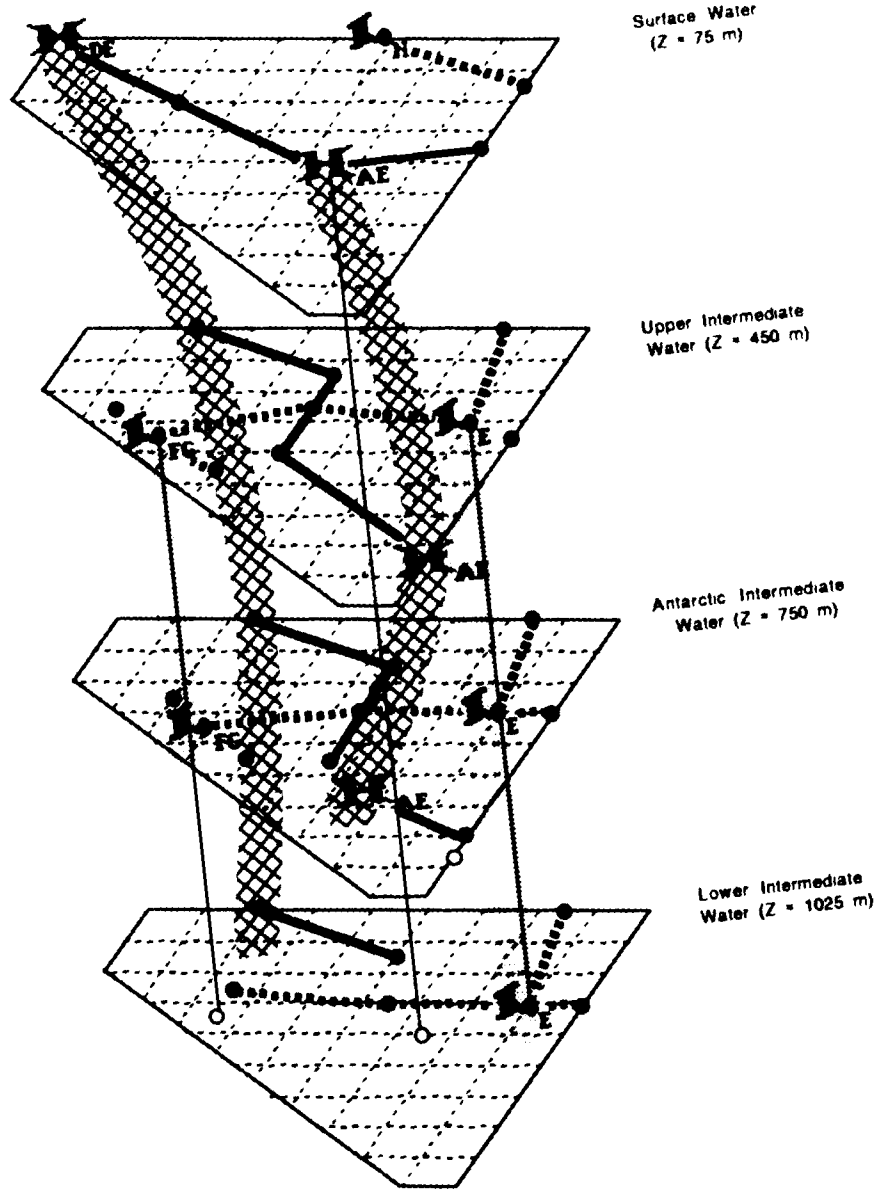


Figure F-6. Same as Figure F-3 for winter (January 1991, WESTRAX 3).

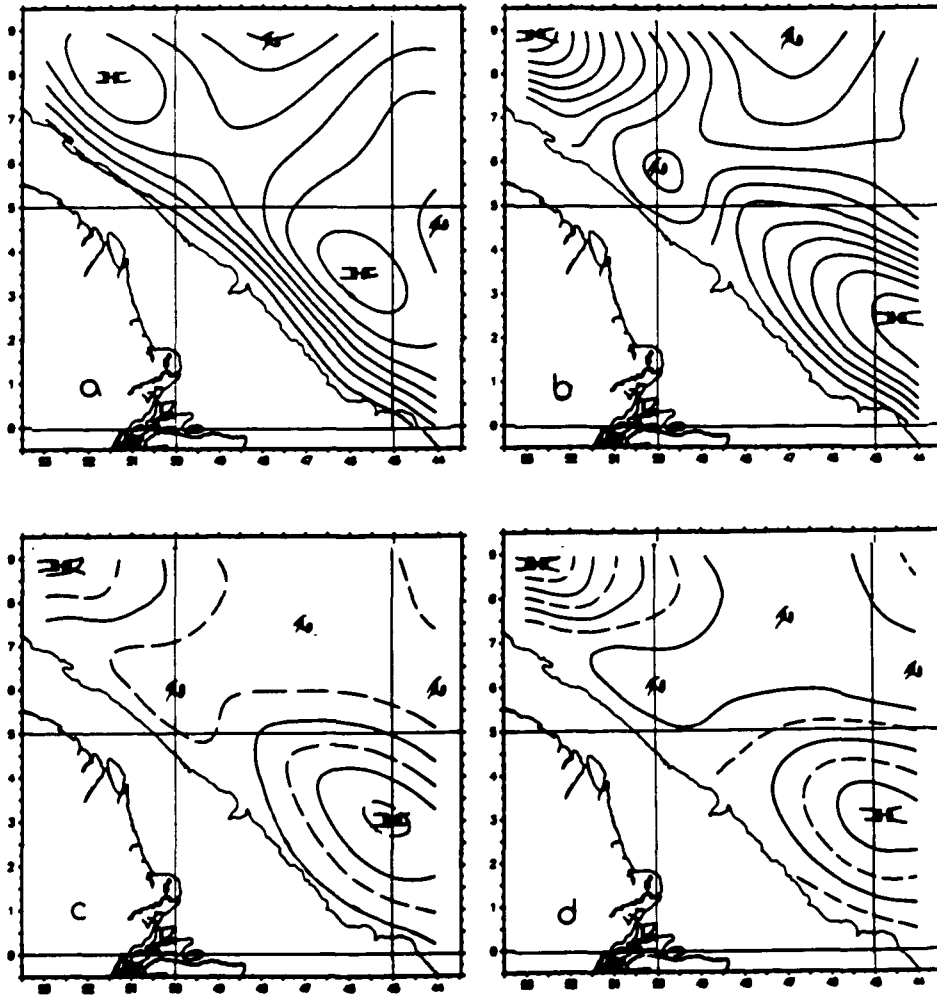


Figure F-7A. Same as Figure F-1A for winter (February 1990, WESTRAX 1).

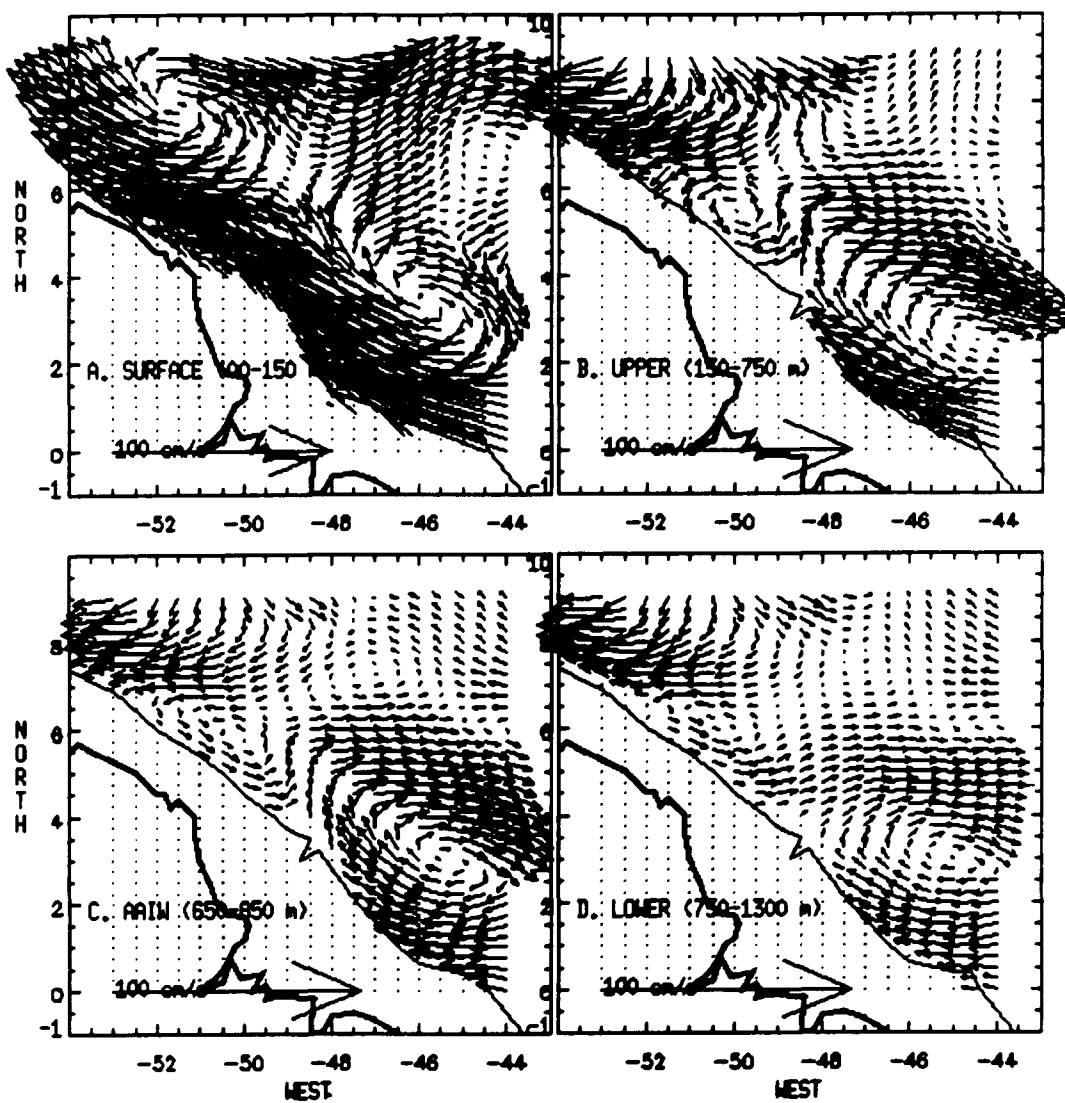


Figure F-7B. Same as Figure F-1B for winter (February 1990, WESTRAX 1).

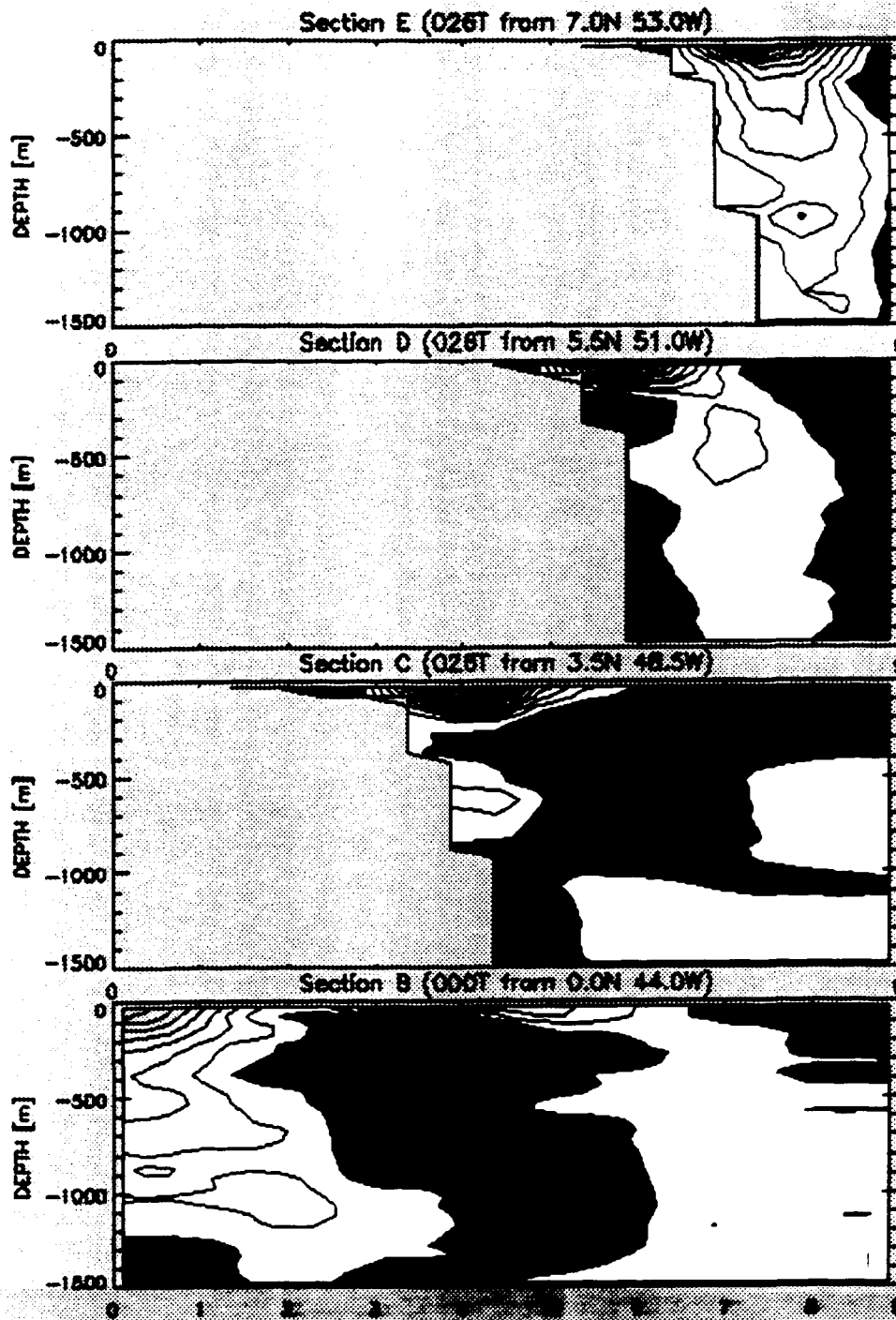


Figure F-8. Same as Figure F-2 for winter (February 1990, WESTRAX 1).

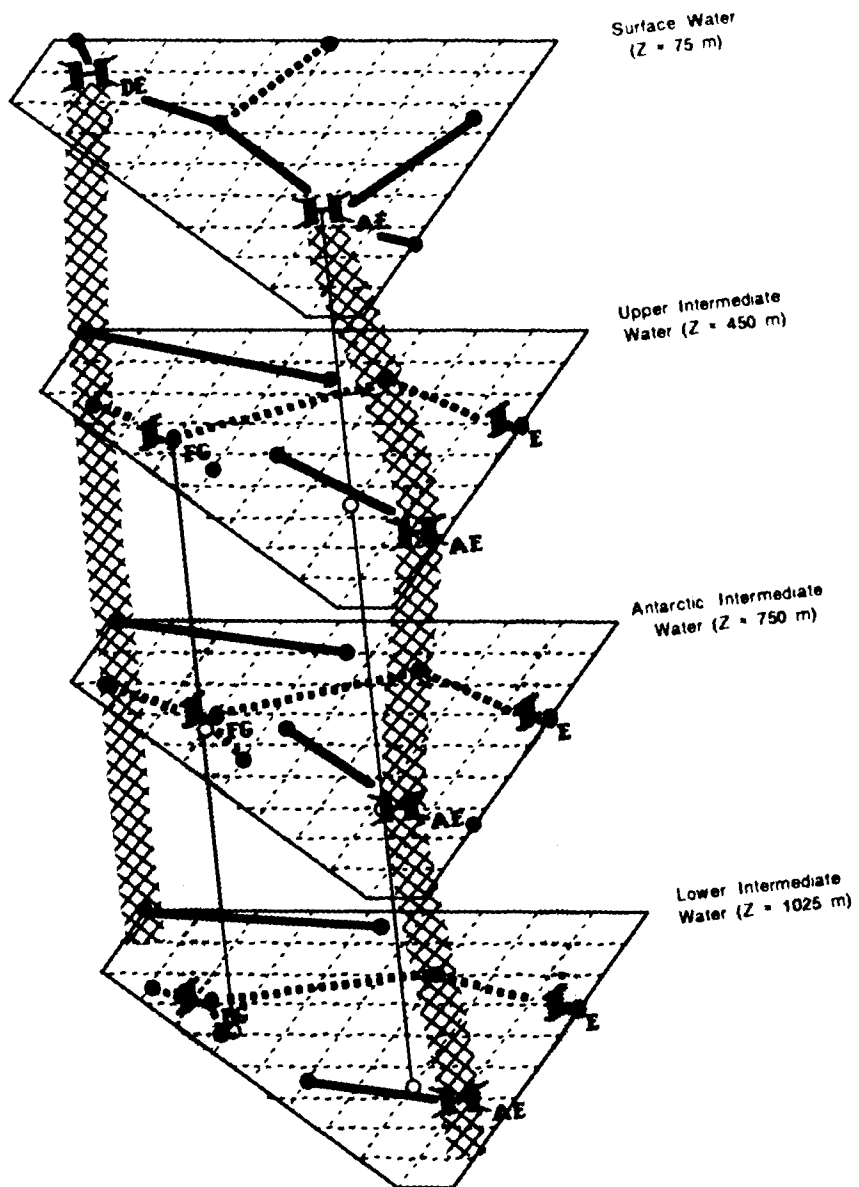


Figure F-9. Same as Figure F-3 for winter (February 1990, WESTRAX 1).

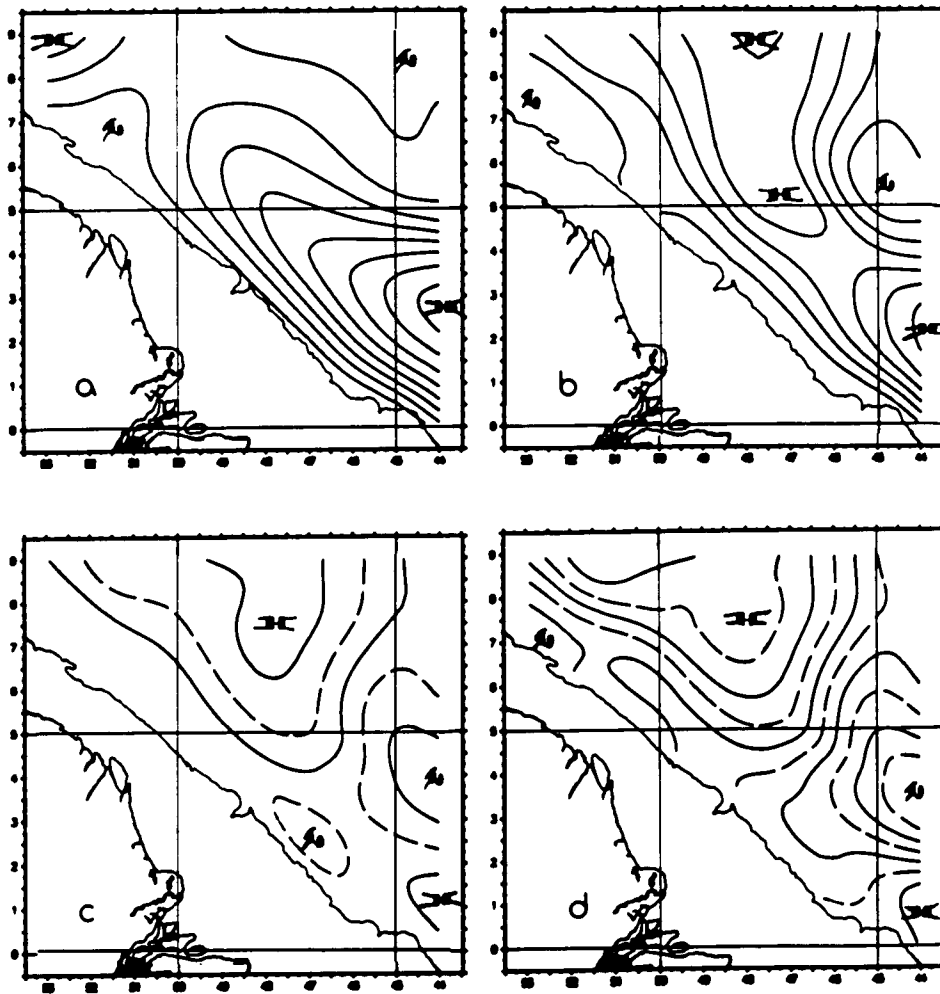


Figure F-10A. Same as Figure F-1A for early summer (June 1991, WESTRAX 4).

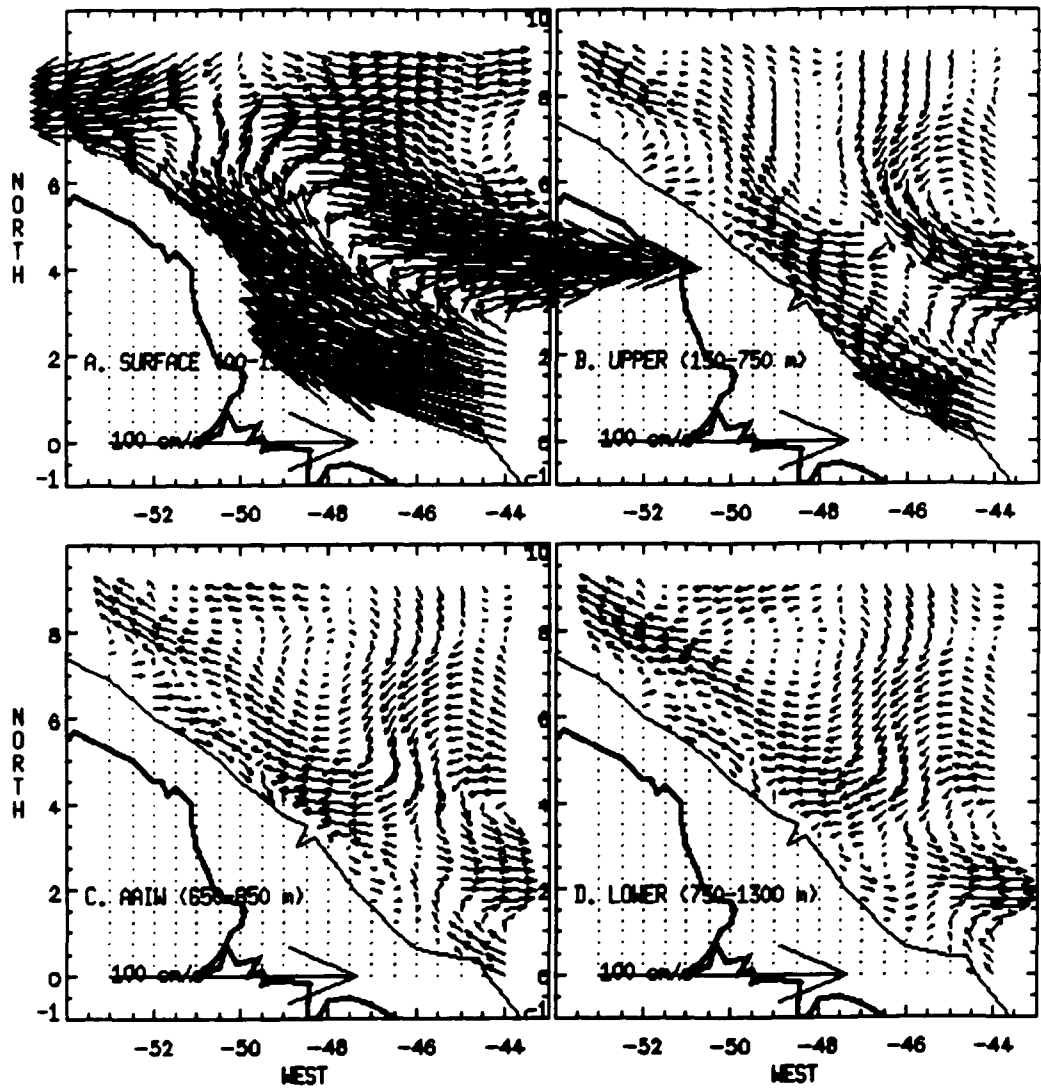


Figure F-10B. Same as Figure F-1B for early summer (June 1991, WESTRAX 4).

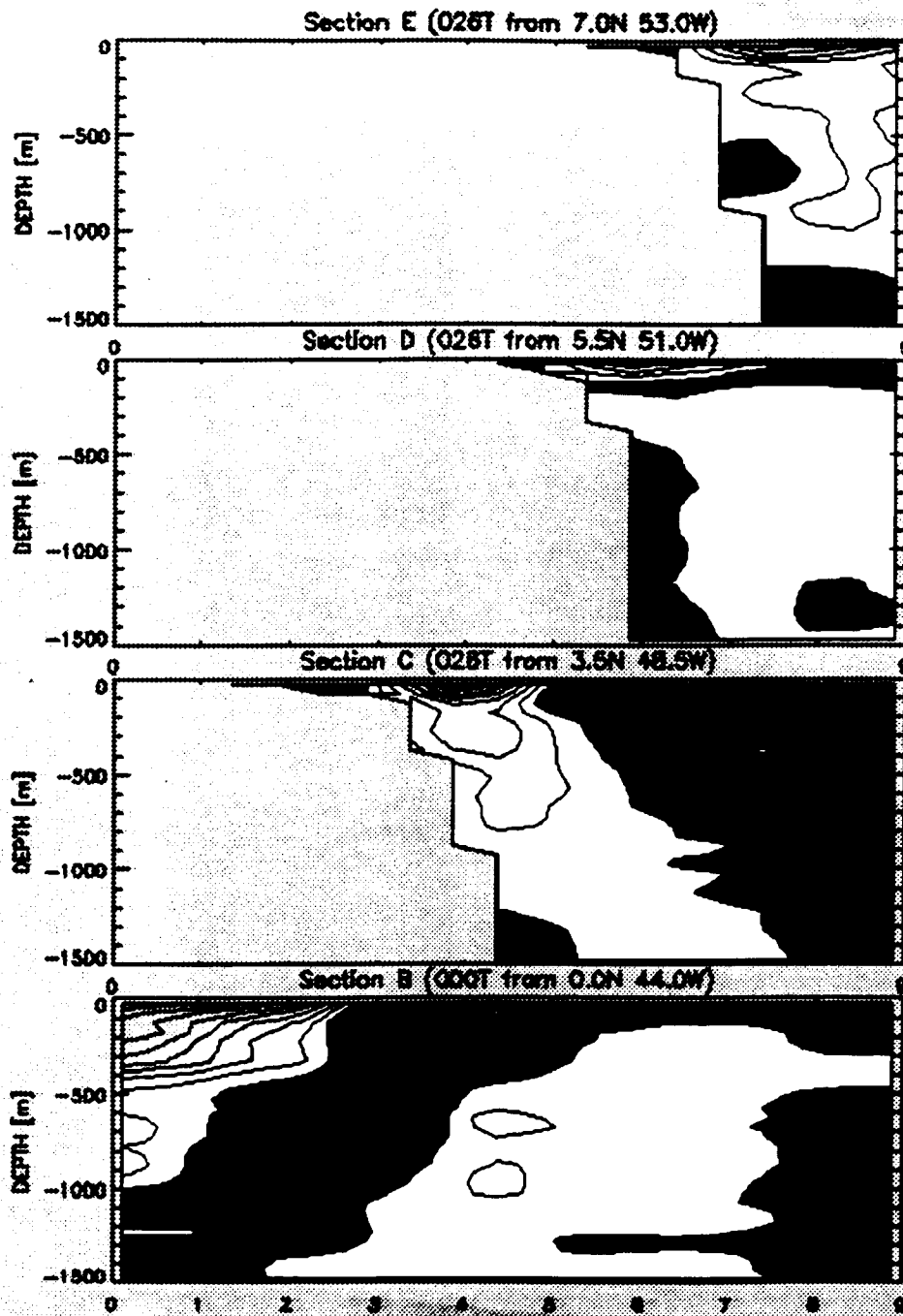


Figure F-11. Same as Figure F-2 for early summer (June 1991, WESTRAX 4).

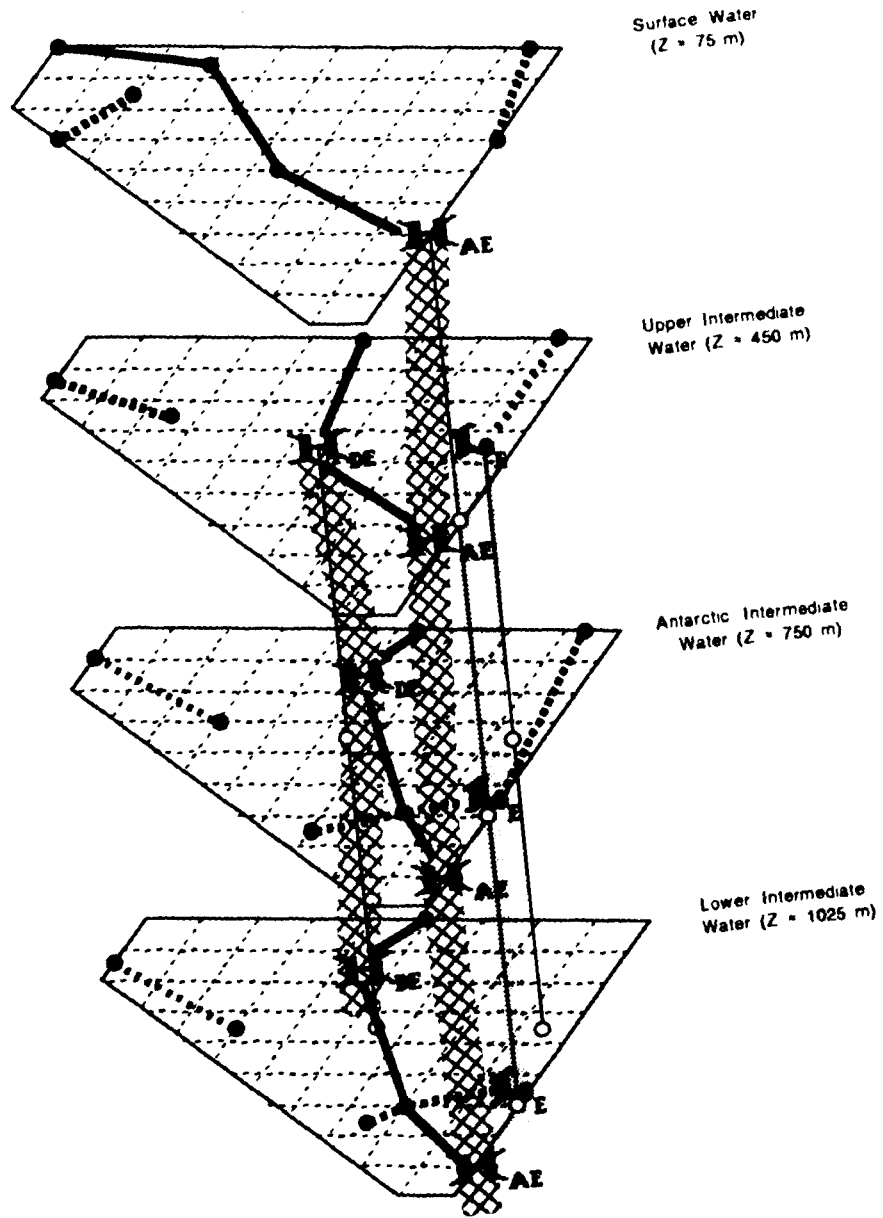


Figure F-12. Same as Figure F-3 for early summer (June 1991, WESTRAX 4).

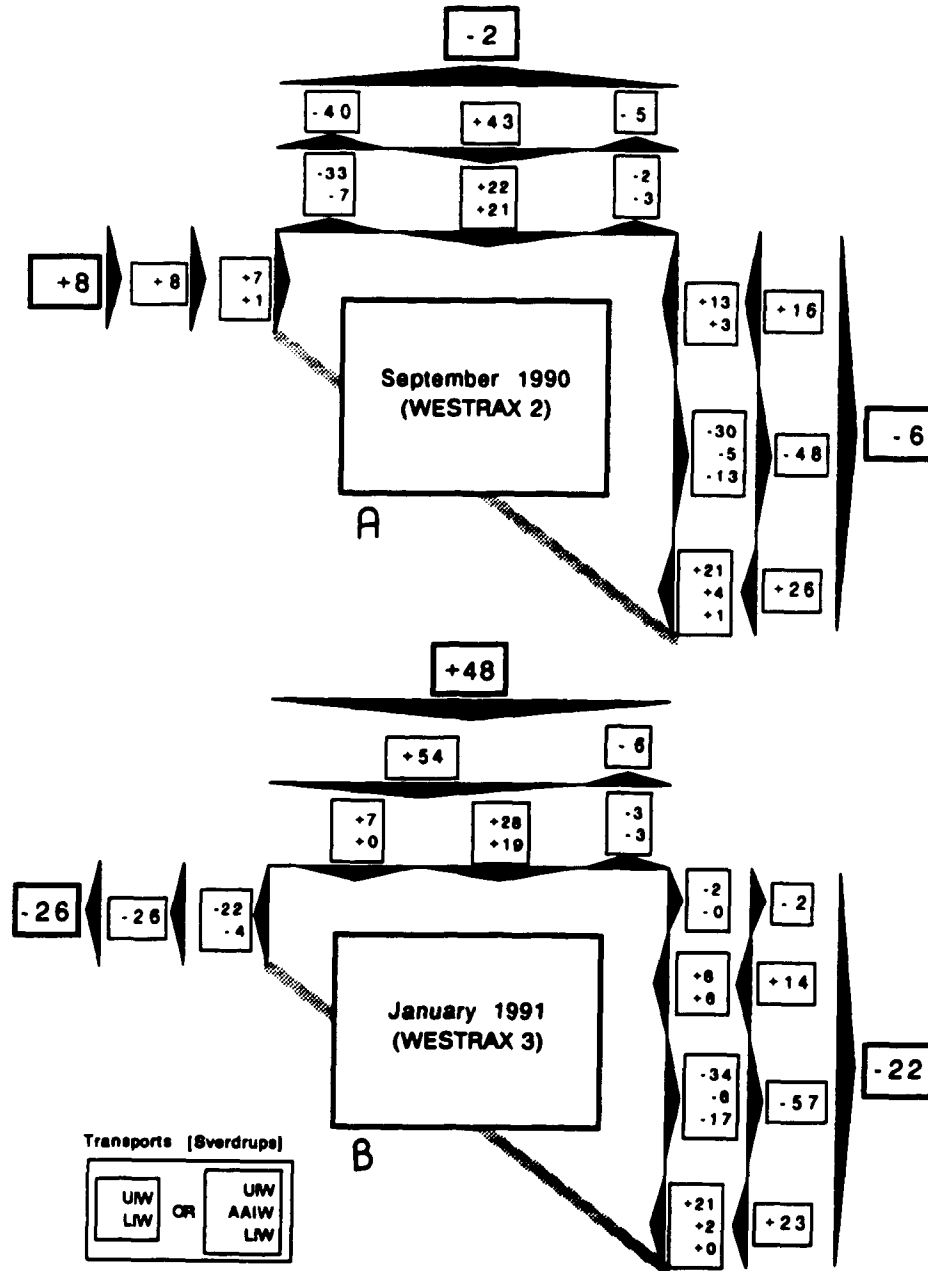


Figure 13A/B. Horizontal, non-divergent Pegasus volume transports through the intermediate layer boundaries of the WESTRAX region. Positive transports in Sverdrups ($1 \text{ Sv} = 10^6 \text{ m}^3/\text{s}$) flow into the region. Transports in the upper, AAIW (as applicable), and lower intermediate water layers are partitioned on the inner bracket. Their sums on the middle bracket depict the major currents. (continued)

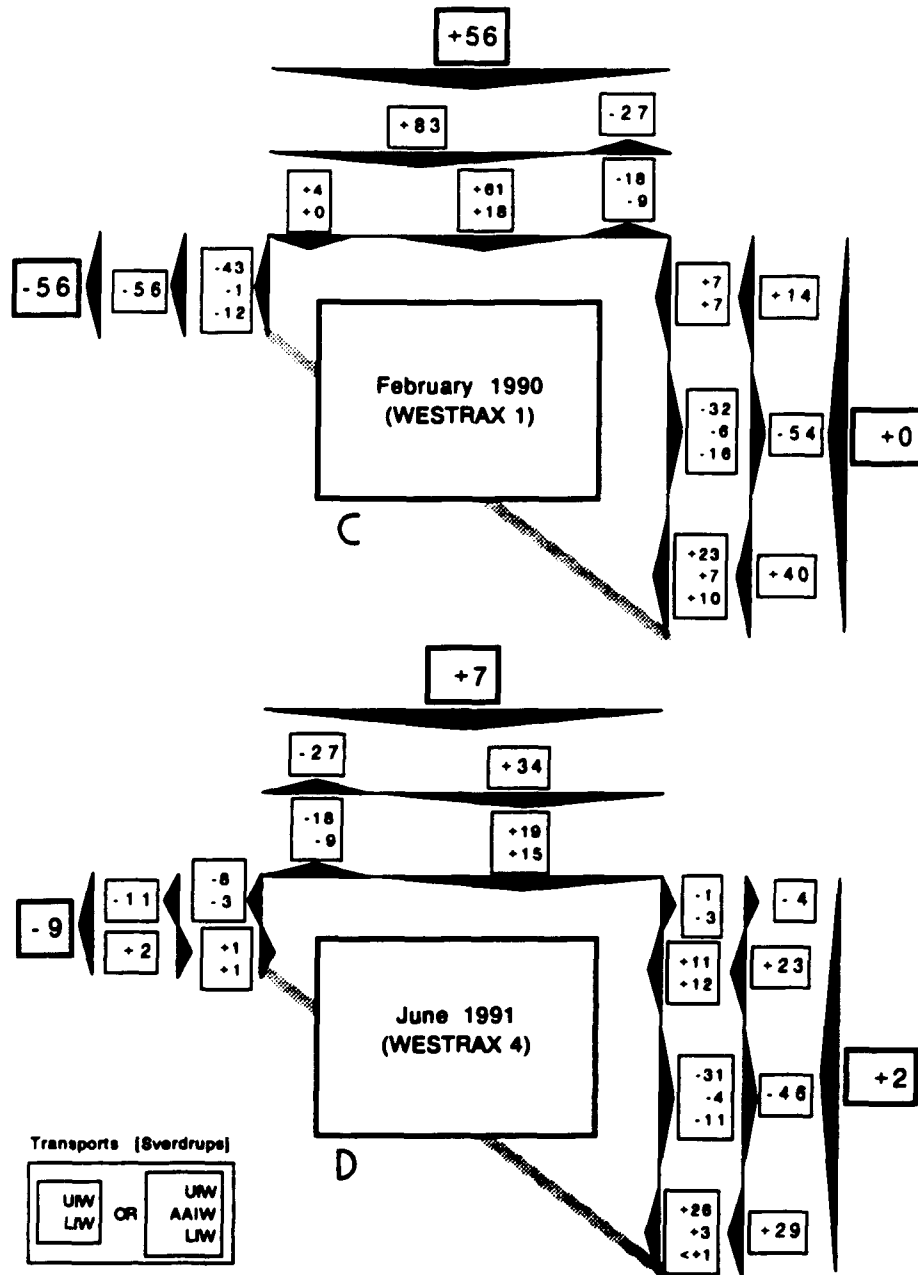


Figure F-13C/D. (continued from Figure 36A/B) Outer brackets show net transports across the region's boundaries.
 (A) Late summer (September 1990, WESTRAX 2)
 (B) Winter (January 1991, WESTRAX 3).
 (C) Winter (February 1990, WESTRAX 1)
 (D) Early summer (June 1991, WESTRAX 4).

APPENDIX G.
HYDROGRAPHIC STRUCTURE

The density, temperature, and salinity structures of the region are described.

Overview...

The hydrographic structure of the region is presented by making a few general observations rather than cataloging the features of each WESTRAX survey. For the most part, cruise-to-cruise temperature and salinity changes are small and difficult to describe meaningfully. The differences that occur become significant when the hydrographic data are applied in the water mass classification scheme presented in section V.

A number of figures, arranged in this appendix by WESTRAX survey, are included. The hydrographic analyses across Section B (44°W) (Figures G-1A, G-4A, G-7A, and G-10A for WESTRAX 2, 3, 1, and 4 respectively) provide insight into: (a) the entry of southern water (the SEC) into the region from the southeast, (b) the Amazon Eddy (*Hae*), (c) the eastern low (*Le*), (d) eastward flow into the NEUC, and (e) the entry of northern water (the NEC) from the northeast (see Figure 19 in the text for nomenclature). Similar analyses at Section D (Figures G-1B, G-4B, G-7B, and G-10B respectively) provide insight into: (f) the Demerara Eddy (*Hde*), (g) the low along the French Guiana coast (*Lfg*), and (h) water which is flowing westward and out of the region.

The boundary between the surface and intermediate layers is defined in section V to be the top of the pycnocline (Figure G-1Aa, etc.), a region in which density increases rapidly with depth. This zone of high density gradient is found

within the thermocline (Figure G-1Ab, etc.) and halocline (Figure G-1Ac, etc.), where temperature and salinity respectively both decrease rapidly with depth. For this study, the sigma theta 26.00 surface has been defined as the upper limit for the intermediate layer. In the western tropical Atlantic Ocean, the four-survey average depth of this surface is 149 m (Table G-1a). Similarly, the lower boundary for intermediate water is defined by the sigma theta 27.65 surface, which is at an average depth of 1281 m. This latter surface is above the relative salinity maximum which marks the top of the deep water (NADW). The sigma theta 27.30 surface, at an average depth of 769 m, divides the upper and lower intermediate layers.

The sigma theta 27.00, 27.25, and 27.45 surfaces were selected to represent the upper, middle, and lower layers of the intermediate water (Table G-1). Plots of the depth of these surfaces across Sections B and D present their south to north slopes and some of their larger topographic features (Figures G-2a, G-5a, G-8a, and G-11a). The plots of temperature (b) and salinity (c) on these representative surfaces provide information about the hydrography of the region. The plan view of density surface topographies in the upper and lower density surfaces, compared with layer velocity structure and temperature and salinity contours on the same density surfaces, are also helpful (Figures G-3, G-6, G-9, and G-12, where A and B signify the upper and lower surfaces at sigma theta 27.00 and 27.45 respectively).

General observations about the region's hydrography...

Usually, temperatures and salinities within the intermediate layer of the WESTRAX region tend to increase with latitude from the south to north (Figures G-1, G-4, G-7, and G-10). These positive slopes are evident within intermediate layer depth-averaged temperatures and salinities across Section B (Table G-2). This observation is crucial to my water mass classification scheme, since temperature-

salinity relationships for the WESTRAX region depend on the fact that, for a given density, a southern water mass is cooler and less salty than its northern counterpart.

Density surfaces are very irregular. For example, the average depth range of the sigma theta 27.30 surface exceeds 200 m (Table G-1a). Because of this, it is perilous to discuss features in the region's flow structure or hydrography by describing features on constant pressure or depth surfaces. To illustrate, a downward deflection of the sigma theta 27.00 surface within the core of the Amazon Eddy is noted during WESTRAX 2 (Figure G-2a, at 2°N on Section B). This produces a relatively warm, salty area at the depth of 400 m. A plot of temperature and salinity on the 400 m surface would lead one to falsely assume that a pocket of northern water mass has been trapped within the center of the Amazon Eddy. When we look at the same area on the sigma theta 27.00 surface (Figure G-3A) however, the water in the supposed pocket is similar to its surroundings (e.g., 'southern' in nature), and the truly warm, salty northern water remains further to the north.

The waters within the region's surface layer are warm and well mixed. There are no thermal signals which could help distinguish differences between southern and northern waters (Figures G-1Ab, etc.). A region of cold intermediate water (e.g., less than 4.5°C) lies along the continental slope between approximately 1000 and 1200 m (Figures G-1Ab, etc.). There is some correspondence between features observed in the isothermal (and isohaline) structure and major features of velocity structure. For example, an area of strong temperature and salinity gradient near 3°N, 200 m deep during WESTRAX 3 (Figure G-4A) is found within the high-velocity core of the NEUC (Figure F-5). A good example of an apparent oceanic frontal zone is seen at Section B during WESTRAX 4 (Figure G-10A, between 3-5°N, 200-400 m). Here, the upward slopes with latitude of both temperature and salinity separate southern and northern

waters of the upper intermediate layer. This front lies within the eastward flow of the NEUC

(Figure F-11).

Salinity maxima which exceed 36.00 psu are evident across most of the survey surface layers between depths of 50 and 100 m (Figures G-1Ac, etc.). Salinity minima of less than 34.50 psu are evident against the continental slope between depths of 600 and 800 m. These minima, which do not extend very far laterally beyond the southeast corner of the region, are associated with AAIW. A layer of minimum salinity is evident throughout the WESTRAX region at depths and sigma thetas of approximately 700 m and 27.25 respectively. Salinity increases with depth below this minimum. Maxima which occasionally exceed 35.00 psu (indicating the presence of NADW) are observed deeper than 1400 m (see Figures G-1Ac, G-1Bc, and G-7Bc).

Along the continental shelf, there are large vertical deflections of the isopycnal, isothermal, and isohaline surfaces. Some examples are seen on the vertical analyses of section D (Figures G-1B, etc.) or the shape of density surfaces (Figures G-9A or G-12A). While these features may be the result of errors due to extrapolation shoreward of the CTD locations, they may also represent the effects of internal waves. Further analysis is beyond the scope of this dissertation. A downward deflection of the sigma theta 27.00 surfaces across Section B has been noted. These indicate upper level convergence and downwelling in the center of the anticyclonic Amazon Eddy. Corresponding temperature and salinity plots indicate this downward motion pushes the warmer, saltier upper level water deeper into the ocean (for examples, see Figures G-2 at 2°N or G-5 at 3°N).

I could seldom correlate the Pegasus derived velocity structure and the topography of density surfaces. The best comparisons between Pegasus structure and geostrophic shear using a thermal wind approximation (e.g., lower density water would be found on the right side of the flow) are found in the upper layer

of the Amazon Eddy (see Figures G-3A or G-9A). There was no such structural correspondence evident within the Demerara Eddy. For example, during WESTRAX 2 at Section D, the density surface at all three levels across *Hde* slopes upward between 6°N and 9°N (Figures G-1B or G-2), indicating southeastward geostrophic shear. The actual Pegasus flow across the shoreward half of Section D is strongly northwestward (Figure G-3Ab).

The mean depths of the mid and lower intermediate water surfaces appear to change seasonally (Table G-1a). For example, the sigma theta 27.25, 27.30, and 27.45 surfaces are deeper during winter compared with summer. At the same time, temperature and salinity changes on these surfaces are small.

Some observations from the analyses of individual surveys...

On the September 1990 sigma theta 27.00 analyses, a tongue of warm, salty (e.g., northern) water extends from the northern border near 9°N 49°W southeastward toward 6°N 44°W (Figure G-3A). A branch of this northern water also flows anticyclonically around the Demerara Eddy and northwestward along the coast.

On the sigma theta 27.00 surface during January 1991, a temperature and salinity front between southern and northern water is evident along approximately 6°N (Figure G-6A). This front corresponds well with the east-west trough in the velocity structure. It is difficult to associate the very deep center on the density surface near 4.5°N 47.5°W with any anticyclonic center within the upper intermediate layer velocity structure (compare Figures G-6Aa and G-6Ab). The upper and lower intermediate layer density structures are very different during this period, supporting the suggestion made in section IV that there is less consistency in vertical structure during the winter (see also appendix F). An interesting cyclonic interplay between northern and southern water around the eastern low (*Le*) is seen on the temperature and salinity analyses at sigma theta

27.45 (Figure G-6B).

A striking feature of the temperature and salinity contours during February 1990 is the area of very warm, salty water along the continental slope. This can be associated with the flow of northern water within the undercurrent around the French Guiana low (*Lfg*) (Figures G-9A and G-9B).

Table G-1. Horizontally averaged depths, temperatures and salinities of selected WESTRAX density surfaces.

G-1a. Mean depths of selected density surfaces.

	WX 1 [Feb90]	WX 2 [Sep90]	WX 3 [Jan91]	WX 4 [Jun91]	1-4 [Means]
[1] Sigma theta 26.00 - top of intermediate water					
Depth (m):	157	154	141	143	149
Standard Dev:	18	27	27	15	22
Minimum:	106	96	92	102	99
Maximum:	18	218	201	176	196
[2] Sigma theta 27.00 - mid upper intermediate water					
Depth (m):	373	341	350	352	354
Standard Dev:	41	42	53	40	44
Minimum:	300	220	263	300	271
Maximum:	472	445	460	489	467
[3] Sigma theta 27.25 - mid AAIW					
Depth (m):	681	679	705	676	685
Standard Dev:	38	39	32	38	37
Minimum:	563	600	650	600	603
Maximum:	750	814	800	800	791
[4] Sigma theta 27.30 - boundary upper/lower intermediate water					
Depth (m):	770	757	790	758	769
Standard Dev:	36	37	35	40	37
Minimum:	633	675	700	675	671
Maximum:	900	883	904	867	888
[5] Sigma theta 27.45 - lower intermediate water					
Depth (m):	1006	977	996	971	987
Standard Dev:	26	36	19	32	29
Minimum:	900	900	950	883	908
Maximum:	1040	1083	1038	1038	1050
[6] Sigma theta 27.65 - bottom of intermediate water					
Depth (m):	1273	1289	1289	1273	1281
Standard Dev:	40	35	25	41	35
Minimum:	1150	1193	1200	1190	1183
Maximum:	1350	1383	1325	1375	1358

G-1b. Mean potential temperatures on selected density surfaces.

	WX 1 [Feb90]	WX 2 [Sep90]	WX 3 [Jan91]	WX 4 [Jun91]	1-4 [Means]
[1] Sigma theta 26.00 - top of intermediate water					
Temp. (theta °C):	17.6	17.8	17.9	17.6	17.7
Standard Dev:	0.4	0.5	0.8	0.5	0.6
Minimum:	16.1	15.6	15.9	16.5	16.0
Maximum:	18.6	18.0	20.2	19.2	19.0
[2] Sigma theta 27.00 - mid upper intermediate water					
Temp. (theta °C):	8.8	9.1	8.9	8.9	8.9
Standard Dev:	0.4	0.3	0.4	0.4	0.4
Minimum:	8.2	8.1	7.9	8.0	8.1
Maximum:	10.2	9.9	10.1	9.9	10.0
[3] Sigma theta 27.25 - mid AAIW					
Temp. (theta °C):	5.7	5.7	5.6	5.8	5.7
Standard Dev:	0.3	0.3	0.3	0.4	0.3
Minimum:	5.1	5.0	5.1	5.0	5.0
Maximum:	6.3	6.4	6.2	6.7	6.4
[4] Sigma theta 27.30 - boundary upper/lower intermediate water					
Temp. (theta °C):	5.2	5.3	5.3	5.4	5.3
Standard Dev:	0.2	0.3	0.3	0.4	0.3
Minimum:	4.8	4.5	4.8	4.6	4.7
Maximum:	5.8	5.8	5.8	6.1	5.9
[5] Sigma theta 27.45 - lower intermediate water					
Temp. (theta °C):	4.7	4.8	4.8	4.8	4.8
Standard Dev:	0.1	0.2	0.2	0.1	0.1
Minimum:	4.5	4.4	4.4	4.6	4.5
Maximum:	5.0	5.0	5.0	5.1	5.0
[6] Sigma theta 27.65 - bottom of intermediate water					
Temp. (theta °C):	4.7	4.7	4.7	4.7	4.7
Standard Dev:	0.1	0.1	0.1	0.1	0.1
Minimum:	4.5	4.5	4.6	4.5	4.5
Maximum:	5.0	5.0	5.0	5.0	5.0

G-1c. Mean salinities on selected density surfaces.

	WX 1 [Feb90]	WX 2 [Sep90]	WX 3 [Jan91]	WX 4 [Jun91]	1-4 [Means]
[1] Sigma theta 26.00 - top of intermediate water					
Salinity (psu)	35.86	35.93	35.96	35.86	35.90
Standard Dev:	0.12	0.12	0.23	0.15	0.16
Minimum:	35.37	35.51	35.55	35.63	35.52
Maximum:	36.19	36.22	36.70	36.35	36.36
[2] Sigma theta 27.00 - mid upper intermediate water					
Salinity (psu)	34.82	34.86	34.83	34.82	34.83
Standard Dev:	0.08	0.07	0.08	0.09	0.08
Minimum:	34.69	34.66	34.64	34.67	34.67
Maximum:	35.10	35.04	35.08	35.05	35.07
[3] Sigma theta 27.25 - mid AAIW					
Salinity (psu)	34.56	34.57	34.56	34.59	34.57
Standard Dev:	0.04	0.04	0.05	0.06	0.05
Minimum:	34.48	34.46	34.48	34.46	34.47
Maximum:	34.67	34.69	34.65	34.73	34.69
[4] Sigma theta 27.30 - boundary upper/lower intermediate water					
Salinity (psu)	34.56	34.57	34.57	34.58	34.57
Standard Dev:	0.05	0.04	0.04	0.05	0.05
Minimum:	34.50	34.46	34.49	34.47	34.48
Maximum:	34.64	34.65	34.65	34.69	34.66
[5] Sigma theta 27.45 - lower intermediate water					
Salinity (psu)	34.68	34.68	34.69	34.69	34.69
Standard Dev:	0.02	0.02	0.02	0.02	0.02
Minimum:	34.64	34.63	34.63	34.65	34.64
Maximum:	34.71	34.72	34.72	34.73	34.72
[6] Sigma theta 27.65 - bottom of intermediate water					
Salinity (psu)	34.93	34.94	34.93	34.92	34.93
Standard Dev:	0.01	0.01	0.02	0.01	0.01
Minimum:	34.89	34.89	34.90	34.90	34.90
Maximum:	34.97	34.97	34.97	34.97	34.97

Table G-2. Intermediate layer depth-averaged temperature and salinity
across Section B (0-9 N, 44 W).

WESTRAX	Layer *	Temperature (°C)		Salinity (psu)	
		Mean	Slope **	Mean	Slope
1 (FEB 90)	UIW	8.31	+0.059	34.79	+0.016
	LIW	4.75	+0.064	34.70	+0.010
	TIW	6.72	+0.067	34.75	+0.014
2 (SEPT 90)	UIW	8.43	+0.005	34.82	+0.006
	LIW	4.77	+0.063	34.72	+0.008
	TIW	6.78	+0.041	34.78	+0.006
3 (JAN 91)	UIW	7.83	+0.062	34.74	+0.014
	LIW	4.73	+0.066	34.72	+0.008
	TIW	6.51	+0.058	34.73	+0.012
4 (JUNE 91)	UIW	8.32	-0.046	34.79	+0.002
	LIW	4.75	+0.050	34.73	+0.002
	TIW	6.76	-0.016	34.77	+0.002

- * UIW: upper intermediate water ($26.00 \geq \sigma_{\theta} \geq 27.30$)
 LIW: lower intermediate water ($27.30 \geq \sigma_{\theta} \geq 27.65$)
 TIW: Total intermediate water ($26.00 \geq \sigma_{\theta} \geq 27.65$)
- ** Slopes in °C or psu per degree latitude north.

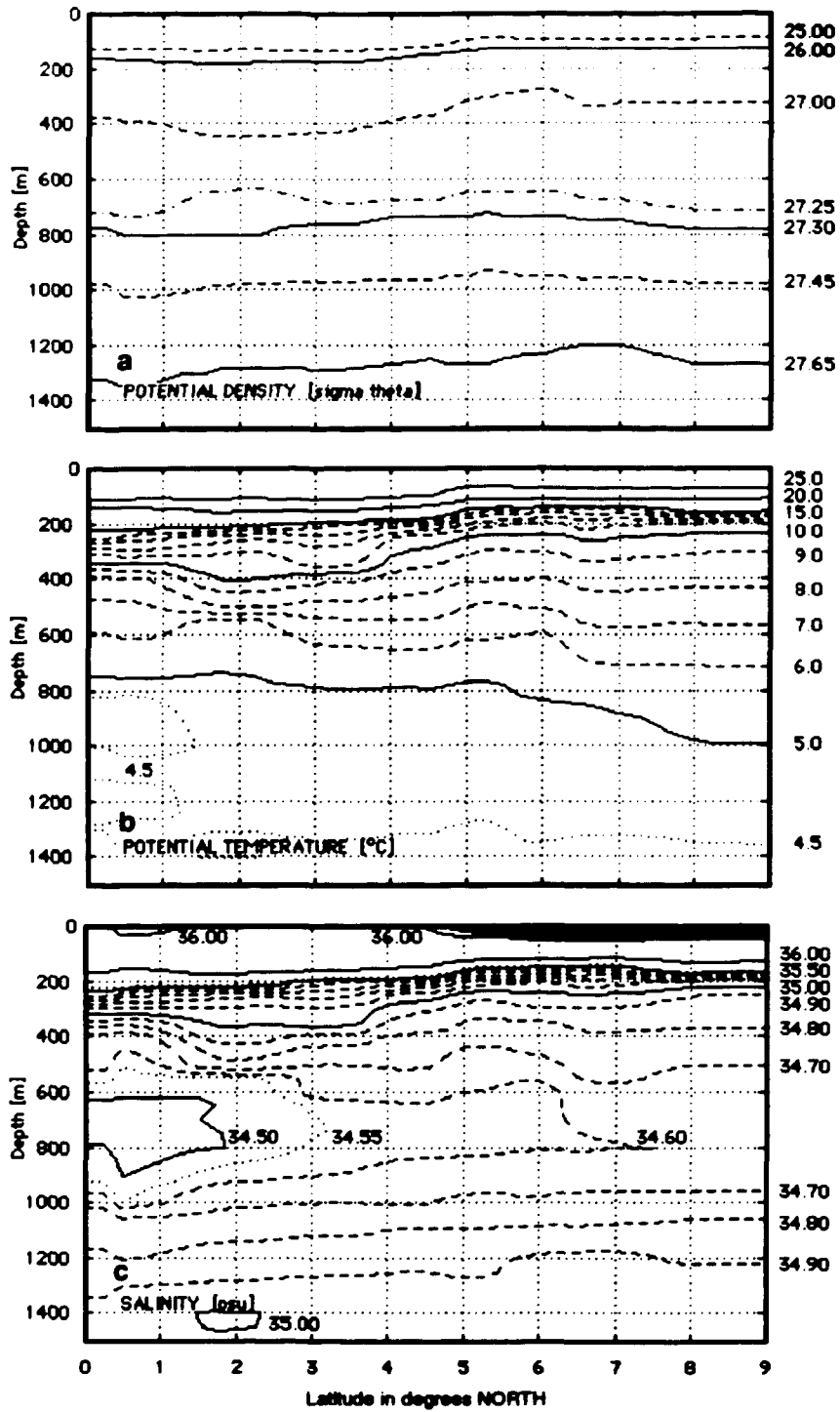


Figure G-1A. Vertical structure of interpolated (a) potential density, (b) potential temperature, and (c) salinity at Section B (44°W) during September 1990 (WESTRAX 2). Values for selected isopleths are indicated to the right.

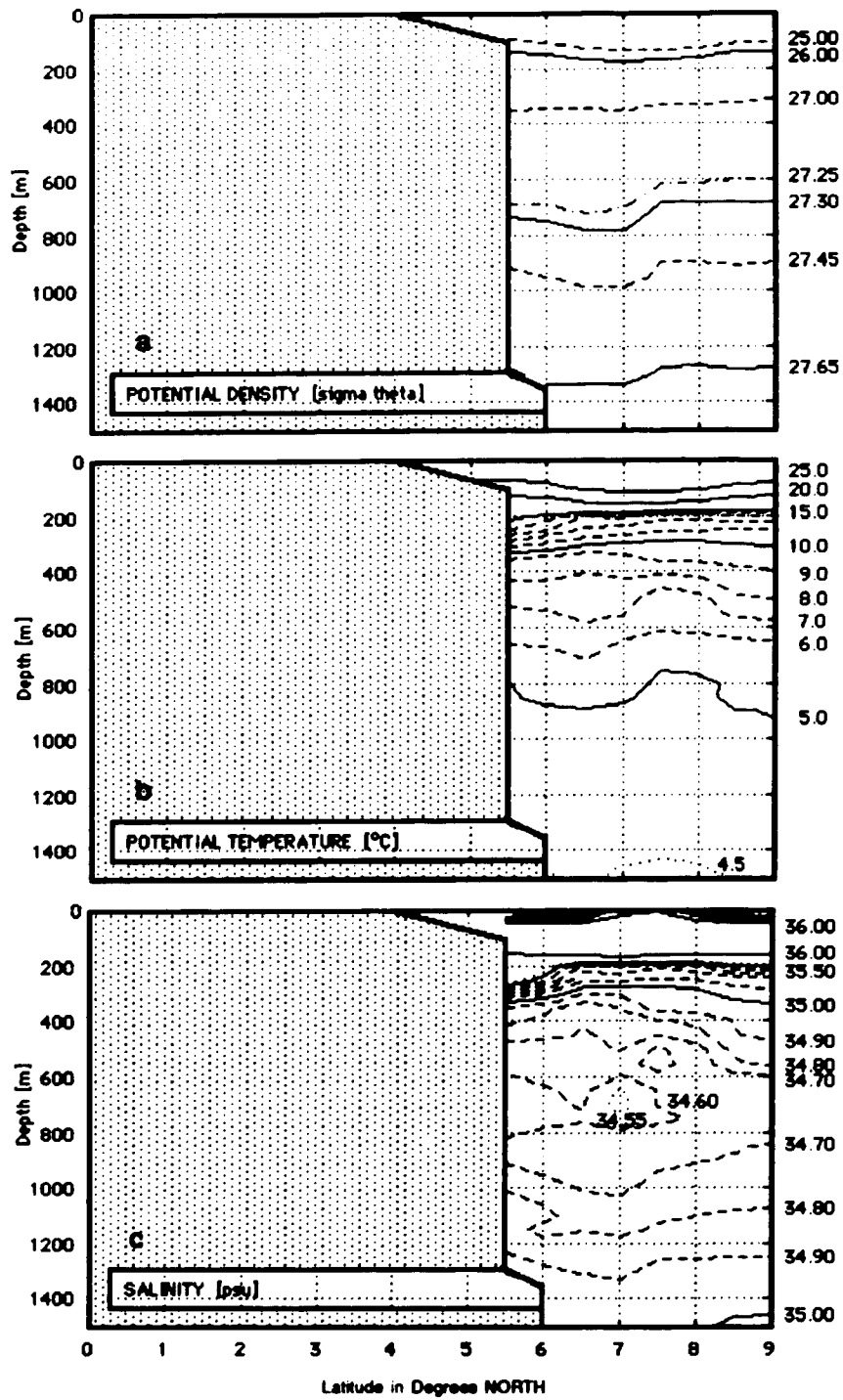


Figure G-1B. Same as Figure G-1A at Section D (between 5.5°N 51°W and 9°N 49.25°W) during September 1990 (WESTRAX 2).

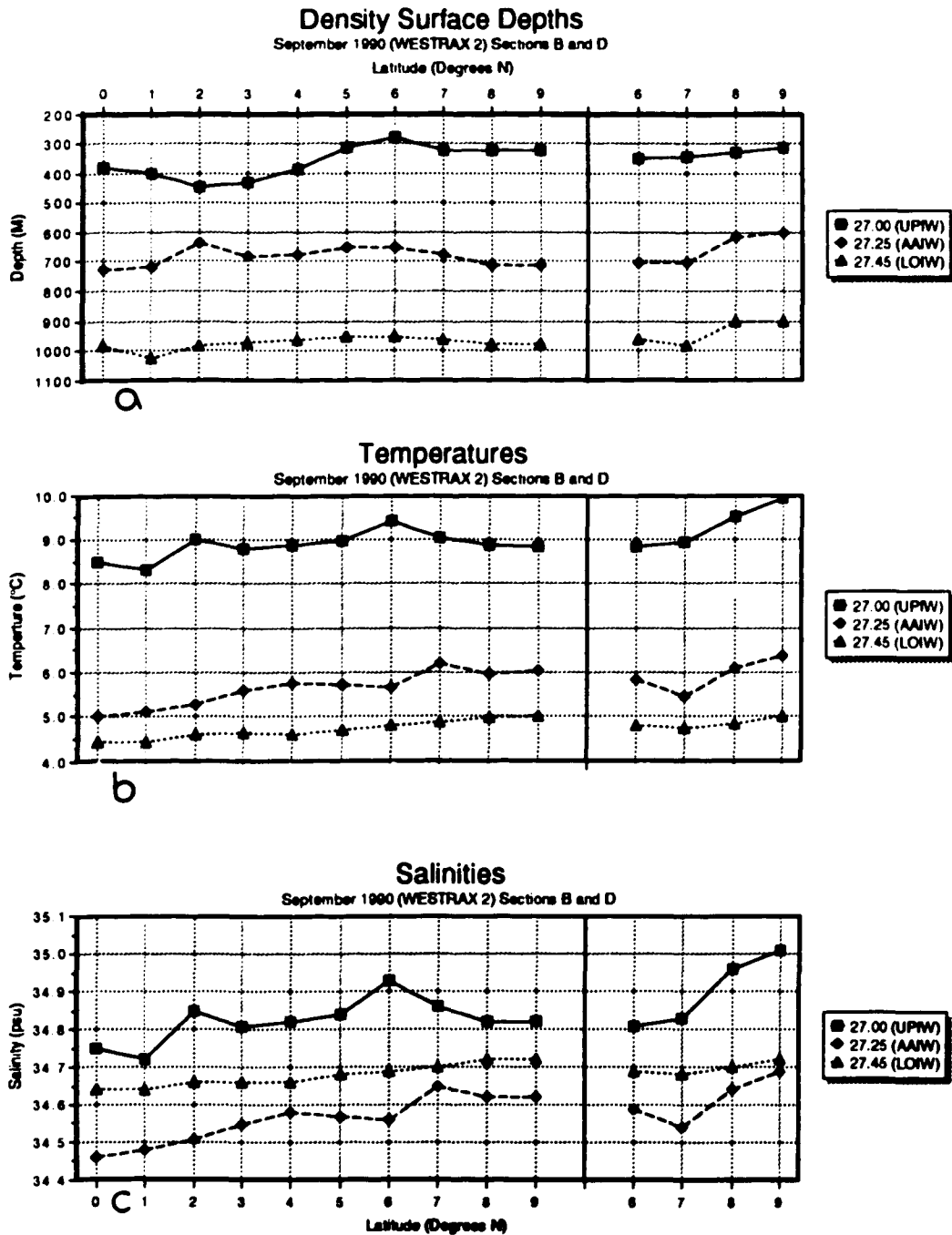


Figure G-2. (a) Depth, (b) potential temperature, and (c) salinity of selected isopycnals across Section B (left of the solid line) and Section D (right) during September 1990 (WESTRAX 2). The sigma theta 27.00 (square), 27.25 (diamond) and 27.45 (triangle) surfaces represent the WESTRAX region upper (UPIW), middle or Antarctic (AAIW), and lower (LOIW) intermediate waters respectively. Note that since the AAIW surface is at a salinity minimum, it is beneath LOIW on panel (c).

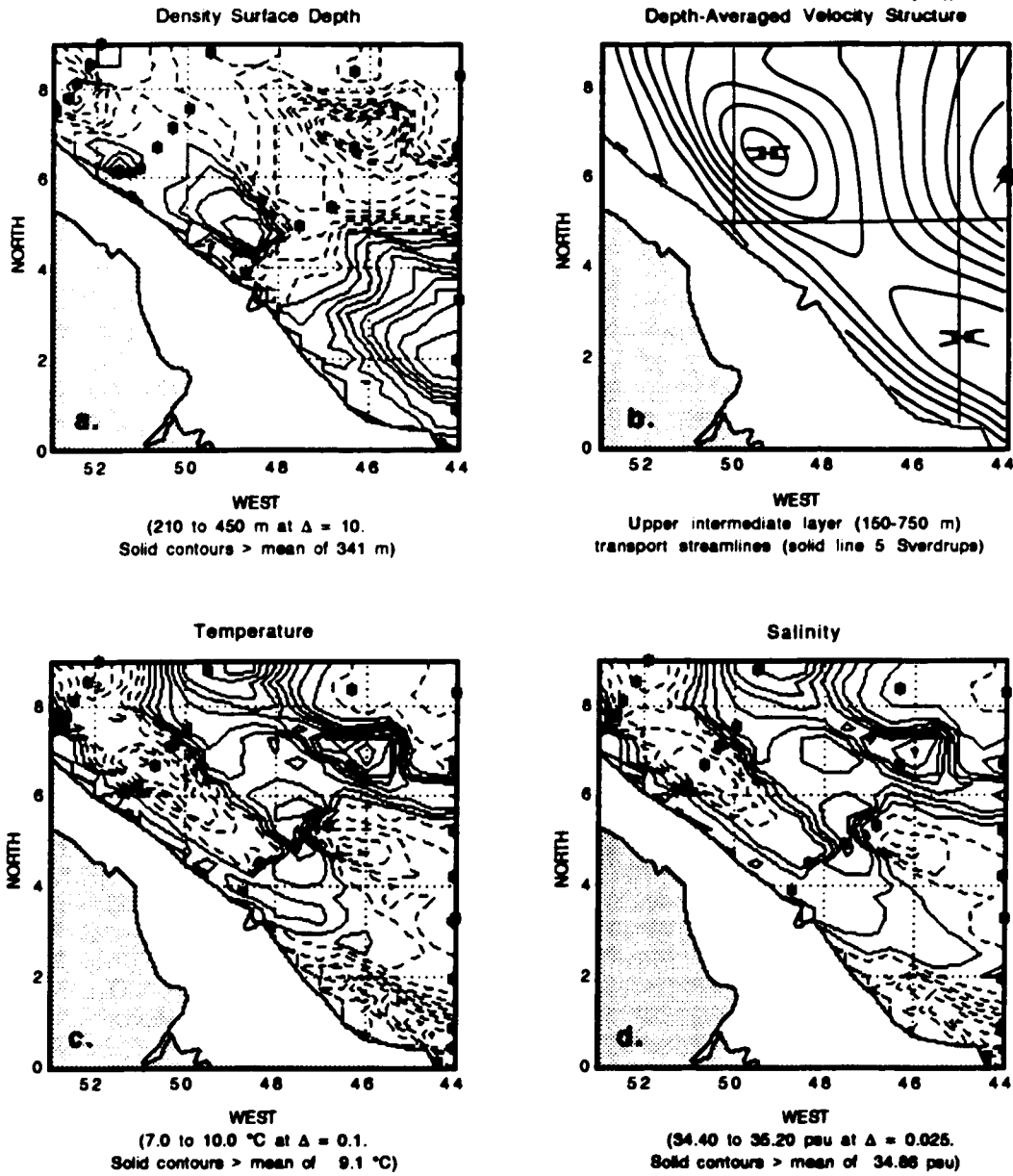


Figure G-3A. Upper intermediate layer: (a) interpolated depth, (b) depth-averaged velocity structure, (c) potential temperature, and (d) salinity on the sigma theta 27.00 density surface during September 1990 (WESTRAX 2). Contours greater than each of the surface's averages are solid.

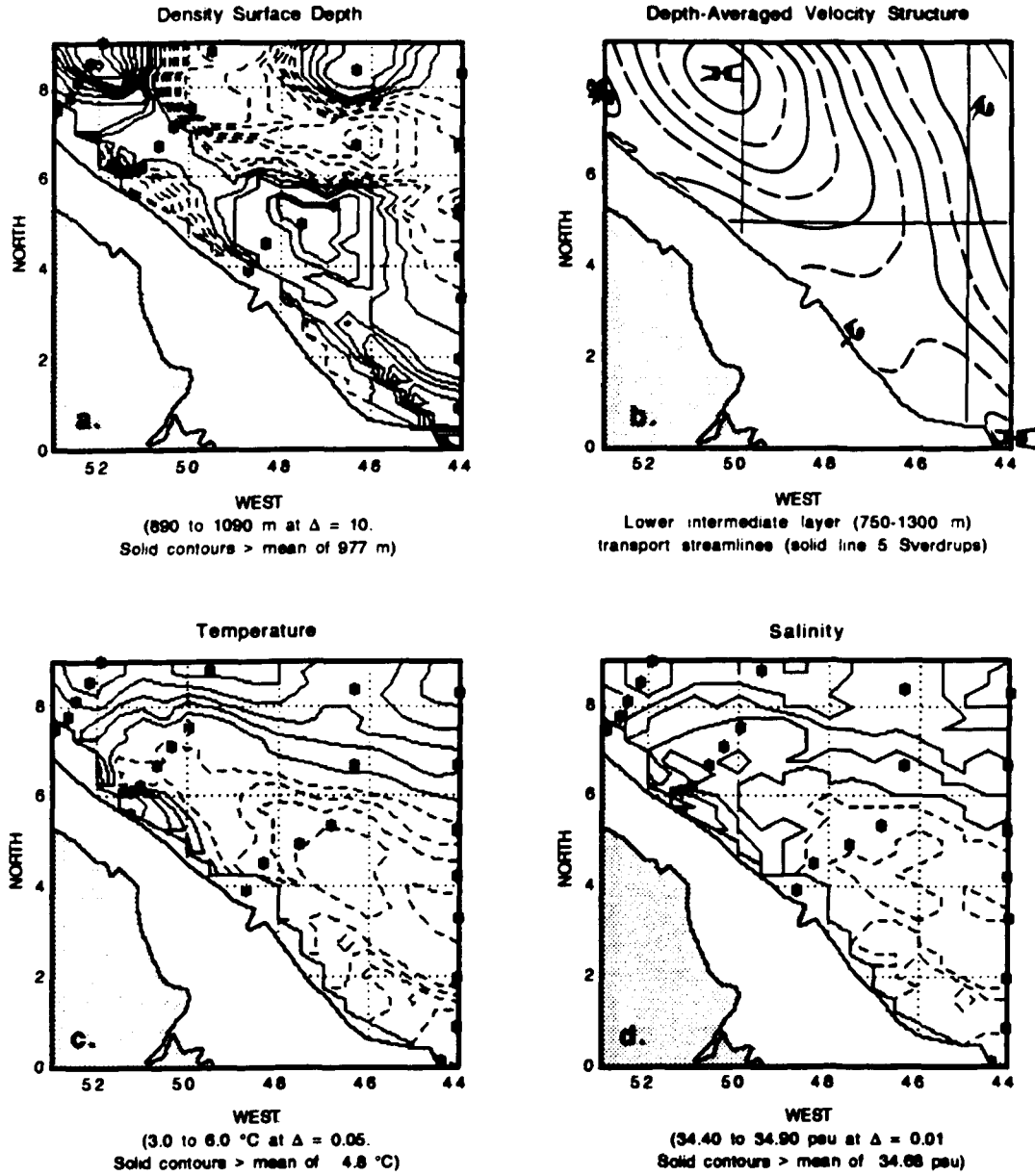


Figure G-3B. Same as Figure G-3A for the sigma theta 27.45 density surface, representing the lower intermediate layer during September 1990.

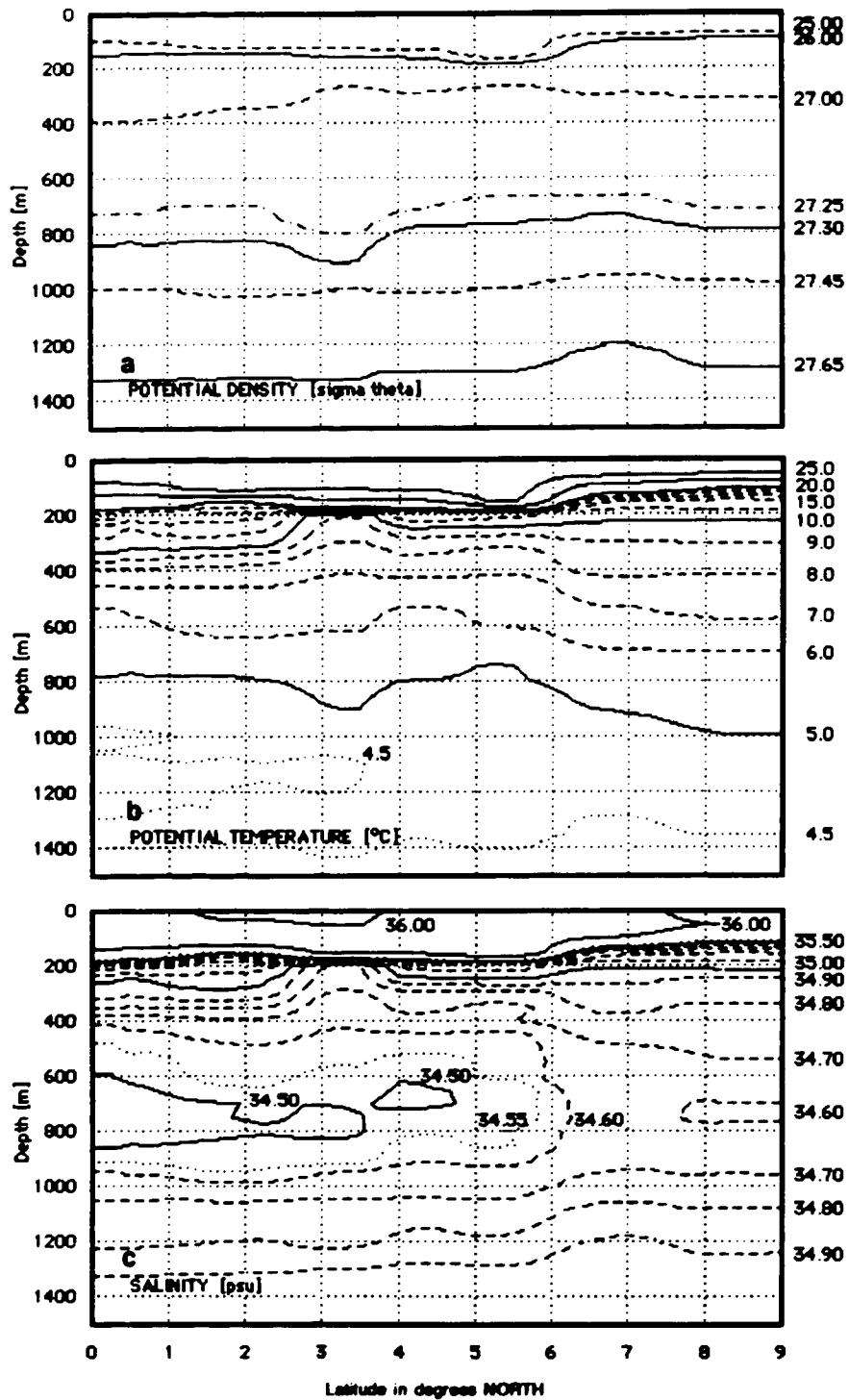


Figure G-4A. Same as Figure G-1A for January 1991 (WESTRAX 3).

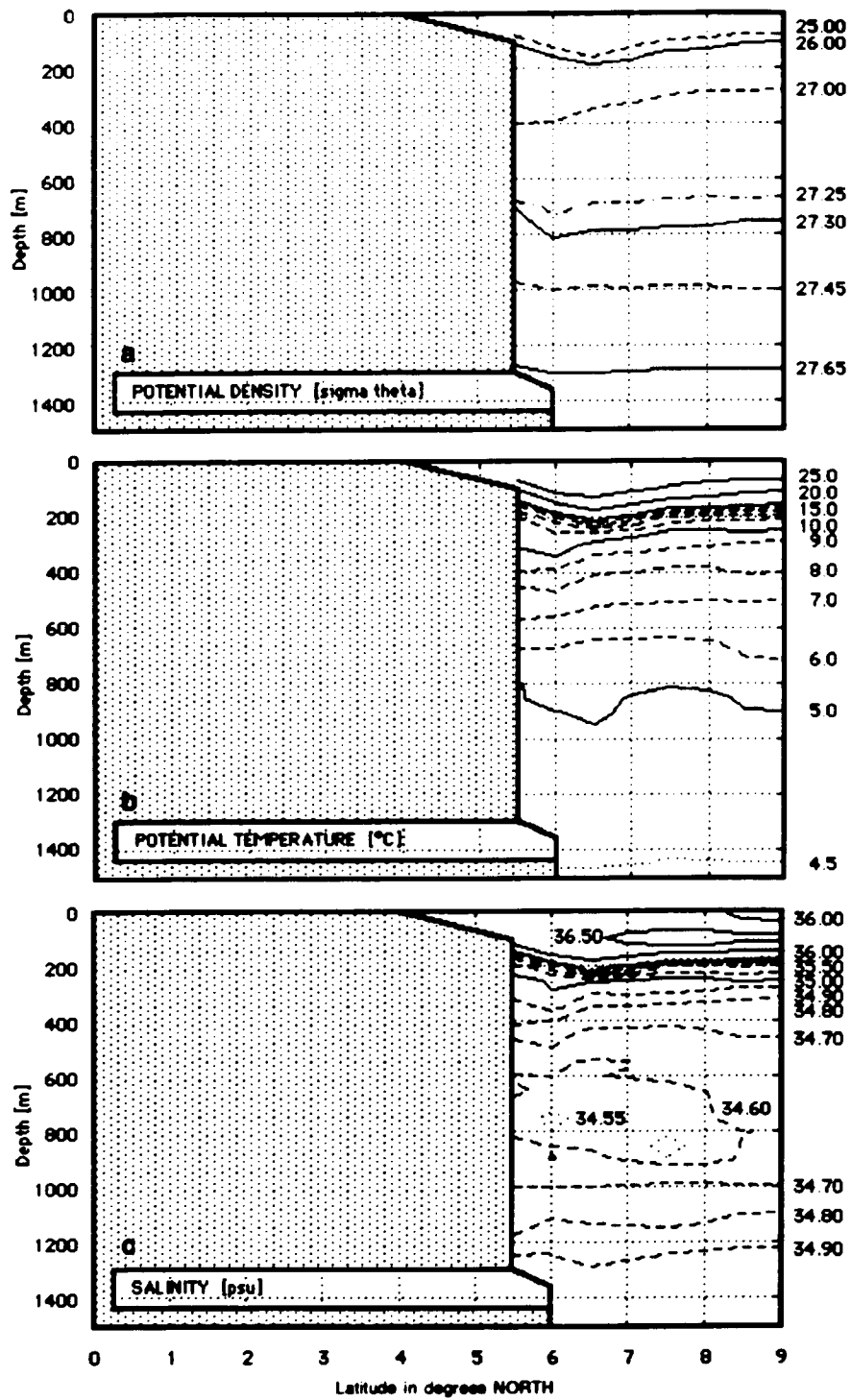


Figure G-4B. Same as Figure G-1B for January 1991 (WESTRAX 3).

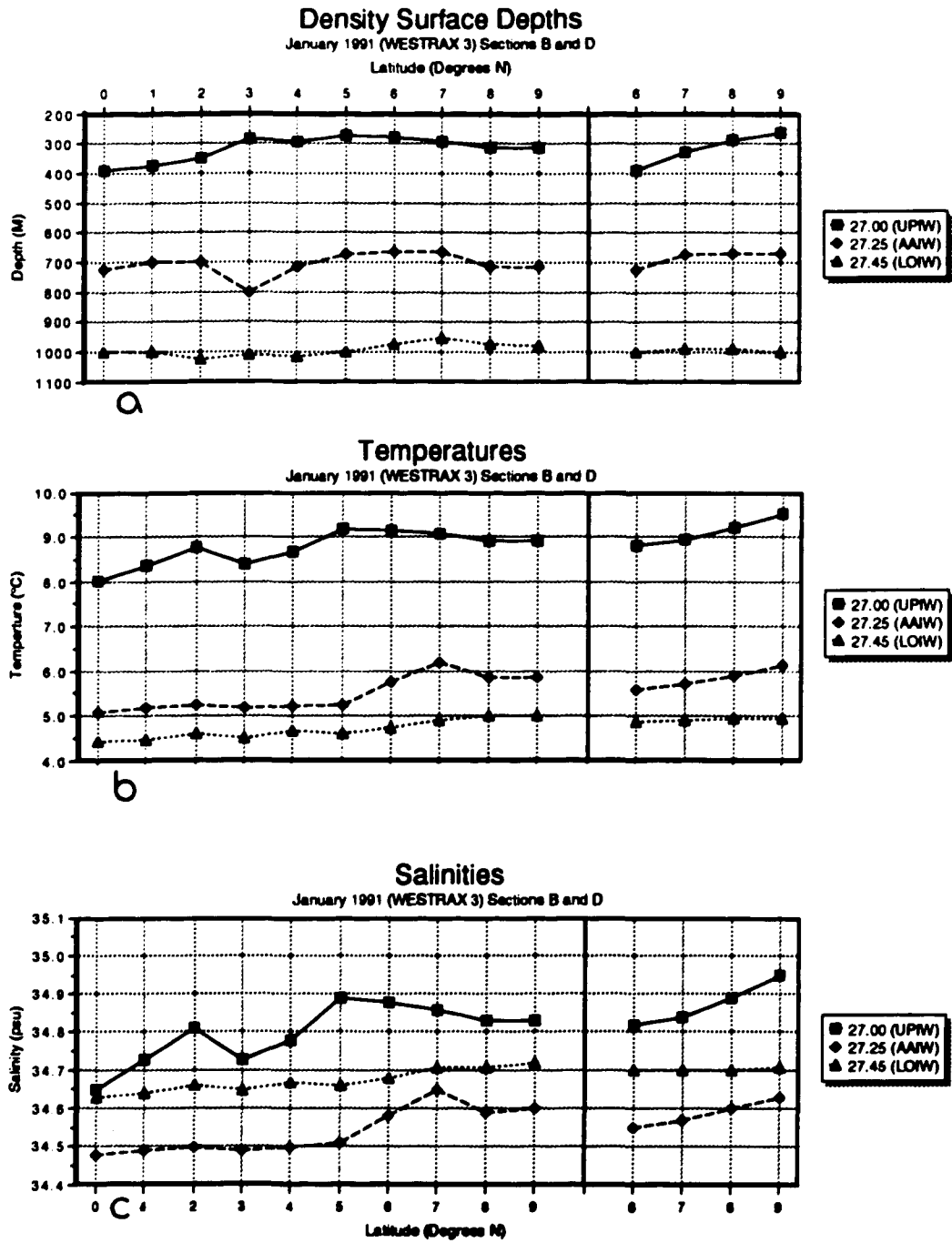


Figure G-5. Same as Figure G-2 for January 1991 (WESTRAX 3).

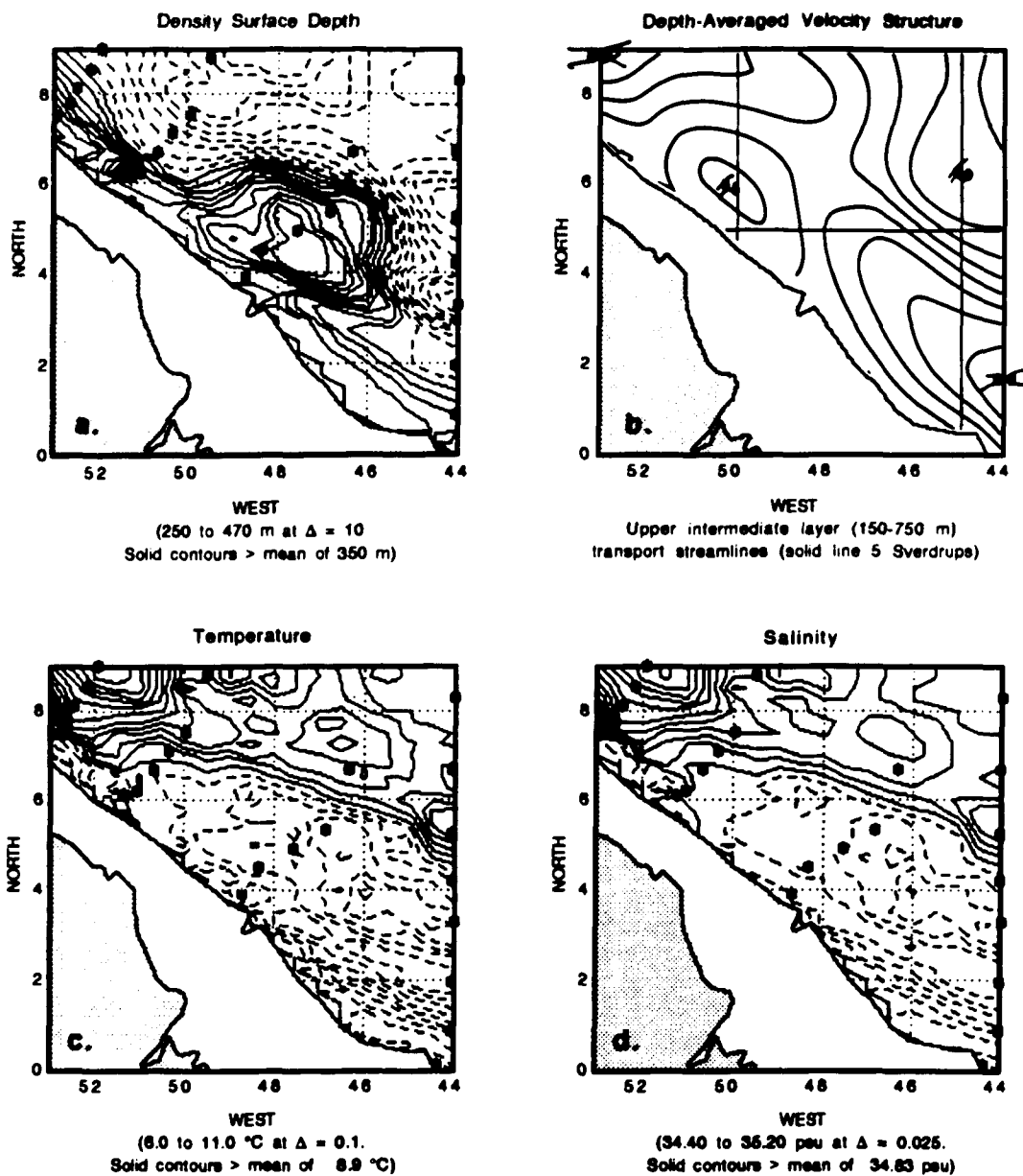


Figure G-6A. Same as Figure G-3A for January 1991 (WESTRAX 3).

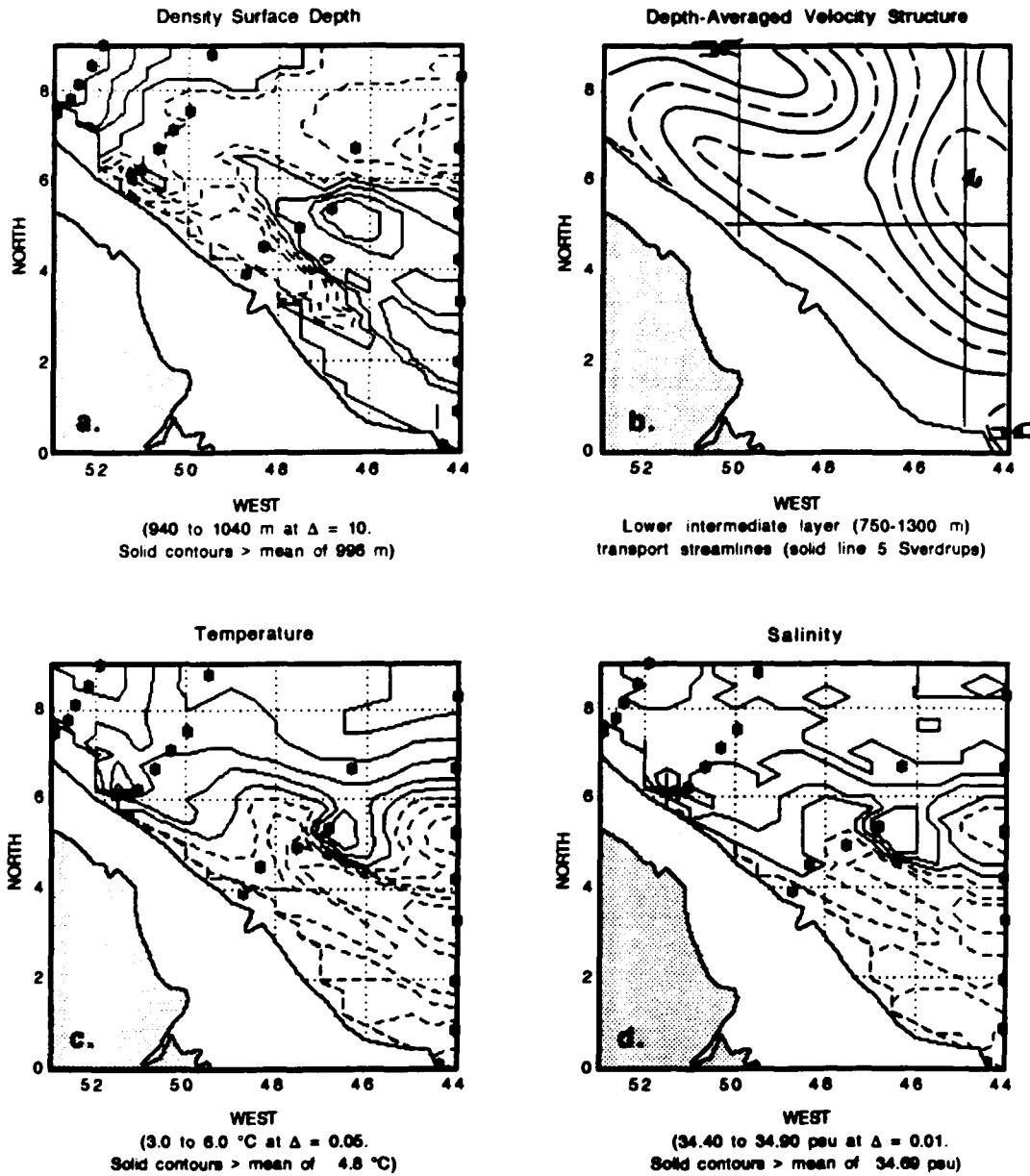


Figure G-6B. Same as Figure G-3B for January 1991 (WESTRAX 3).

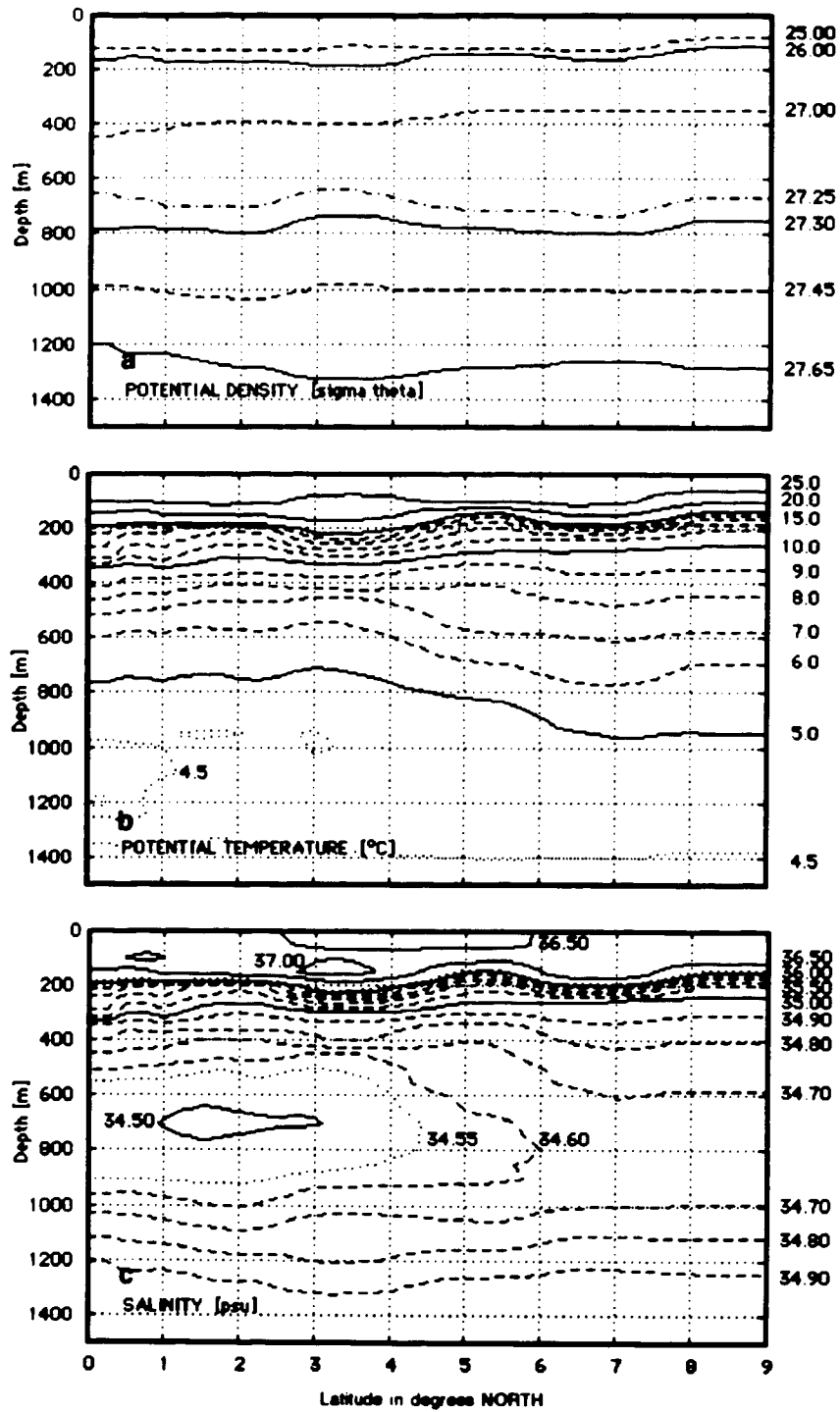


Figure G-7A. Same as Figure G-1A for February 1990 (WESTRAX 1).

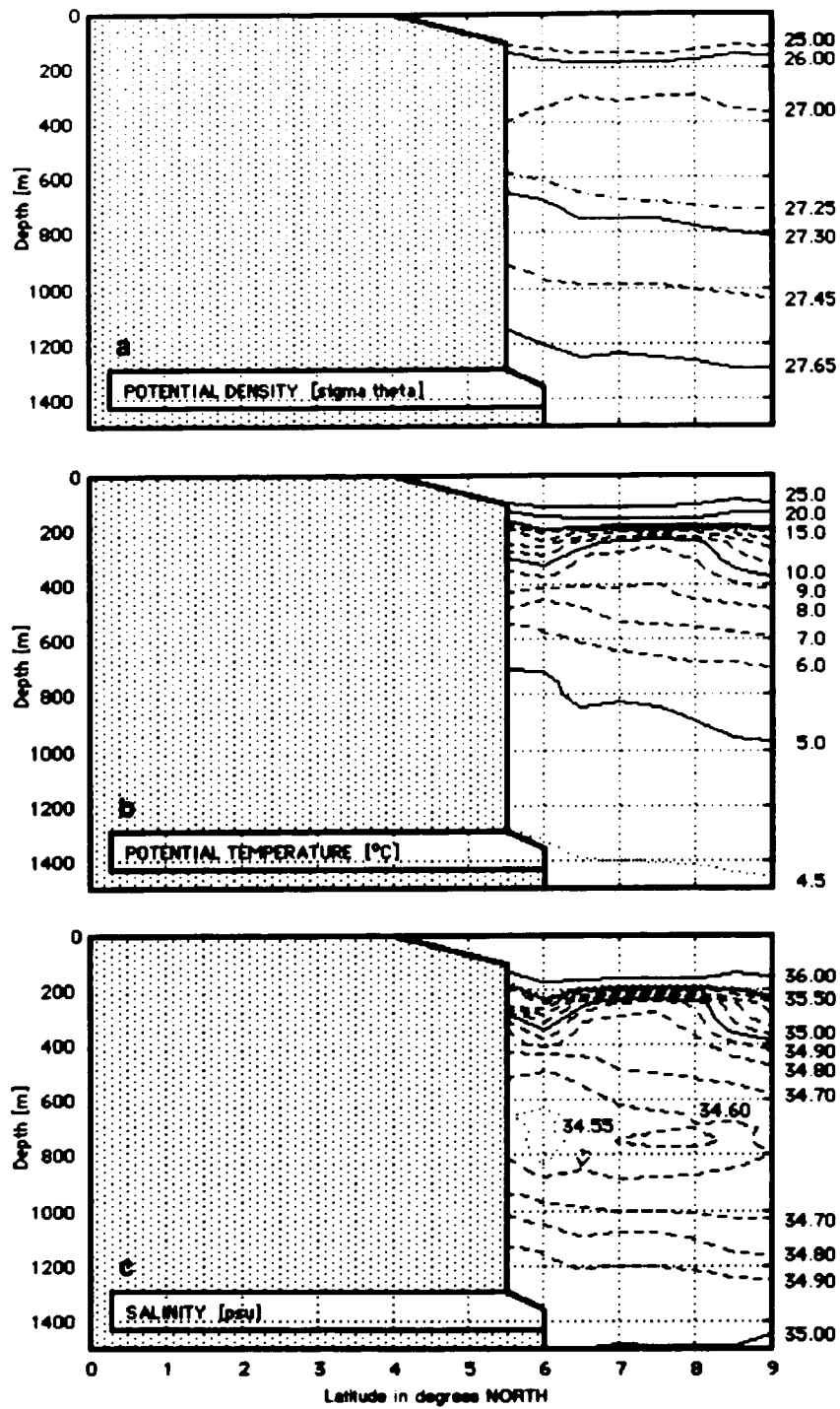


Figure G-7B. Same as Figure G-1B for February 1990 (WESTRAX 1).

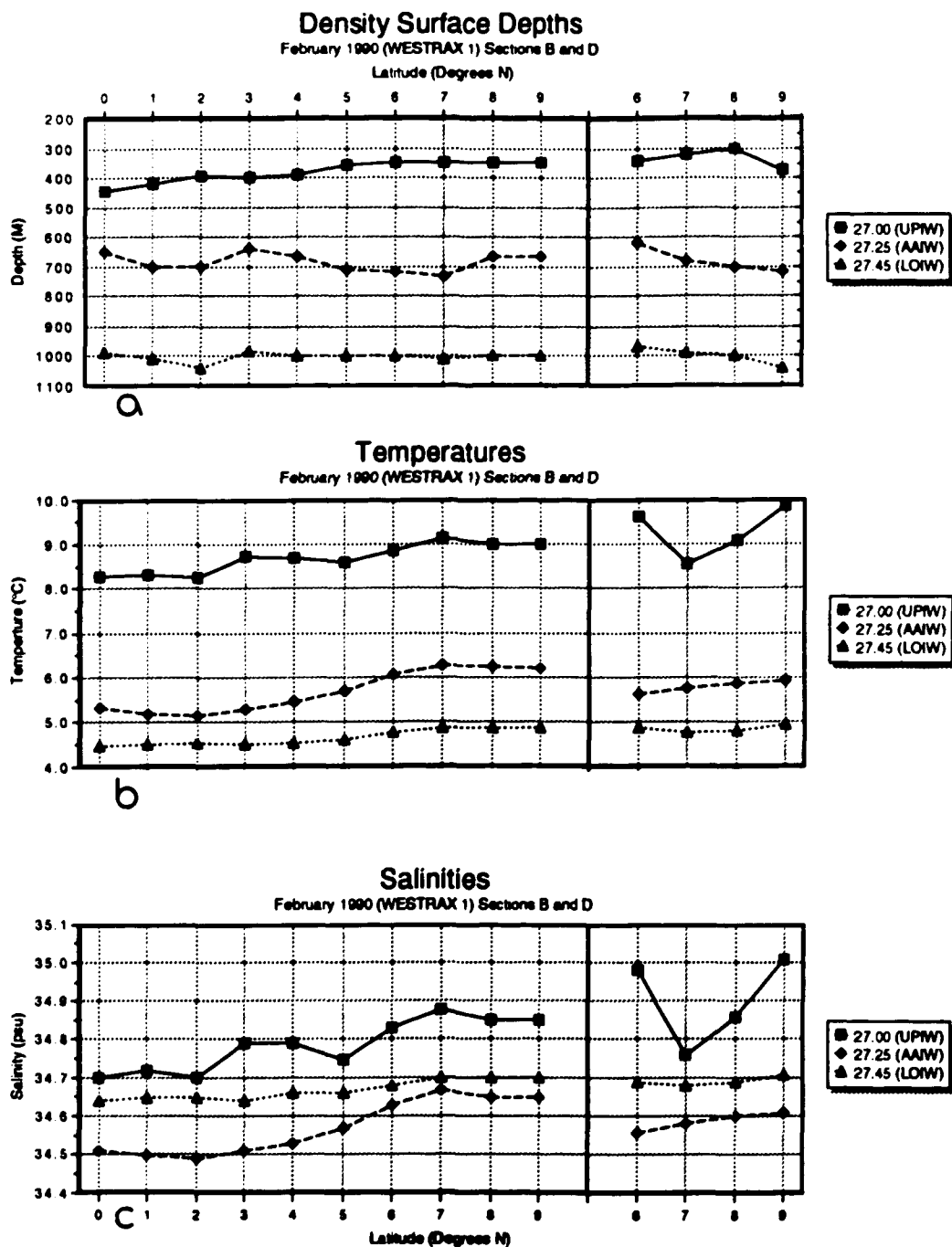


Figure G-8. Same as Figure G-2 for February 1990 (WESTRAX 1).

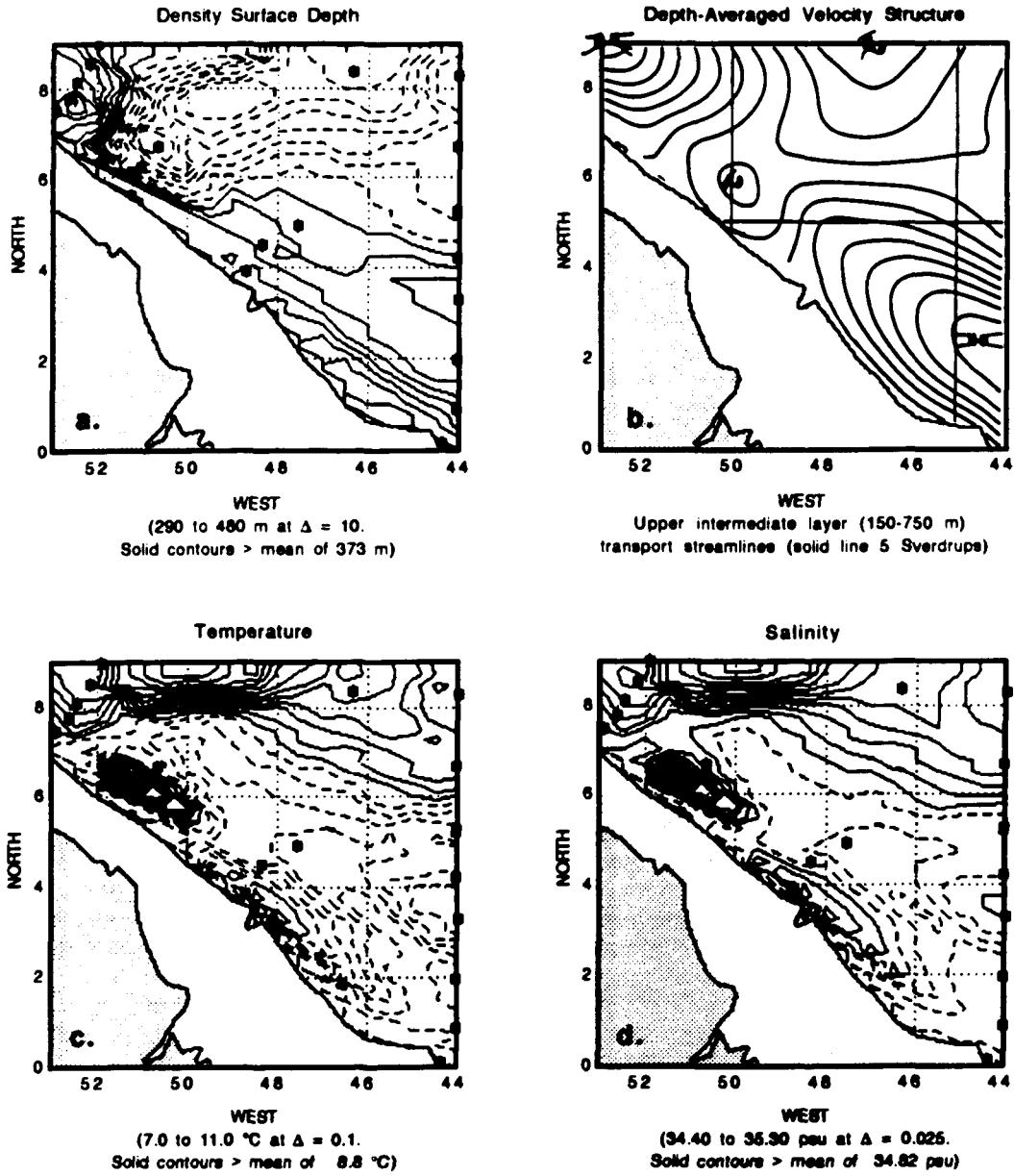


Figure G-9A. Same as Figure G-3A for February 1990 (WESTRAX 1).

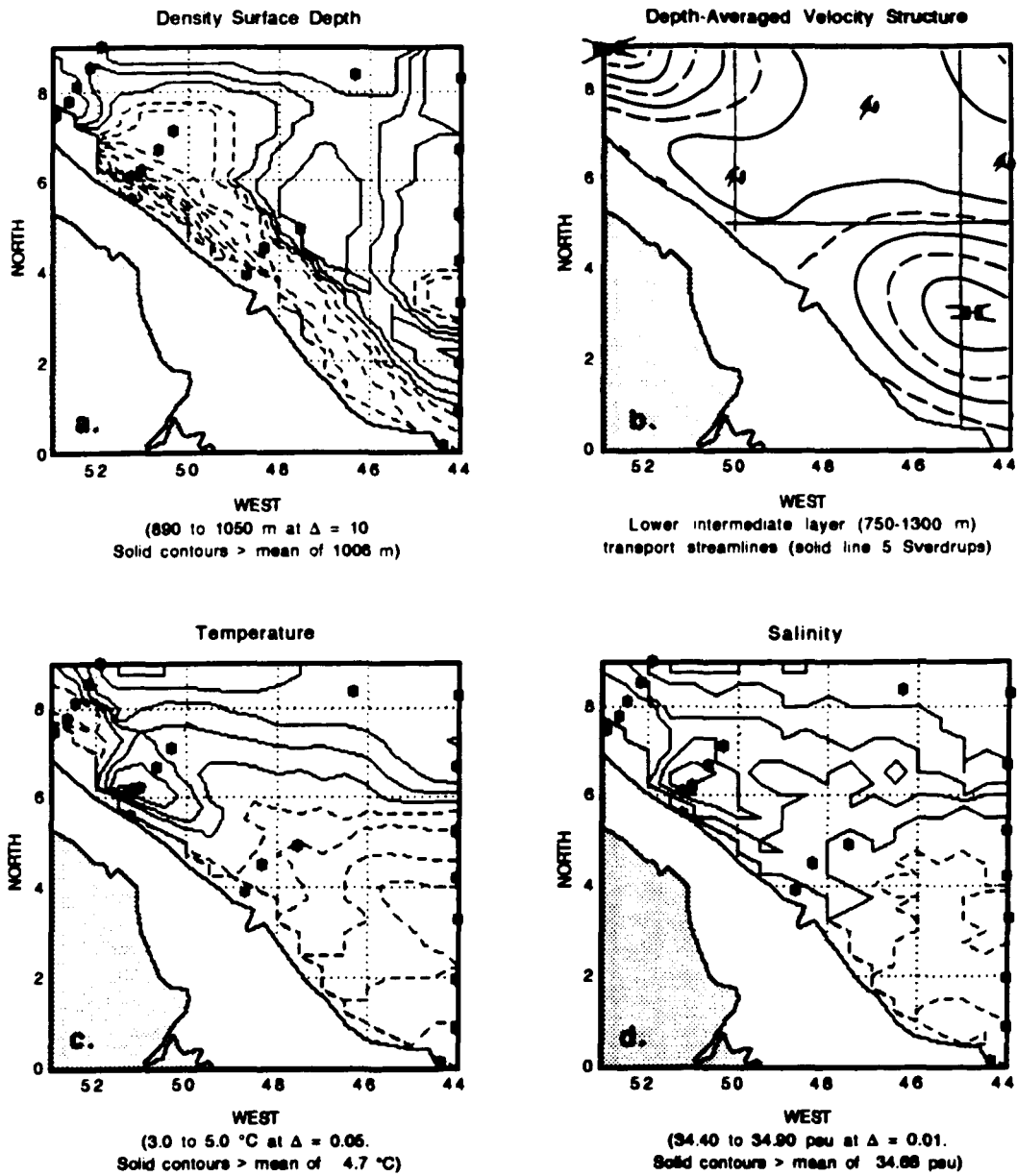


Figure G-9B. Same as Figure G-3B for February 1990 (WESTRAX 1).

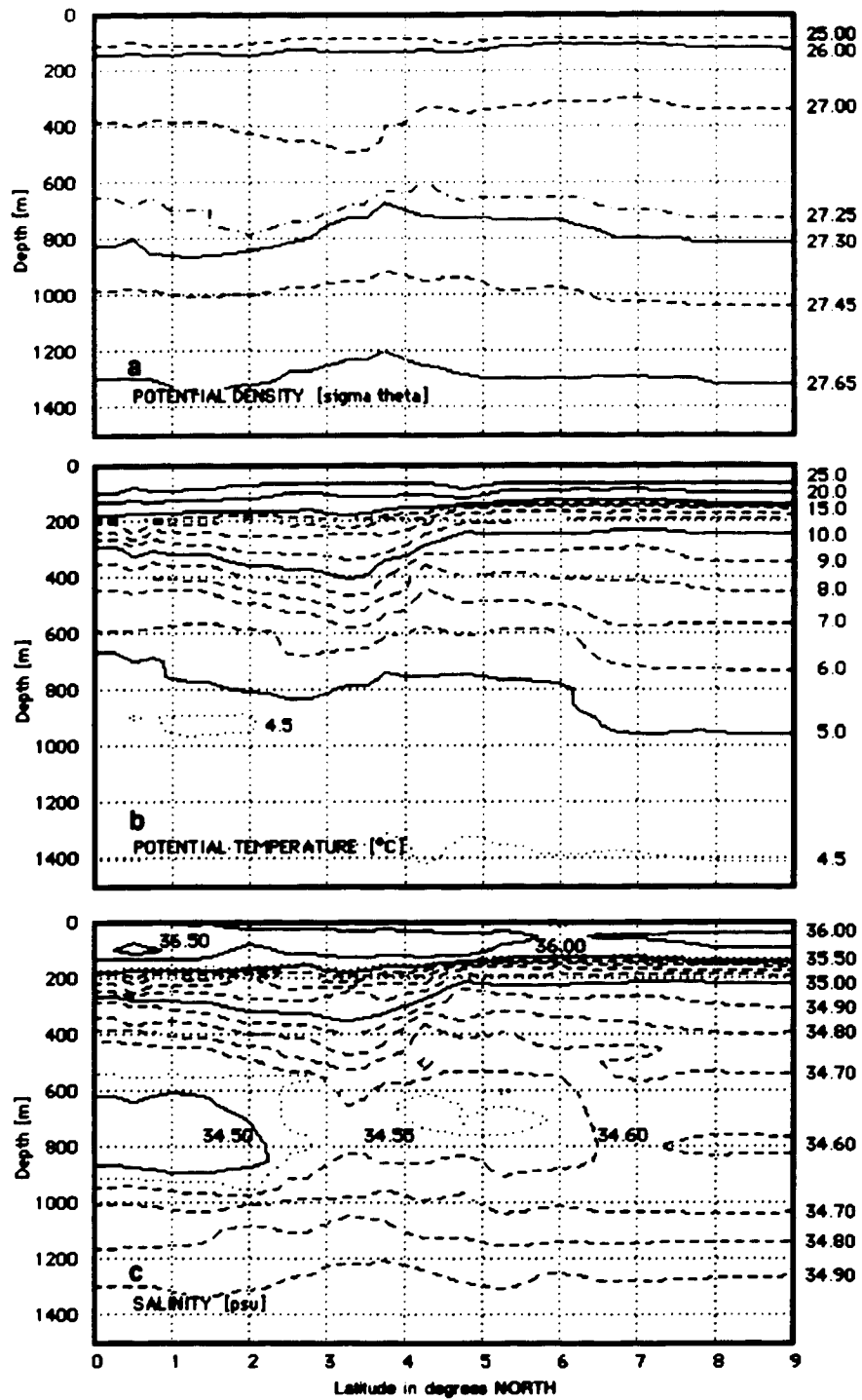


Figure G-10A. Same as Figure G-1A for June 1991 (WESTRAX 4).

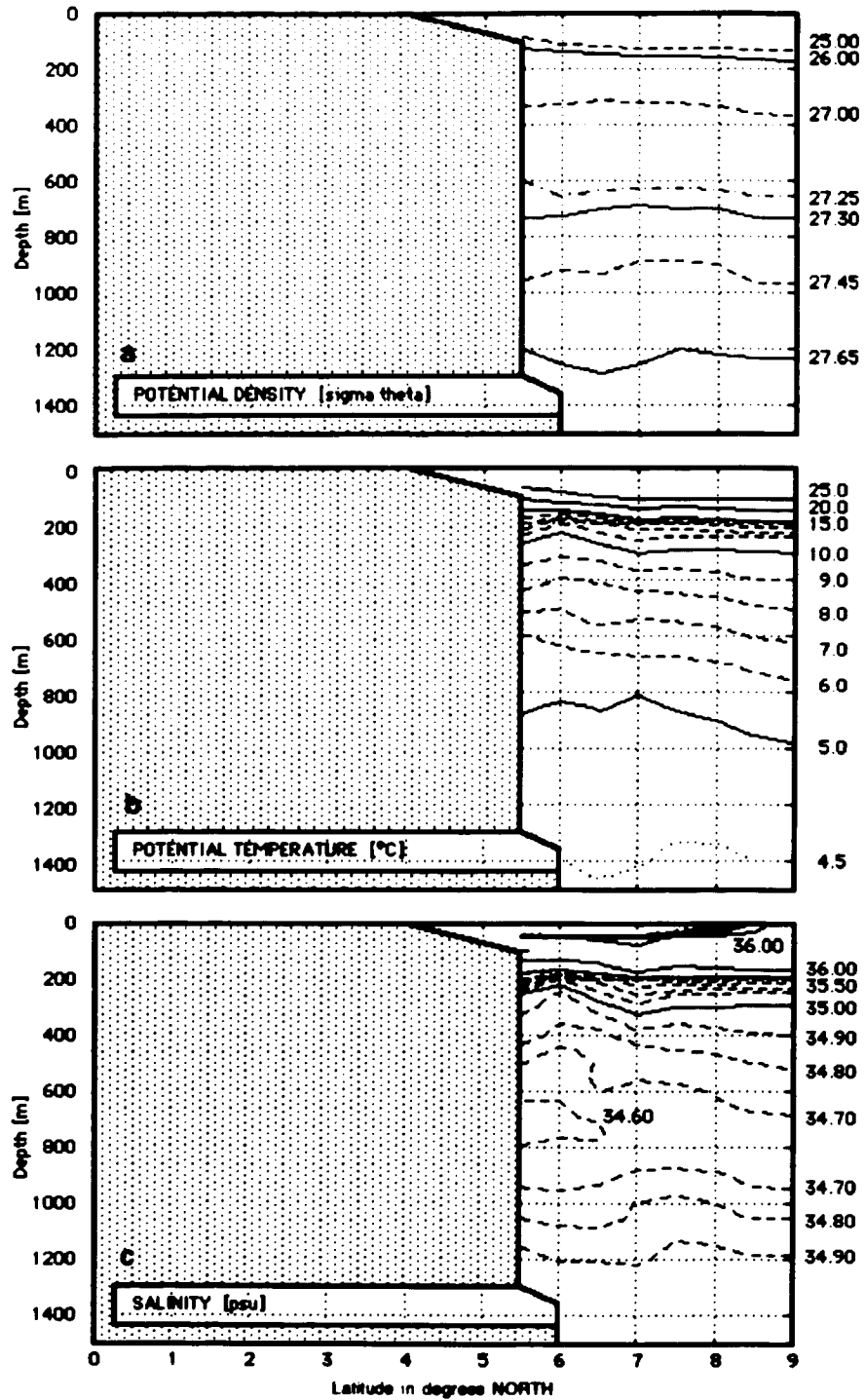


Figure G-10B. Same as Figure G-1B for June 1991 (WESTRAX 4).

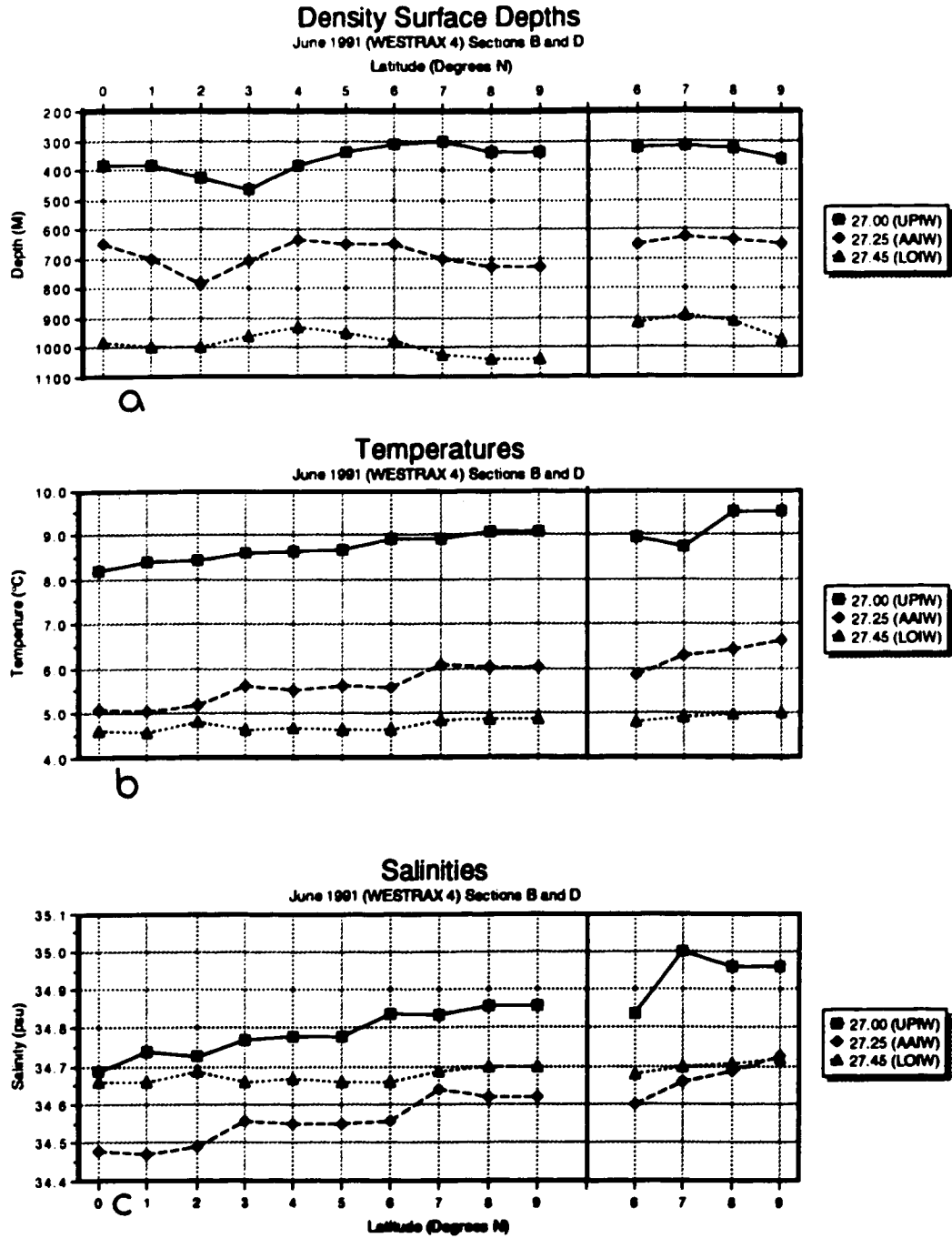


Figure G-11. Same as Figure G-2 for June 1991 (WESTRAX 4).

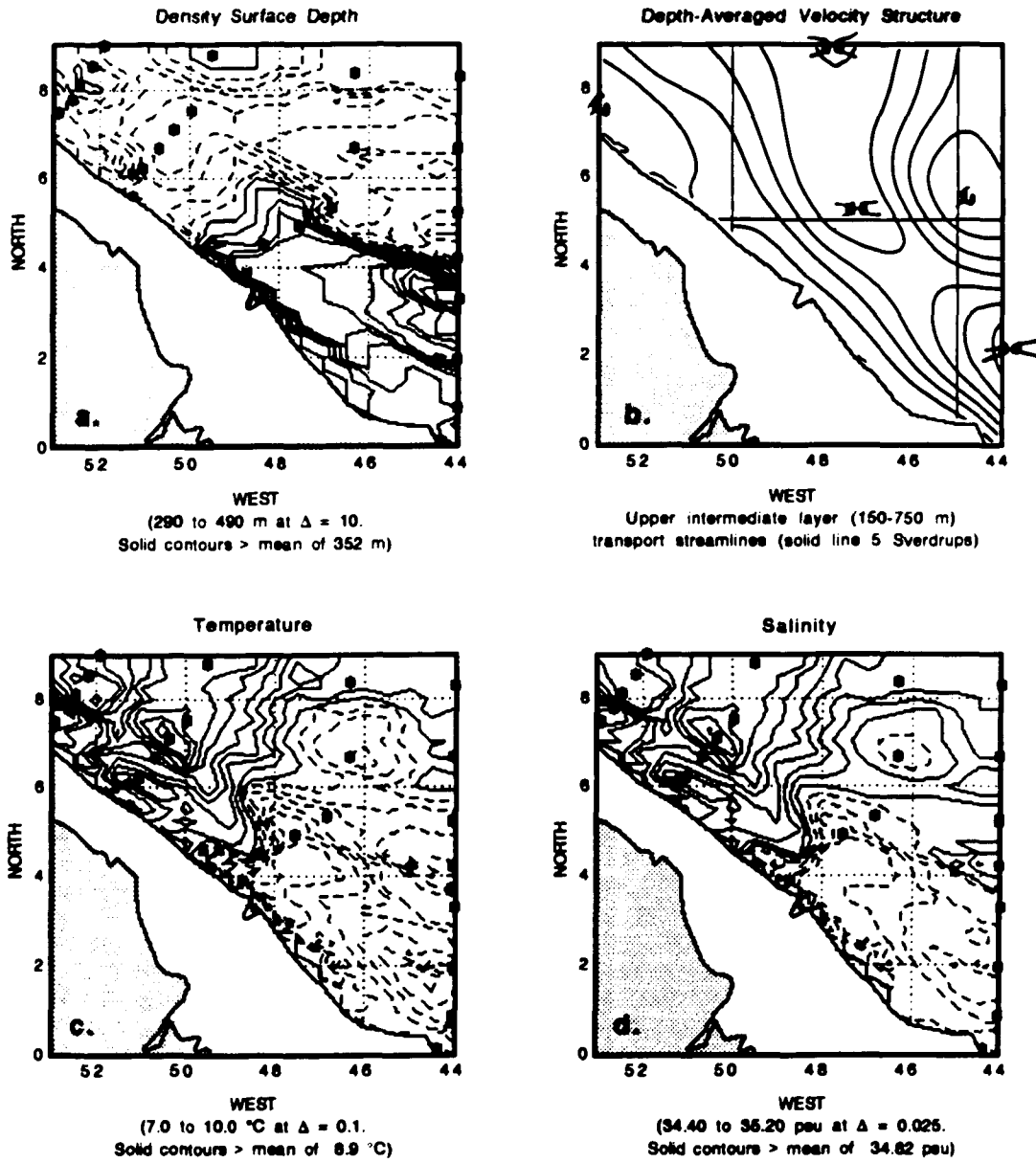


Figure G-12A. Same as Figure G-3A for June 1991 (WESTRAX 4).

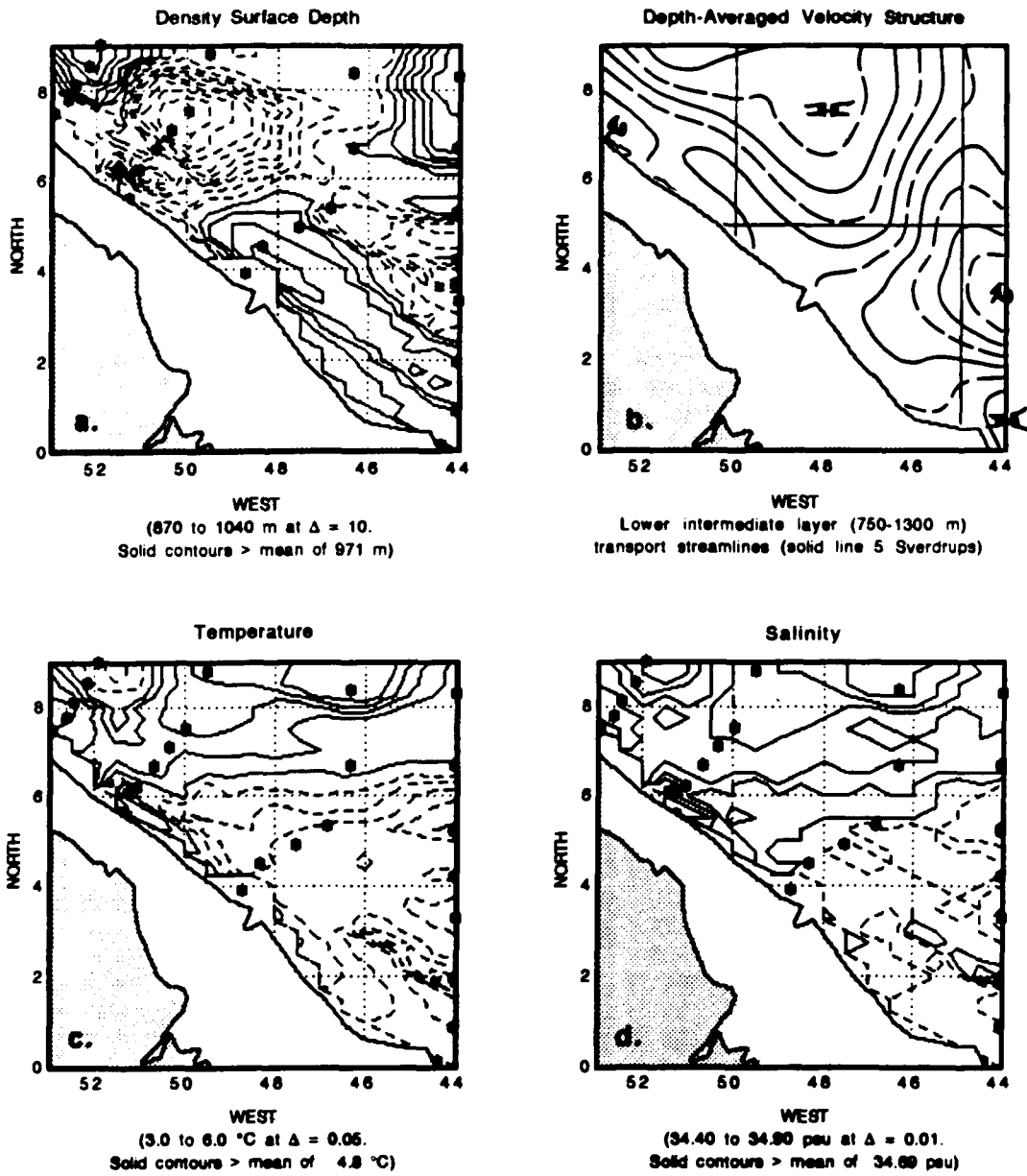


Figure G-12B. Same as Figure G-3B for June 1991 (WESTRAX 4).

APPENDIX H.
THE ANALYSIS OF WATER MASS FORMATION, MOVEMENT, AND MIXING
USING A TEMPERATURE-SALINITY DIAGRAM

The analysis of oceanic temperature-salinity (T-S) relationships is illustrated using Figure H-1. A water mass can be represented in T-S space as a point (e.g., water type), line, or area. A 'mixing line' connecting a pair of water types represents a continuous blend between the temperatures and salinities of its endpoints (e.g., the thin lines AB, BC and CA on Figure H-1c). Three straight mixing lines enclose a 'mixing triangle' (ABC). If the temperatures and salinities for the water types at the vertices of a mixing triangle are known, T-S relationships for any point within the triangle can be determined. By providing T and S at the three sources (e.g., water types A, B and C), the proportions (m) which each source water type contribute to a selected water type (x) enclosed by the mixing triangle (ABC) can be determined according to

$$\begin{aligned}m_A + m_B + m_C &= 1 , \\m_A S_A + m_B S_B + m_C S_C &= S_x , \\m_A T_A + m_B T_B + m_C T_C &= T_x .\end{aligned}\tag{H-1}$$

When a water mass is a mixture of four water types, the system can only be solved explicitly if another conservative parameter is measured and an additional set of relationships is established. During WESTRAX, dissolved oxygen was measured but it is not a conservative tracer in the upper ocean and it could not be used in this manner.

The mixing triangle described by Figure H-1 is a simplification of 'real

ocean' T-S relationships. While there are often more than three sources for the water masses of a region, it is possible to use regional observations to construct an appropriate set of mixing triangles to characterize the relationships on a T-S diagram (See the discussion related to Figure 32 in section V).

The water types and water masses of a hypothetical ocean are presented in Figure H-1. This is a simplification of the water mass structure of the WESTRAX region. Sources A, B, and C represent the subtropical surface, North Atlantic Deep, and Antarctic Intermediate water types respectively.

The two mixing triangles which were constructed for the WESTRAX region are schematically illustrated by Figure H-2 (see section V). As shown, the upper (ANI-SASI-NASI) and lower (SAD-SAI-NAI) mixing triangles can be used to determine the proportions of source water types which contribute to intermediate water masses of the region at a point in T-S space. For example, the arbitrary water type 'X' is composed of 40% ANI, 40% NASI and 20% SASI respectively, and is thus primarily of South Atlantic origin. A second water type 'Y' is composed of 40% SAD, 40% SAI and 20% NAI respectively. We can algebraically determine the ratios between the four water types which make up 'Y' as: 40% SAD, 48% ANI, 4% SASI and 8% NASI respectively .

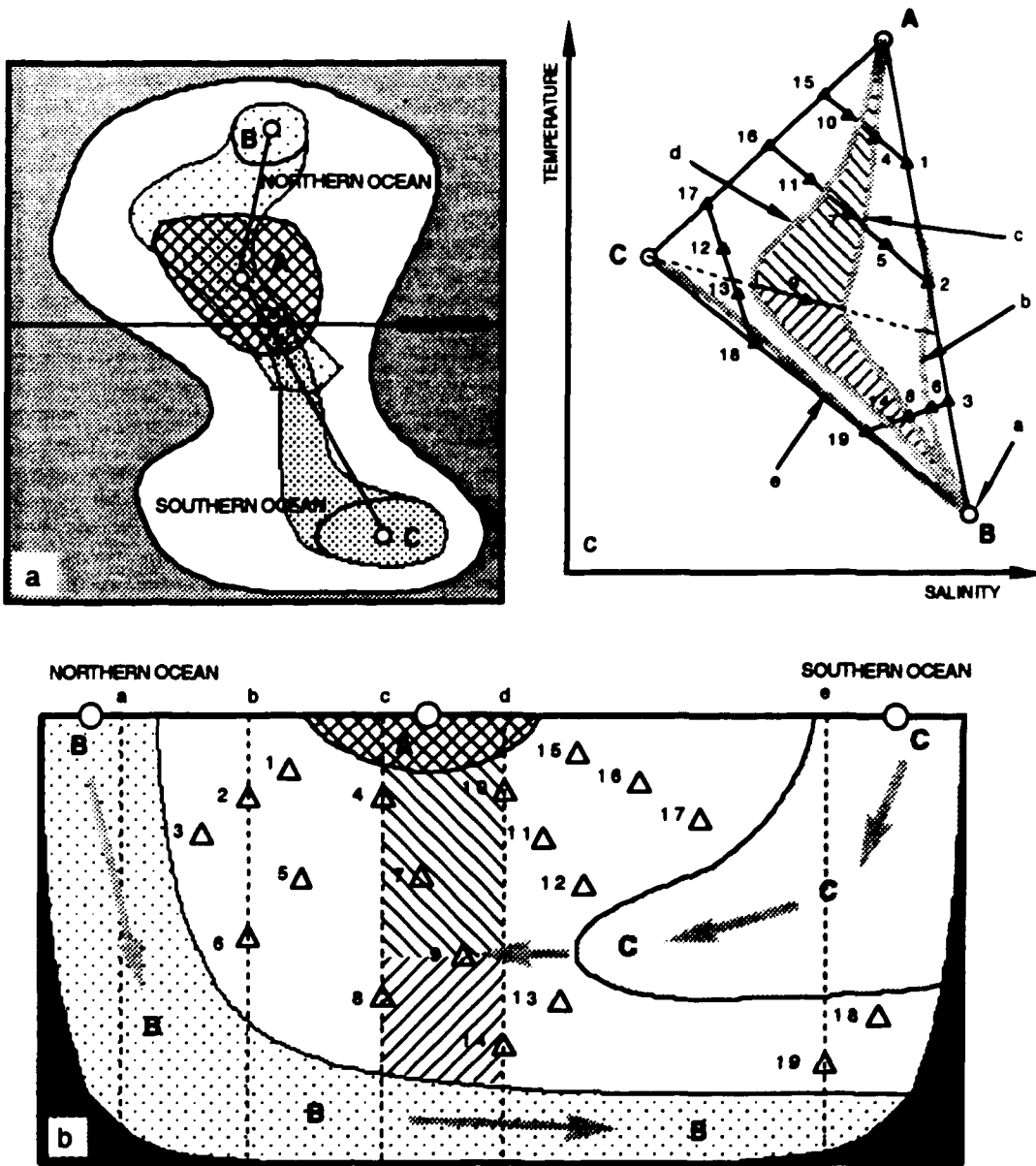


Figure H-1. Cartoon to illustrate the formation, movement and interactions of three water types in a hypothetical ocean using the T-S diagram.

Panel (a) Demonstrates three formation regions and the lateral paths which the resultant water types might follow. Water type A (hatched) is designated tropical ocean surface water with high temperature, moderate salinity and low density. Water type B (sparsely dotted) is a northern ocean deep water with low

(Figure H-1 continued) temperature, high salinity and high density. Water type C (densely dotted) is a southern ocean intermediate water with moderate temperature and density and low salinity. Water type B flows southward along the bottom away from its formation region. Water type C flows northward at depths between A and B.

Panel (b) A vertical ocean section along the line BAC (panel a) showing the pathways the water types follow after formation in the source regions (open dots). Water type B, the densest water, sinks to the bottom after formation and flows southward. Water type A, the lightest water, remains as a lens on the tropical ocean's surface. Water type C sinks to an intermediate depth as it flows toward the equator. In the unshaded regions between A, B and C, the water types are assumed to mix, with the numbered triangles (D) representing differing mixtures between adjacent water types. The vertical dashed lines a to e represent the profiles used for the T-S relationships presented on panel (c).

Panel (c) The T-S diagram illustrating various relationships formed by mixtures between water types A, B, and C. The volume proportions of water types which compose an intermediate water type are inversely related to the distance a point is from the mixed sources in T-S space. For example, mixing between A and B produces the water types 1, 2, and 3. Water type 3 consists of $1/4$ volume A and $3/4$ volume B. Similarly, water type 19 on the C-B mixing line represents a blend of $1/3$ C and $2/3$ B. Water types 6, 8, and 14 are blends of water types 3 and 19. Thus water type 6 is $3/4$ water type 3 and $1/4$ water type 19. It can be shown through simple algebra that water type 6 consists of $(3/16)$ A, $(9/16 + 2/12)$ B and $(1/12)$ C.

The T-S relationship for profile a (panel b) which only passes through water type B, is indicated on panel (c) as the point B. Profile b starts between water types A and B (between 1 and 2) on the ocean's surface, passes through points 2 and 6, and enters water type B at depth. Profile b's T-S relationship is defined by the heavy line labeled b on panel (c). Profile c (and its associated T-S relationship) begins within water type A, passes through 4, between 5 and 7, through 8 and into water type B. Profile d follows a similar route through 10, between 7 and 11, between 9 and 13, and through 14 before entering B. The hatched region which is between c and d in both the hypothetical ocean (panel b) and T-S space (panel c) represents upper and lower intermediate water masses in a region bounded by these profiles. Profile e passes through C, between 13 and 18, through 19 and into B. There is tendency for all T-S relationships between A and B to inflect toward C at the dotted line. This occurs as C, or its products, continues to mix with waters above and beneath. The influence of C is thus felt considerably further north than the extent of its "pure" core.

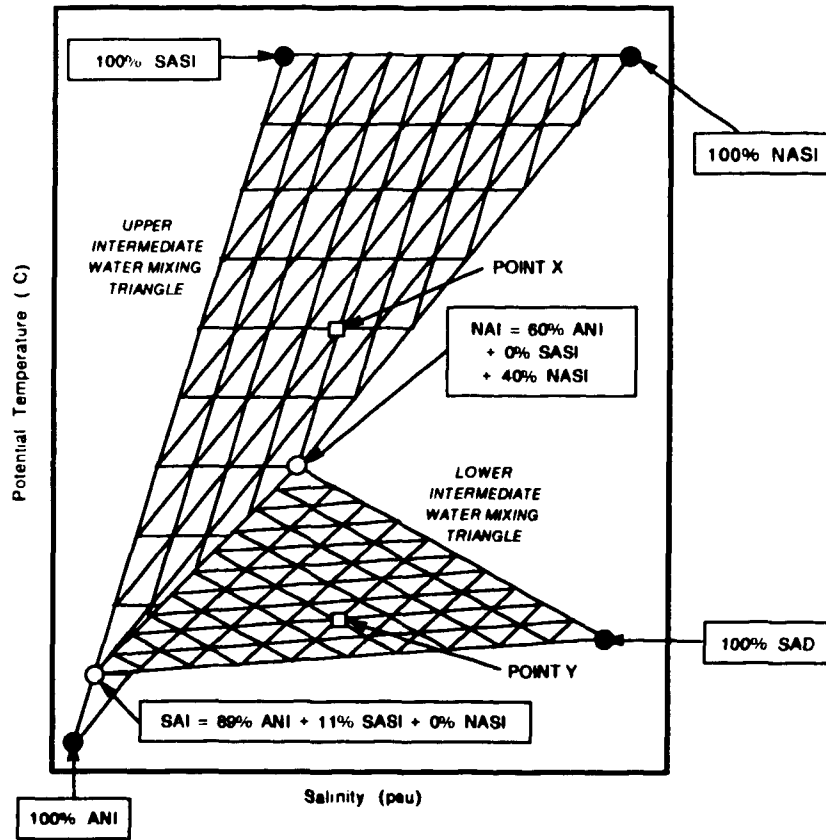


Figure H-2. T-S diagram mixing nomogram for WESTRAX region intermediate waters (based on Mamayev 1975). Solid dots mark the primary water types: Antarctic Intermediate water (ANI); South Atlantic Deep water (SAD), South Atlantic Surface Index (SASI); and North Atlantic Surface Intercept (NASI). Open dots are secondary water types SAI and NAI, as discussed in the text. Parallel lines divide the mixing triangles into 10% intervals between water types ranging from 100% at the vertex to 0% on the opposite side. This drawing is not to scale. The open squares locate examples discussed in the text. The thermohaline index for point "X" is 8 lines removed from SASI, indicating a 20% contribution by that water type. This same point is 6 lines from both ANI and NASI, indicating the contributing ratios by each of these water types is 40%.

APPENDIX I.
WATER MASS STRUCTURE

The water mass structures on horizontal density surfaces and across vertical transects B, C, D, and E are described. The sigma theta 27.00, 27.30, and 27.45 density surfaces are used to represent the water mass structures of the WESTRAX region upper, middle, and lower intermediate layers (Table G-1).

The late summer 1990 water mass structure...

During September 1990 (WESTRAX 2), the southern water masses SACW and AAIW enter the WESTRAX region along the continental slope, retroflect around the Amazon Eddy, and flow eastward into the NEUC (Figures I-1 and I-2). This retroflection of southern water appears to be confined to the southeastern portion of the region, as neither SACW nor AAIW are evident as far west as section C (Figure I-2). There is very little SACW evident on the sigma theta 27.00 surface during September 1990, although the anticyclonic circulation around the Amazon Eddy there is neatly traced by MXU1.

Although AACP appears to trace a large retroflection cell within the lower intermediate layer, such a circulation feature is not evident on the corresponding velocity structure (*cf.* Figures I-1 and F-1). Instead, AACP retroflects within a small area very close to the continental slope. The observation of AACP further to the west at both sections C and D, suggests that most of this southern water mass is being swept northwestward as a part of the Demerara Eddy.

A branch of the northern water mass NACW crosses 9°N and flows southeastward toward the NEUC (see the sigma theta 27.00 and 27.30 surfaces in

Figure I-1). A large area of NACW in the northern part of section D, and a ribbon of NACW within the southern portion of section C, suggest a portion of this northern water mass is flowing anticyclonically around the Demerara Eddy (Figure I-2) and mingling with the northwestward flowing southern water masses.

The winter 1991 water mass structure...

The following January 1991 (WESTRAX 3), the southern water masses SACW, MXU1, AAIW, and AACP all neatly trace the retroflexion around the Amazon Eddy (Figures I-3 and I-4). The larger expanse of these southern water masses (particularly AAIW) across both sections B and C indicate a more northwestward extent of the retroflexion than was evident during the summer (Figure I-3). The mid-level retroflexion of AAIW is extensive and some of this water mass appears to be escaping the Amazon Eddy and flowing northwestward. Areas of MXU1 at sections C, D, and E (and an area of SACW at section E) suggest these southern water masses are feeding across the region in an alongshore current.

At section D, a southeastward flow of MXU1 and MXU2 is evident against the continental shelf as part of the cyclonic circulation around the French Guiana low (*cf.* Figures I-4 and F-5). This undercurrent was observed in the CME model by Schott and Böning (1990). On the sigma theta 27.45 surface, the small area of AACP retroflexion is confined to the extreme southeastern corner of the region. Most of the AACP at this level flows *en mass* southeastward at this time.

The northern water mass NACW is confined to a small portion of the ridge in the northwestern corner, indicating a dominant presence by southern water masses within the region during winter. On the sigma theta 27.00 surface, very little NACW is evident (Figure I-3). No NACW or NACL flows eastward across section B within the NEUC (*cf.* Figures I-4 and F-5).

While the cyclonic circulation around the French Guiana low contains

mostly southern water, some NACW also appears within the southeastward undercurrent which flows toward the Amazon Eddy.

Across section D, the ribbons of NACL within MIXL demonstrate the lower intermediate layer interleaving of water masses, a phenomena which made lower intermediate classification difficult, as mentioned in section V.

The winter 1990 water mass structure...

There are many similarities between the winter water mass structures during January 1991 and February 1990 (WESTRAX 1) (Figures I-5 and I-6). During 1990, the retroflexion of southern water masses is extensive, and once again little NACW contributes to the winter NEUC (Figure I-5). In fact, southern water masses again dominate the upper layer, with NACW confined above 7 N.

On section D (Figure I-6) and on the sigma theta 27.00 surface (Figure I-5), the flow of northern water masses around the French Guiana low and into a southeastward undercurrent is nicely illustrated. The presence of MXU1 on every section again suggests a continuous northwestward flow of this southern water mass during the winter.

The areas of SACW and AACP which are evident at section E, but absent from section D, provide further evidence for the isolation of southern water masses within a retroflexion eddy which has earlier separated from the Amazon Eddy (Figure I-6)

The early summer 1991 water mass structure...

As noted previously, the June 1991 (WESTRAX 4) survey captures the WESTRAX region in a transition period between the summer and winter regimes (Figures I-7 and I-8). Southern water masses cover a large part of section B and, with the exception of AAIW, extend westward into section C (Figure I-7). Northern water masses dominate sections D and E.

On the sigma theta 27.00 and 27.25 surfaces, a meridional ridge is evident along approximately 47.5 W (*cf.* Figure I-7 and F-10). The southern part of this ridge (near 5 N 47 W) is composed mainly of southern water masses, while the northern part contains large proportions of NACW and NACL. This water mass structure, coupled with the velocity structure presented in Appendix F, suggests to me the following scenario: In the north, a large anticyclonic eddy, embedded in the westward flow of the North Atlantic gyre (*e.g.*, the NEC), has moved southwestward into the WESTRAX region. In the south, a retroflection eddy has separating from the Amazon Eddy and moved northward, rather than along the northwestward track of most retroflection eddies (see section IV). At the time of the WESTRAX 4 survey, these anticyclones are in the process of merging.

Compared with the previous analyses, there is a larger amount of water mass fragmentation during June 1991. This is illustrated by the ribbons which cross sections B and C, and the spotty distribution of water masses on the sigma theta 27.45 surface.

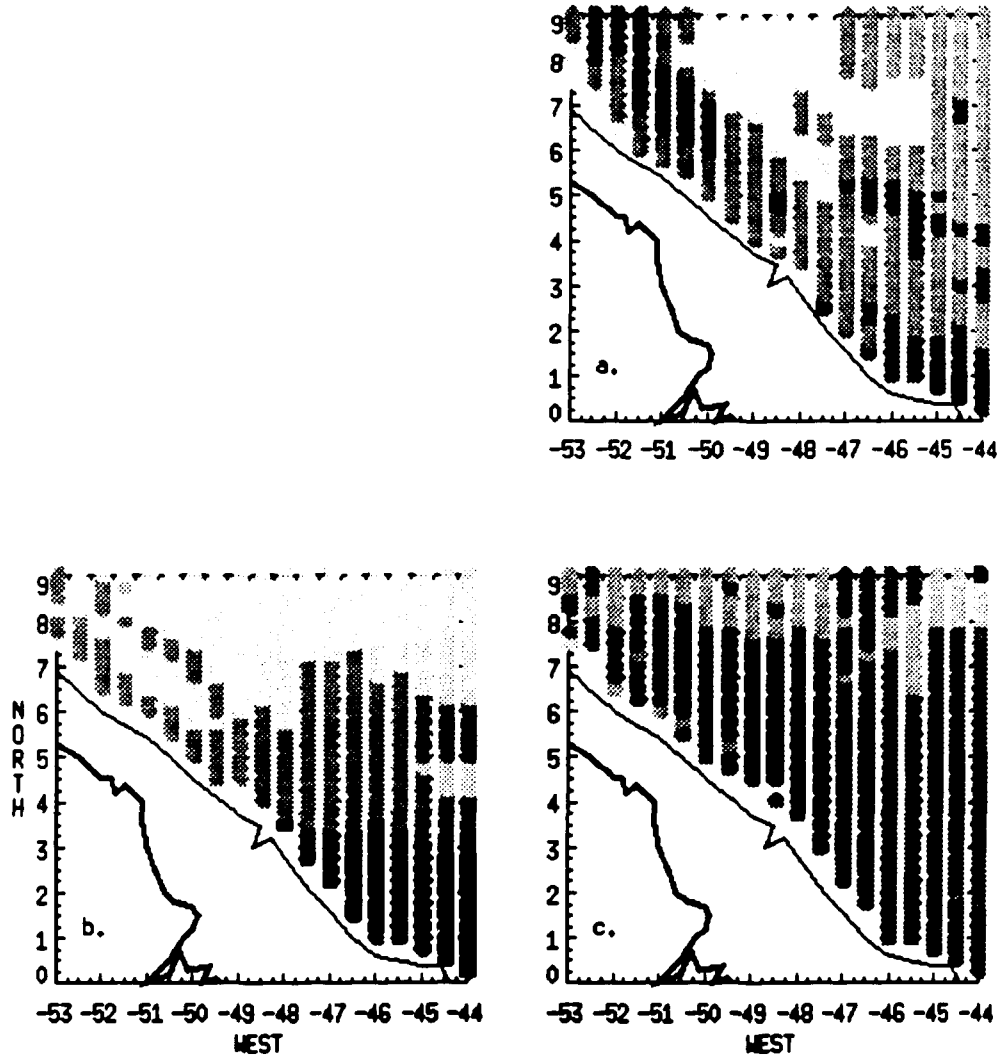


Figure I-1. Water mass distribution on representative density surfaces during September 1990 (WESTRAX 2). Water masses are coded by layer from southern (darkest) to northern (lightest) on the sigma theta surfaces:
 (a) 27.00 (upper intermediate layer): SACW, MXU1, MXU2, NACW
 (b) 27.25 (middle or Antarctic Intermediate layer): AAIW, MXU2, NACW
 (c) 27.45 (lower intermediate layer): AACP, upper branch, MIXL, NACL.

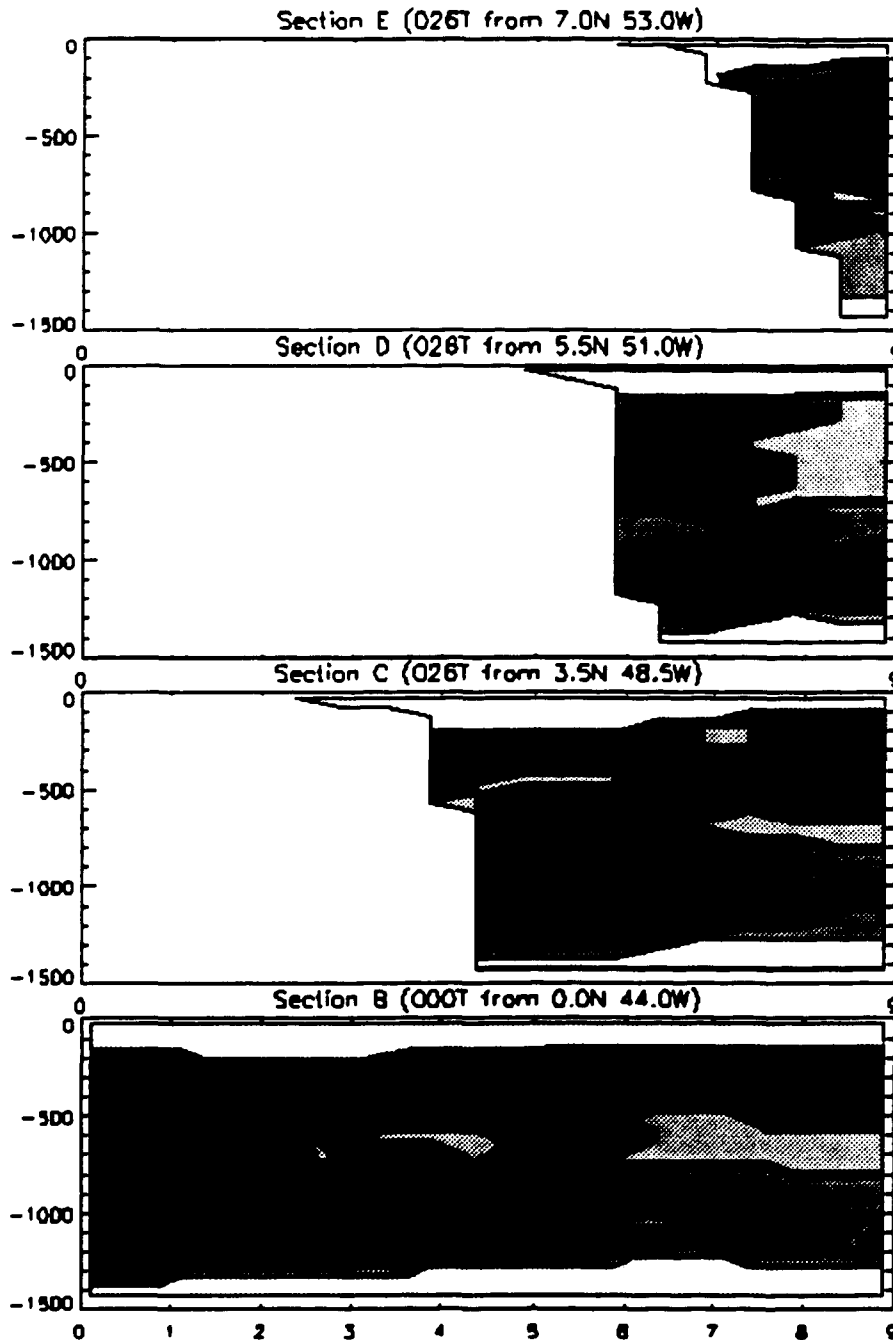


Figure I-2. Intermediate water mass structure across sections B, C, D, and E during September 1990 (WESTRAX 2). Viewed looking westward, vertical sections extend from the equator to 9°N. Water masses are coded by layer from southern (dark) to northern (light):

Upper layer - SACW, MXU1, MXU2, and NACW

Middle layer - AAIW (darkest)

Lower layer - AACW, upper branch, MIXL, and NACL

The surface layer above, and NADW below, are very light.

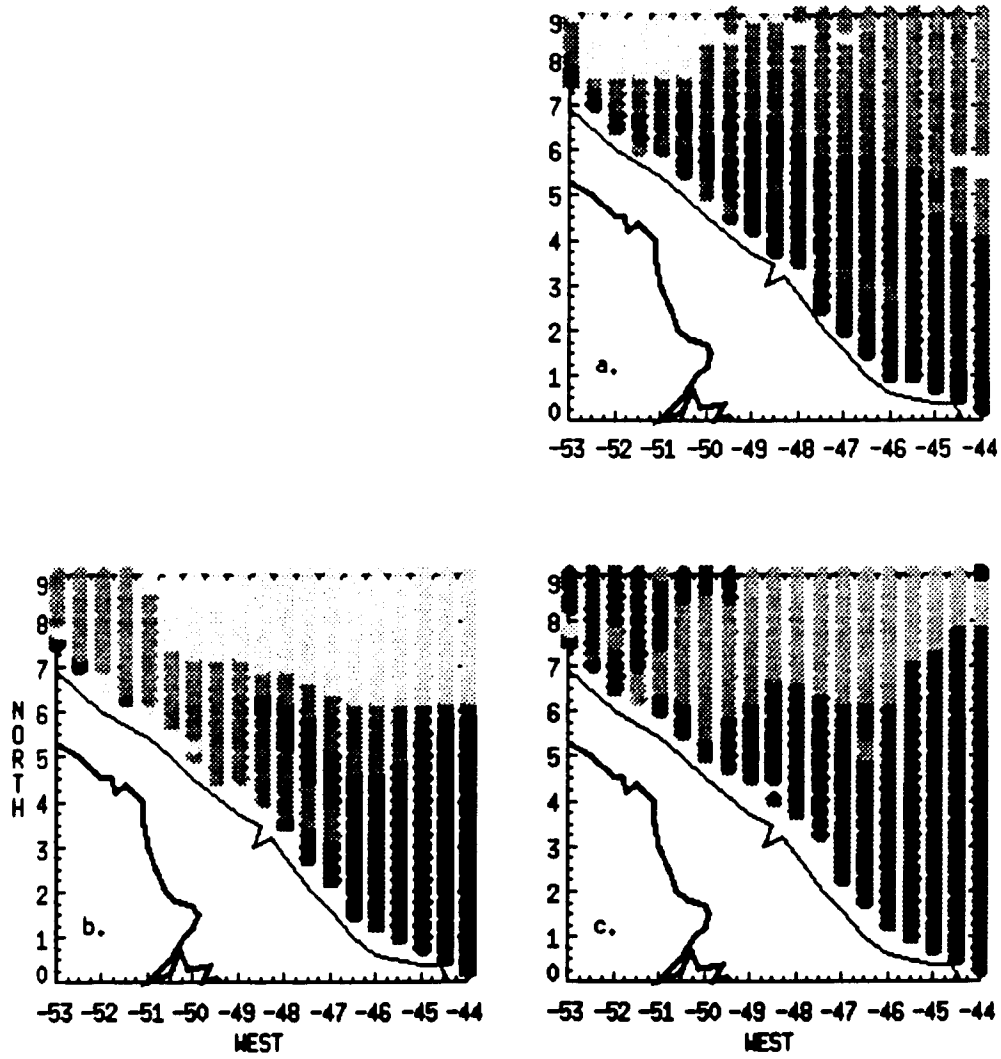


Figure I-3. Same as Figure I-1 for January 1991 (WESTRAX 3).

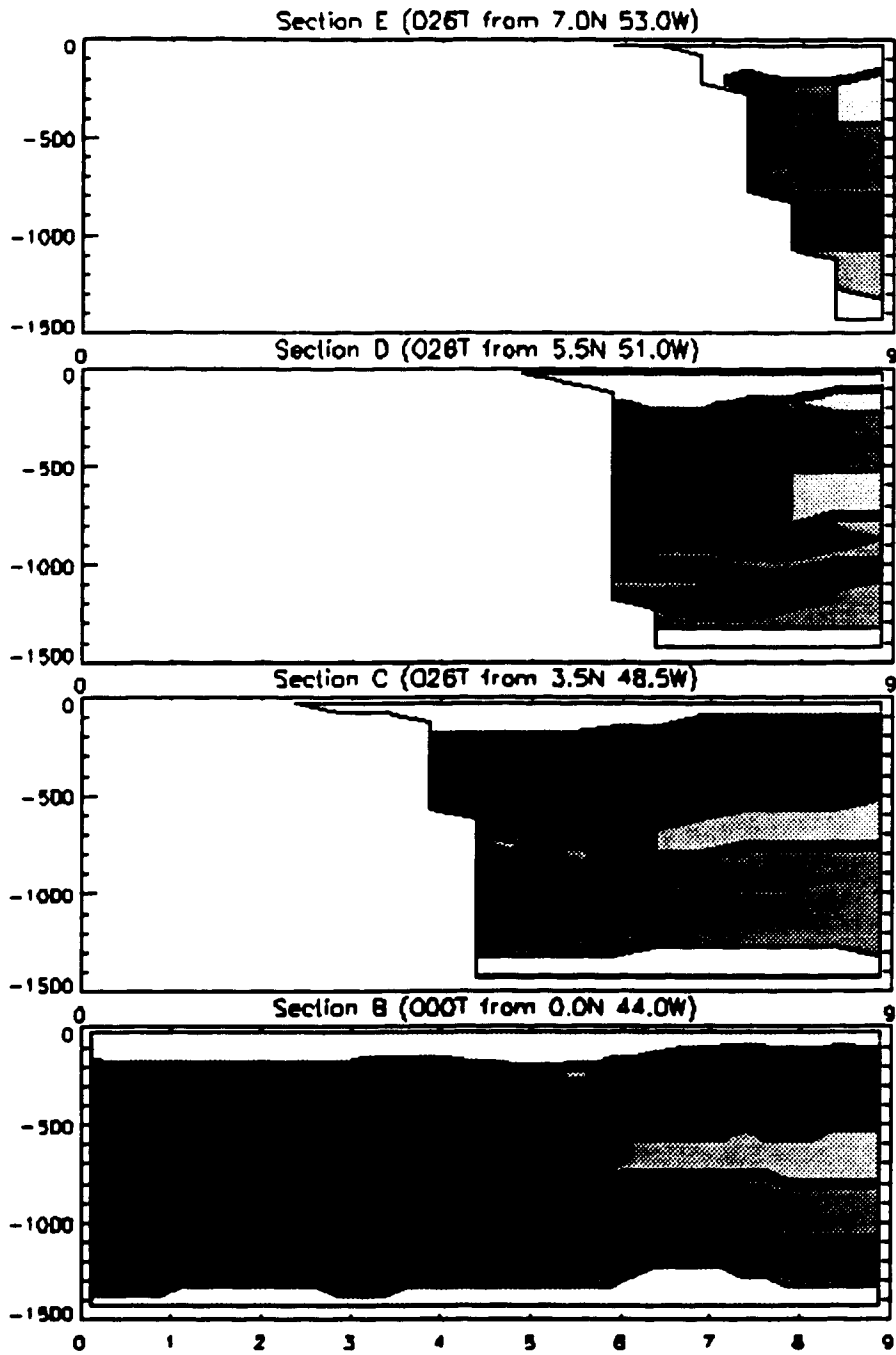


Figure I-4. Same as Figure I-2 for January 1991 (WESTRAX 3).

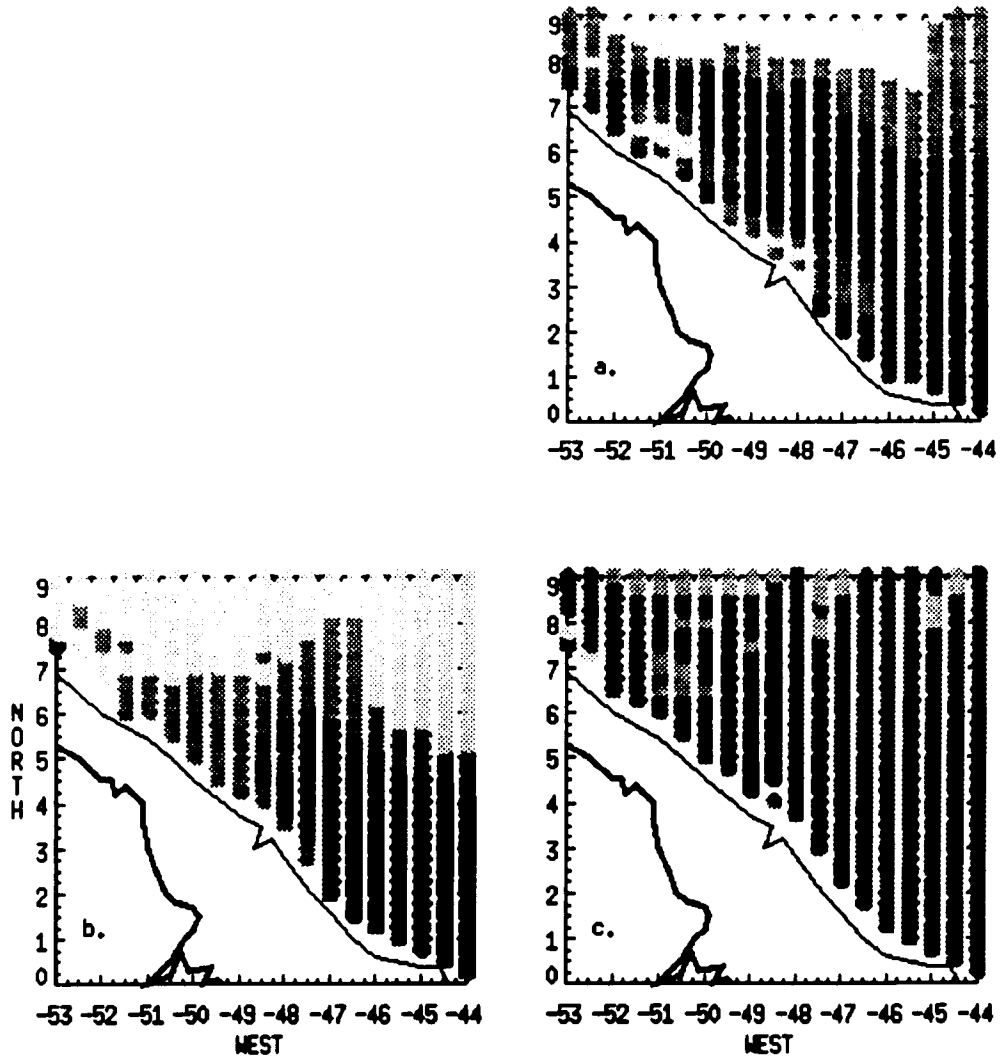


Figure I-5. Same as Figure I-1 for February 1990 (WESTRAX 1).

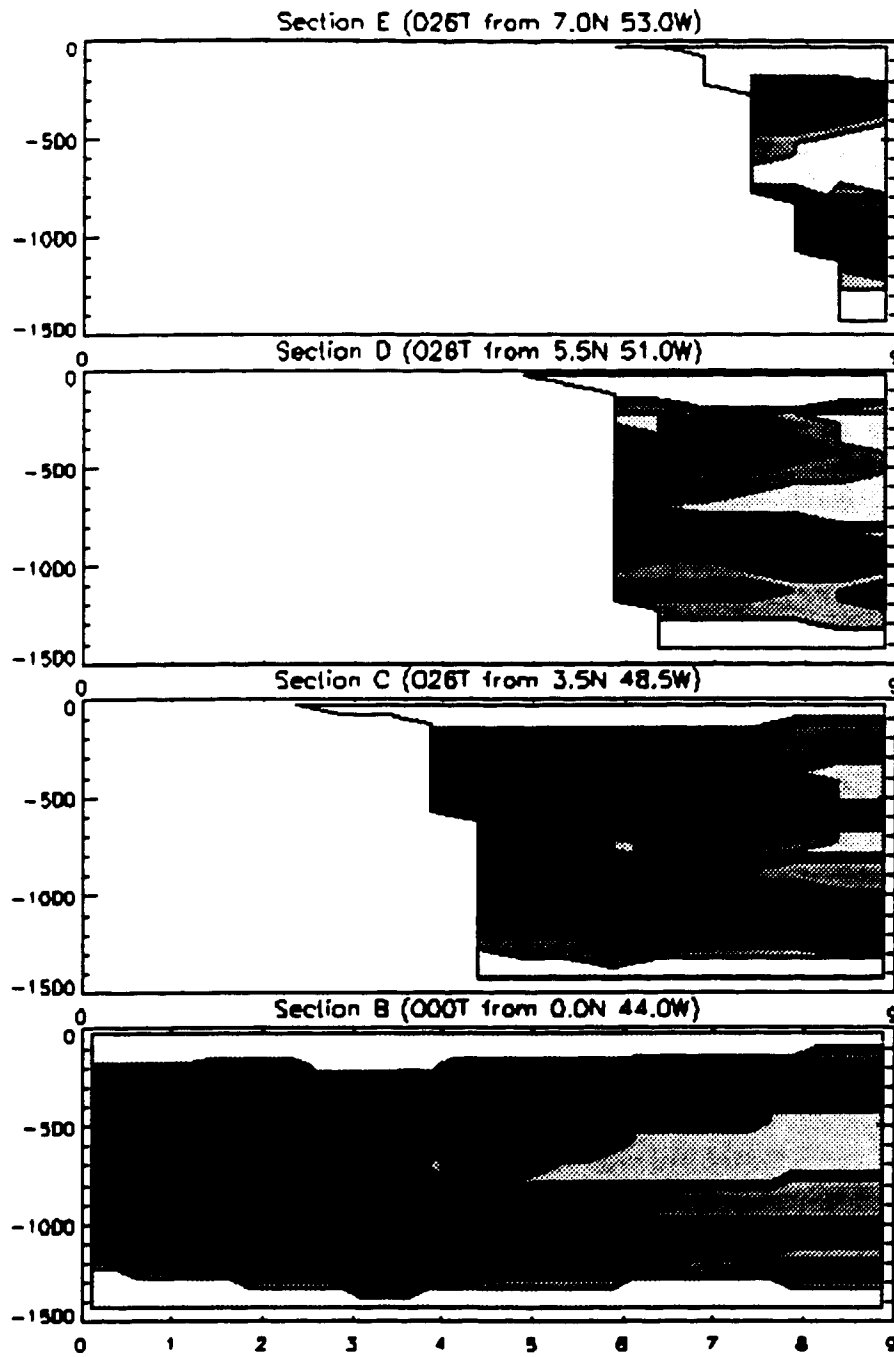


Figure I-6. Same as Figure I-2 for February 1990 (WESTRAX 1).

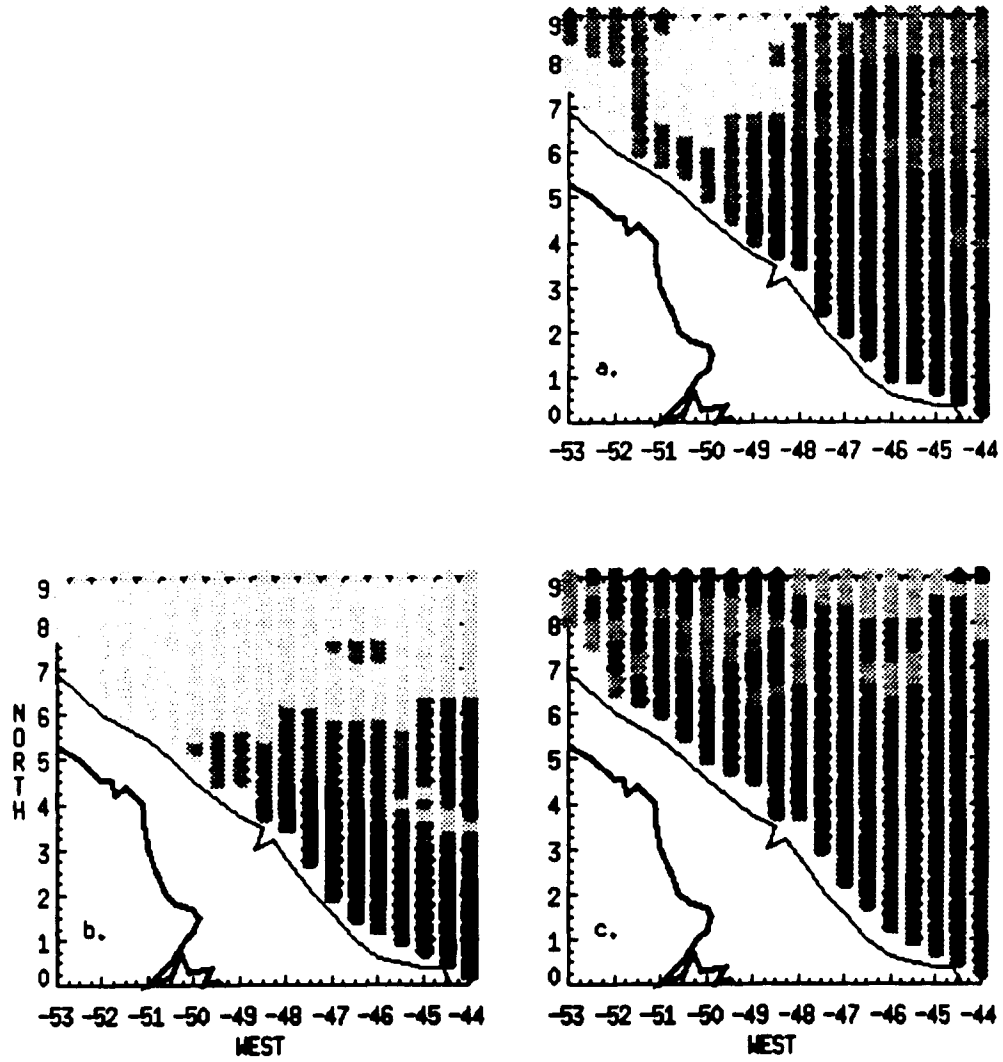


Figure I-7. Same as Figure I-1 for June 1991 (WESTRAX 4).

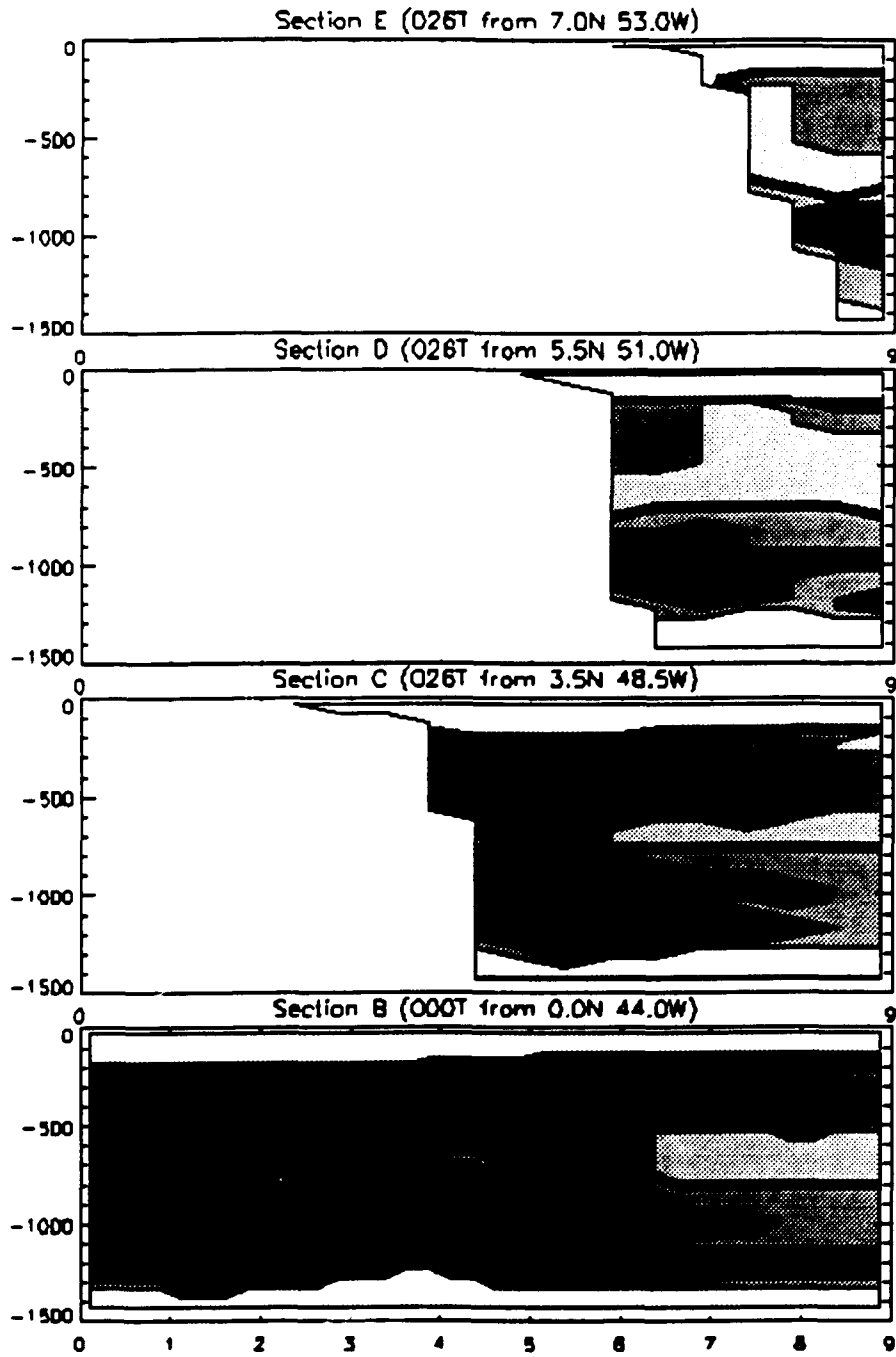


Figure I-8. Same as Figure I-2 for June 1991 (WESTRAX 4).

APPENDIX J.

VOLUME, SALT, TEMPERATURE, AND FRESHWATER TRANSPORT CALCULATIONS

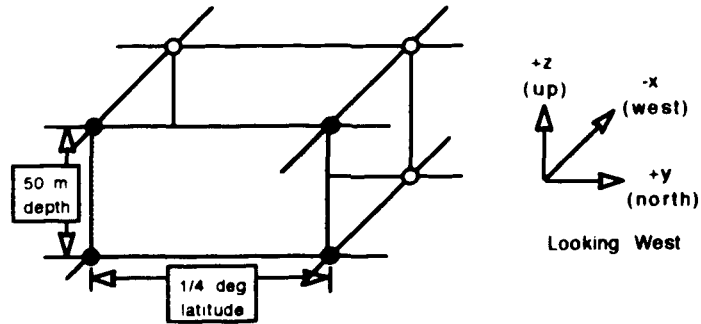


Figure J-1. Segment on east-west oriented section.

The volume transport (VT) in Sverdrups ($1 \text{ Sv} = 10^6 \text{ m}^3/\text{s}$) through each $1/4$ degree wide by 50 m deep segment (Figure J-1) was computed according to

$$VT = A \times \bar{V} \quad (\text{J-1a})$$

where the segment area is

$$A = (0.25 \text{ deg}) \times (50 \text{ m}) \times \frac{111.1 \text{ km}}{\text{deg}} \times \frac{1000 \text{ m}}{\text{km}} = 1.3888 \times 10^6 \text{ m}^2 . \quad (\text{J-1b})$$

and \bar{V} is the mean of the velocities at the four corners of the segment (the dots on Figure J-1) according to

$$\bar{V} = \bar{v} \frac{\text{cm}}{\text{s}} \times \frac{1 \text{ m}}{100 \text{ cm}} = \bar{v} \times 10^{-2} \frac{\text{m}}{\text{s}} . \quad (\text{J-1c})$$

VT is thus determined by

$$\begin{aligned}
 VT &= A \times \bar{V} = (1.3888 \times 10^6 \text{ m}^2) \times \frac{1 \text{ m}}{100 \text{ cm}} \times (\bar{v} \times 10^{-2} \frac{\text{m}}{\text{s}}) = \\
 &\bar{v} \times 1.3888 \times 10^4 \frac{\text{m}^3}{\text{s}} \times \frac{1 \text{ Sv}}{10^6 \frac{\text{m}^3}{\text{s}}} = \\
 &\bar{v} \times 1.3888 \times 10^{-2} \text{ Sv} ,
 \end{aligned}$$

$$\text{with } \bar{v} \text{ in cm/s.} \quad (\text{J-1d})$$

Salt mass transport (SMT) is computed after assuming that the mean density of sea water is 1027 kg/m^3 . The salinity of a segment is the mean of the salinities at the four corners (\bar{S} psu or parts per thousand) and the mass of salt (SM) in a cubic meter of sea water is determined by

$$SM = \bar{S} \times 10^{-3} \times 1027 \frac{\text{kg}}{\text{m}^3} = \bar{S} \times 1.027 \frac{\text{kg}}{\text{m}^3} . \quad (\text{J-2a})$$

For each cubic meter of water transported, the salt mass transport (SMT) through a segment is thus

$$\begin{aligned}
 \text{SMT} &= \bar{S} \times 1.027 \frac{\text{kg}}{\text{m}^3} \times VT \text{ Sv} = (\bar{S} \times 1.027 \frac{\text{kg}}{\text{m}^3}) \times (\bar{v} \times 1.3888 \times 10^4 \frac{\text{m}^3}{\text{s}}) = \\
 &(\bar{S} \times \bar{v}) \times 1.4263 \times 10^4 \frac{\text{kg}}{\text{s}} \times \frac{1 \text{ metric ton}}{1000 \text{ kg}} = \\
 &(\bar{S} \times \bar{v}) \times 14.263 \frac{\text{metric ton}}{\text{s}} ,
 \end{aligned}$$

$$\text{with } \bar{v} \text{ in cm/s and } \bar{S} \text{ in psu.} \quad (\text{J-2b})$$

Temperature transport (TT) for each segment is computed relative to 0°C. After volume transport (VT) is determined and the temperature at each corner averaged to produce \bar{T}

$$TT = (\bar{T} - C) \times (VT Sv) = \bar{T} \times VT (C - Sv) =$$

$$(\bar{T} \times \bar{v}) \times 1.3888 \times 10^4 \frac{C \cdot m^3}{s},$$

$$\text{with } \bar{v} \text{ in cm/s and } \bar{T} \text{ in } ^\circ\text{C.} \quad (J-3)$$

Freshwater mass transport (FWMT) is computed by subtracting the mass transport of salt from the mass transport of saltwater. By again assuming the mean density of seawater is 1027 kg/m^3 , the saltwater mass transport (SWMT) is

$$SWMT = (VT Sv) \times (1027 \frac{\text{kg}}{\text{m}^3}) = VT \times 1.027 \times 10^3 \frac{\text{Sv} \cdot \text{kg}}{\text{m}^3}. \quad (J-4a)$$

Freshwater mass transport is thus

$$\begin{aligned} FWMT &= SWMT - SMT = VT \times 1.027 \times 10^3 \frac{\text{Sv} \cdot \text{kg}}{\text{m}^3} - \bar{S} \times 1.027 \frac{\text{kg}}{\text{m}^3} \times VT Sv = \\ &VT \times 1.027 \frac{\text{Sv} \cdot \text{kg}}{\text{m}^3} (1000 - \bar{S}). \end{aligned} \quad (J-4b)$$

Freshwater volume transport (FWVT) is then determined by dividing by a mean freshwater density of 1000 kg/m^3

$$FWVT = \frac{FWMT}{1000 \frac{\text{kg}}{\text{m}^3}} = \frac{VT \times 1027 \frac{\text{Sv} \cdot \text{kg}}{\text{m}^3} (1 - \bar{S}/1000)}{1000 \frac{\text{kg}}{\text{m}^3}} =$$

$$VT \times (1 - \bar{S}/1000) \times 1.027 \text{ Sv},$$

$$\text{with } VT \text{ in Sv and } \bar{S} \text{ in psu.} \quad (J-4c)$$

LIST OF REFERENCES

- Akima, H. (1978) "A Method of Bivariate Interpolation and Smooth Surface Fitting for Irregularly Distributed Data Points," *ACM Transactions on Mathematical Software*, 4 (2), 148-159.
- Brown, W. S., W. E. Johns, K. D. Leaman, et al. (1992) "A Western Tropical Atlantic Experiment (WESTRAX)," *Oceanography*, 5(1), 73-77.
- Bruce, J. G. (1984) "Comparison of Eddies off the North Brazilian and Somali Coasts," *Journal of Physical Oceanography*, 14(4), 825-832.
- Bruce, J. G. and J. L. Kerling (1984) "Near Equatorial Eddies in the North Atlantic," *Geophysical Research Letters*, 11 (8), 779-782.
- Carton, J. A. and E. J. Katz (1990) "Estimates of the Zonal Slope and Seasonal Transport of the Atlantic North Equatorial Countercurrent," *Journal of Geophysical Research*, 95 (C3), 3091-3100.
- Clare, F., D. Kennison and B. Lackman (1987) *NCAR Graphics User's Guide (Version 2.0 ed.)* Boulder, CO, National Center for Atmospheric Research, 643.
- Cochrane, J. D. (1963) "Equatorial Undercurrent and Related Currents off Brazil in March and April 1963," *Science*, 142, 669-671.
- Cochrane, J. D. (1969) "Low Sea-surface Salinity off Northeastern South America in Summer 1964," *Journal of Marine Research*, 27(3), 327-334.
- Cochrane, J. D., F. J. Kelly and C. R. Olling (1979) "Subthermocline Countercurrents in the Western Equatorial Atlantic Ocean," *Journal of Physical Oceanography*, 9(7), 724-738.
- Cromwell, T., R. B. Montgomery, and E. D. Stroup (1954) "Equatorial Undercurrent in the Pacific Ocean Revealed by New Methods," *Science*, 119, 648-649.
- Emery, W. J. (1975) "Dynamic Height from Temperature Profiles," *Journal of Physical Oceanography*, 5(4), 369-375.
- Emery, W. J. and J. S. Dewar (1982) "Mean Temperature-Salinity, Salinity-Depth and Temperature-Depth Curves for the North Atlantic and North Pacific," *Progress in Oceanography*, 11, 219-305.
- Emery, W. J. and J. Meincke (1986) "Global Water Masses: Summary and Review," *Oceanologica Acta*, 9(4), 383-391.
- Flagg, C. N., R. L. Gordon and S. McDowell (1986) "Hydrographic and Current Observations on the Continental Slope and Shelf of the Western Equatorial Atlantic," *Journal of Physical Oceanography*, 16 (8), 1412-1429.
- Fofonoff, N. P. and R. C. Millard Jr. (1983) *Algorithms for Computation of*

Fundamental Properties of Seawater (Unesco Technical Papers in Marine Sciences 44) Unesco, 53.

- Garzoli, S. L. and E. J. Katz (1983) "The Forced Annual Reversal of the Atlantic North Equatorial Countercurrent," *Journal of Physical Oceanography*, 13 (11), 2082-2090.
- Johns, E., and A. M. Wilburn (1993) *Hydrographic Observations in the Western Tropical and Subtropical North Atlantic Ocean: Atlantic Climate Change Program (ACCP) and Western Tropical Atlantic Experiment (WESTRAX) during 1991 (ERL AOML-23)*, Atlantic Oceanographic and Meteorology Laboratory, Miami, FL March 1993.
- Johns, W. E., T. N. Lee, F. Schott, et al. (1990) "The North Brazil Current Retroreflection: Seasonal Structure and Eddy Variability," *Journal of Geophysical Research*, 95 (C12), 22103-22120.
- Katz, E. J. (1981) "Dynamic Topography of the Sea Surface in the Equatorial Atlantic," *Journal of Marine Research*, 39(1), 53-63.
- Leaman, K. D. and P. S. Vertes (1983) *The Subtropical Atlantic Climate Study (STACS), 1982: Summary of RSMAS "Pegasus" Observations in the Florida Straits (83012)*, University of Miami, Rosenstiel School of Marine and Atmospheric Science
- Mamayev, O. I. (1975) *Temperature-Salinity Analysis of World Ocean Waters* Amsterdam: Elsevier 374.
- Mayer, D. A. and R. H. Weisberg (1993) "A Description of COADS Surface Meteorological Fields and the Implied Sverdrup Transports for the Atlantic Ocean from 30°N to 60°N," *Journal of Physical Oceanography* (23) (10) 2201-2221.
- McCartney, M. S. (1993) "Crossing of the Equator by the Deep Western Boundary Current in the Western Atlantic Ocean," *Journal of Physical Oceanography*, 23 (9) 1953-1974.
- Metcalf, W. G. (1968) "Shallow Currents Along the Northeastern Coast of South America," *Journal of Marine Research*, 26(3), 232-244.
- Metcalf, W. G. and M. C. Stalcup (1967) "Origin of the Atlantic Equatorial Undercurrent," *Journal of Geophysical Research*, 72,(C5), 4959-4975.
- Metcalf, W. G., A. D. Voorhis and M. C. Stalcup (1962) "The Atlantic Equatorial Undercurrent," *Journal of Geophysical Research*, 67(6), 2499-2508.
- Molinari, R. L., B. Voituriez and P. Duncan (1981) "Observations in the Subthermocline Undercurrent of the Equatorial South Atlantic Ocean: 1978-1980," *Oceanologica Acta*, 4(4), 451-456.
- Neumann, G. (1960) "Evidence for an Equatorial Undercurrent in the Atlantic Ocean," *Deep Sea Research*, 6, 328-334.
- Peterson, R. G. and L. Stramma (1991) "Upper Level Circulation in the South Atlantic Ocean," *Progress in Oceanography*, 26, 1-73.

- Philander, S. G. H. and R. C. Pacanowski (1986a) "The Mass and Heat Budget in a Model of the Tropical Atlantic Ocean," *Journal of Geophysical Research*, 91 (C12), 14212-14220.
- Philander, S. G. H. and R. C. Pacanowski (1986b) "A Model of the Seasonal Cycle in the Tropical Atlantic Ocean," *Journal of Geophysical Research*, 91 (C12), 14192-14206.
- Reid, J. L. (1989) "On the Total Geostrophic Circulation of the South Atlantic Ocean: Flow Patterns, Tracers, and Transports," *Progress in Oceanography*, 23, 149-244.
- Reid, J. L., W. D. Nowlin and W. C. Patzert (1977) "On the Characteristics of the South Atlantic Ocean," *Journal of Physical Oceanography*, 7(1), 62-91.
- Richardson, P. L., G. Hufford, R. Limeburner, W. S. Brown (1993) "North Brazil Current Retroflection Eddies," *Journal of Geophysical Research* (submitted)
- Routt, J. A., and W. D. Wilson (1992), *Shipboard Acoustic Doppler Current Profiler Data Collected during the Western Tropical Atlantic Experiment (WESTRAX) 1991 (ERL AOML-72)*, Atlantic Oceanographic and Meteorology Laboratory, Miami, FL November 1992.
- Schmitz, W. J., Jr. and M. S. McCartney (1993) "On the North Atlantic Circulation," *Reviews of Geophysics*, 31 (1), 29-49.
- Schott, F. A. and C. W. Böning (1991) "The WOCE Model in the Western Equatorial Atlantic: Upper Layer Circulation," *Journal of Geophysical Research*, 96 (C4), 6993-7004.
- Send, U. (1993) "The Accuracy of Current Profile Measurements - Effect of Tropical and Mid-latitude Internal Waves," *Journal of Geophysical Research*, (submitted)
- Spain, P. F., D. L. Dorson and H. T. Rossby (1981) "PEGASUS: A Simple, Acoustically Tracked, Velocity Profiler," *Deep Sea Research*, 28A (12), 1553-1567.
- Sverdrup, H. U., M. W. Johnson, and R. H. Fleming, (1942). *The Oceans, Their Physics, Chemistry and General Biology*. Prentice-Hall, Inc., Englewood Cliffs, NJ, 1087.
- Tomczak, M., and D. G. B. Large, "Optimum Multiparameter Analysis of Mixing in the Thermocline of the Eastern Indian Ocean," *Journal of Geophysical Research*, 94(C11), 16141-16149.
- Worthington, L. V. (1976) *On the North Atlantic Circulation* Baltimore: Johns Hopkins University Press 110.
- Wunsch, C., and Barbara Grant (1982) "Towards the General Circulation of the North Atlantic Ocean," *Progress in Oceanography*, 11, 1-59.